

**NASA CONTRACTOR
REPORT**

NASA CR-1235



NASA
CR
1233
v.3
c.1

NASA CR-1235



TECH LIBRARY KAFB, NM

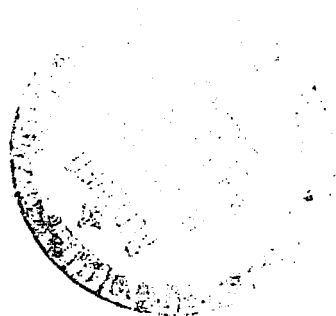
LOAN COPY: RETURN TO
AFWL (WLIL-2)
KIRTLAND AFB, N MEX

A LUNAR GRAVITY SIMULATOR

VOLUME III

by Dennis A. Millett

Prepared by
CASE WESTERN RESERVE UNIVERSITY
Cleveland, Ohio
for Langley Research Center



NATIONAL AERONAUTICS AND SPACE ADMINISTRATION • WASHINGTON, D. C. • DECEMBER 1968



0060561

NASA CR-1235

A LUNAR GRAVITY SIMULATOR

VOLUME III

By Dennis A. Millett

Distribution of this report is provided in the interest of information exchange. Responsibility for the contents resides in the author or organization that prepared it.

From a thesis entitled "The Design of a Magnetic Air Bearing for Use in a Lunar Gravity Simulator" submitted to Case Institute of Technology in partial fulfillment of the requirement for the Degree of Master of Science in Mechanical Engineering.

Prepared under Contract No. NAS 1-7459 by
CASE WESTERN RESERVE UNIVERSITY
Cleveland, Ohio

for Langley Research Center

NATIONAL AERONAUTICS AND SPACE ADMINISTRATION

For sale by the Clearinghouse for Federal Scientific and Technical Information
Springfield, Virginia 22151 - CFSTI price \$3.00

ABSTRACT

Magnetic air bearings for use as low friction overhead support fixtures in a vertical lunar gravity simulator are investigated. This device consists of a flat magnetic disc with a central air orifice. The theoretical analyses of the air bearing are in good agreement with experiment. Theoretical magnet force ranges from 15% to 35% above the experimental value. Disc ceramic magnets are theoretically optimized based on maximum force-to-weight ratio and design curves are presented.

TABLE OF CONTENTS

	<u>Page</u>
ABSTRACT	iii
TABLE OF CONTENTS.	v
LIST OF ILLUSTRATIONS	viii
LIST OF SYMBOLS	xiii

Section

1.0 INTRODUCTION	1
2.0 THEORETICAL AND EXPERIMENTAL ANALYSIS OF THE AIR BEARING	4
2.1 THE SUPPLY ORIFICE	8
2.2 ANALYSIS OF SUPERSONIC FLOW	12
2.3 THE SUBSONIC FLOW REGION	22
2.4 THE SHOCK WAVE	33
2.5 THEORETICAL LOAD GAP CHARACTERISTICS	37
2.6 COMPARISON OF THEORETICAL AND EXPERIMENTAL RESULTS	61
2.7 DISCUSSION OF SECONDARY EFFECTS.	77
3.0 THEORETICAL AND EXPERIMENTAL ANALYSIS OF THE MAGNET	79
3.1 SURVEY OF POTENTIAL MAGNET DESIGNS.	79

<u>Section</u>	<u>Page</u>
3.2 MAGNETIC MATERIALS	85
3.3 ANALYSIS OF DISC CERAMIC MAGNET FORCE CHARACTERISTICS	91
3.3.1 The Magnetic Circuit	93
3.3.2 Electrical Analogy.	96
3.3.3 The Energy in the Magnetic Field System.	105
3.3.4 Magnetic Reluctance	110
3.3.5 Flux Density Distribution in the Shell and Ceiling.	130
3.3.6 Theoretical Magnet Force Characteristic	142
3.4 MAGNET OPTIMIZATION.	151
3.5 COMPARISON OF THEORETICAL AND EXPERIMENTAL RESULTS	165
4.0 MAGNETIC AIR BEARING DESIGN.	174
5.0 CONCLUSION	188
List of References	190

<u>Section</u>	<u>Page</u>
Appendix A - Dynamic Analysis of the Case Vertical Suspension Type Simulator.	192
Appendix B - Computer Program for Predicting Air Bearing Performance	207
Appendix C - Theoretical Air Force Versus Gap Characteristics	211
Appendix D - Computer Programs for Predicting and Optimizing Magnet Performance .	229

LIST OF ILLUSTRATIONS

<u>Figure No.</u>		<u>Page</u>
2.1	Flow Chart for Air Bearing Computer Program	38
2.2	Theoretical Pressure Distribution	44
2.3	Theoretical Shock Wave Position Versus Air Gap	45
2.4	Theoretical Flow Versus Air Gap	46
2.5	Theoretical Air Force Versus Gap.	48
2.6	Stiffness Versus Orifice Radius - 3" Outside Radius.	51
2.7	Stiffness Versus Orifice Radius - 2" Outside Radius.	52
2.8	Stiffness Versus Orifice Radius - 1" Outside Radius.	53
2.9	Stiffness Versus Outside Radius - .0625" Orifice Radius	55
2.10	Stiffness Versus Outside Radius - .09375" Orifice Radius	56
2.11	Stiffness Versus Outside Radius - .125" Orifice Radius.	57
2.12	No Load Gap Versus Orifice Radius - 3" Outside Radius.	59
2.13	No Load Gap Versus Orifice Radius - 2" Outside Radius.	60

<u>Figure No.</u>		<u>Page</u>
2.14	Apparatus for Measuring Air Bearing Characteristics	62
2.15	Slider Plate and Test Bearing.	63
2.16	Comparison of Theoretical and Experimental Pressure Profiles	64
2.17	Comparison of Theoretical and Experimental Flow Characteristics	66
2.18	Air Bearing Flow Gradient Versus Orifice Radius	68
2.19	Comparison of Theoretical and Experimental Air Bearing Force Characteristics - 3" Outside Radius, .0625" Inside Radius, 70 psig Supply Pressure.	69
2.20	Comparison of Theoretical and Experimental Air Bearing Force Characteristics - 3" Outside Radius, .09375" Inside Radius, 50 psig Supply Pressure.	70
2.21	Comparison of Theoretical and Experimental Air Bearing Force Characteristics - 3" Outside Radius, .125" Inside Radius, 50 psig Supply Pressure.	71
2.22	Comparison of Theoretical and Experimental Air Bearing Force Characteristics - 2" Outside Radius, .15625" Inside Radius, 70 psig Supply Pressure.	72
2.23	Comparison of Theoretical and Experimental Air Bearing Force Characteristics - 1" Outside Radius, .15625" Inside Radius, 50 psig Supply Pressure.	73

<u>Figure No.</u>		<u>Page</u>
2.24	Comparison of Theoretical and Experimental Air Bearing Force Characteristics - 2" Outside Radius, .1875" Inside Radius, 50 psig Supply Pressure.	74
2.25	Comparison of Theoretical and Experimental Air Bearing Force Characteristics - 1" Outside Radius, .1875" Inside Radius, 70 psig Supply Pressure.	75
3.1	Potential Magnet Designs	81
3.2	Force Characteristics of Potential Magnet Designs.	82
3.3	Force-to-Weight Ratio of Potential Magnet Designs Versus Air Gap.	83
3.4	Demagnetization Curves for Two Oriented Barrium Ferrite Materials	86
3.5	Virgin Magnetization Curves for Soft Magnetic Materials	90
3.6	Geometries of Inside and Outside Shell Designs	111
3.7	Radial Flux Density Distribution in the Design A Shell at Zero Gap.	133
3.8	Radial Flux Density Distribution in the Design B Shell at Zero Gap.	137
3.9	Curves for Optimum Design of Inside Shell Magnet - Indox VI-A, 16 Kilogauss Flux Density	155
3.10	Magnetic Force and Weight of Optimum Inside Shell Magnet - Indox VI-A, 16 Kilogauss Flux Density	156

<u>Figure No.</u>	<u>Page</u>
3.11 Curves for Optimum Design of Inside Shell Magnet - Indox VI-A, 14 Kilogauss Flux Density	157
3.12 Magnetic Force and Weight of Optimum Inside Shell Magnet - Indox VI-A, 14 Kilogauss Flux Density	158
3.13 Curves for Optimum Design of Inside Shell Magnet - Indox V, 16 Kilogauss Flux Density	159
3.14 Magnetic Force and Weight of Optimum Inside Shell Magnet - Indox V, 16 Kilogauss Flux Density	160
3.15 Curves for Optimum Design of Inside Shell Magnet - Indox V, 14 Kilogauss Flux Density	161
3.16 Magnetic Force and Weight of Optimum Inside Shell Magnet - Indox V, 14 Kilogauss Flux Density	162
3.17 Comparison of Theoretical and Experimental Magnet Force Characteristics - Outside Shell Design	166
3.18 Comparison of Theoretical and Experimental Magnet Force Characteristics - Outside Shell Design	167
3.19 Comparison of Theoretical and Experimental Magnet Force Characteristics - Outside Shell Design	168
3.20 Comparison of Theoretical and Experimental Magnet Force Characteristics - Inside Shell Design	169

<u>Figure No.</u>		<u>Page</u>
3.21	Comparison of Theoretical and Experimental Magnet Force Characteristics - Inside Shell Design	170
3.22	Mean Error Between Theoretical and Experimental Magnet Force and K Factor Versus Air Gap	172
4.1	Inside Shell Magnetic Air Bearing	176
4.2	Theoretical Air Force at 6 Mils Versus Orifice	181
4.3	Prototype Magnetic Air Bearing Cluster.	185
4.4	Force Characteristic of a Prototype Magnetic Air Bearing	187

LIST OF SYMBOLS

Air Bearing Analysis

c	- local speed of sound
C_d	- discharge coefficient
C_p	- specific heat at constant pressure
C_v	- specific heat at constant volume
f	- friction factor
G	- mass flow rate
h	- bearing clearance
K	- ratio of specific heats
K_g	- thermal conductivity
L	- a characteristic bearing length
M	- Mach number
P	- pressure
r	- radius
R	- outer radius of the bearing
R_g	- universal gas constant
t	- time
T	- temperature
u	- radial velocity
z	- coordinate normal to the plane of the bearing
θ	- angular coordinate

- τ - shear stress
- ρ - density
- μ - viscosity
- λ - a dimensionless parameter ($\lambda \equiv r_i f / h$)
- ψ - a function of radius

Subscripts

- a - ambient
- d - downstream of shock wave
- i - inlet hole
- o - supply condition
- s - shock wave
- u - upstream of shock wave

Superscripts

- *
 -
- critical condition
 - normalized parameter

Magnet Analysis

- A - area
- B - flux density
- Br - residual flux density
- E - energy

F - force
H - magnetic field strength
Hc - coercive force
h - air gap
I - flux
L - length
P - permeance
R - reluctance
r - radius
T - thickness
V - magnetic potential
Wt - weight
 Γ - force-to-weight ratio
 μ - permeability
 μ_0 - permeability of free space
 ϕ - flux
 τ - volume

Subscripts

c - ceiling
g - air gap
L - leakage
m - magnet

- o - open circuit
- r - recoil line
- s - shell
- v - virgin property

1.0 INTRODUCTION

In preparation for man's planned trip to the moon via the Apollo space program, there have been recent efforts to design and build lunar gravity simulators.

The purpose of this thesis is to analyze and design a device known as a magnetic air bearing, which is a component of such a simulator. The magnetic air bearing is used as an overhead support at ceiling level. This device allows a supported object to move freely with minimal friction. The test subject is suspended from constant force springs in a marionette-like fashion. These springs, which are connected to magnetic air bearings, negate 5/6 of the subject's weight. A detailed description of this simulator is given in The Design of a Vertical Lunar Gravity Simulator by R. J. Morgen.⁽¹⁾

As an overhead support, the magnetic air bearing yields three degrees of freedom. The first two degrees are horizontal translation in a plane parallel to the ceiling. The third degree of freedom is rotation, either clockwise or counter-clockwise.

The device is structurally simple. It consists of a flat disc with an air orifice at its center. A permanent magnet is imbedded in the disc and an air line feeds compressed air to the orifice. When the magnetic air bearing is placed in contact with an overhead steel plate and air pressure is applied, the device will float at some small distance from the ceiling.

In this operating mode, the magnetic air bearing is capable of stably supporting a load. It can be said that the magnet develops the lifting force and the air flow stabilizes it. Although this comment refers to static stability, no problems have been encountered with dynamic instability; and the chosen air bearing design has proved to have very good dynamic characteristics when compared to other configurations.⁽²⁾

A dynamic analysis of the vertical suspension-type simulator was conducted for the purpose of evaluating simulator performance. An abbreviated version of this analysis is given in Appendix A.

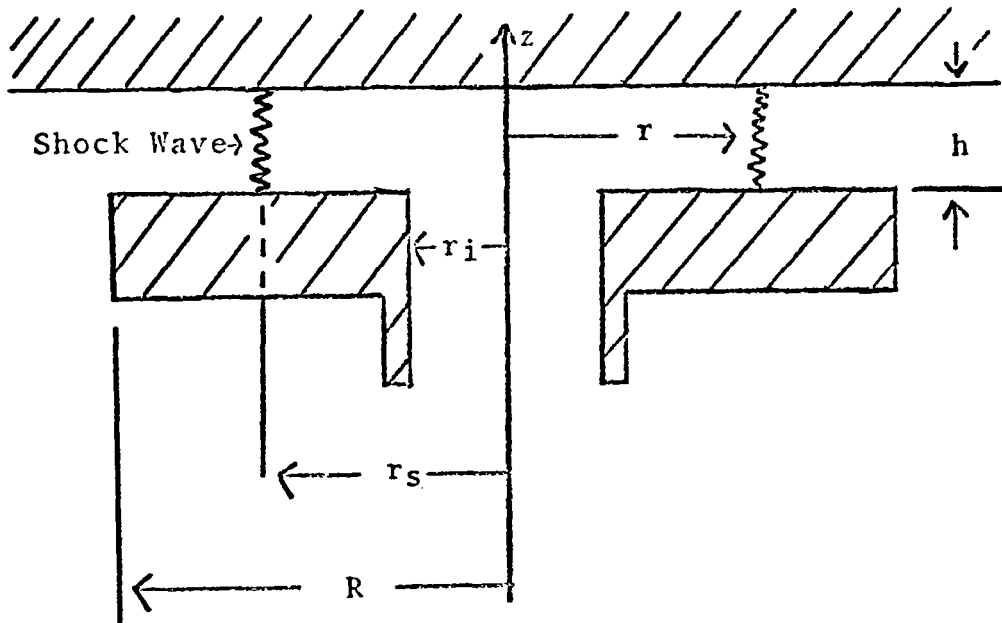
As the result of calculation based on this work⁽¹⁾ it was found that the degree of simulation attained

was a critical function of overhead weight. Thus, from the standpoint of simulator performance, the magnetic air bearing should have minimum weight.

The analysis of the magnetic air bearing system will consists of detailed separate analyses of the air bearing and the magnet. The main objective of these analyses is to determine the respective force-versus-gap characteristics for both the components. Once obtained, the force characteristics can be summed, resulting in the overall force-versus-gap characteristic of the magnetic air bearing.

2.0 THEORETICAL AND EXPERIMENTAL ANALYSIS OF THE AIR BEARING

The air flow model is shown diagrammatically in the following figure:



Externally pressurized air is introduced at the bearing orifice. The subsequent developed pressure forces the bearing surfaces apart.

As the supply pressure is increased, the radial velocity at the orifice radius will increase to the speed of sound; and, at larger radii, the fluid

velocity will be subsonic. If the supply pressure is increased beyond this point, the flow at the orifice radius will remain sonic. However, at larger radii, the flow will accelerate to supersonic velocities.⁽³⁾ If supersonic flow does not exist at the outer radius of the bearing, a normal shock wave will occur at some intermediate radius between the inner and outer radii of the bearing. In reality, a series of oblique shock waves rather than a normal shock wave will occur.

The main purpose of the following analysis is to determine the external load characteristic of the air bearing. To accomplish this goal, the pressure distribution between the bearing surfaces is analyzed.

Assumptions

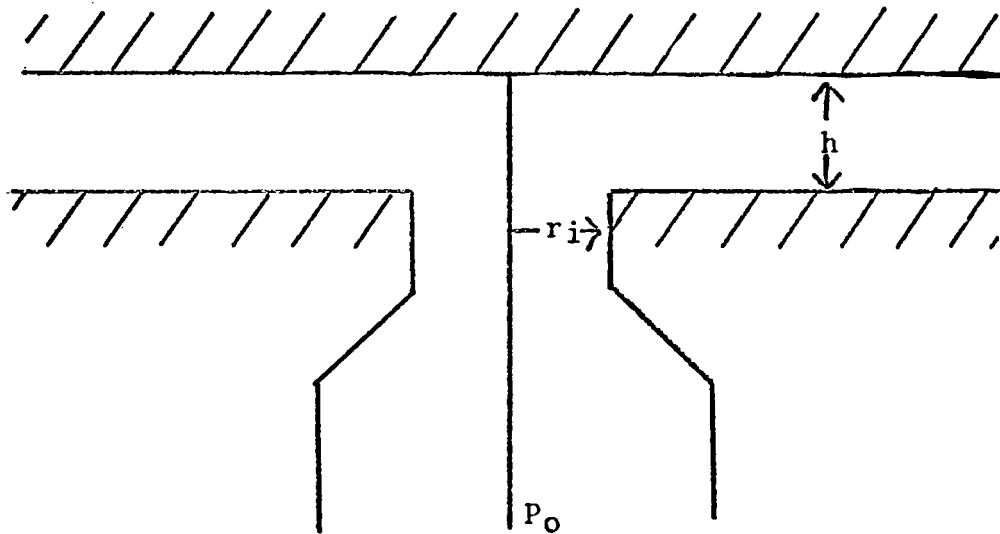
The following assumptions are made in the analysis of the air flow between the bearing surfaces:

1. The gap between the disc and the surface is of constant thickness.
2. The flow consists of supersonic and subsonic regimes.
3. The flow entering the supersonic region is choked and therefore has sonic velocity and critical pressure.
4. The flow in the supersonic region is adiabatic radial flow with friction at the walls.
5. The flow in the subsonic region is isothermal.
6. Inertial effects in the subsonic region are negligible.
7. The flow in the subsonic region is laminar and fully developed.
8. The flow is steady.

9. A normal shock wave separates the supersonic and subsonic flows.
10. Relative velocity of the pad and surface is small in comparison to fluid velocities and therefore can be neglected.
11. The annular area between the central orifice and the surface is the limiting area of the flow.
12. The working fluid is a perfect gas.
13. The flow is radial.
14. The fluid in the subsonic region is Newtonian.

2.1 THE SUPPLY ORIFICE

The geometry of the supply orifice is shown in the following figure:

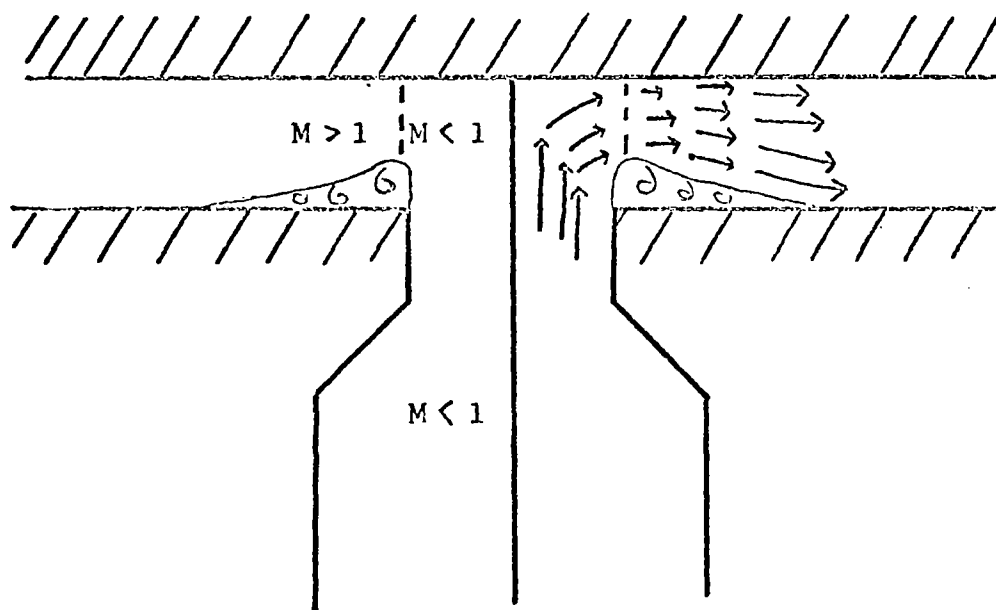


Given this geometry, it is possible to have either the circular area (πr_i^2) or the annular area ($2\pi r_i h$) be the restricting area of the flow. In this analysis and subsequent design, it will be assumed that the annular area will be smaller than the circular area and will therefore restrict the flow. Mathematically, this constraint can be stated

$$\frac{r_i}{2h} > 1 \quad (2.1)$$

In addition, it will be assumed that the flow is always choked at r_i , and therefore a Mach one condition exists at this radius. The theoretical requirements for choking to occur are presented in Section 2.3.

The following figure shows schematically a possible flow condition in the region of the supply orifice.



As the flow enters the bearing, it is forced to negotiate a right-angle turn around a sharp corner. In the process of turning the corner, the flow would expand to a relatively high Mach number

locally and consequently have a low static pressure. As opposed to this train of events, it is hypothesized that the flow actually separates from the lower bearing surface at the supply radius and passes into the bearing in smooth streamlines rather than around a sharp right angle.⁽⁴⁾ At some radius larger than the inlet radius, the flow will attach itself to the lower bearing surface. If this separation does indeed occur, the limiting area of the flow will be somewhat less than the annular area ($2\pi r_i h$) and the Mach one condition will not necessarily exist at the inlet radius.

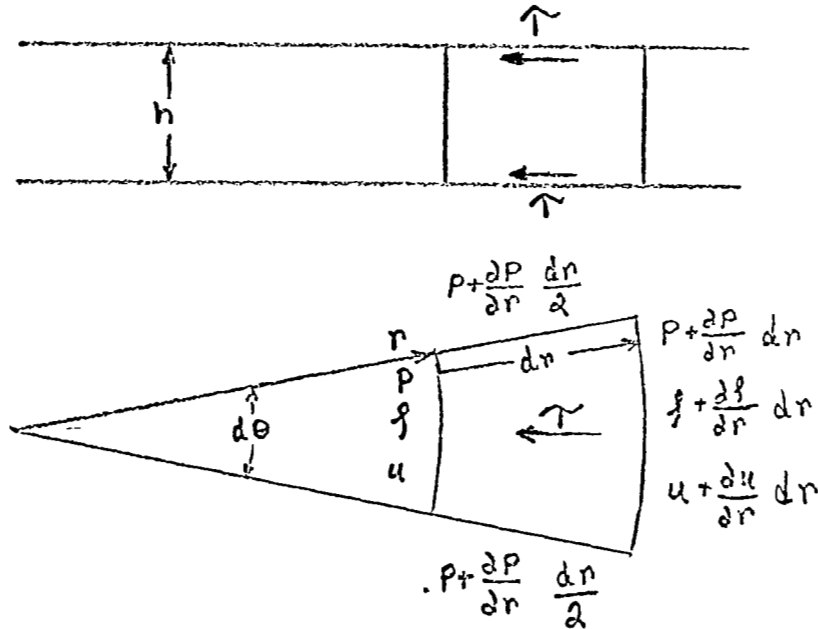
A theoretical description of this flow separation will not be presented. However, its effects on the flow at radii larger than the inlet radius will be included. The Mach one condition will still be assumed to exist at the inlet radius. However, the limiting area of the flow will be modified by an experimentally-measured discharge coefficient. It is this discharge coefficient that will contain the net effects of the presence of the separation bubble.

Since it has been assumed that the flow conditions are critical at the inlet radius, we can write the following expression for the inlet mass flow:

$$G = C_d 2\pi r_i h g^* u^* \quad (2.2)$$

2.2 ANALYSIS OF SUPERSONIC FLOW

Consider the forces acting on the elemental volume shown in the following figure:



The sum of the forces acting on the element in the radial direction is given by

$$\sum \text{Forces} = -r \frac{\partial P}{\partial r} dr d\theta h - 2\tau r d\theta dr$$

The momentum flux through the control volume surfaces is given by

$$\Delta \text{Mom.} = 2\rho r u \frac{\partial u}{\partial r} dr d\theta h + u^2 f dr d\theta h + u^2 r \frac{\partial f}{\partial r} dr d\theta h$$

The statement of conservation of mass for the element is given by

$$\rho r \frac{\partial u}{\partial r} dr + ur \frac{\partial \rho}{\partial r} dr + \rho u dr = 0$$

Using the continuity expression, the change in momentum can be simplified to

$$\Delta \text{Mom.} = \rho ur \frac{\partial u}{\partial r} dr d\theta h$$

The rate of momentum efflux is equal to the net force acting on the fluid within the control volume. The following momentum equation is therefore obtained:

$$\rho u \frac{\partial u}{\partial r} = -\frac{\partial p}{\partial r} - \frac{2\tau}{h}$$

The assumption is now made that pressure, density and velocity are functions of radius only.

$$\begin{aligned} p &= p(r) \\ \rho &= \rho(r) \\ u &= u(r) \end{aligned}$$

The momentum equation can then be rewritten without the partial derivatives

$$f u \frac{du}{dr} = - \frac{dP}{dr} - \frac{2\tau}{h} \quad (2.3)$$

The drag coefficient or friction factor is now introduced. This friction factor is defined as the ratio of the shear stress at the wall to the dynamic head of the stream or, in other words, it is a measure of the relative significance of the viscous and momentum effects.

$$f \equiv \tau / f u^2 / 2 \quad (2.4)$$

The friction factor is known to be a function of the Reynolds number and the relative roughness of the surfaces. In this analysis, however, the friction factor will be assumed to be a constant.

Upon substitution of Equation (2.4) into the momentum equation, we obtain

$$f u \frac{du}{dr} = - \frac{dP}{dr} - f \frac{u^2 f}{h} \quad (2.5)$$

The ideal gas law is given by

$$P = f R_g T \quad (2.6)$$

The energy equation for steady adiabatic flow of a perfect gas is written

$$C_p dT + d\left(\frac{u^2}{2}\right) = 0 \quad (2.7)$$

Taking the logarithmic differential Equation (2.6),

$$\frac{dP}{P} = \frac{dP}{f} + \frac{dT}{T}$$

and upon solving for the temperature differential, we obtain

$$dT = \frac{dP}{f R_g} - \frac{P df}{R_g f^2} \quad (2.8)$$

Substituting Equation (2.8) into the energy equation, we obtain

$$\frac{C_p}{R_g} d\left(\frac{P}{f}\right) + d\left(\frac{u^2}{2}\right) = 0$$

This expression is integrable. Integrating from the orifice radius,

$$\frac{C_P}{Rg} \int_{r_i}^r d\left(\frac{P}{f}\right) = - \int_{r_i}^r d\left(\frac{u^2}{2}\right)$$

At the orifice radius the flow is choked, and therefore,

$$\begin{aligned} \frac{P^*}{P_0} &= \left(\frac{2}{K+1}\right)^{\frac{K}{K-1}} \\ \frac{f^*}{f_0} &= \left(\frac{2}{K+1}\right)^{\frac{1}{K-1}} \\ u^* &= \sqrt{\frac{KP^*}{f^*}} \end{aligned}$$

In addition, it can be easily shown that

$$\frac{C_P}{Rg} = \frac{K}{K-1}$$

The energy equation can now be written

$$\frac{P}{f} = \left(\frac{K+1}{2}\right) \frac{P^*}{f^*} - \left(\frac{K-1}{2K}\right) u^2 \quad (2.9)$$

The statement of continuity can be expressed

$$u = \frac{1}{f} \frac{r_i}{r} \sqrt{K P^* f^2} \quad (2.10)$$

Substituting the above equation for radial velocity into Equation (2.8), we obtain

$$\left(\frac{K-1}{2}\right) \left(\frac{r_i}{r}\right)^2 \frac{P^*}{P} \left(\frac{f^*}{f}\right)^2 + \frac{f^*}{f} - \left(\frac{K+1}{2}\right) \frac{P^*}{P} = 0$$

Solving for the density ratio,

$$\frac{f^*}{f} = \frac{-1 \pm \sqrt{1 + (K^2 - 1) \left(\frac{r_i}{r}\right)^2 \left(\frac{P^*}{P}\right)^2}}{(K-1) \left(\frac{r_i}{r}\right)^2 \frac{P^*}{P}} \quad (2.11)$$

Since the density ratio must always be a positive quantity, the negative sign in front of the radical has no physical significance.

Now, defining a parameter,

$$\Psi \equiv \sqrt{1 + (K^2 - 1) \left(\frac{r_i}{r} \right)^2 \left(\frac{\rho r_i^2}{\rho} \right)^2} \quad (2.12)$$

Ψ is a function of the radius and of pressure. However, since the pressure can be expressed as a function of radius,

$$\Psi = \Psi(r)$$

Now we can relate the pressure, density and velocity to Ψ and radius. Solving Equation (2.12) for the pressure ratio, we obtain

$$\frac{\rho}{\rho_i} = \frac{r_i}{r} \sqrt{\frac{K^2 - 1}{\Psi^2 - 1}} \quad (2.13)$$

Upon substitution of Equations (2.12) and (2.13) into Equation (2.11),

$$\frac{f}{f_i} = \frac{r_i}{r} \sqrt{\frac{(K-1)(\Psi+1)}{(K+1)(\Psi-1)}} \quad (2.14)$$

Substituting Equations (2.13) and (2.14) into Equation (2.10),

$$\frac{u}{u^*} = \sqrt{\frac{(K+1)(\psi-1)}{(K-1)(\psi+1)}} \quad (2.15)$$

Defining the following dimensionless parameters,

$$\begin{aligned} \bar{p} &\equiv p/p^* \\ \bar{f} &\equiv f/f^* \\ \bar{u} &\equiv u/u^* \\ \bar{r} &\equiv r/r_i \end{aligned}$$

The momentum equation can be normalized

$$\frac{1}{K} \frac{d\bar{p}}{d\bar{r}} + \lambda \bar{f} \bar{u}^2 = -\bar{f} \bar{u} \frac{d\bar{u}}{d\bar{r}} \quad (2.16)$$

where

$$\lambda \equiv \frac{r_i \rho}{h}$$

Equation (2.13) can be rewritten in normalized form as

$$\bar{p} = \frac{1}{\bar{r}} \sqrt{\frac{K^2 - 1}{\psi^2 - 1}}$$

Upon differentiation,

$$\frac{d\bar{p}}{d\bar{r}} = -\frac{1}{\bar{r}^2} \sqrt{\frac{K^2 - 1}{\psi^2 - 1}} - \frac{\sqrt{K^2 - 1}}{\bar{r}(\psi^2 - 1)^{3/2}} \psi \frac{d\psi}{d\bar{r}}$$

From Equation (2.15), the normalized velocity is given by

$$\bar{u} = \sqrt{\frac{(K+1)(\psi-1)}{(K-1)(\psi+1)}}$$

Upon differentiation,

$$\frac{d\bar{u}}{d\bar{r}} = \frac{\sqrt{K+1}}{\sqrt{K-1} (\psi+1)^{3/2} \sqrt{\psi-1}} \frac{d\psi}{d\bar{r}}$$

Now upon substituting these derivatives into the momentum equation, we obtain the following non-linear differential equation in Ψ and \bar{r} :

$$(\Psi-K) \frac{d\Psi}{d\bar{r}} - \frac{1}{\bar{r}} (\Psi^2-1)(K-1) + \lambda (\Psi-1)^2 (\Psi+1) = 0 \quad (2.17)$$

Once the above equation is solved for Ψ and the resulting solution is substituted into Equation (2.13), the supersonic pressure distribution can be obtained. At this point, the supersonic flow problem is solved with the exception of the solution of Equation (2.17). Since a closed form solution of this equation is probably impossible, it was solved numerically. This solution is discussed in Section 2.5.

2.3 THE SUBSONIC FLOW REGION

The assumption that the subsonic flow is isothermal can be verified by the following order-of-magnitude argument. We know from the laws of transient heat transfer that, if a slab of material is ΔT above or below two constant temperature boundaries, the temperature differential at the center of the slab will decrease to $\Delta T/3$ in the time given by the following equation:

$$T_c = 0.13 \frac{C_p f h^2}{K_g}$$

Now, if we can show that this time is much less than some mean time necessary for the gas to traverse the bearing, the isothermal assumption is verified. The following expression will be used to represent this traversal time

$$T_t = \frac{L}{u}$$

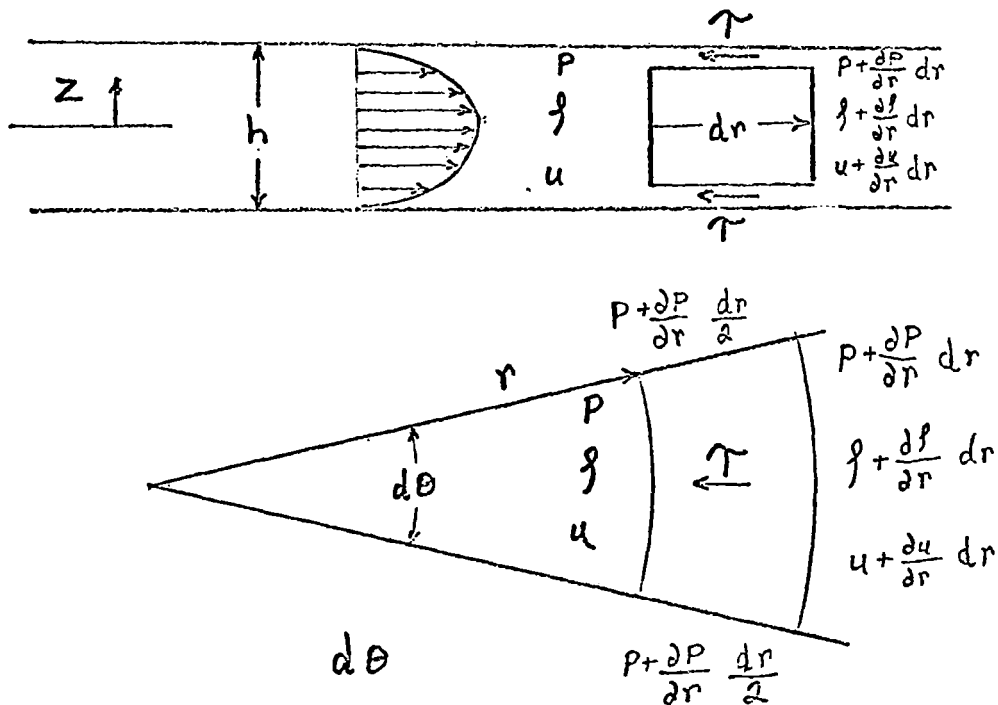
where L is distance representing the length of the bearing and u is some mean subsonic velocity.

Typically, T_c is of the order of 3μ seconds, whereas T_t is of the order of 150μ seconds. Therefore,

$$T_t \gg T_c$$

and heat will be conducted away faster than it is produced. The subsonic flow is therefore considered isothermal for all practical purposes. (5)

Consider the infinitesimal fluid element shown below:



The equation for static equilibrium of this fluid element can be written:

$$2 P r d \theta z - 2 \left(P + \frac{\partial P}{\partial r} dr \right) (r + dr) \cdot$$

$$d \theta z + 2 \left(P + \frac{\partial P}{\partial r} \frac{dr}{2} \right) (r + dr - r) \cdot$$

$$d \theta z - 2 \tau \left(r + \frac{dr}{2} \right) d \theta dr = 0$$

Or, upon simplification,

$$-2 r \frac{\partial P}{\partial r} dr d \theta z - 2 \tau r d \theta dr = 0 \quad (2.18)$$

Using Newton's equation relating shear stress to rate of strain,

$$\tau = -\eta \frac{\partial u}{\partial z} \quad (2.19)$$

and combining Equations (2.18) and (2.19), we obtain

$$du = \frac{z}{\eta} dz \frac{dP}{dr}$$

Integrating this equation with respect to z and applying the boundary conditions,

$$u = \frac{1}{\eta} \frac{dP}{dr} \int z dz$$

$$u = \frac{1}{\eta} \frac{dP}{dr} \frac{z^2}{2} + C$$

$$\begin{array}{lll} \text{B.C.} & u = 0 & z = h/2 \\ & u = 0 & z = -h/2 \end{array}$$

Then the integration constant can be expressed

$$C = -\frac{1}{\eta} \frac{dP}{dr} \frac{h^2}{8}$$

The velocity distribution across the gap can now be written

$$u = \frac{1}{2\eta} \frac{dP}{dr} \left[z^2 - \frac{h^2}{4} \right] \quad (2.20)$$

This result gives the parabolic distribution shown in the previous figure.

The average velocity across the gap is given by

$$u_{ave} = \frac{1}{h} \int_{-h/2}^{h/2} u \, dz$$

$$u_{ave} = -\frac{h^2}{12\eta} \frac{dP}{dr}$$

The expression for conservation of mass is

$$\int u_{ave} r = \text{const.}$$

From the equation of state and the isothermal assumption, the following barotropic relationship is derived:

$$\frac{p}{\rho} = \text{const.}$$

Then, upon combination with the continuity equation, we obtain

$$\rho u_{ave} r = c_0$$

where c_0 is a constant. Or, upon substituting for the average radial velocity,

$$\rho \frac{dr}{dt} = - \frac{12\gamma c_0}{h^2} \frac{dr}{r}$$

Integrating, we obtain the following equation for pressure:

$$\frac{p^2}{2} = - \frac{12\gamma c_0}{h^2} \ln r + c_1$$

Now, for the sake of simplicity, let

$$c_2 = - \frac{24\gamma c_0}{h^2}$$

and

$$c_3 = 2c_1$$

Then,

$$P^2 = c_2 \ln r + c_3$$

Now applying the boundary conditions at the shock wave and outer diameter of the disc

$$P = P_d \quad \text{at} \quad r = r_s$$

$$P = P_a \quad \text{at} \quad r = R$$

The equation for the pressure distribution becomes

$$\frac{P}{P_d} = \left\{ 1 - \left[1 - \left(\frac{P_a}{P_d} \right)^2 \right] \frac{\ln(r/r_s)}{\ln(R/r_s)} \right\}^{1/2} \quad (2.21)$$

Now that the pressure distribution is known, the average radial velocity and the mass flow rate can be calculated.

The gradient of the pressure with radius is

$$\frac{dP}{dr} = - \frac{[P_d^2 - P_a^2]}{2rP \ln(R/r_s)}$$

Then the average radial velocity is given by

$$u_{ave} = \frac{h^2 [P_d^2 - P_a^2]}{24\eta r P \ln(R/r_s)} \quad (2.22)$$

The mass flow rate is

$$G = \int u_{ave} 2\pi r h \quad (2.23)$$

Using the ideal gas law to eliminate the density and substituting Equation (2.22) for the average velocity into Equation (2.23), the following expression for the mass flow is obtained:

$$G = \frac{\pi h^3 [P_d^2 - P_a^2]}{12\eta R_g T \ln(R/r_s)} \quad (2.24)$$

The determination of the conditions necessary for choking to occur at the inlet has been postponed until this time because it is necessary to have an expression for the subsonic average velocity distribution.

Assuming that the supply pressure is not high enough to permit choking, the entire bearing will be subsonic. The radial fluid velocity at the supply

orifice can then be expressed as

$$u_{ave i} = \frac{h^2 (P_i^2 - P_a^2)}{24 \gamma r_i P_i \ln(R/r_i)}$$

where the subscript i designates the condition at the supply orifice. The local speed of sound at this point is

$$c_i = \sqrt{K \frac{P_i}{\rho_i}}$$

Using the barotropic relationship derived from the isothermal assumption, the speed of sound can be rewritten as

$$c_i = \sqrt{K \frac{P_a}{\rho_a}}$$

The Mach number at the inlet is then given by

$$M_i = \frac{h^2 (P_i^2 - P_a^2)}{24 \gamma r_i P_i \ln(R/r_i) \sqrt{K P_a / \rho_a}} \quad (2.25)$$

The minimum pressure at the inlet radius at which choking will occur is given by the solution of Equation (2.25) for P_1 with the Mach number set at one.⁽⁶⁾ The equation for P_1 can be expressed in the following binomial form:

$$P_i^2 - P_i \frac{[24 \gamma r_i \ln(R/r_i) \sqrt{K P_a / g_a}]}{h^2} - P_a^2 = 0$$

Or, upon solving for P_1 ,

$$P_i = \frac{[24 \gamma r_i \ln(R/r_i) \sqrt{K P_a / g_a}]}{2 h^2} \pm \frac{1}{2} \sqrt{\frac{[24 \gamma r_i \ln(R/r_i) \sqrt{K P_a / g_a}]^2}{h^2} + 4 P_a^2} \quad (2.26)$$

The negative sign in front of the radical is not considered because a negative absolute pressure has no physical significance.

Now that we have the pressure at the radius necessary for choking, the minimum supply pressure consistent with this value of P_1 can be calculated from the following equation:

$$P_{o\min} = P_i \left[\frac{k+1}{2} \right]^{k/(k-1)} \quad (2.27)$$

At this value of supply pressure, the conditions at the inlet orifice will be critical. However, the flow throughout the rest of the bearing will be subsonic. At supply pressures greater than $P_{o\min}$, the conditions at the inlet orifice will still be critical. However, the flow will accelerate to supersonic velocities and then shock to subsonic conditions at some radius larger than the inlet.

2.4 THE SHOCK WAVE

It has been assumed that a normal shock wave ties the two flow regimes together.

The equation for a normal shock wave in a perfect gas relating the pressure ratio across the shock to the upstream Mach number is⁽⁷⁾

$$\frac{P_d}{P_u} = \frac{2K}{K+1} M_u^2 - \frac{K-1}{K+1} \quad (2.28)$$

The upstream Mach number is given by

$$M_u = \frac{U_u}{C_u}$$

where

$$C_u = \sqrt{\frac{K P_u}{\rho_u}}$$

Then, using Equation (2.10), we obtain

$$M_u = \frac{n_i}{r} \sqrt{\frac{P^*}{P_u} \frac{\rho^*}{\rho_u}} \quad (2.29)$$

Upon substitution of Equations (2.13) and (2.14) into the above equation, we obtain

$$M_u = \sqrt{\frac{\Psi_u - 1}{K - 1}}$$

Then the pressure ratio across the shock wave can be written in terms of the upstream value of the function Ψ .

$$\frac{P_d}{P_u} = \frac{2K(\Psi_u - 1)}{(K^2 - 1)} - \frac{K - 1}{K + 1} \quad (2.30)$$

The expression for the mass flow in the subsonic regime is given by

$$G = \frac{\pi h^3 [P_d^2 - P_a^2]}{12\eta R_g T \ln(R/r_s)}$$

Upon equating the mass flow in the subsonic and supersonic regions

$$C_d g^* u^* 2\pi r_i h = \frac{\pi h^3 (P_d^2 - P_a^2)}{12\gamma R_g T \ln(R/r_s)}$$

Solving for the downstream pressure

$$P_d = \left\{ P_a^2 + \frac{24\gamma r_i C_d R_g T \ln(R/r_s) \sqrt{K P^* g^*}}{h^2} \right\}^{1/2} \quad (2.31)$$

For a given geometry, Equation (2.31) relates the downstream pressure to the position of the shock wave.

If Equation (2.30) is also solved for the downstream pressure,

$$P_d = P^* \frac{r_i}{r_s} \left[2K \sqrt{\frac{(\psi_u - 1)}{(\psi_u + 1)(K^2 - 1)}} - \frac{(K - 1)}{\sqrt{\psi_u^2 - 1}} \right] \quad (2.32)$$

where Ψ_u is a function of r_s only.

The simultaneous solution of Equations (2.31) and (2.32) for r_s gives the position of the shock wave.

Since the function Ψ is not known explicitly, a closed form solution for the shock wave position in terms of the other parameters of the system is not possible. These equations, however, have been solved numerically for specific cases.

2.5 THEORETICAL LOAD GAP CHARACTERISTICS

The three major independent variables which determine the load characteristic of the air bearing are the orifice radius, the outside radius and the supply pressure. Other parameters such as supply temperature, ambient pressure and ambient temperature will be relatively constant during the operation of the device; and, therefore, the effects of these variables will not be considered.

Method of Solution

Because a closed form solution for the bearing load characteristic was not considered feasible, the problem was solved numerically using a digital computer.

This computer program is presented in Appendix B. A simplified flow chart for this computer program is shown in Figure 2.1. The approach taken was to first determine whether or not the flow at the orifice radius is sonic at a particular gap. If the flow is not sonic, the pressure distribution under the bearing

FLOW CHART FOR
AIR BEARING
COMPUTER PROGRAM

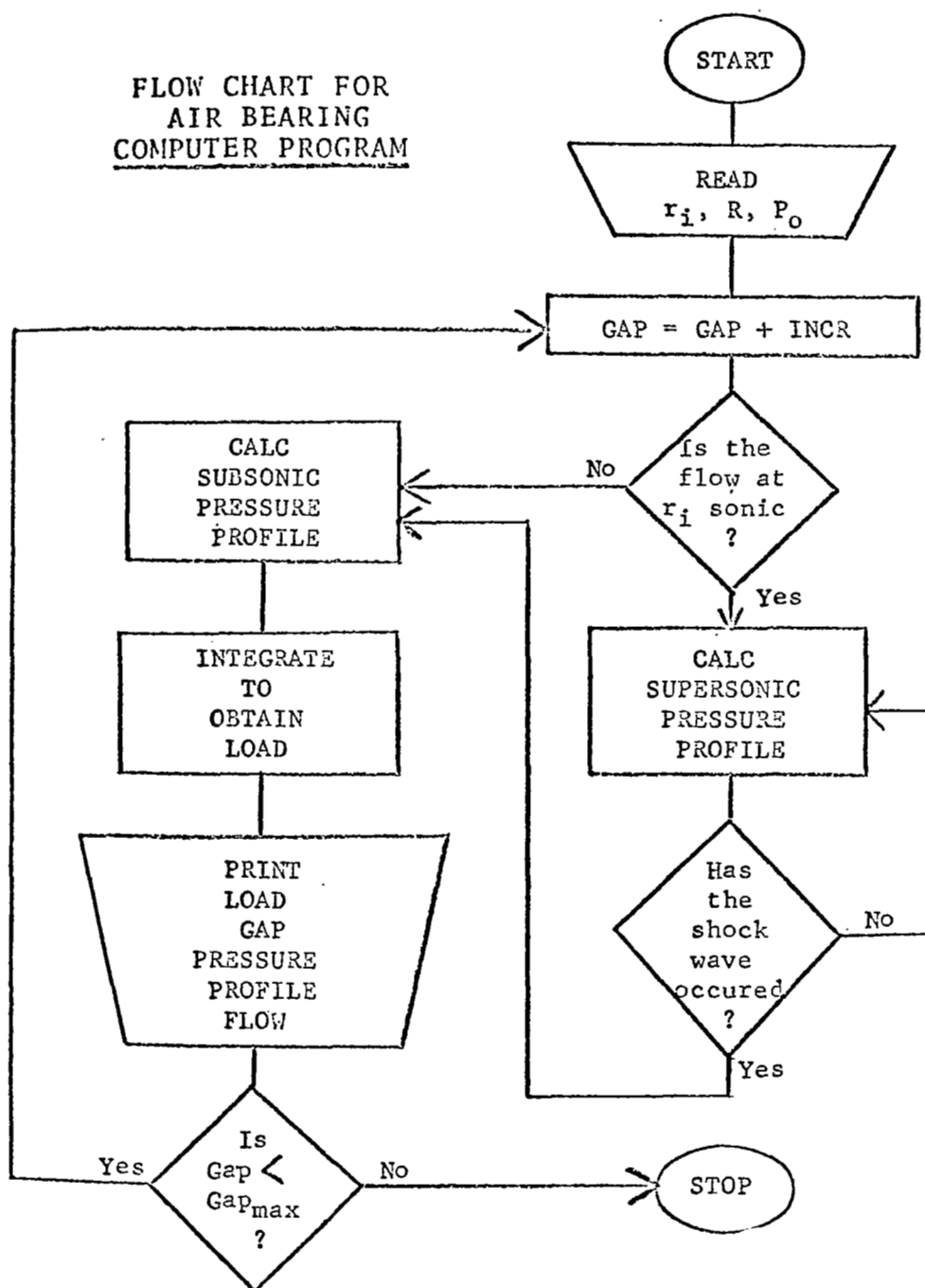


Figure 2.1

is calculated for subsonic flow and then integrated numerically to obtain the load. If the flow at the orifice radius is determined to be sonic, the supersonic pressure distribution is calculated. This is done by solving Equation (2.17) with a finite difference technique. The method of Milne was chosen for this task. This method, as applied to the solution of Equation (2.17), is presented in the following discussion.

Since the first derivative of Ψ with respect to \bar{r} is infinite at the orifice radius, it was necessary to consider \bar{r} as a function of Ψ rather than the converse in the vicinity of the orifice. The following Taylor series was generated for \bar{r} near the orifice radius:

$$\begin{aligned} \bar{r} \cong & 1 + \left. \frac{d\bar{r}}{d\Psi} \right|_i (\Psi - \Psi_i) + \left. \frac{d^2\bar{r}}{d\Psi^2} \right|_i \frac{(\Psi - \Psi_i)^2}{2!} \\ & + \left. \frac{d^3\bar{r}}{d\Psi^3} \right|_i \frac{(\Psi - \Psi_i)^3}{3!} + \left. \frac{d^4\bar{r}}{d\Psi^4} \right|_i \frac{(\Psi - \Psi_i)^4}{4!} \end{aligned} \quad (2.33)$$

The boundary condition on the function Ψ is

$$\Psi = k \quad \text{at} \quad \bar{r} = 1$$

Ψ is now increased incrementally three times and \bar{r} is evaluated at these values of Ψ .

$$\begin{aligned}\Psi_1 &= \Psi + \Delta \\ \Psi_2 &= \Psi_1 + \Delta \\ \Psi_3 &= \Psi_2 + \Delta\end{aligned}$$

From Equation (2.33) we obtain \bar{r}_1 , \bar{r}_2 and \bar{r}_3 for each value of Ψ . The first derivative of Ψ with respect to \bar{r} can now be evaluated from

$$\frac{d\bar{r}}{d\Psi} = \frac{\Psi - K}{\frac{1}{\bar{r}}(\Psi^2 - 1)(K - 1) - \lambda(\Psi - 1)^2(\Psi + 1)} \quad (2.34)$$

The fourth value of \bar{r} can be predicted using the following equation:⁽⁸⁾

$$\bar{r}_4 = 1 + \frac{4\Delta}{3} \left(2 \frac{d\bar{r}}{d\Psi} \Big|_1 - \frac{d\bar{r}}{d\Psi} \Big|_2 + 2 \frac{d\bar{r}}{d\Psi} \Big|_3 \right)$$

or, in general, the $(n + 1)$ th value of \bar{r} can be predicted from

$$\bar{r}_{n+1} = \bar{r}_{n-3} + \frac{4\Delta}{3} \left(2 \frac{d\bar{r}}{d\Psi} \Big|_{n-2} - \frac{d\bar{r}}{d\Psi} \Big|_{n-1} + 2 \frac{d\bar{r}}{d\Psi} \Big|_n \right) \quad (2.35)$$

Once the $(n + 1)$ th value of \bar{r} is determined, the corresponding value of the first derivative can

be calculated. Based on the $(n + 1)$ th value of the first derivative, the $(n + 1)$ th value of \bar{r} can be checked using the following closed formula:

$$\bar{r}'_{n+1} = \bar{r}_{n+1} + \frac{\Delta}{3} \left(\frac{d\bar{r}}{d\psi} \Big|_{n-1} + 4 \frac{d\bar{r}}{d\psi} \Big|_n + \frac{d\bar{r}}{d\psi} \Big|_{n+1} \right) \quad (2.36)$$

This procedure is then repeated until the value of \bar{r}_{n+1} is within an acceptable agreement with the preceding value.

At some convenient radius larger than the orifice radius, the technique given above is stopped and ψ is considered as a function of \bar{r} . This is necessary because $\frac{d\bar{r}}{d\psi}$ gets very large and would cause computer overflow. The equations for predicting the $(n + 1)$ th value of ψ are the same as Equations (2.35) and (2.36) with \bar{r} replaced by ψ and $\frac{d\bar{r}}{d\psi}$ replaced by $\frac{d\psi}{d\bar{r}}$.

For each step in radius, the pressure is calculated using Equation (2.13). In addition, a test is made to see if the conditions are right for the shock wave to occur. This test consists of searching for the point at which Equations (2.31) and (2.32) are

simultaneously satisfied. Once the shock wave occurs, the subsonic pressure distribution is calculated and the entire pressure profile is integrated to obtain the load.

Theoretical Results

For Mach numbers greater than one and gap Reynolds numbers varying from 25,000. to 7,000,000., the friction factor will vary from .002 to .003.⁽⁹⁾ Theoretical gap Reynolds numbers in the supersonic region vary from a high of approximately 70,000. to a low of 4,000. Since the friction factor is somewhat of a weak function of the Reynolds number, a constant value of .0025 was chosen for all the theoretical calculations.

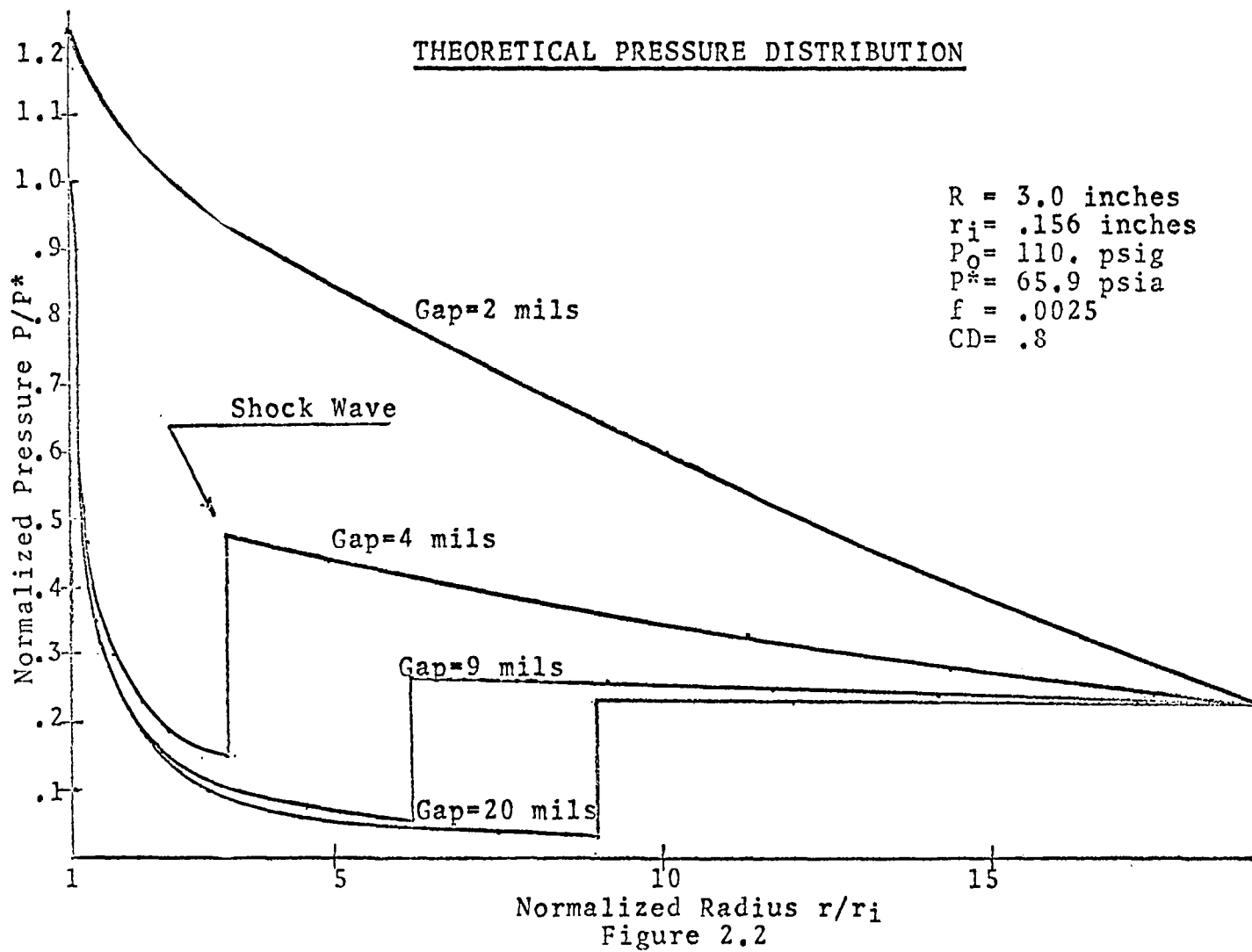
The discharge coefficient of the orifice was experimentally measured. It was found that this number was not a function of gap from 0 to 20 mils and had a value of approximately .8 in the orifice range considered.

Figure 2.2 shows a typical theoretical pressure distribution under an air bearing. It should be noted that at 1 mil the flow is completely subsonic, and thus no shock wave is present. At the larger gaps the flow has a supersonic region followed by a shock wave and a subsonic region. As the flow accelerates to supersonic velocities, the static pressure drops quickly to values below atmospheric pressure.

Because of the low pressure in the supersonic region, the air bearing in some cases will be able to support a load directed away from the bearing surfaces.

Figure 2.3 shows the theoretical shock wave position as a function of gap for an orifice radius of .156 inches and an outside radius of 3. inches.

A typical theoretical flow characteristic for a discharge coefficient of .8 is given in Figure 2.4. Since the discharge coefficient is assumed to be independent of gap, the flow rate increases linearly with gap.



THEORETICAL SHOCK WAVE POSITION
VERSUS AIR GAP

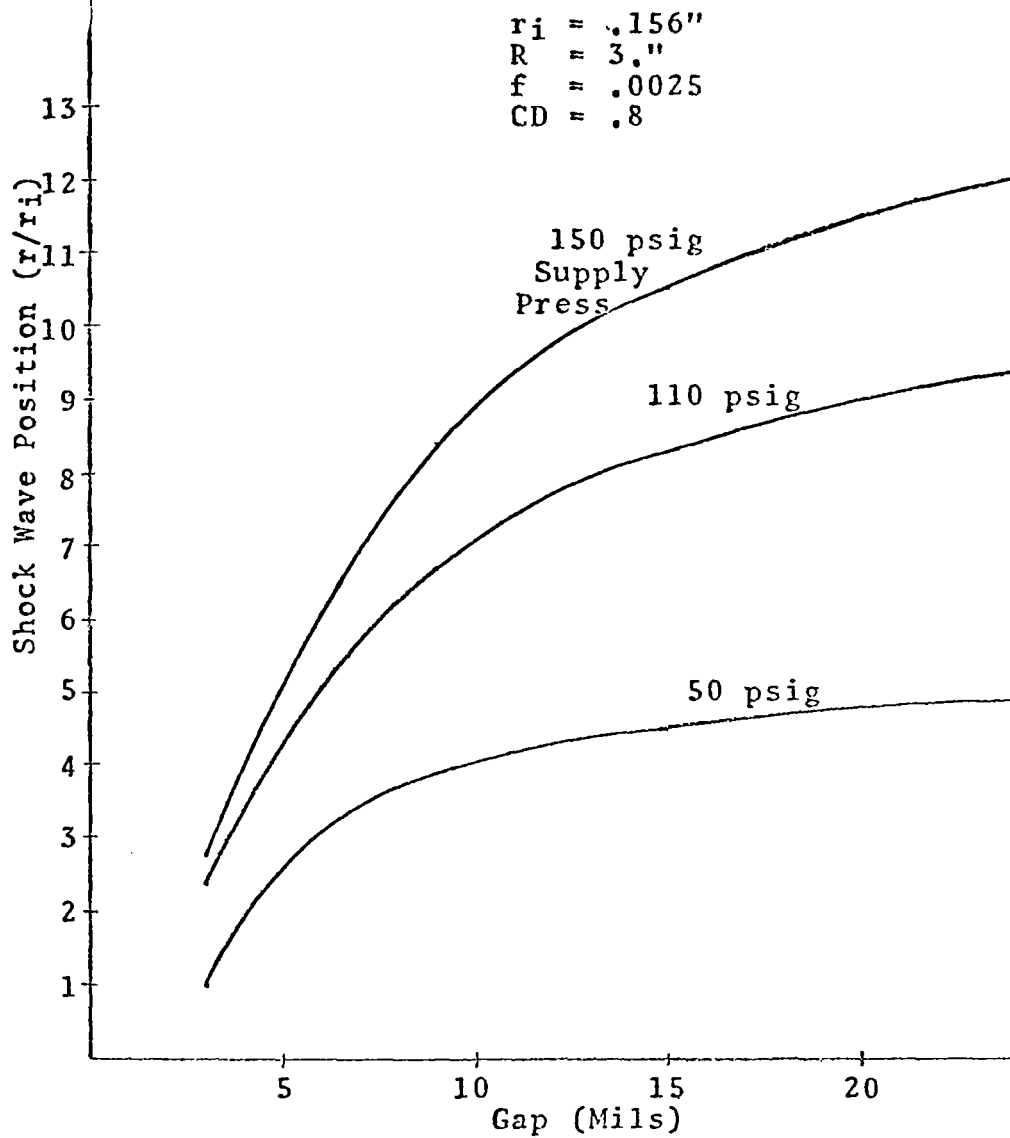


Figure 2.3

THEORETICAL FLOW
VERSUS AIR GAP

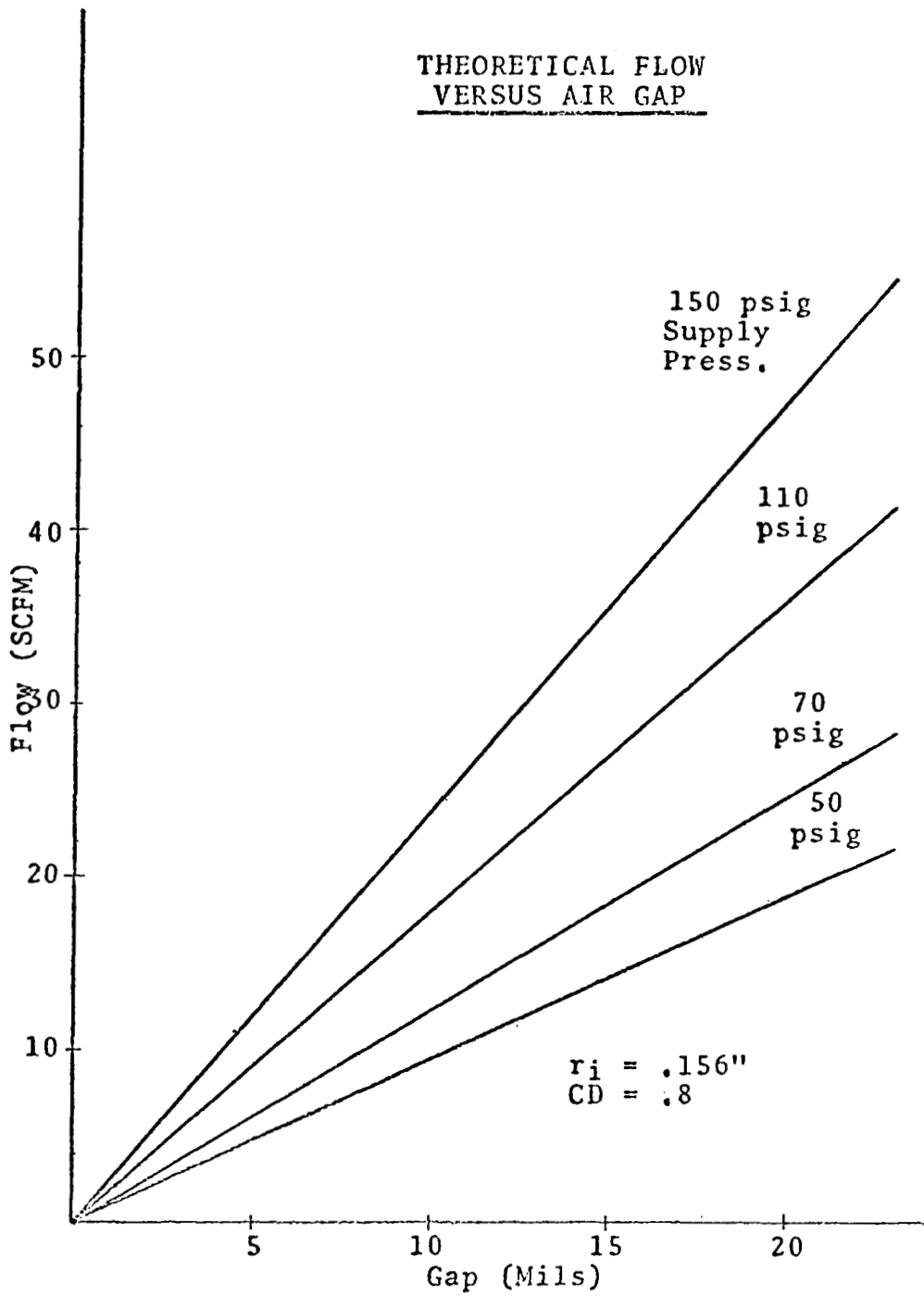


Figure 2.4

A typical set of load-versus-gap curves is presented in Figure 2.5. At small gaps, an increase in supply pressure causes an increase in negative load. The negative sign indicates that a compressive load is being applied to the bearing. Also, an increase in supply pressure results in an increase in positive load carrying ability (force tending to pull the bearing away from the surface). As has been previously mentioned, this effect is caused by subatmospheric pressure in the supersonic region.

The positive force region will not be used in the magnetic air bearing design because the force gradient, or stiffness, is low; and a magnetic air bearing operating in this region would fall from the ceiling on reduction of air pressure.

Since the evaluation of the air bearing force characteristic is the main objective of the air flow analysis, detailed theoretical load-versus-gap characteristics are presented in Appendix C. These characteristics cover the following independent variable values:

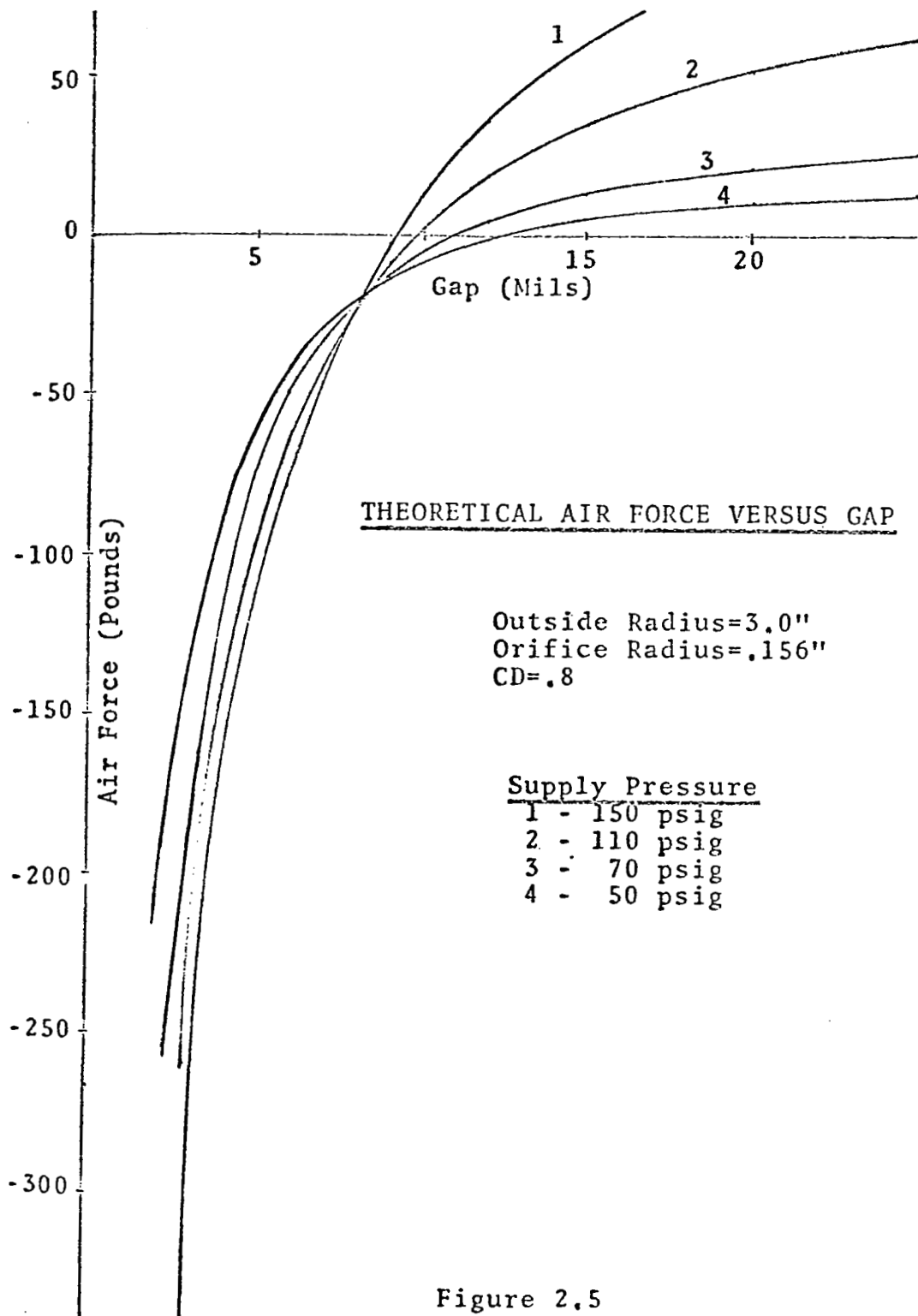


Figure 2.5

Supply Pressure: 50, 70, 110, and 150 psig

Orifice Radius: .0313, .0625, .0938, .125,
.156, and .188 inches

Outside Radius: 1., 2., and 3. inches

Since the magnet will develop all of the magnetic air bearing's holding force, and since this force decreases with increasing gap, it is desirable from the standpoint of maximum developed force to operate at minimum gap. There is, however, a practical limit to this minimum gap due to surface tolerances. This limit is approximately 4 mils. This, as well as other practical magnetic air bearing design considerations, will be discussed in more detail in Section 4.

Because it is desirable to operate the bearing as close to the surface as possible, the designed gap operating range of the device will be in the area of from 4 to 6 mils. In this range, the slope of the air force-versus-gap curve, or stiffness, is important because it is a measure of the stabilizing effect that the air bearing will have on the magnet characteristic. The parameter called stiffness will hereafter

be defined as the secant slope of the air force-versus-gap characteristic from 4 to 6 mils.

It is desirable from the standpoint of stability alone to have as large a stiffness as possible. However, in a design of a magnetic air bearing, certain compromises must be made for the sake of practicability which will limit the stiffness. These limitations will be discussed further in Section 4.

Theoretical stiffness-versus-orifice radius curves are presented in Figures 2.6, 2.7, and 2.8. It can be seen in Figure 2.6 for a 3-inch outside radius and in Figure 2.7 for a 2-inch outside radius that the stiffness varies almost linearly with orifice radius and increases with supply pressure. The stiffness for a 1-inch outside radius, shown in Figure 2.8, increases with orifice radius out to .09 inches in the supply pressure range from 50 to 150 psig. At this orifice radius and a supply pressure of 150 psig, the stiffness reaches a maximum and begins to drop off. This also occurs at an orifice radius of .11 for a supply pressure of 110 psig. The reason for

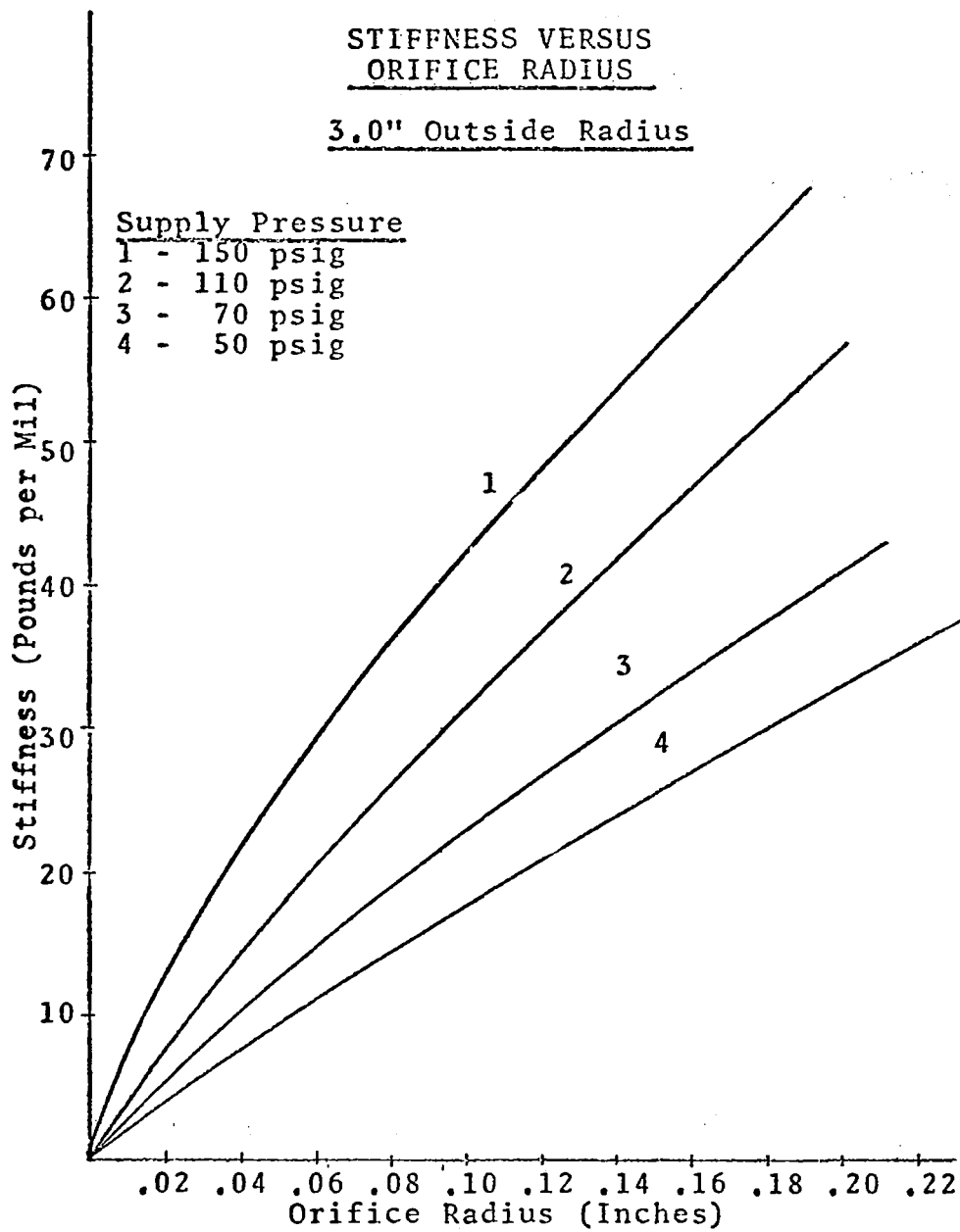


Figure 2.6

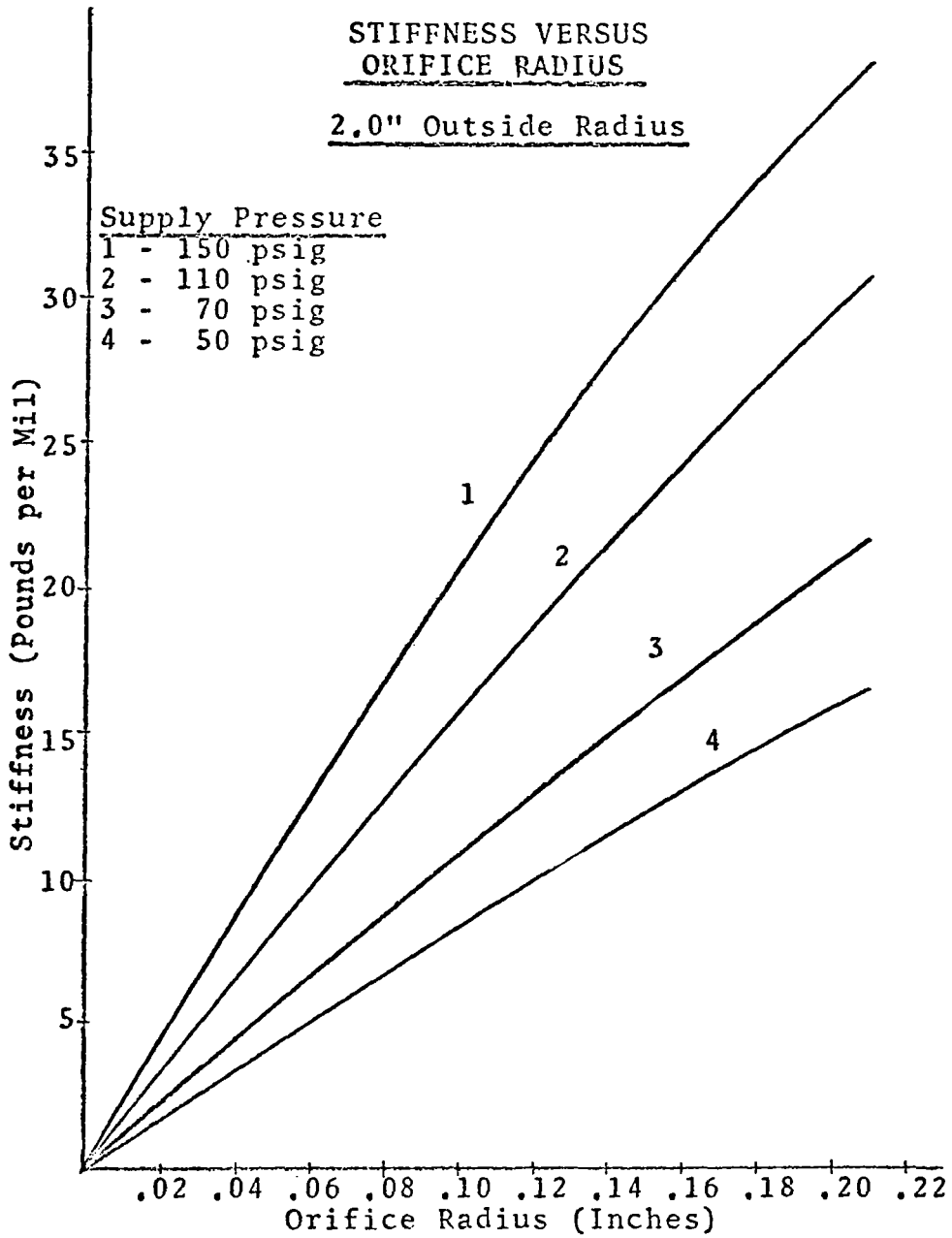


Figure 2.7

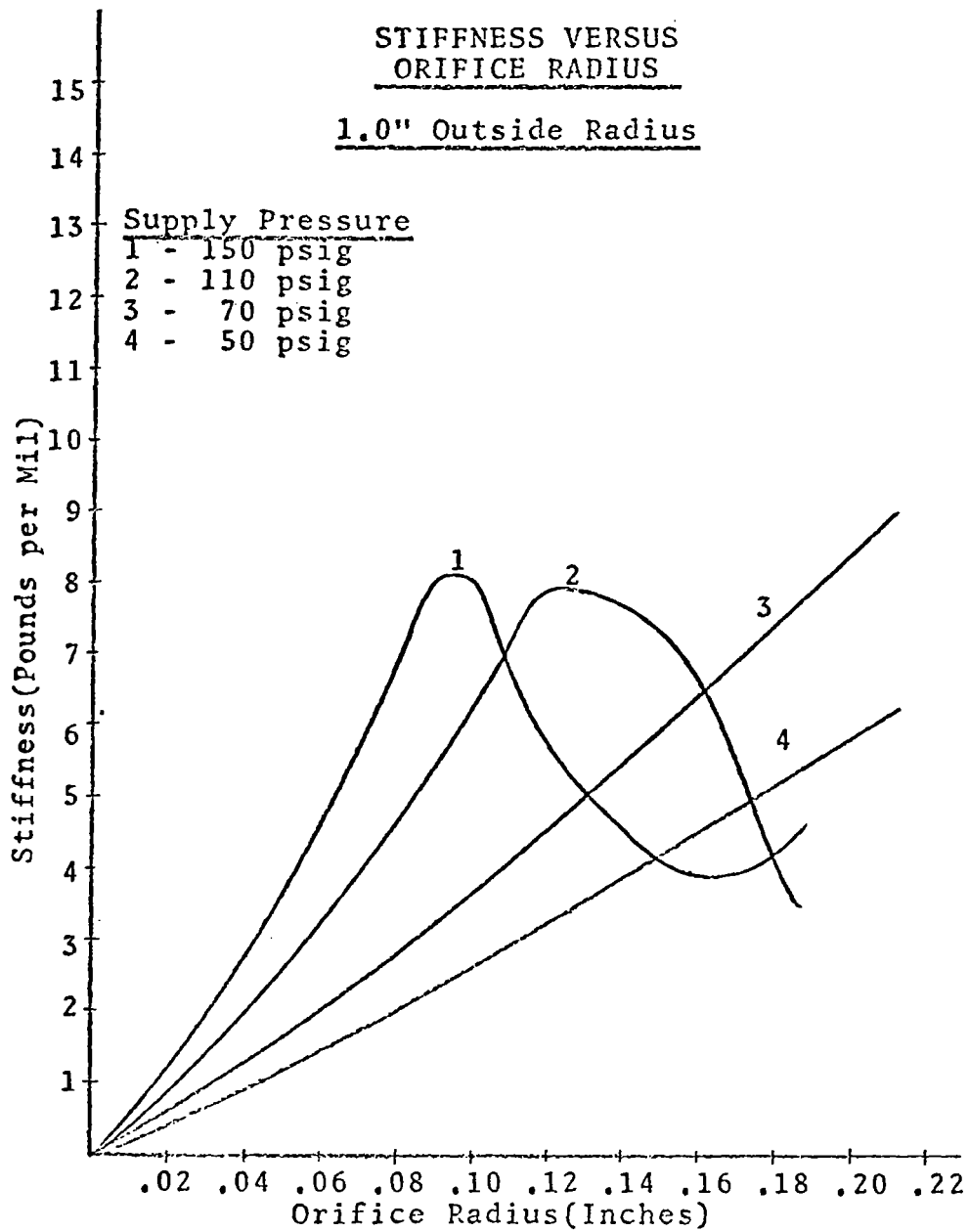


Figure 2.8

this loss in stiffness with increasing orifice radius and supply pressure is that the shock wave has approached the outside radius of the bearing and the flow regime is completely supersonic. As has been mentioned, the supersonic flow has associated with it a low static pressure. It is therefore possible with a 1-inch outside radius to obtain a higher theoretical stiffness with a lower supply pressure. If supply pressures in the range of 110 to 150 psig are used in a 1-inch outside radius bearing, the orifice radius should not exceed the radii of these maximums. This limitation would also have been observed for the 2- and 3-inch outside radius bearings if the orifice radii had been increased to sufficiently large values.

Figures 2.9, 2.10, and 2.11 show stiffness as a function of outside radius for .0625", .09375", and .125" orifice radii respectively. For all the parameter ranges considered, the stiffness increases with the bearing's outer radius. The low stiffness shown in Figure 2.11 at an outside radius of 1 inch and a supply pressure of 150 psig is again caused by

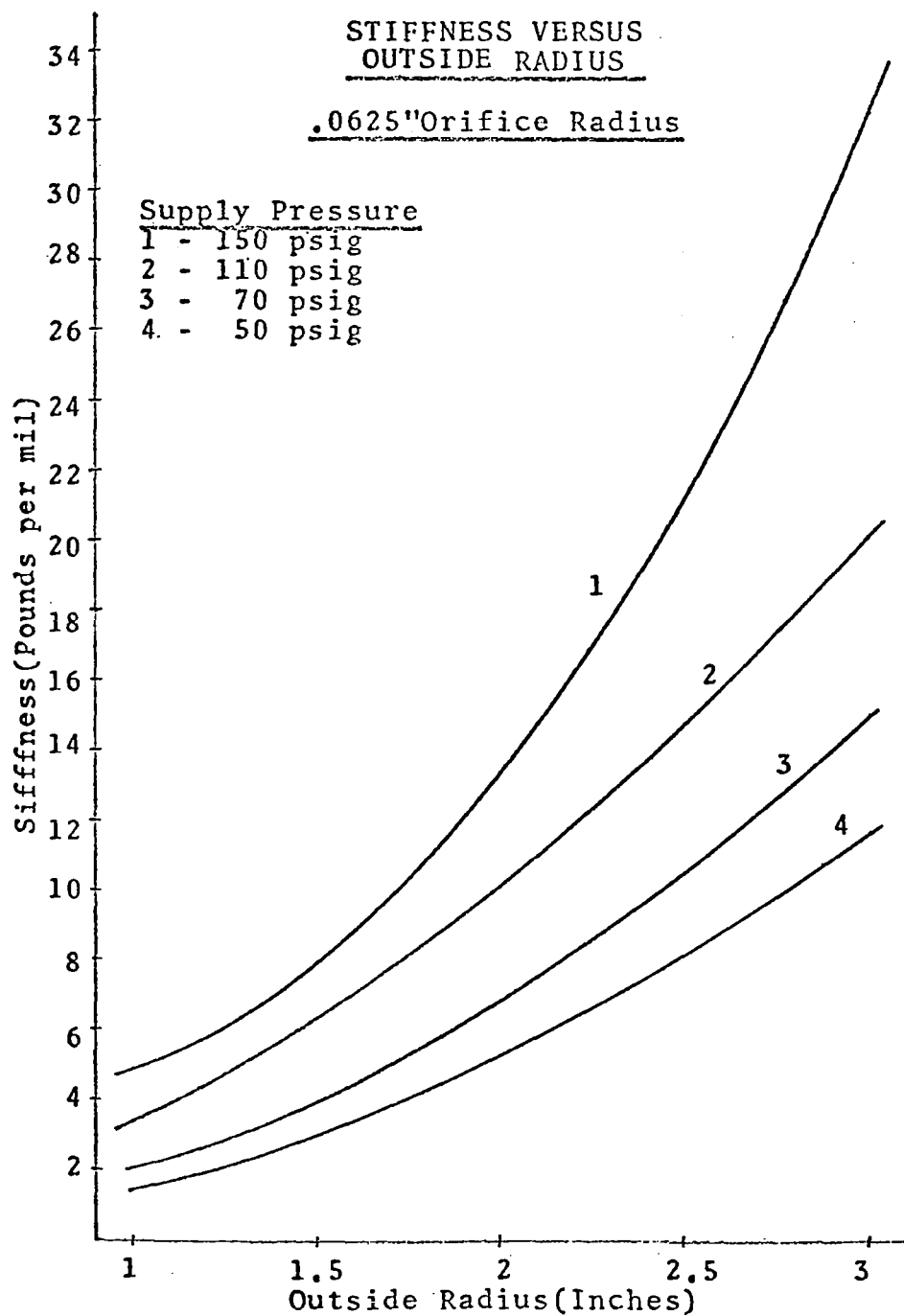


Figure 2.9

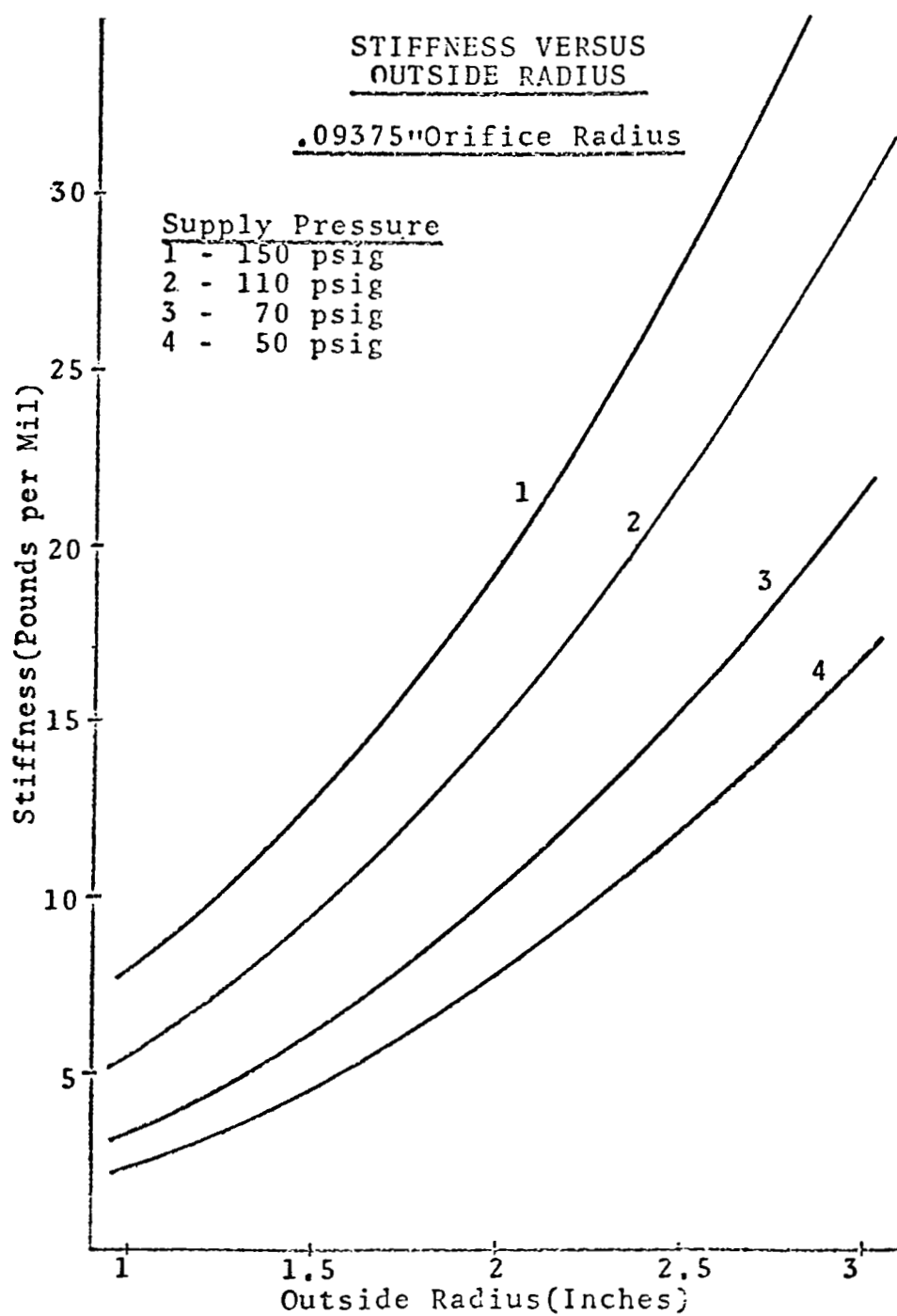


Figure 2.10

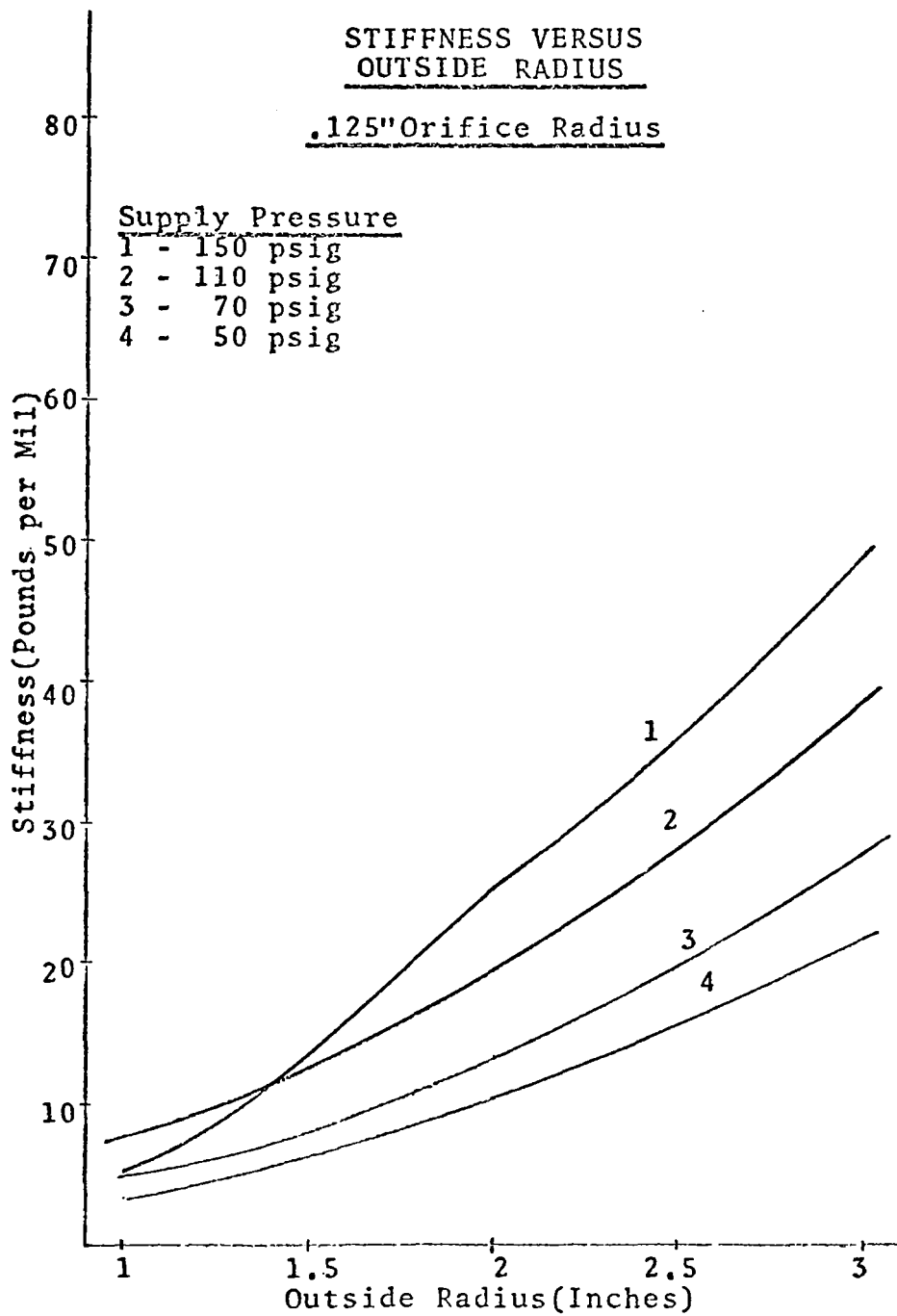


Figure 2.11

the shock wave.

Another parameter which should be investigated is the "no load gap" or the theoretical gap at which the air bearing would float if it had zero weight. In order to utilize the magnet's force to its full potential, it is desirable to have the no load gap as small as possible without exceeding the practical limitations of the system. No load gap as a function of orifice radius is shown in Figures 2.12 and 2.13. It can be seen from these figures that the no load gap generally decreases with increasing orifice radius to some minimum. It also should be noted that this parameter increases with increasing outside radius and decreases with increasing supply pressure.

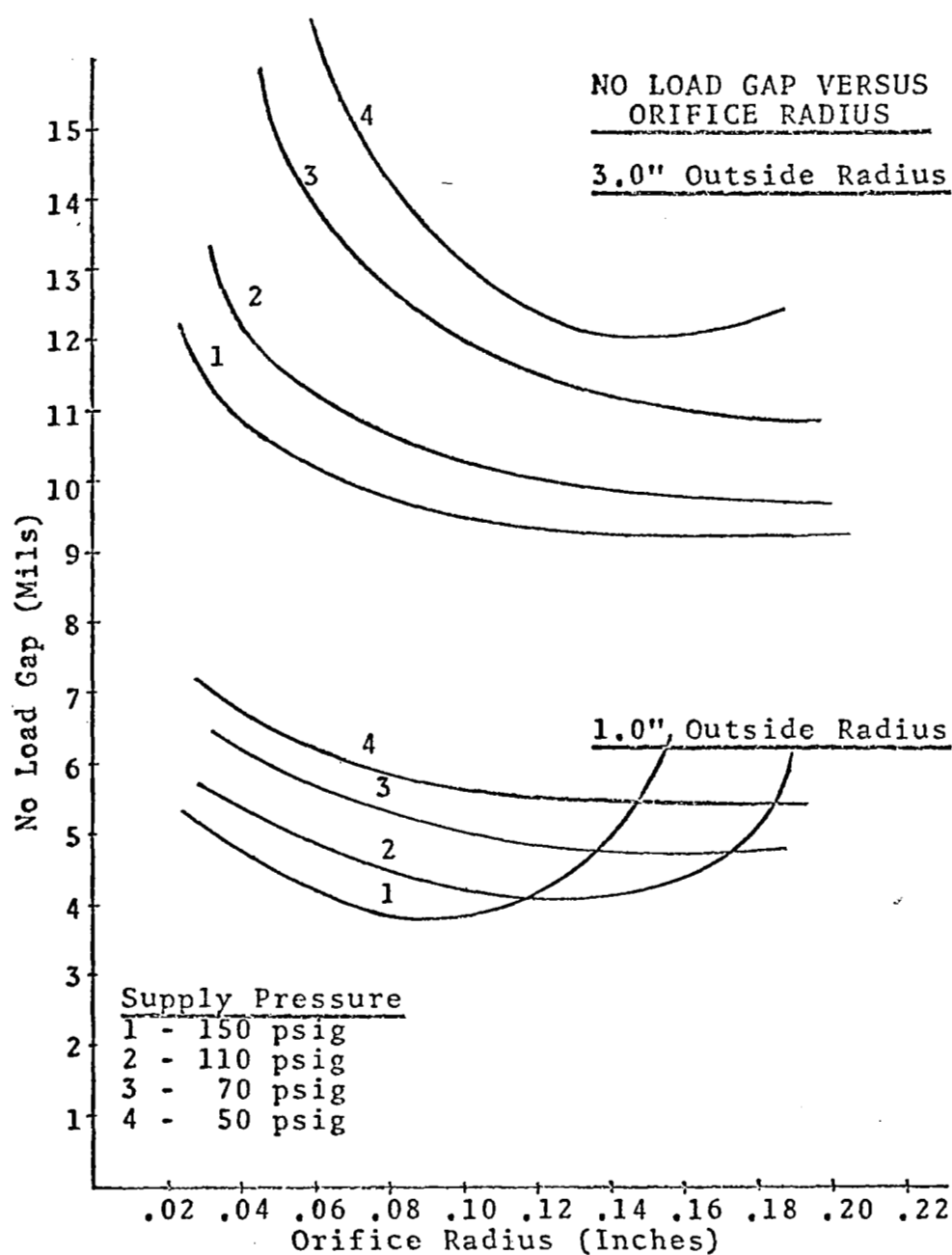


Figure 2.12

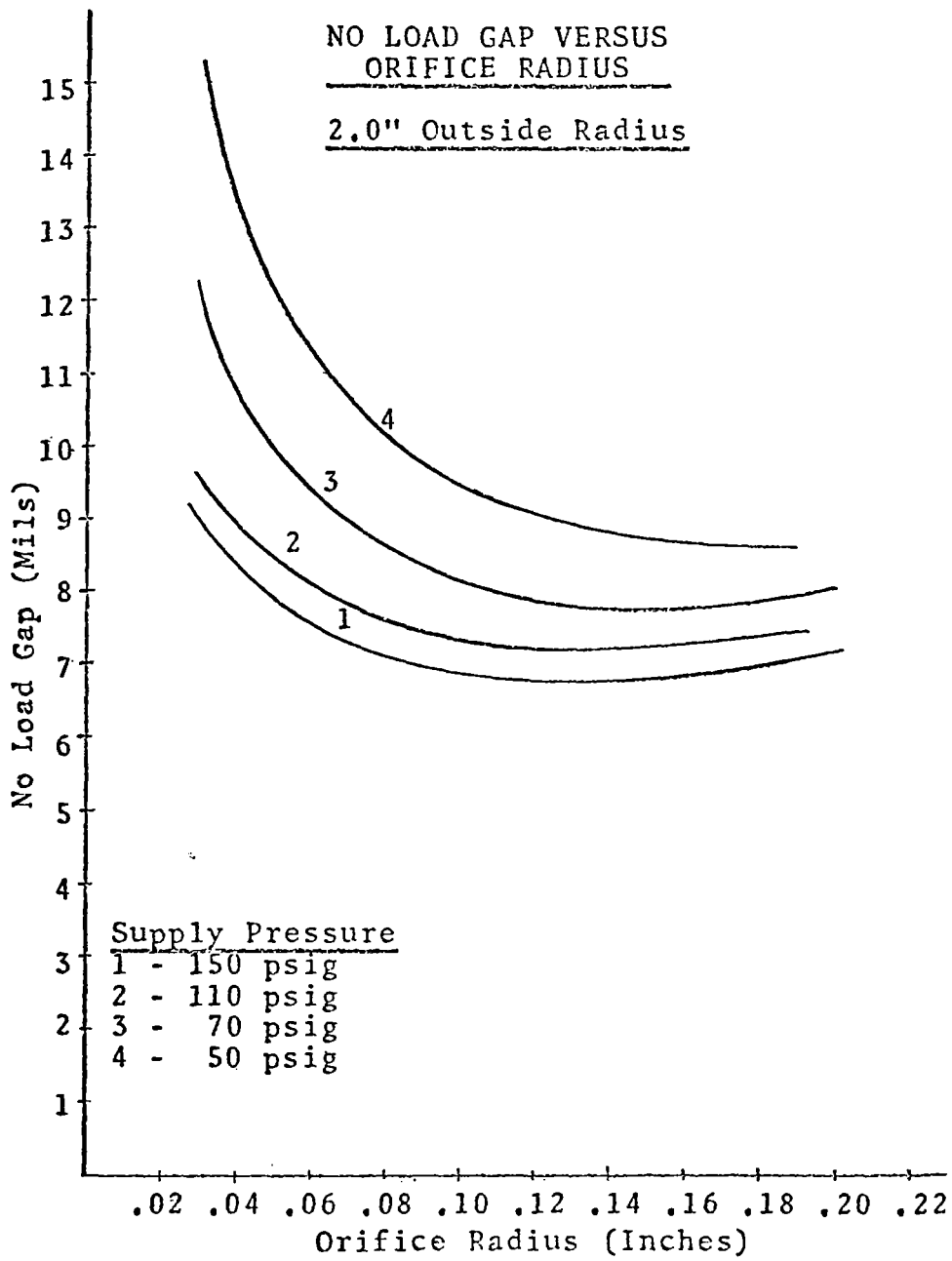


Figure 2.13

2.6 COMPARISON OF THEORETICAL AND EXPERIMENTAL RESULTS

The experimental investigation of the air bearing's characteristics was conducted using the apparatus shown in Figure 2.14.

The pressure distribution under the bearing was measured using a sliding plate with a .013" diameter hole in its surface. This hole was connected by a line to a pressure-measuring device. By sliding the plate under the bearing, the pressure can be measured at any radius. The sliding plate pressure-measuring device and a typical test air bearing are shown in Figure 2.15.

Figure 2.16 shows some typical bearing pressure profiles and compares them to the theory. It should be noted that the largest error between theory and experiment occurs in the subsonic region at low gaps and small radii. This error is caused because as the air gap decreases, the entrance Mach number to the subsonic flow regime increases. In fact, if the gap decreases to the point where the shock wave

APPARATUS FOR MEASURING AIR BEARING CHARACTERISTICS

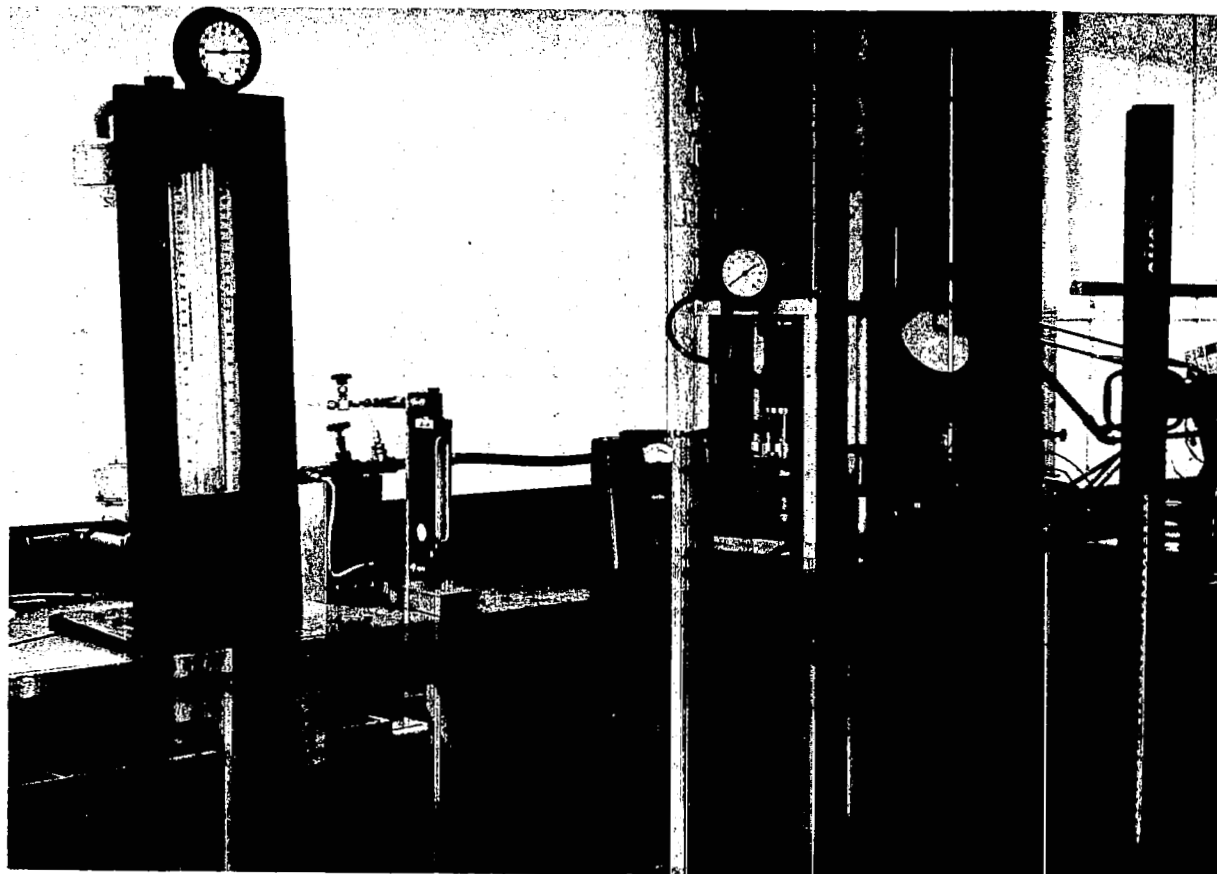


Figure 2.14

SLIDER PLATE AND TEST BEARING

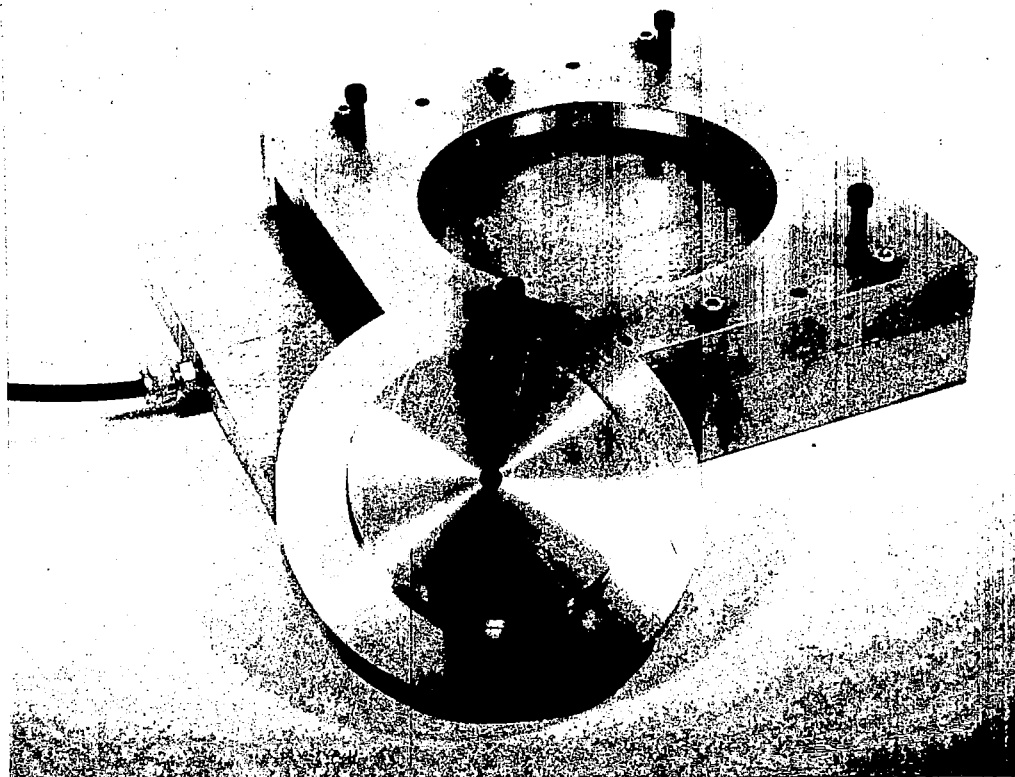


Figure 2.15

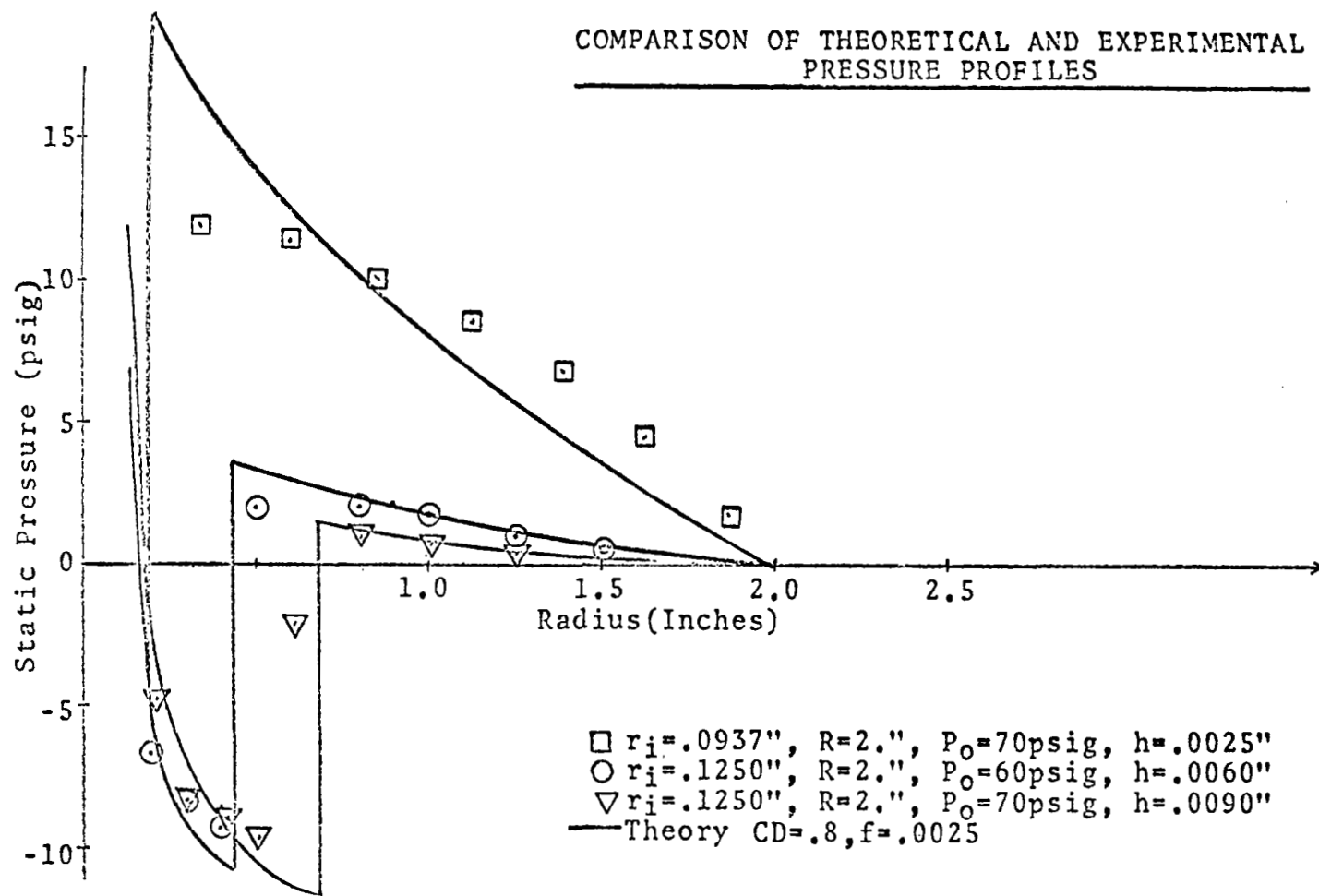


Figure 2.16

approaches the orifice radius, the entrance Mach number to the subsonic regime must approach one. The error is caused because the momentum effects were neglected in the subsonic flow theory; therefore, one would not expect very good experimental agreement at high subsonic velocities. The presence of this error does not degrade the usefulness of the theory as applied to the magnetic air bearing since the device's operating gap will be large enough to lower the subsonic entrance Mach number.

From the pressure profiles it can be seen that the theoretical shock wave position is in good agreement with experiment. However, by using the slider plate, it was found that the shock wave occurs over a radius range of approximately $1/8$ ". This means that, instead of a single normal shock wave occurring as was assumed in the theory, a series of oblique shock waves must occur.

Experimental flow data for several air bearings are shown in Figure 2.17. Theoretical flow characteristics are also shown in this figure for purposes of comparison. It can be seen that the experimental

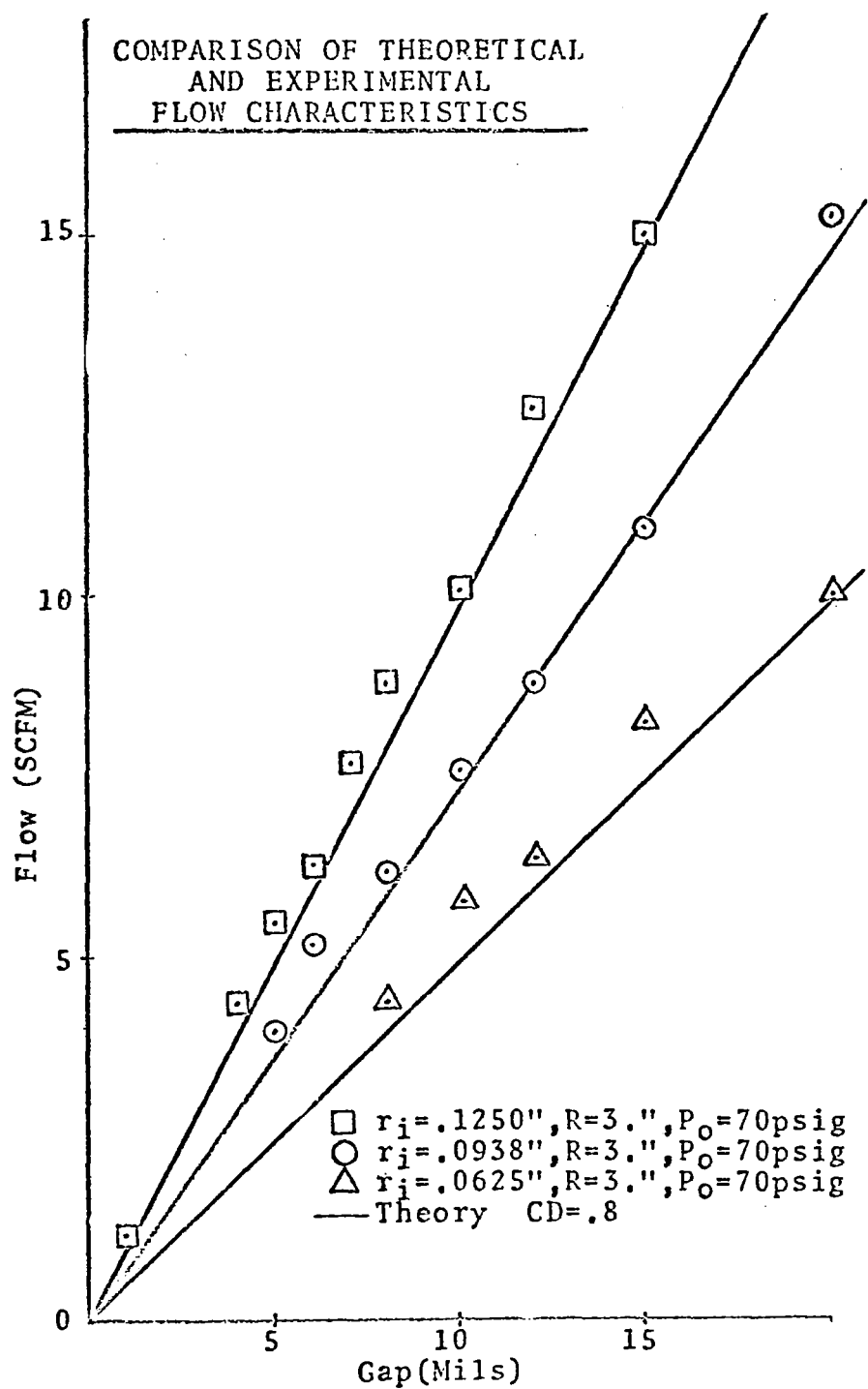


Figure 2.17

flow is directly proportional to the gap in the range considered. The theoretical flow characteristics are slightly below the experimental data. This small error could have been eliminated by increasing the .8 discharge coefficient.

Since theoretical and experimental flow-versus-gap curves are straight lines through the origin, a complete flow characteristic can be represented by the rate of change of flow with gap. This flow gradient is plotted against orifice radius in Figure 2.18. Again, it can be seen that the theory is in good agreement with experiment. This set of curves can be used to determine the flow characteristic of an air bearing of any orifice size operating in the pressure range of 50 to 150 psig.

A comparison of theoretical and experimental force characteristics are presented in Figures 2.19 through 2.25. Since these force characteristics were the prime objective of the analysis, it is encouraging to note that the theory is in excellent agreement with experiment. Looking at these graphs,

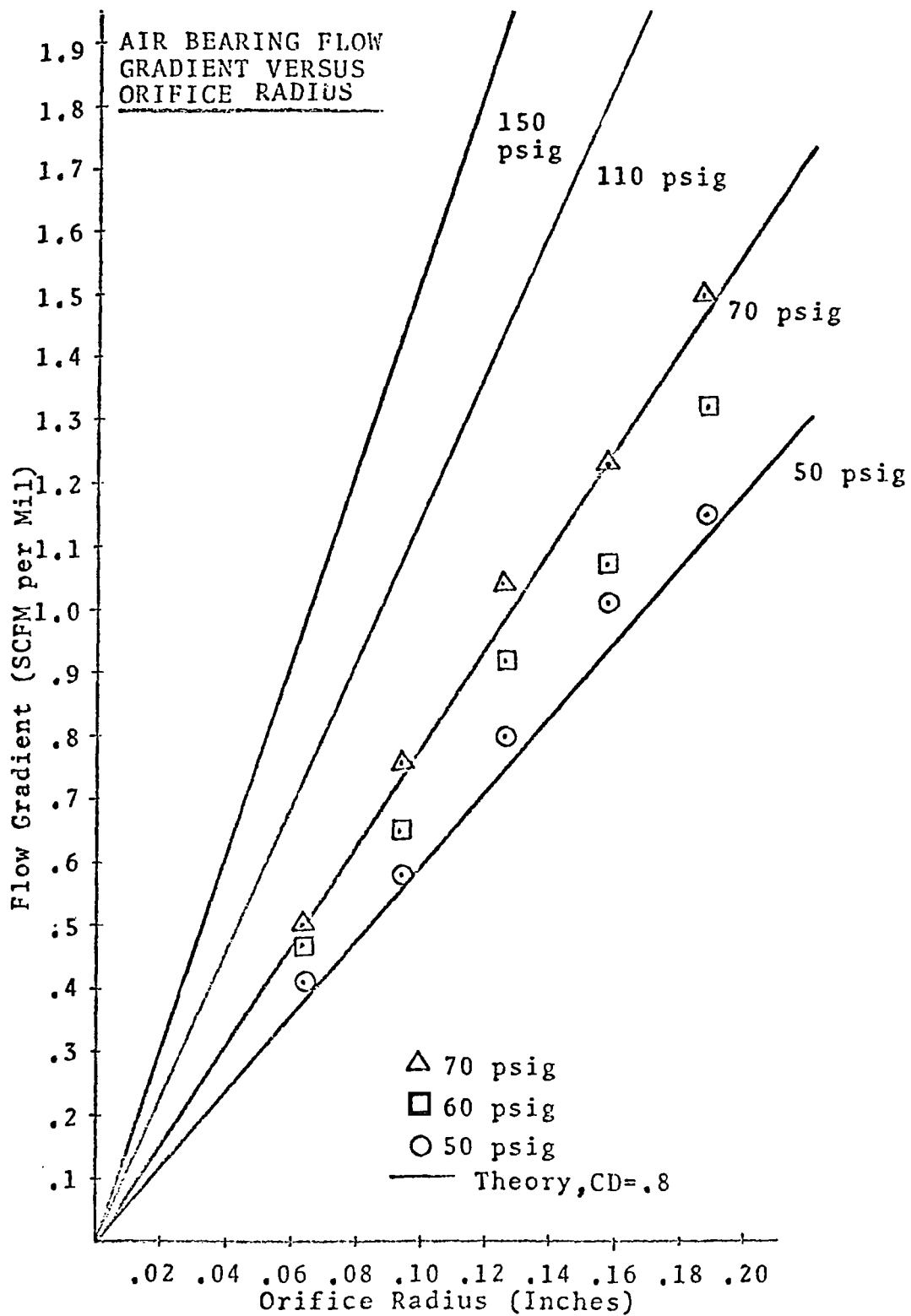


Figure 2.18

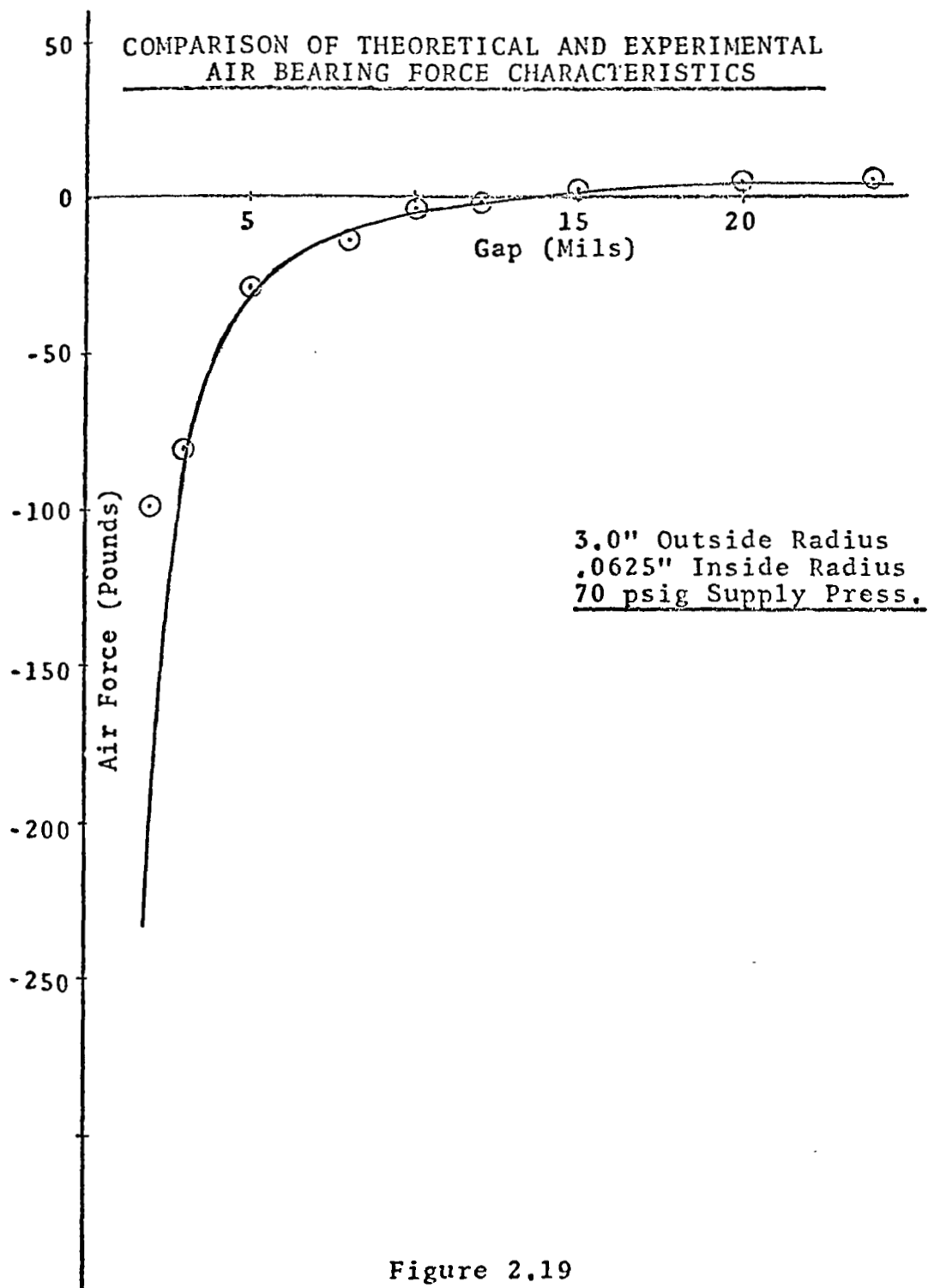
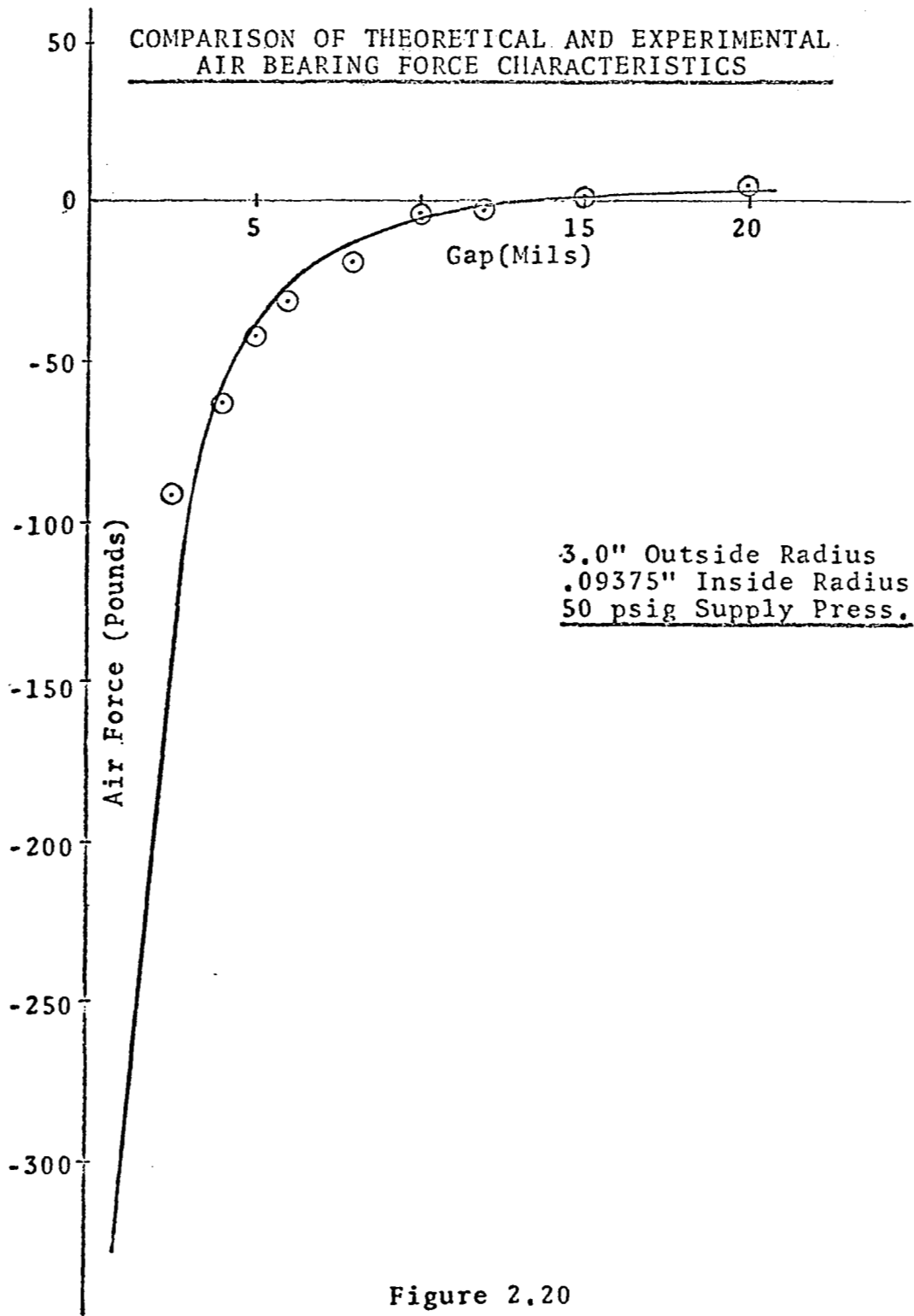


Figure 2.19



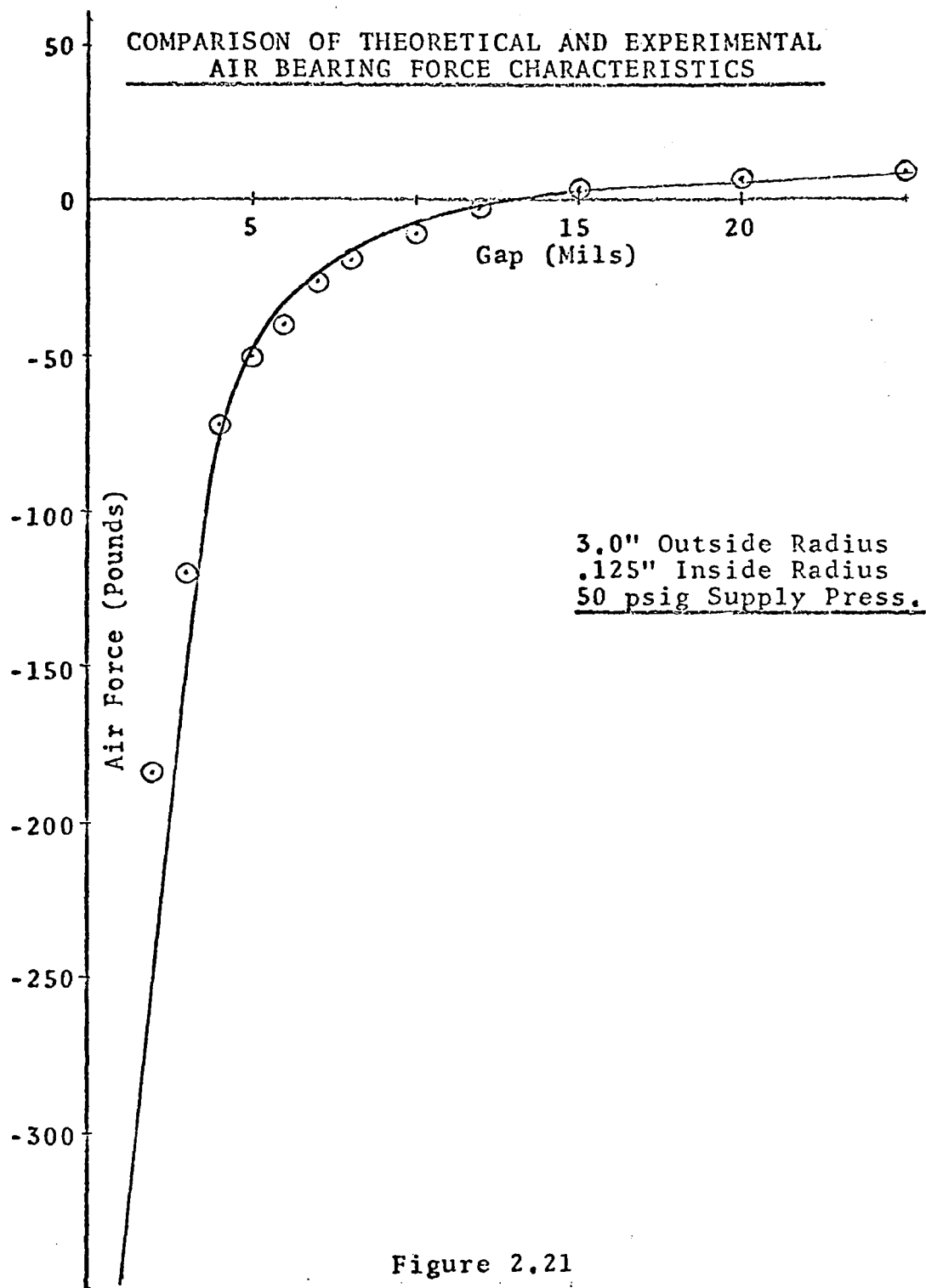


Figure 2.21

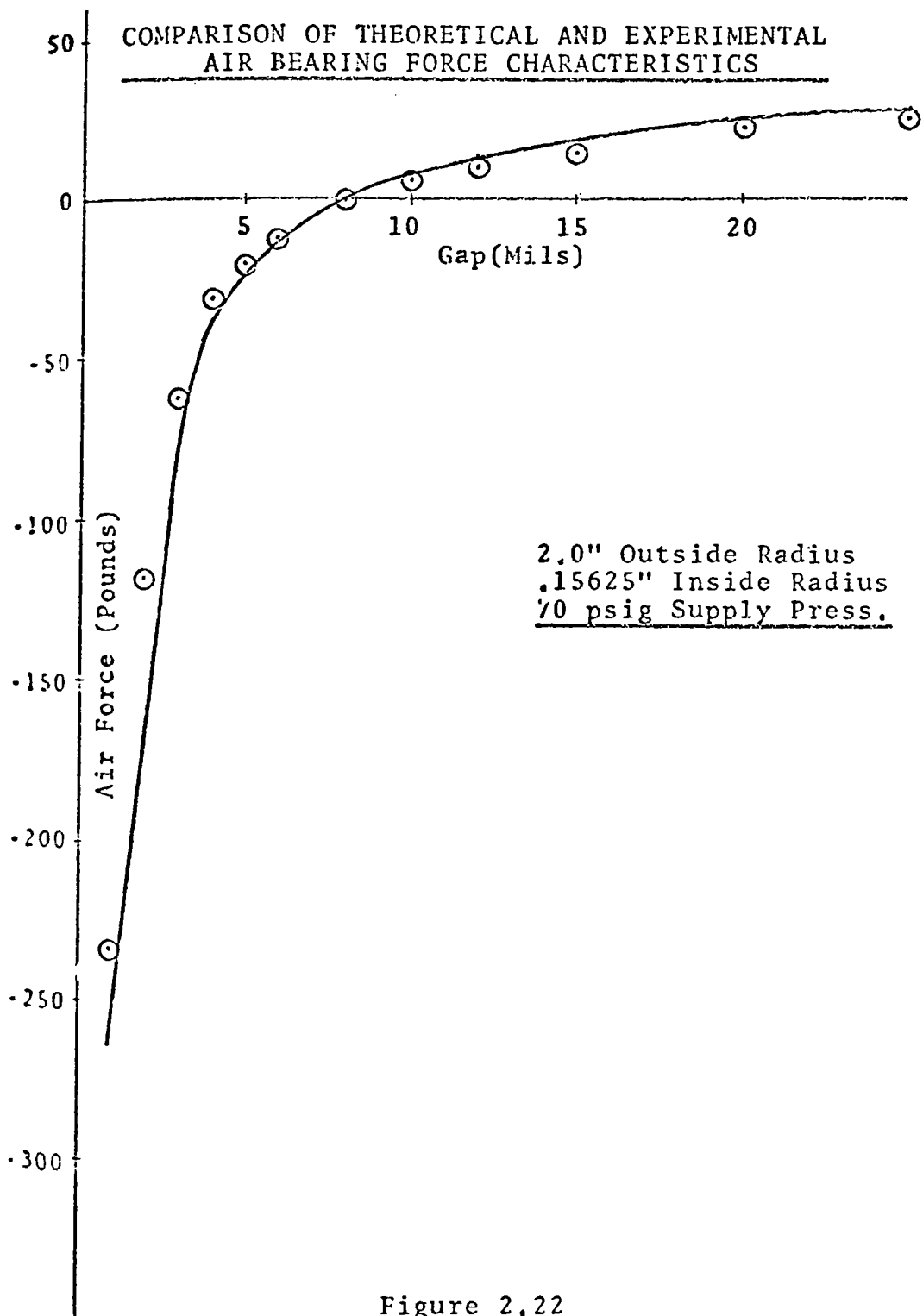


Figure 2.22

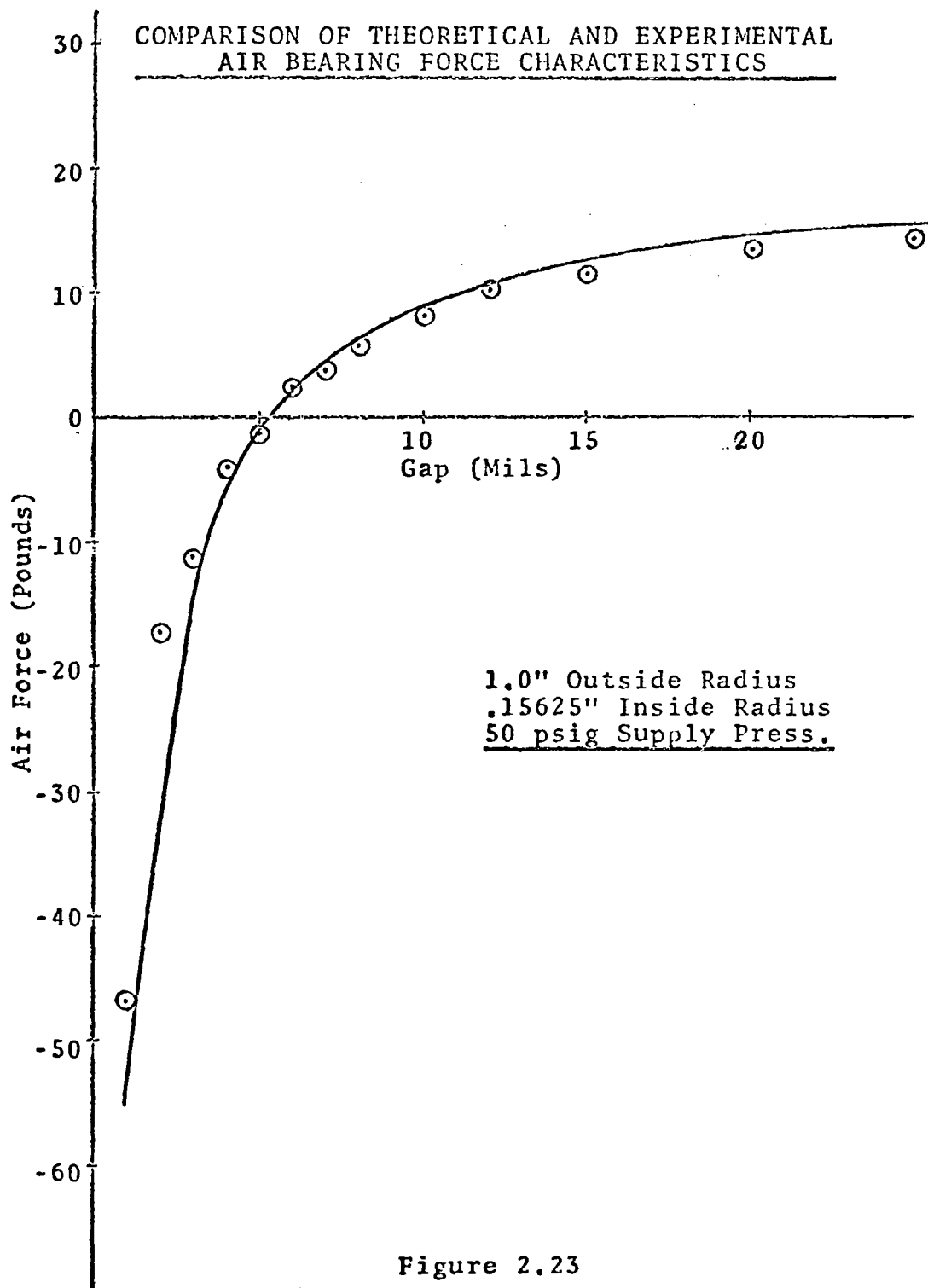


Figure 2.23

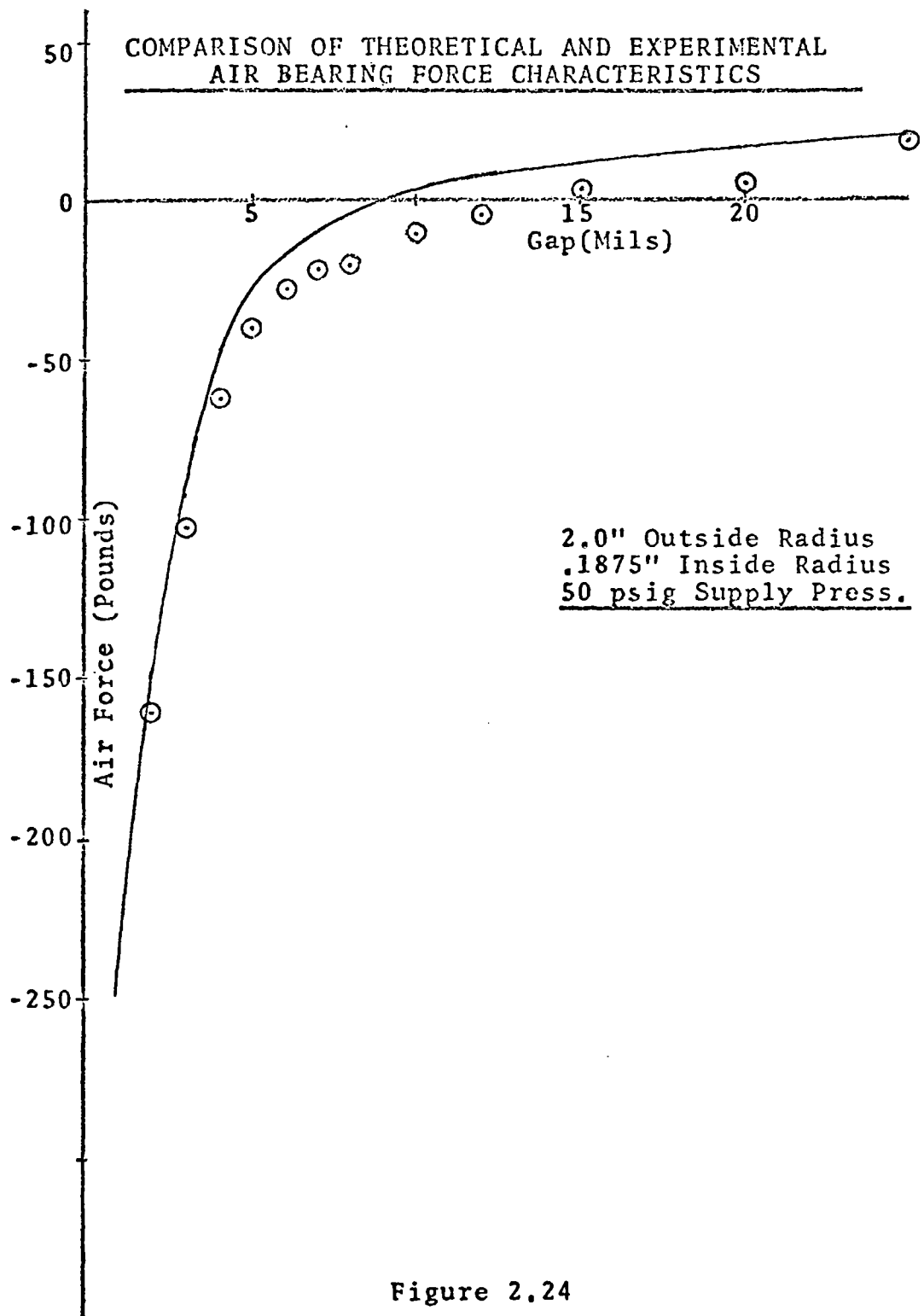


Figure 2.24

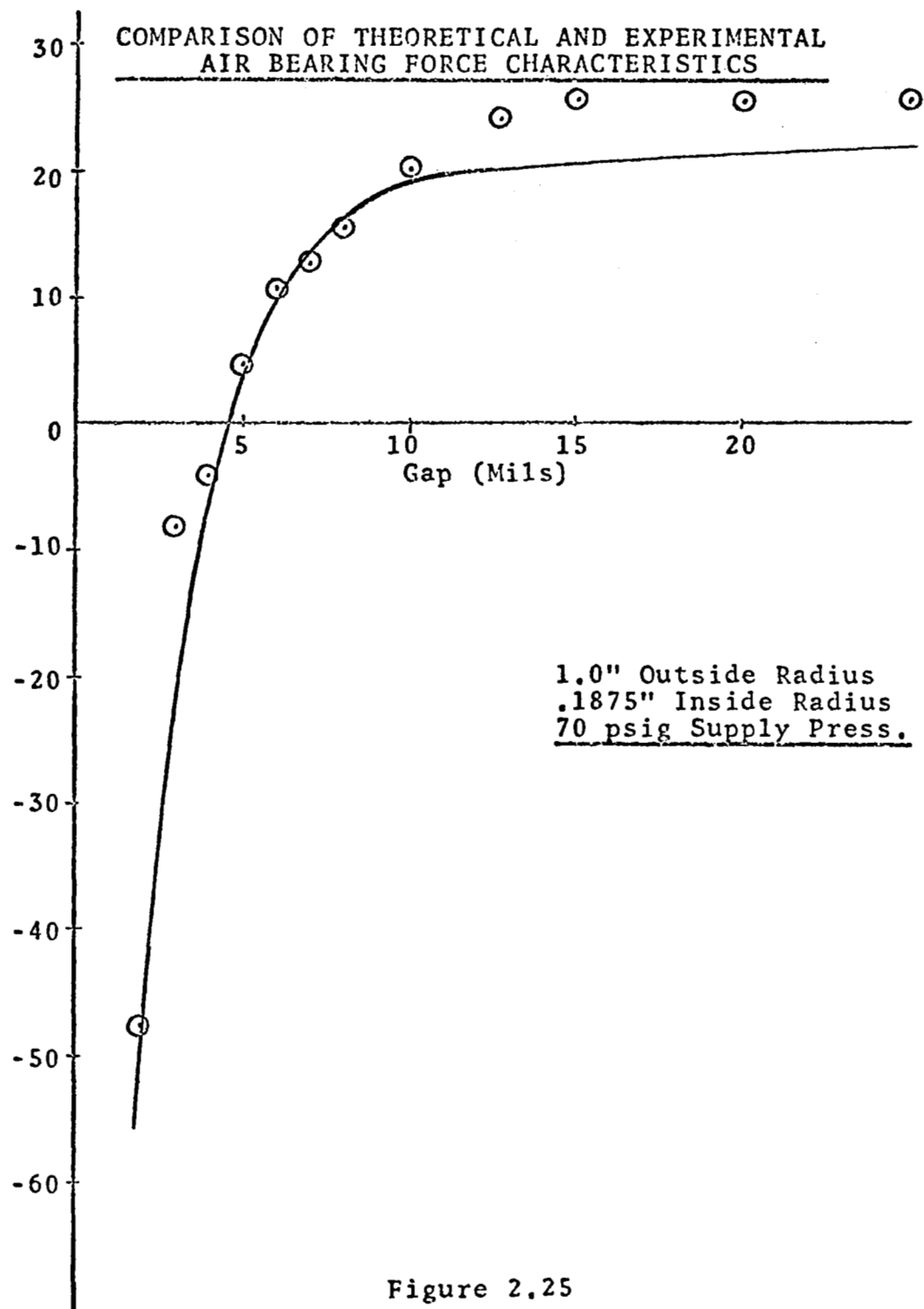


Figure 2.25

it is difficult to pinpoint any consistent errors. It was anticipated that the theory would predict a higher stiffness in the low gap region (below approximately 3 mils) than that found by experiment because momentum effects in the subsonic flow were neglected resulting in a higher-than-actual pressure distribution. This cannot be conclusively observed, however, in the comparison of theoretical and experimental force characteristics.

Because of the general good agreement between theory and experiment, it is believed that the use of theoretical results is adequate in the design of a magnetic air bearing.

2.7 DISCUSSION OF SECONDARY EFFECTS

The Supply Line

The line connecting the air bearing to the air supply will have somewhat of a degrading effect on the performance of the device. It has been shown that the stiffness of a bearing decreases with supply pressure. Also, the pressure drop across the line will increase with the flow through the line or with increase in air bearing gap; hence, the air bearing's force characteristics will be modified. For this reason, the supply line should be considered in the design of the system.

Once the desired operating pressure and gap are known, one can calculate the source pressure required to maintain the design supply pressure. The line should also be of sufficient diameter to prevent a large percentage change in bearing supply pressure with flow variation through the bearing's operating range.

Moment Stability

The air bearing must have sufficient stiffness to compensate for the magnet's instability in the vertical direction. Since a magnet is also unstable in a tipping mode, the air bearing must also supply a stabilizing moment. It is known from prototype magnetic air bearings that this stabilizing moment does exist.

It is theorized that, as the air bearing tips, the shock wave will move in on the close side and out on the far side. This movement of the shock wave will cause subsonic flow to be predominant on the close side and thereby increase pressure in that area. On the far side, the subatmospheric pressure associated with the supersonic region will cause a downwards force. This can be described as a type of internal feedback which senses tipping and generates a correcting moment.

3.0 THEORETICAL AND EXPERIMENTAL ANALYSIS OF THE MAGNET

3.1 SURVEY OF POTENTIAL MAGNET DESIGNS

The initial selection of potential magnet designs was based on the following considerations:

- a. High force-to-weight ratio
- b. Size and shape compatibility with the air bearing
- c. Minimum force gradient through the operating range of the bearing
- d. Long-term stability of magnetic properties
- e. Minimum required ceiling thickness for proper operation.

The second design consideration confines the study to magnets which are circular in shape. This limitation is reasonable since a rectangular or a horseshoe-shaped magnet would require filling of the surrounding space with some nonmagnetic material and thereby increase the weight of the design with no net increase in magnet force.

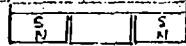
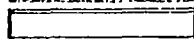
Figure 3.1 shows eight potential magnet designs which meet this shape limitation. Since these particular magnets all use the same weight of magnetic material (0.27 pounds), it is therefore possible to compare them directly for selection in this application.

The force-versus-air gap characteristic of these magnets is shown in Figure 3.2. A better method for comparing the effectiveness of each design is the force-to-total assembly weight ratio versus air-gap characteristic shown in Figure 3.3.⁽¹⁰⁾

It can be seen that designs 1 and 4 have the lowest force gradient over the operating range (approximately from 0 to .015 of an inch). However, they are ruled out as design candidates due to their poor force-to-weight ratio. Designs 7 and 2 can also be eliminated due to low force-to-weight ratio. Design 8 has an excellent force-to-weight ratio at zero gap; however, its force gradient is the highest of any of the designs, and thus its performance drops off quickly with gap. This design is therefore eliminated as a candidate.

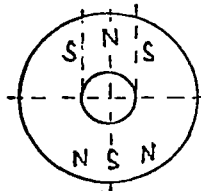
POTENTIAL MAGNET DESIGNS

Index I Non-Oriented Ceramic

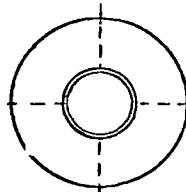


$W_t = .35$ lbs
 $T_c = .05$ in

$W_t = .66$ lbs
 $T_c = .20$ in

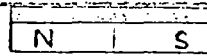
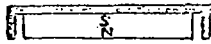


Design 1



Design 2

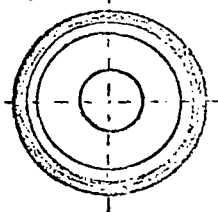
Index V Oriented Ceramic



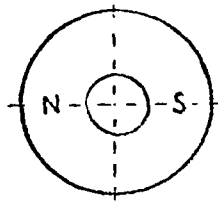
$W_t = .54$ lbs
 $T_c = .11$ in

$W_t = .50$ lbs
 $T_c = .20$ in

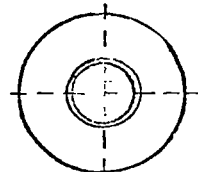
$W_t = .72$ lbs
 $T_c = .25$ in



Design 3



Design 4



Design 5

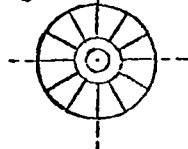
Alnico V



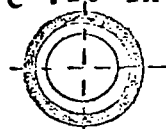
$W_t = .27$ lbs
 $T_c = .20$ in

$W_t = .72$ lbs
 $T_c = .20$ in

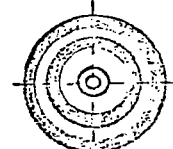
$W_t = 1.0$ lbs
 $T_c = .20$ in



Design 6



Design 7



Design 8

Shaded areas represent mild steel.

Figure 3.1

FORCE CHARACTERISTICS OF
POTENTIAL MAGNET DESIGNS

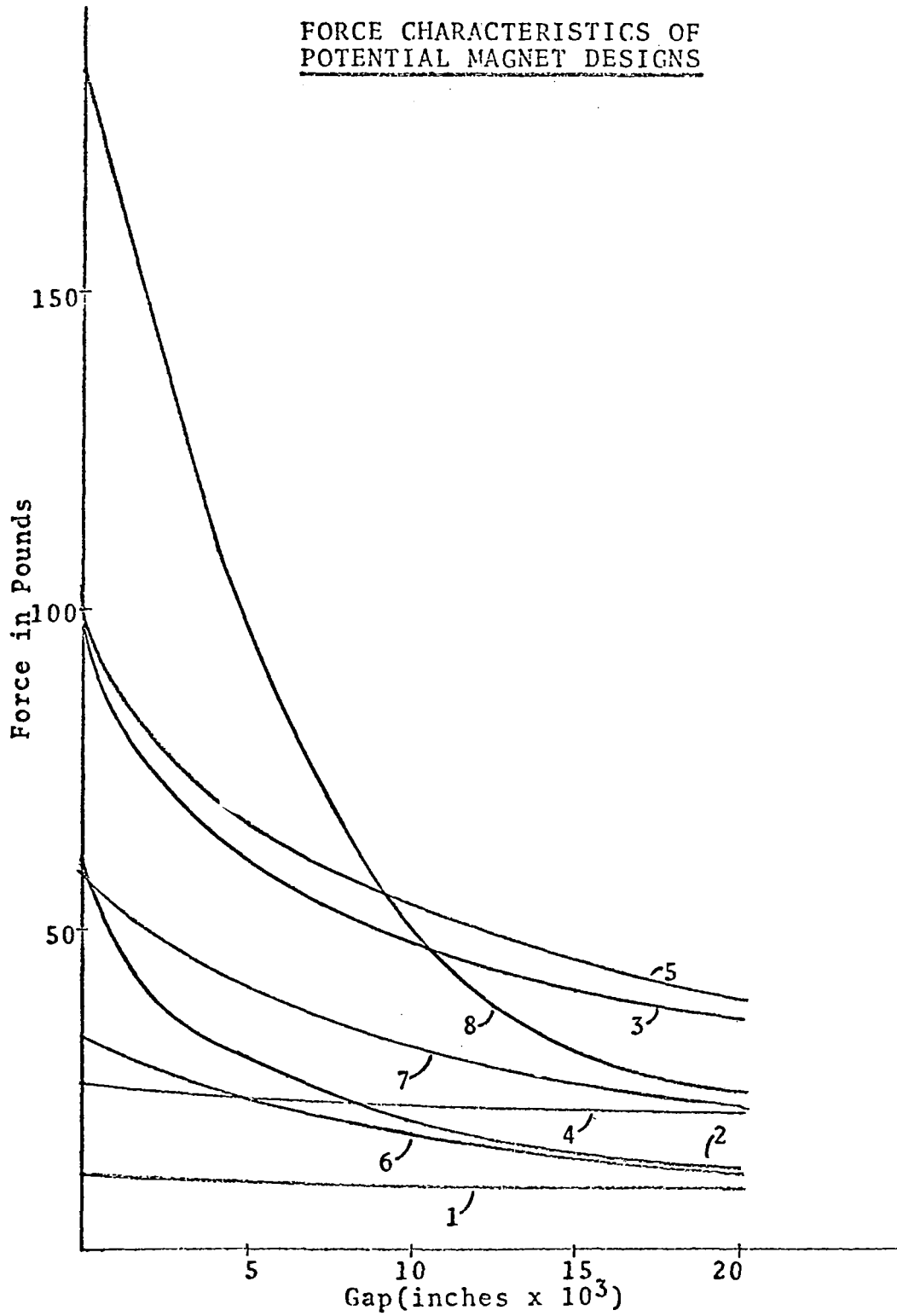


Figure 3.2

FORCE-TO-WEIGHT RATIO
OF POTENTIAL MAGNET DESIGNS
VERSUS AIR GAP

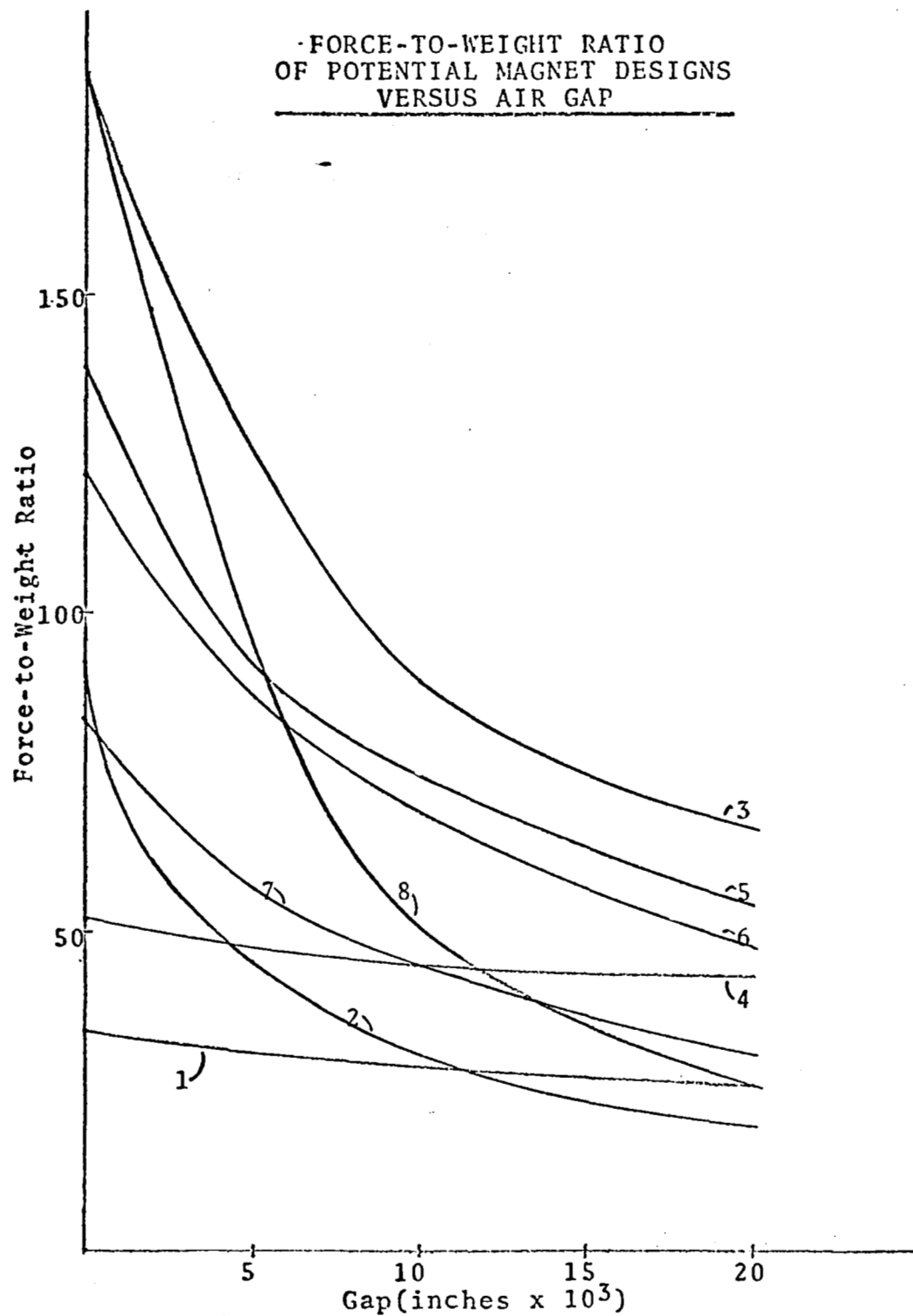


Figure 3.3

This leaves magnets 3, 5 and 6 as potential designs. It is obvious from Figure 3.3 that the outside shell ceramic disc magnet (design 3) is superior to designs 5 and 6 throughout the operating range. In addition, the required ceiling thickness to develop maximum force is smaller for this design than for designs 5 and 6.

The inside shell oriented ceramic disc magnet (design 5) has the second-best force-to-weight ratio and, due to its ideal disc shape, will be kept as a prime design candidate. The main disadvantage of this design is that it requires a thicker ceiling to develop maximum force than the other two. Design 6 has been used successfully in prototype magnetic air bearings, but its availability in different sizes is extremely limited. In addition, the magnetic material used in this design is Alnico V, which has a lower degree of long-term magnetic stability than the oriented ceramic material used in designs 3 and 5. For these reasons, design 6 will not be considered for further design studies.

3.2 MAGNETIC MATERIALS

Oriented barium ferrite ceramic permanent magnet materials have been selected as the optimum material for the design of the magnetic air bearing.

Oriented barium ferrite has the highest coercive force of any of the commercially available magnetic materials.⁽¹¹⁾ This means that it has a high resistance to external demagnetizing influences. The high coercive force also implies that the optimum magnet length will be much shorter for this material than for a metallic magnetic material with a lower coercive force.

Another advantage of barium ferrite is that it is considerably lighter than metallic permanent magnet materials. It has a density of approximately 65% of Alnico V. The demagnetization curves for two oriented barium ferrite materials are shown in Figure 3.4.

These materials have been developed by the Indiana General Corporation and will hereafter be

DEMAGNETIZATION CURVES FOR
TWO ORIENTED BARIUM FERRITE MATERIALS

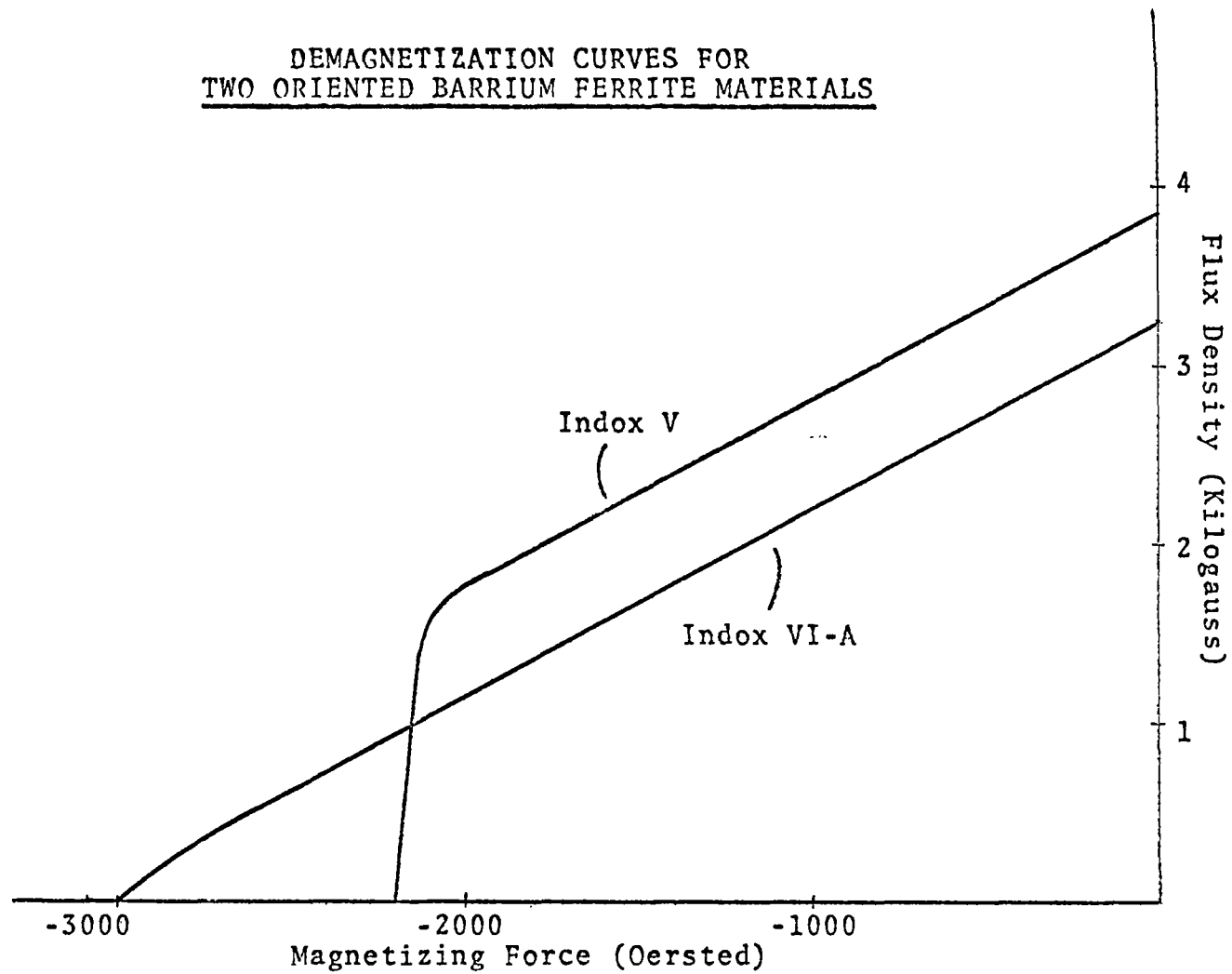


Figure 3.4

referred to by their respective trade names, Indox V and Indox VI-A. The physical properties for these materials are given in the following table: (12)

	<u>Indox V</u>	<u>Indox VI-A</u>
Coercive force, oersted	2 200.	3 000.
Residual induction, gauss	3 840.	3 300.
Peak energy product, gauss-oersted	3.5×10^6	2.6×10^6
Reversible permeability	1.05	1.06
Field strength for saturation, oersted	10 000.	10 000.
Density, pounds per cubic inch	.181	.162

The magnetic properties given above apply only in the direction of material orientation. The magnetic properties in directions other than this are almost negligible. For the disc ceramic magnets, the directions of orientation and magnetization are parallel to the axis of the disc.

Since Indox V has a larger energy product than Indox VI-A, it has the potential of delivering a greater attractive force than the same volume of Indox VI-A.

In order to utilize the full potential of Indox V, however, it must be operated above the knee in its demagnetization curve. Experimentation has shown that Indox V discs magnetized before assembly are below this knee. This means that, if Indox V is to be used to its full potential, it must be magnetized after assembly in its steel shell.

On the other hand, even though Indox VI-A has a lower energy product, it may be magnetized before assembly without any loss of available energy. This is true because Indox VI-A has the unusual characteristic that its recoil line coincides with its demagnetization curve. Indox VI-A also has the advantage that it has a lower density than Indox V.

These materials are formed into magnets by pressing barium ferrite powder under high pressure in a die. The direction of magnetic orientation corresponds to the direction of pressing. The compact is then sintered. During this sintering process, it shrinks to approximately $7/8$ of its pressed size. Because of this shrinkage, the surface of the magnet

is not suitably flat to be used as the bearing surface. These materials can be finished by grinding only. Because of manufacturing limitations, magnets employing these materials are limited to a maximum thickness of 1 inch and a minimum thickness of approximately .2 inch. In addition, magnet discs must have an area of at least 2 square inches.

The soft steel areas employed in the two designs are used simply as a conductor of flux. To be efficient in this purpose, the steel parts must be worked at flux densities reasonably below the saturation value of the chosen material. Magnetization curves for three common soft ferromagnetic materials are shown in Figure 3.5. Because of its availability and low cost, mild steel is chosen for this design. This material saturates at approximately 21 000 gauss.⁽¹³⁾ However, to maintain reasonable efficiency in conducting flux, it should not be operated beyond a flux density of 16 000 gauss. At this point, the material has a permeability of approximately 276. in the cgs system.

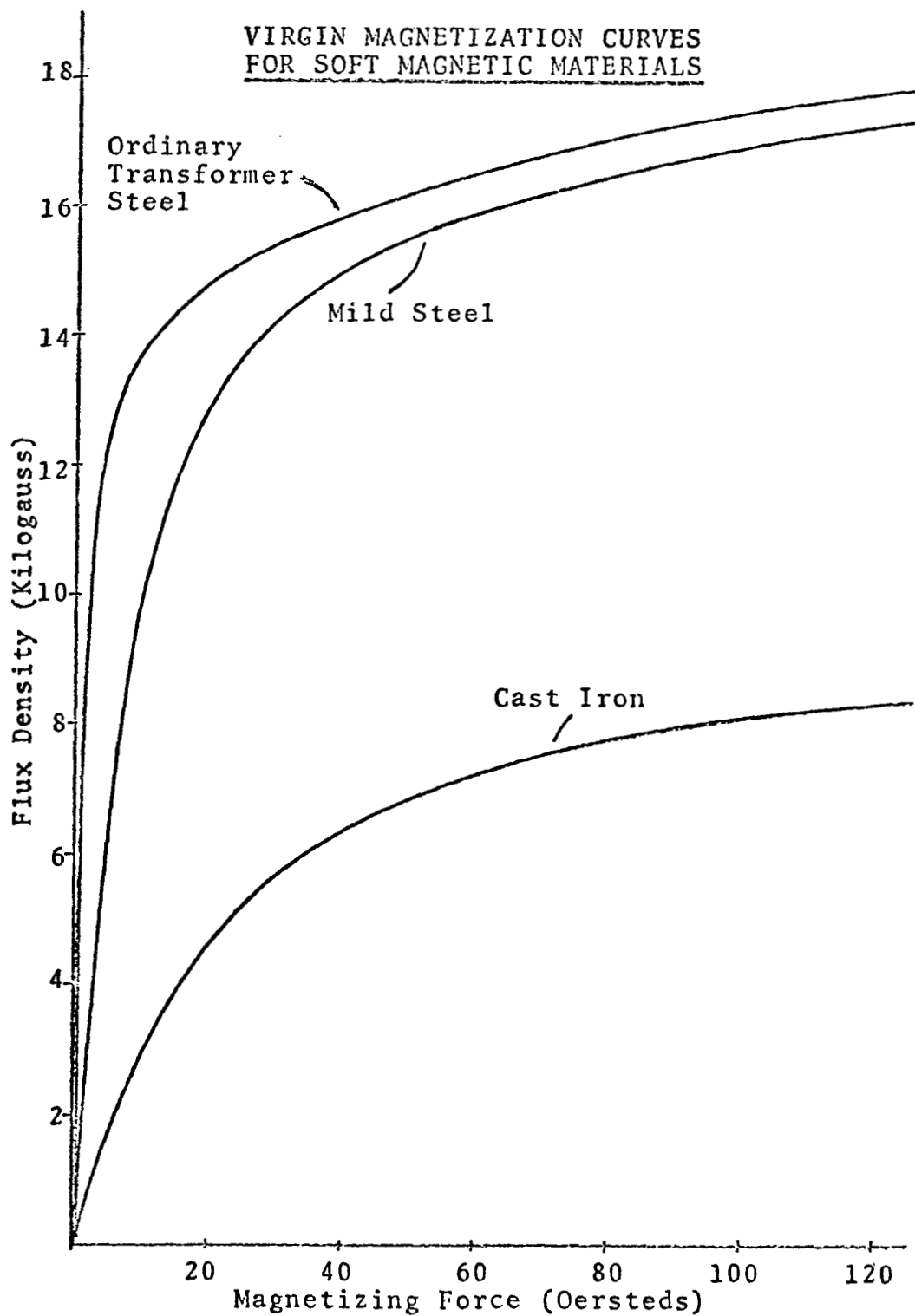


Figure 3.5

3.3 ANALYSIS OF DISC CERAMIC MAGNET FORCE CHARACTERISTIC

Due to the complexity of the general magneto-static boundary value problem, an approximate engineering approach will be taken for the force analysis of the magnets. This method depends on setting up an analogy between the magnetic circuit and an electrical circuit.

There are several limitations to this analogy. It must be assumed that the magnetic flux, like the current in the electrical case, is confined to pass through each individual circuit component. For the electrical circuit, this is a good assumption, since the ratio of the material conductivity to the conductivity of air is extremely large. In the magnetic circuit, the ratio of the permeability of a component to the permeability of air is not always large. This means that some of the magnetic flux will bypass the component through the surrounding air.⁽¹⁴⁾ This limitation can be somewhat overcome if one anticipates the leakage and accounts for its presence by a

parallel resistor. Another limitation to this analysis is that the flux density and magnetizing force must be assumed to be constant across each component in the magnetic circuit.

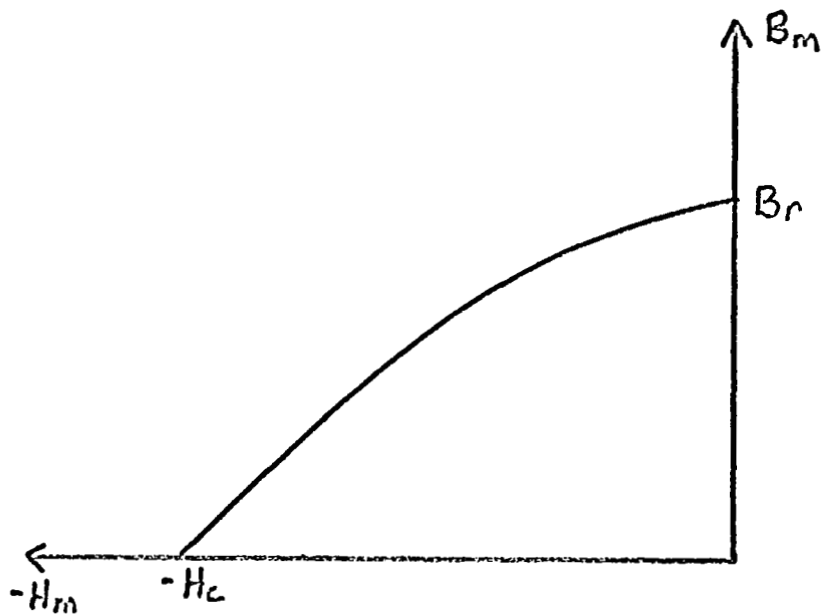
In spite of these drawbacks, this method allows the development of a parametric model which would be all but impossible using more exact methods.

Since the magnetic air bearing operates at small gap width, the following magnet analysis is intended to be valid for small air-gap widths only. In other words, the air gap will be assumed to be much smaller than any dimension of the magnet.

3.3.1 The Magnetic Circuit

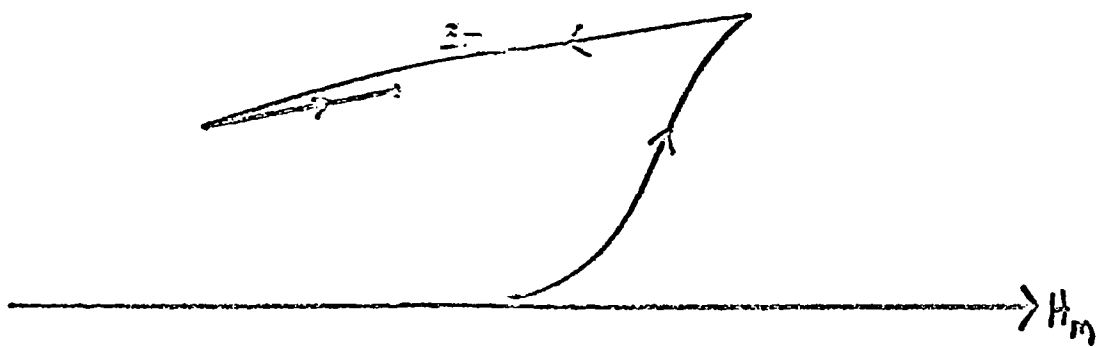
In this analysis, each component of the magnetic circuit will be included as a lumped parameter element.

Before proceeding with the force analysis, it is first necessary to determine the magnetic state of the permanent magnet. The term "state of the magnet" refers to the point on the demagnetization curve at which the magnet exists. A schematic representation of a demagnetization curve is shown below:



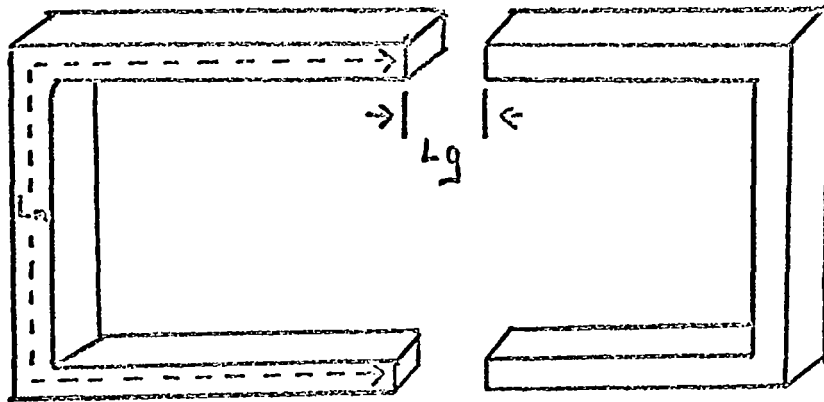
For the present, it will be assumed that the magnet was not magnetized within its shell. During magnetization, a magnetizing force sufficient to saturate the magnetic material is applied. Upon removal of the external magnetizing force, the state of the magnet recoils to the residual flux density B_r and zero magnetic field strength point. If the magnet were now removed from the magnetizing device, the state of the magnet would recoil still further to some point on the demagnetization curve. This phenomenon is said to occur because of the magnet's self-demagnetization. The degree of recoil would depend on the magnet's geometry provided that there were no other ferromagnetic materials in the vicinity.

Now if some ferromagnetic material were brought near the magnet (e.g., the shell is installed), the magnet state would advance up a recoil line and not necessarily back up the demagnetization curve. This train of events is shown diagrammatically in the following figure:



3.3.2 Electrical Analogy

To give mathematical basis to the preceding discussion and to develop the electrical analogy, consider the following magnetic circuit:



The cross-sectional area of this magnet is set at a constant value of A_m . It will be assumed that leakage external to the air gap L_g is negligible. This is a good assumption if the air gap is smaller than any dimension of the magnetic circuit.

If the air gap is set at zero, and the magnet is brought up the saturation point with an external magnetizing force, and this magnetizing force is then

released; the flux density in the circuit will be equal to the residual flux density of the material B_r . Now, taking some small gap into account, the scalar magnetic potential around this circuit is zero since the path does not pass through any current loops.

$$\oint \underline{H} \cdot d\underline{l} = 0$$

Assuming that the magnetizing force is constant in the magnet and the air gap, upon integration, we obtain

$$H_m \ell_m + H_g \ell_g = 0 \quad (3.1)$$

In addition, we know that the flux is a constant through this circuit

$$\Phi = \int_s \underline{B} \cdot d\underline{A}$$

or

$$B_m A_m = B_g A_g \quad (3.2)$$

We also know that in the air gap

$$B_g = \mu_0 H_g \quad (3.3)$$

Now combining Equations (3.1), (3.2) and (3.3), we obtain the equation of what is commonly known as the air gap shearing line.

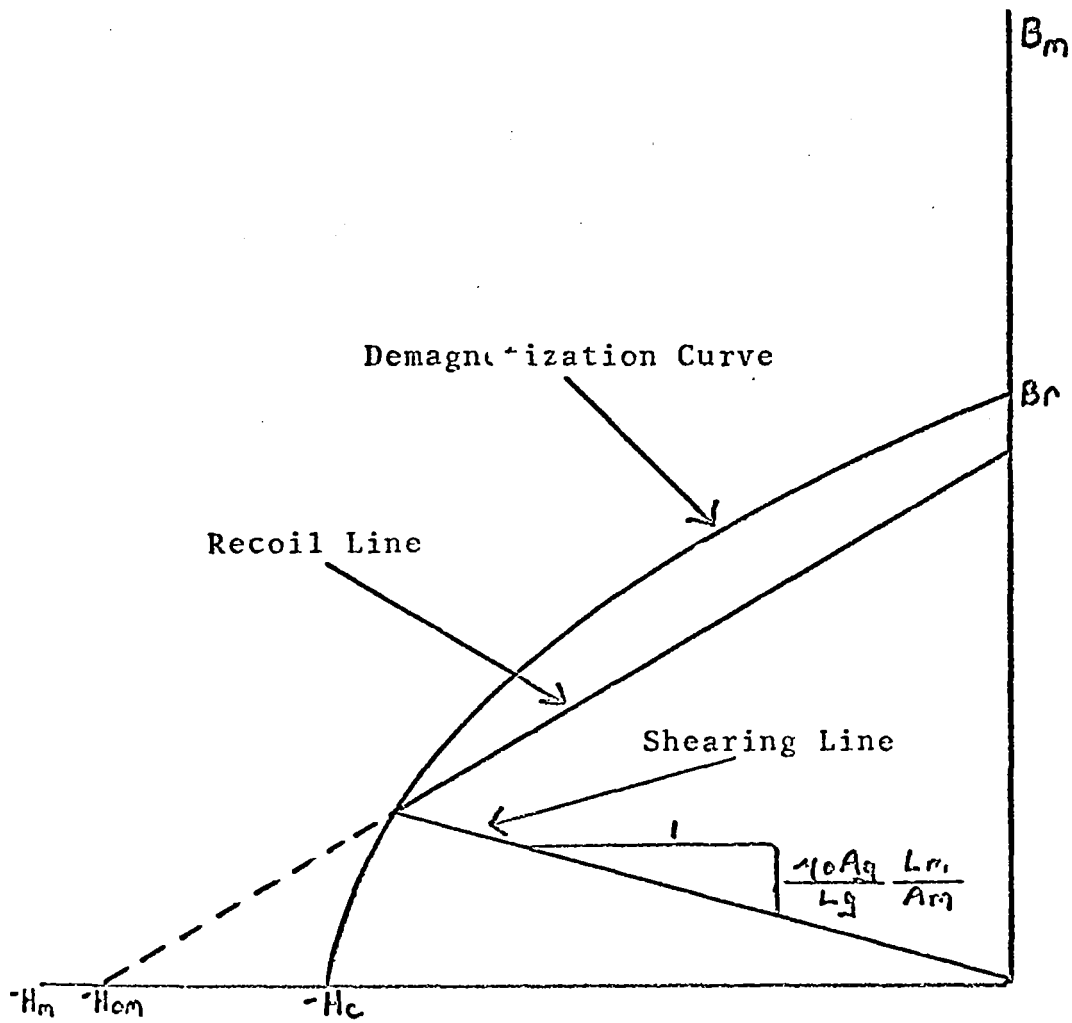
$$B_m = - \left(\frac{\mu_0 A_g}{L_g} \right) \frac{L_m}{A_m} H_m \quad (3.4)$$

The simultaneous solution of the shearing line and the magnet demagnetization curve gives the magnetic state of the magnet.

The term in the brackets in Equation (3.4) is known as the gap permeance and is analogous to conductance or the reciprocal of resistance in an electrical circuit.

$$R_g = \frac{L_g}{\mu_0 A_g}$$

R_g is called the reluctance of the gap. Now, if the gap reluctance is decreased, the state of the magnet will proceed to some point on the magnet recoil line. This is shown in the following figure:



The equation of the recoil line can be written

$$B_m = \mu_{mr} (H_m + H_{om}) \quad (3.5)$$

where H_{om} is the intersection of the recoil line with the H axis.

Written in terms of the electrical analogy, this

equation can be expressed

$$I_m = \frac{1}{R_{mr}} (V_m + V_{om}) \quad (3.6)$$

where the flux I_m is analogous to current, and V_m , the scalar magnetic potential, is analogous to voltage in the electrical case. These terms have the following relationships to the magnetic parameters:

$$I_m = B_m A_m$$

$$V_m = H_m L_m$$

$$V_{om} = H_{om} L_m$$

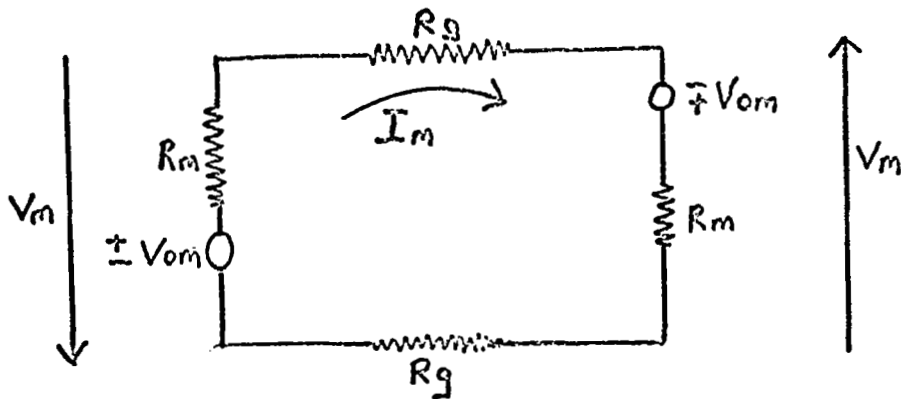
$$R_{mr} = \frac{L_m}{\mu_{mr} A_m}$$

To find the new state of the magnet on the recoil line due to a decrease in gap, we combine Equations (3.4) and (3.5).

$$H_m = \frac{(L_g' / \mu_0 A_g) H_{om}}{(L_m / \mu_{mr} A_m) + (L_g' / \mu_0 A_g)}$$

$$B_m = \frac{\mu_{mr} (L_m / \mu_{mr} A_m) H_{om}}{(L_m / \mu_{mr} A_m) + (L_g' / \mu_0 A_g)}$$

where L_g' is the new gap. The same result could have been obtained by considering the following simple circuit:

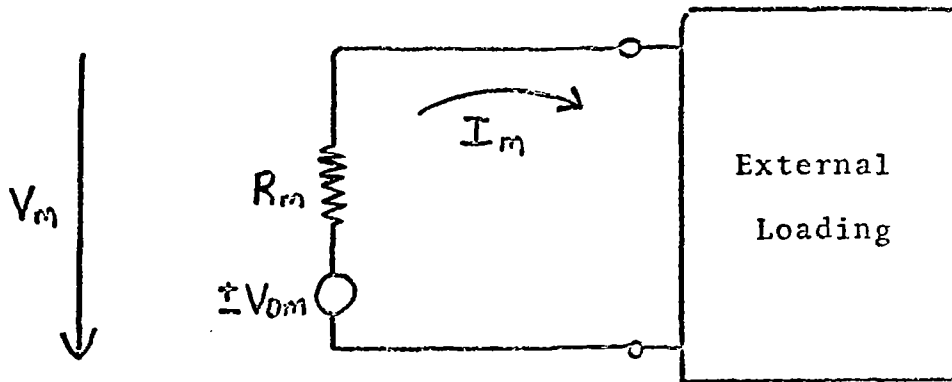


For this circuit

$$V_m = - \frac{R_g V_{om}}{R_{mr} + R_g}$$

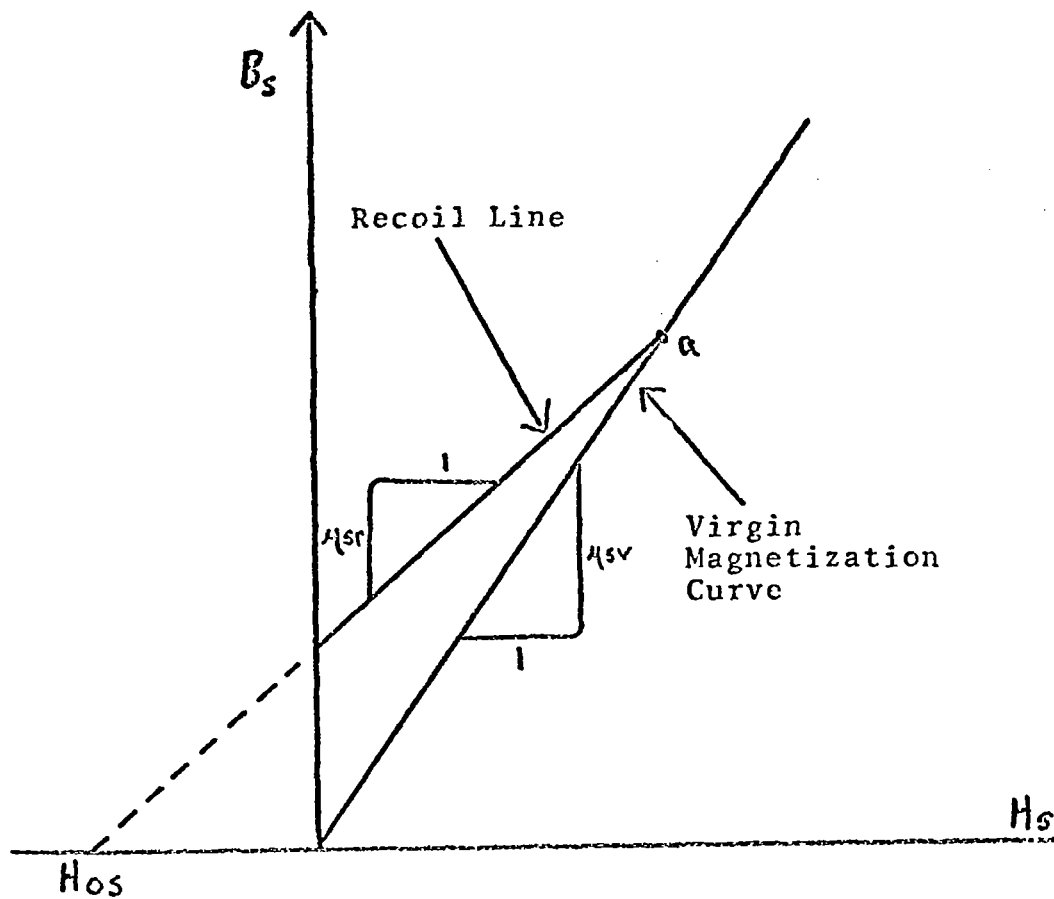
$$I_m = \frac{V_{om}}{R_{mr} + R_g}$$

Therefore, once the magnet is on a recoil line, it has the following model:



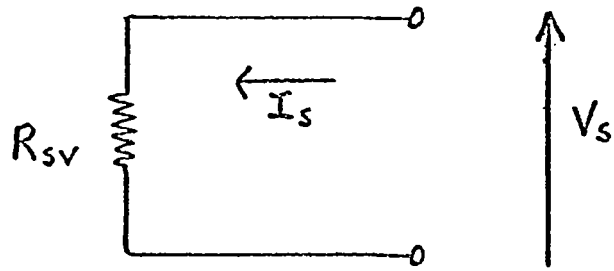
It should be noted that the magnetic potential V_m is always measured opposite to the polarity of the source potential V_{om} .

The effects of steel components in a magnetic circuit can be modeled in a similar manner. The B-H characteristics of the steel are assumed to be straight lines. This characteristic is shown schematically in the following figure:

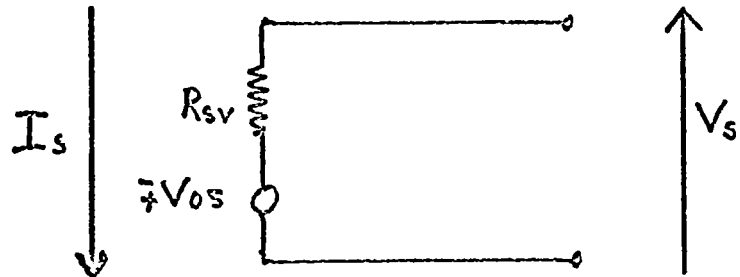


If a piece of steel is magnetized for the first time, it will travel up the virgin magnetization curve to, say, point a . Now if the magnetizing force is decreased, the state of the steel will move down the steel recoil line. The intersection of this line with the H_s axis will be known as H_{os} .

While on the virgin magnetization curve, the steel is modeled as a pure reluctance.



Once on the recoil line, the steel has the following electrical model:



where R_{sv} and R_{sr} are the virgin and recoil reluctances respectively of the steel; and the following relationships hold by definition:

$$V_s = H_s L_s$$

$$V_{os} = H_{os} L_s$$

3.3.3 The Energy in the Magnetic Field System

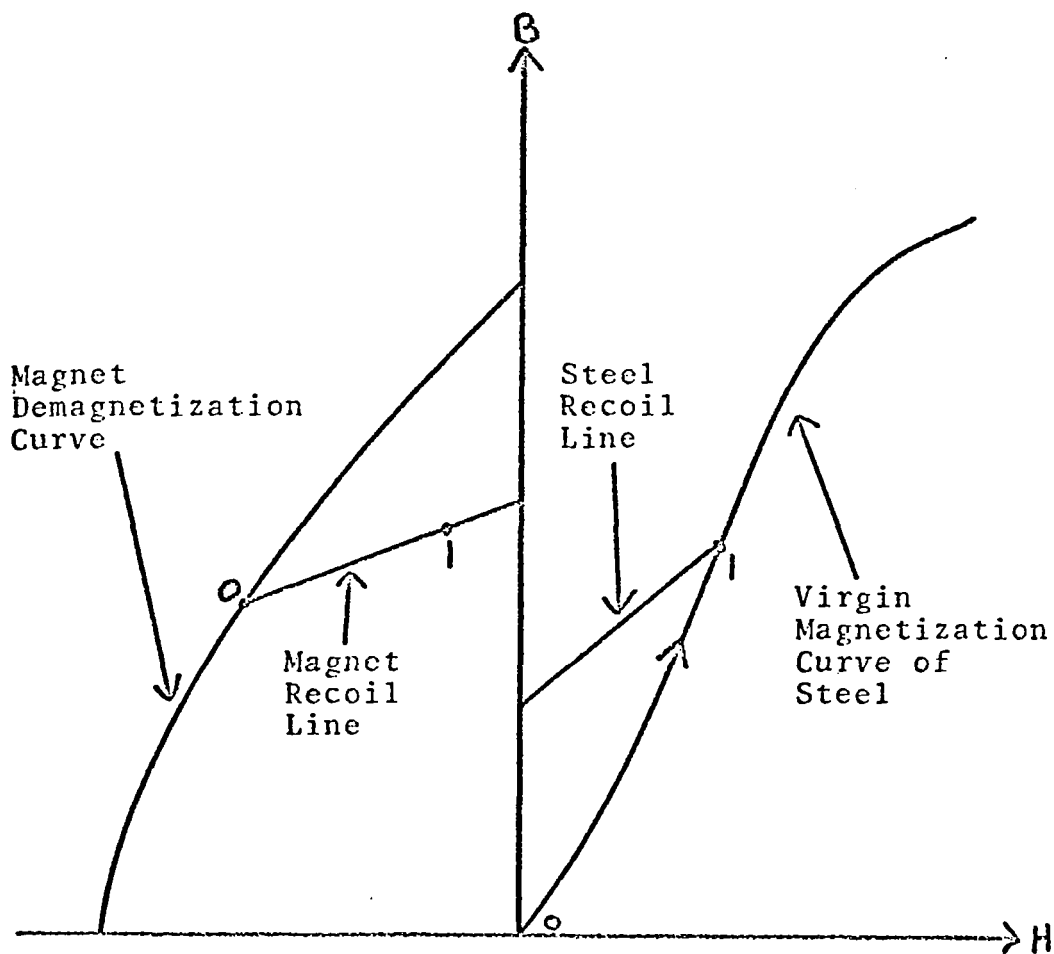
Consider a volume of magnetic material placed in a magnetic field. If it is assumed that the flux density and the field intensity vectors are parallel, we can write the expression for the change energy stored in the volume due to a change in flux density.

$$E = \int_{\tau} \int_{B_1}^B H dB d\tau$$

If we assume that H and B are constant throughout the volume, the energy expression simplifies to

$$E = \tau \int_{B_1}^B H dB \quad (3.7)$$

Now imagine a general magnet which is brought into contact with a virgin steel plate. In the process of bringing the magnet into contact with the plate, the magnet state will advance along its recoil line toward the point of zero magnetic field strength. Concurrently, the state of the steel will be moving up its virgin magnetization characteristic. This is shown schematically in the following figure as motion of the magnetic state of both materials from points 0 to 1.



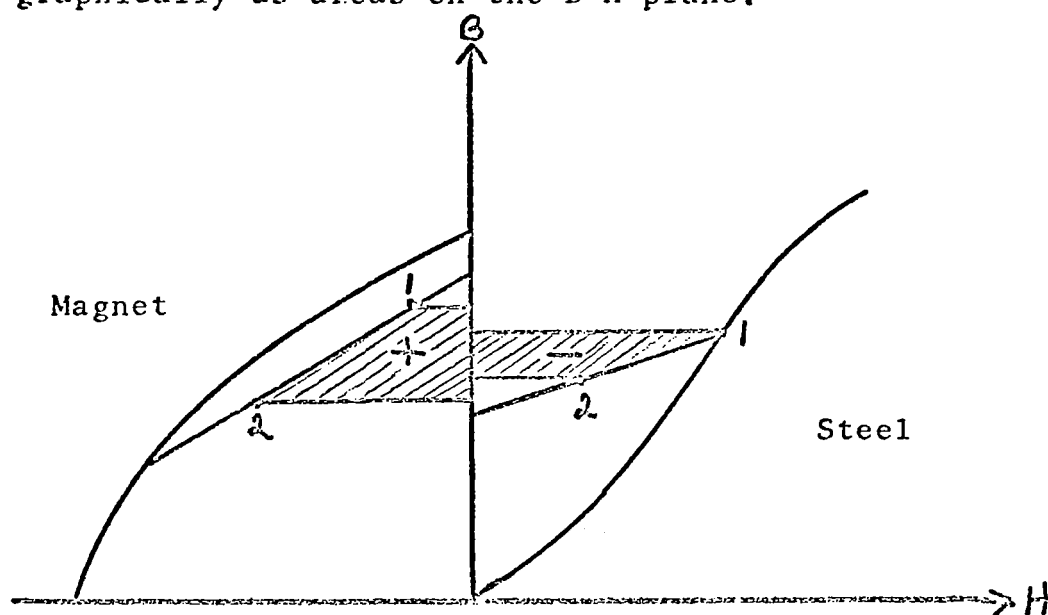
At point 1, the magnet is in contact with the steel. We shall define this point as the energy datum or zero energy state. When the magnet is retracted some distance away from the steel, the state of the steel and magnet will move down their respective recoil lines from points 1. The energy change in the magnet is given then by

$$E_m = \tau_m \int_{B_{m1}}^{B_m} H_m dB_m$$

and similarly, the energy change in the steel is

$$E_s = \tau_s \int_{B_{s1}}^{B_s} H_s dB_s$$

The integrals themselves represent a change in energy density with the materials and are shown graphically as areas on the B-H plane.



It should be noted that during this transition the magnet gained energy, whereas the steel lost

energy. Using the equations of the magnet and steel recoil lines, these two energy components can be written

$$E_m = \tau_m \left[(B_m^2 - B_{m1}^2) / 2 \mu_{mr} - H_{om} (B_m - B_{m1}) \right]$$

$$E_s = \tau_s \left[(B_s^2 - B_{s1}^2) / 2 \mu_{sr} - H_{os} (B_s - B_{s1}) \right]$$

In terms of the electrical circuit analogy, these energy components can be expressed

$$E_m = \frac{R_{mr}}{2} (I_m^2 - I_{m1}^2) - V_{om} (I_m - I_{m1}) \quad (3.8)$$

$$E_s = \frac{R_{sr}}{2} (I_s^2 - I_{s1}^2) - V_{os} (I_s - I_{s1}) \quad (3.9)$$

In a general magnetic circuit, energy is also stored in surrounding space and in the air gap. The flux passing through this space will be known as the leakage flux. The energy stored in this leakage is given by:

$$E_l = \frac{R_l}{2} (I_l^2 - I_{l1}^2) \quad (3.10)$$

The energy stored in the air gap can be written

$$E_g = \frac{R_g}{2} I_g^2 \quad (3.11)$$

Therefore, the total change in the energy of the magnetic system in the transition from 1 to some other point is given by

$$E = E_m + E_s + E_l + E_g \quad (3.12)$$

This net increase in stored energy in the magnetic system is actually coming from an externally applied force which is acting to increase the air gap. The force can be related to the magnetic energy through the following relationship:

$$E = \int_0^h \underline{F} \cdot \underline{dh} \quad (3.13)$$

or

$$F = \frac{\partial E}{\partial h} \quad (3.14)$$

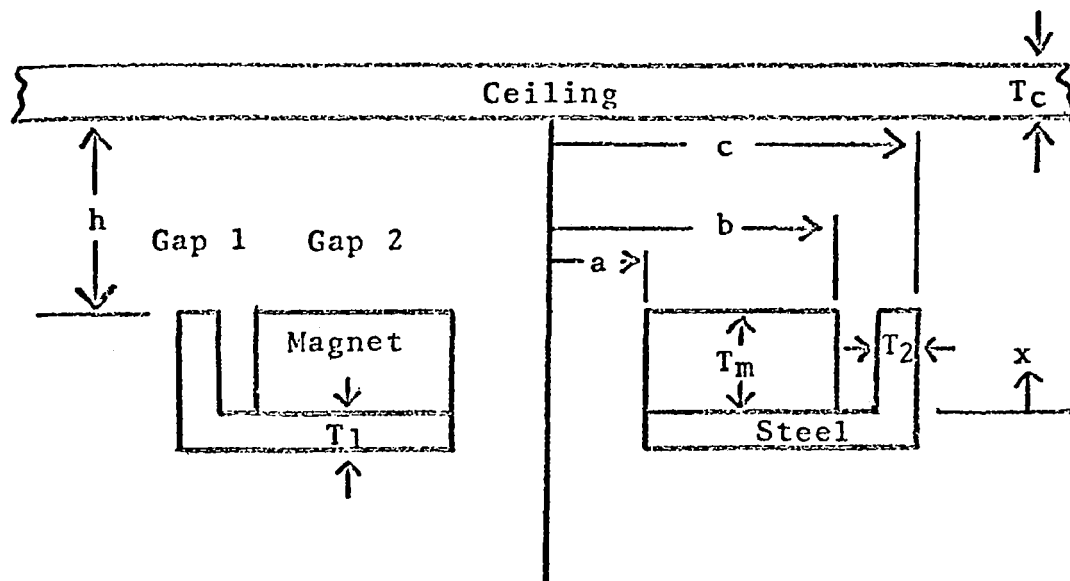
Therefore, the force developed by the magnet can be calculated by taking the partial derivative of the change in energy from the zero gap point with respect to gap.

3.3.4 Magnetic Reluctance

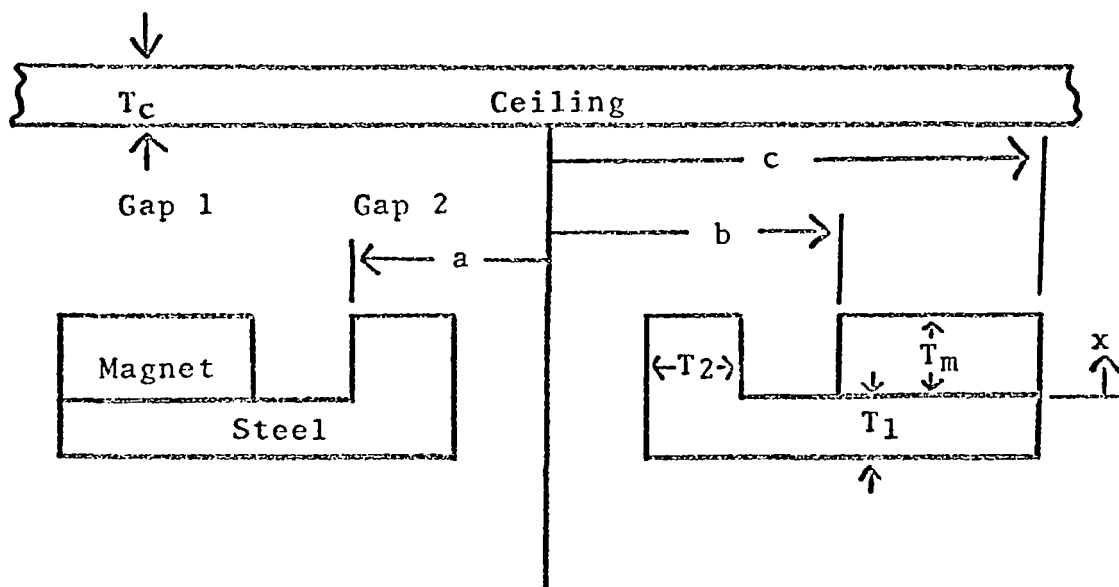
The definition of reluctance in a magnetic system is the ratio of the magnetic potential across two equipotential surfaces to the total flux passing through those surfaces. The method taken in this analysis is to break the magnetic system into simple three-dimensional shapes and then estimate the probable path that the flux will take. In several cases, the expressions for reluctance derived using this method will be nothing more than engineering estimates. This approach is common in this field and it is felt that a more exact analysis would be inconsistent with other parts of the lumped parameter analysis. This method is comparable in accuracy to flux plotting for two-dimensional systems.⁽¹⁵⁾

Since the reluctances for both the outside and inside shell magnet designs will be derived simultaneously, the geometries of both designs are defined in Figure 3.6. In the following discussion the outside shell magnet will be referred to as Design A and the inside shell magnet as Design B.

GEOMETRY OF INSIDE AND OUTSIDE SHELL MAGNET DESIGNS



Outside Shell (Design A)

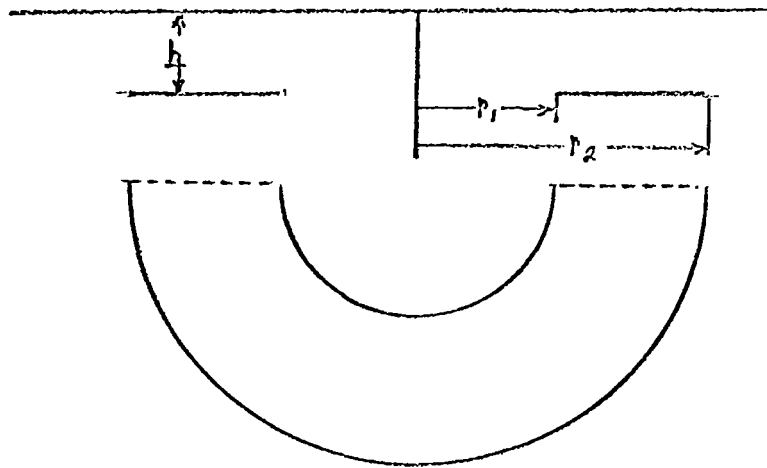


Inside Shell (Design B)

Figure 3.6

Air Gap Reluctance

Consider an annular surface placed at some small distance and parallel to an infinite plane. The flux paths are assumed to be perpendicular to these surfaces and fringe effects are neglected. This situation is shown in two dimensions below:



For a uniform field, the flux passing through these surfaces is given by

$$\mathcal{I} = B \pi (r_2^2 - r_1^2)$$

The magnetic potential between these surfaces

is

$$V = Hh$$

Therefore, the reluctance of the region can be expressed

$$R_g = \frac{V}{I} = \frac{Hh}{B\pi(r_2^2 - r_1^2)}$$

or

$$R_g = \frac{h}{\mu_0 \pi (r_2^2 - r_1^2)}$$

Then for Design A the reluctances of both air gaps are given by

$$R_{g1} = \frac{h}{2\pi\mu_0 cT_2} \quad (3.15)$$

$$R_{g2} = \frac{h}{\mu_0 \pi (b^2 - a^2)} \quad (3.16)$$

and for Design B

$$R_{g1} = \frac{h}{\mu_0 \pi (c^2 - b^2)} \quad (3.17)$$

$$R_{g2} = \frac{h}{2\pi\mu_0 (a - T_2/2)T_2} \quad (3.18)$$

Leakage Reluctance

It is desired to calculate the reluctance of the cylindrical volumes between the shell and the magnet in either of the magnet designs. It is assumed that the flux paths are purely radial and that there is no potential drop along the bounding length of the steel shell.

The potential increase through the magnet can be written

$$V = \int_0^x H_m dx = H_m x$$

The reluctance of an elemental annular volume of depth dx for Design B is

$$R_\ell = \ln\left(\frac{b}{a}\right) \frac{1}{2\pi\mu_0 dx}$$

The elemental permeance then is given by

$$d\rho = \frac{2\pi\mu_0 dx}{\ln\left(\frac{b}{a}\right)}$$

Then we know that

$$V dp = dI$$

or

$$\frac{2 \pi \mu_0 H_m x dx}{\ln(b/a)} = dI$$

The total flux is

$$I_T = \frac{2 \pi \mu_0 H_m}{\ln(b/a)} \int_0^{T_m} x dx$$

or

$$I_T = \frac{\pi \mu_0 H_m T_m^2}{\ln(b/a)}$$

The total potential drop across the magnet is

$$V_T = H_m T_m$$

Then the effective leakage for Design B can be written

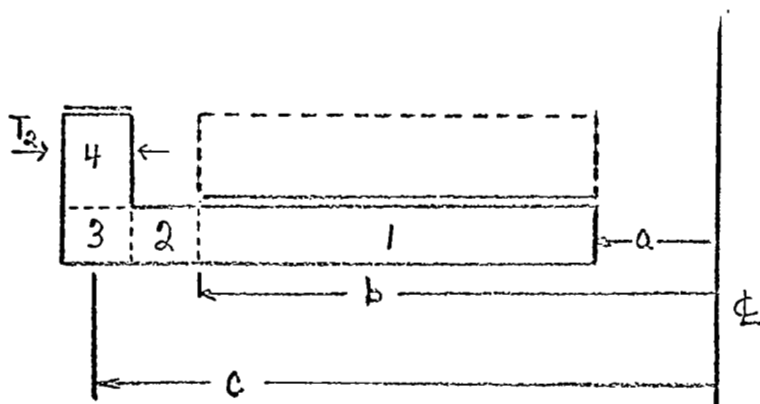
$$R_L = \frac{V_T}{I_T} = \frac{\ln(b/a)}{\pi \mu_0 T_m} \quad (3.19)$$

and for Design A

$$R_L = \frac{\ln \left(\frac{c - T_2/2}{b} \right)}{\pi \gamma_0 T_m} \quad (3.20)$$

Design A Shell Reluctance

The steel shell is subdivided into four volumes to simplify calculations. This is shown in the figure below:



The problem is to determine an approximate value for the reluctance between the two equipotential surfaces designated by the double lines.

If one considers region 1 alone and forces the cylindrical area between region 1 and region 2 to become an equipotential surface, the result will yield infinite flux density at the intersection of the equipotential surfaces and zero reluctance. Actually, this is not the case; and this problem arises because the volume was arbitrarily subdivided. When problems like this arise, the general plan of attack will be to estimate the mean flux path and the mean area of the flux tube and then calculate the reluctance of the volume by using the following equation:(15)

$$R \simeq \frac{L_{\text{mean}}}{\mu A_{\text{mean}}}$$

Using the above-mentioned method and others similar to ones previously developed in this section, the following approximate equations are obtained for the subdivided volumes of the shell:

$$R_1 = \frac{b-a}{\pi \mu (b^2 - a^2 + 2bT_1)} \quad (3.21)$$

$$R_2 = \frac{\ln \left(\frac{c-T_2/2}{b} \right)}{2\pi \mu T_1} \quad (3.22)$$

$$R_3 = \frac{T_1 + T_2}{8\mu [(c - T_2/2) T_1 + c T_2]} \quad (3.23)$$

$$R_4 = \frac{T_m}{2\pi\mu c T_2} \quad (3.24)$$

The total reluctance of the shell is then simply given by

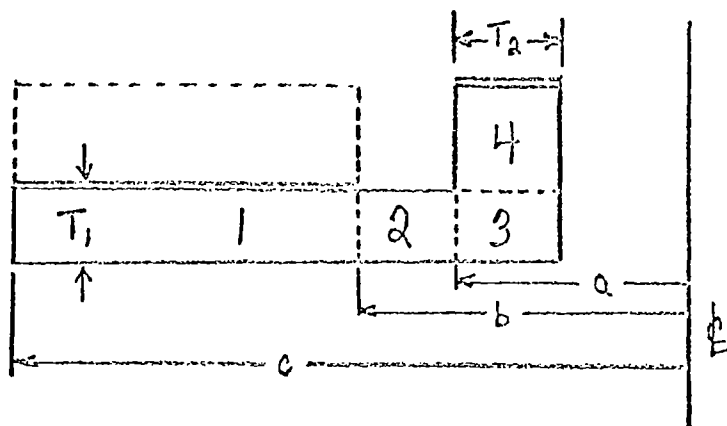
$$R_5 = R_1 + R_2 + R_3 + R_4 \quad (3.25)$$

Provided that the steel parts are not too near saturation, the permeability of the steel will be much greater than that of air and the magnet. This means that the reluctance of the steel parts will be considerably lower than the reluctances of other components in the magnetic circuit. Therefore, errors incurred in estimating reluctances in the steel parts should not have too great an effect on the resulting theoretical force characteristic.

Design B Shell Reluctance

The method employed for determining the reluctance

of the shell of the inside shell design is the same as that used for the outside shell. The Design B shell is shown subdivided into four regions in the following figure:



Again, the two equipotential surfaces are designated by the parallel lines. The approximate reluctances for these volumes are given by

$$R_1 = \frac{c-b}{\pi \mu (c^2 - b^2 + 2bt_1)} \quad (3.26)$$

$$R_2 = \frac{\ln(b/a)}{2\pi \mu t_1} \quad (3.27)$$

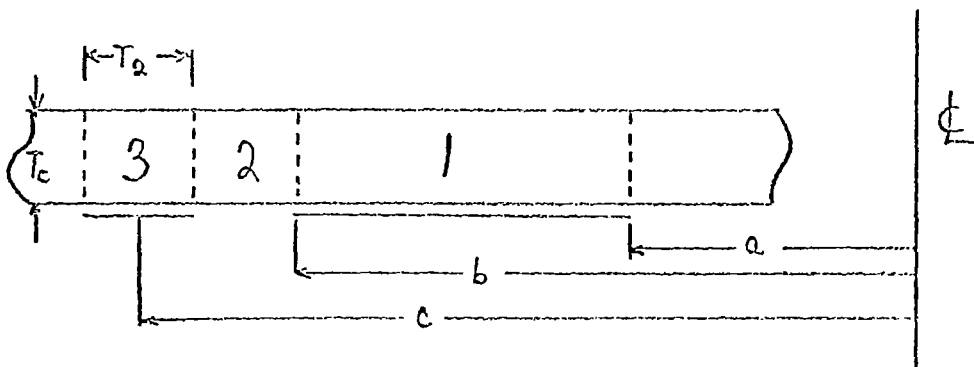
$$R_3 = \frac{T_1 + T_2}{8\mu [aT_1 + (a - T_2/2)T_2]} \quad (3.28)$$

$$R_4 = \frac{T_m}{2\pi\mu (a - T_2/2)T_2} \quad (3.29)$$

Then, the total reluctance of this shell is simply the sum of these component reluctances.

Ceiling Reluctance for Design A

The figure below shows the ceiling for the outside shell magnet design.



The volumes considered for this derivation are those in the immediate proximity of the magnet. The assumed equipotential surfaces are designated by the double lines. Using previously developed methods, the following reluctances are derived for the respective volumes:

$$R_1 = \frac{b-a}{\pi \mu (b^2 - a^2 + 2bT_c)} \quad (3.30)$$

$$R_2 = \frac{\ln \left(\frac{c - T_2/2}{b} \right)}{2\pi \mu T_c} \quad (3.31)$$

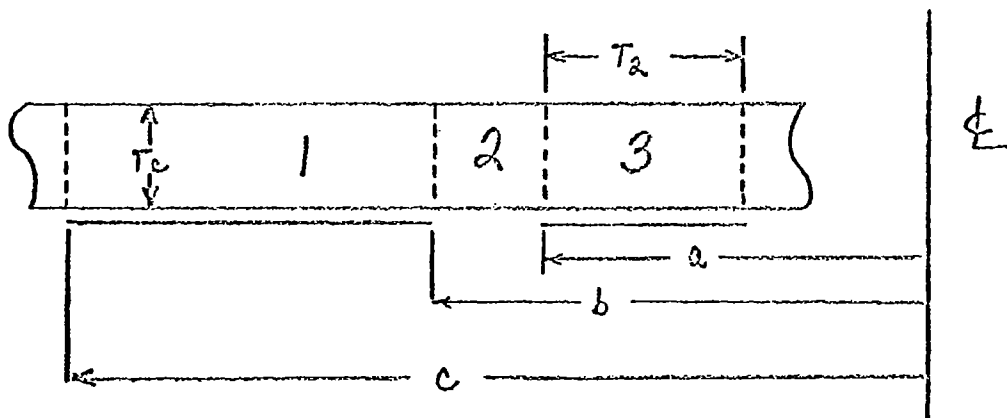
$$R_3 = \frac{T_c + T_2}{8\mu \left[(c - T_2/2) T_c + c T_2 \right]} \quad (3.32)$$

The total reluctance for the ceiling with the outside shell design is

$$R_c = R_1 + R_2 + R_3 \quad (3.33)$$

Ceiling Reluctance for Design B

The following figure shows the subdivision of the ceiling in the immediate vicinity of the inside shell magnet design:



The equipotential surfaces are shown in this figure by double lines. The approximate ceiling reluctances for the inside shell design are given by

$$R_1 = \frac{c-b}{\pi \mu (c^2 - b^2 + 2 b T_c)} \quad (3.34)$$

$$R_2 = \frac{\ln(b/a)}{2\pi\mu T_c} \quad (3.35)$$

$$R_3 = \frac{T_2 + T_c}{8\mu [aT_c + (a - T_2/2)T_2]} \quad (3.36)$$

Then, the total ceiling reluctance for this design is simply given by the sum of the component reluctances.

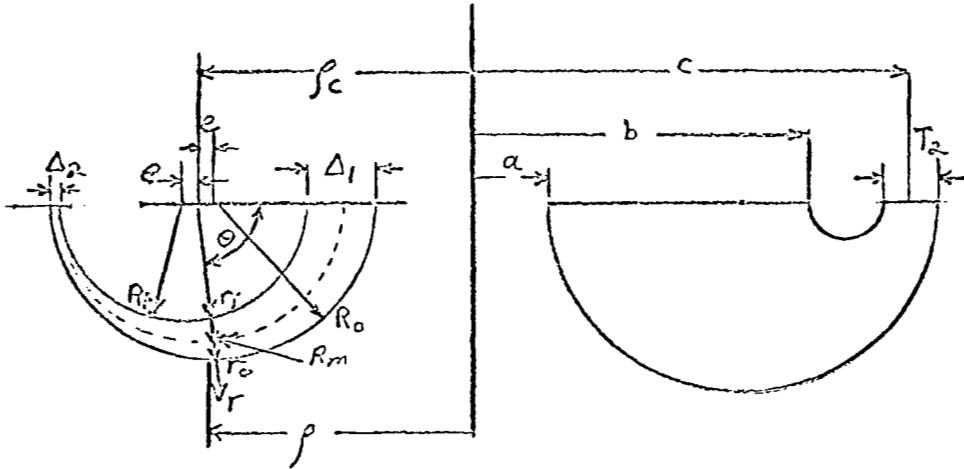
Open Circuit Reluctance

If Indox V is used in a magnet which has been magnetized with the shell in place, it is necessary to determine the open circuit¹ state of the magnet before the force characteristic can be calculated. This is not the case for a material such as Indox VI-A because the demagnetization curve and recoil lines are always coincident.

¹The phrase "open circuit" implies that the magnet is far from any other ferromagnetic materials.

Before the open circuit magnet state can be determined, it is first necessary to develop a model for the reluctance exterior to the magnet when the magnet is placed far from all other ferromagnetic materials.

The outside shell design will be considered first. The assumed flux envelope is shown below:(16)



Looking at the elemental flux tube, the equation of the outside circle is given by

$$r_o^2 - 2er_o \cos \theta + e^2 - R_o^2 = 0$$

and, for the inside circle,

$$r_i^2 + 2er_i \cos \theta + e^2 - R_i^2 = 0$$

Solving for the inside and outside radii,

$$r_o = e \cos \theta + \sqrt{e^2 \cos^2 \theta - (e^2 - R_o^2)}$$

$$r_i = -e \cos \theta + \sqrt{e^2 \cos^2 \theta - (e^2 - R_i^2)}$$

Since

$$e \ll R$$

e^2 can be neglected in comparison to R_o^2 and R_i^2 .

The equations for the outside and inside radii reduce to

$$r_o = e \cos \theta + R_o$$

$$r_i = -e \cos \theta + R_i$$

The cross-sectional area of the flux tube is given by

$$A = 2\pi f (r_o - r_i)$$

or

$$A = 2\pi \left[(2f_c e - R_m (R_o - R_i)) \cos \theta - 2e R_m \cos^2 \theta + f_c (R_o - R_i) \right]$$

The mean area of the tube can then be written

$$A_m = \frac{1}{\pi} \int_0^{\pi} A d\theta$$

The following relation between Δ_1 and Δ_2 must hold for geometric compatibility

$$\frac{\Delta_1}{\Delta_2} = \frac{b-a}{r_2}$$

In addition, from the figure above, it can be seen that

$$\Delta_1 = R_o - R_i + 2e$$

and

$$\Delta_2 = R_o - R_i - 2e$$

After some manipulation of terms, the following expression can be obtained for the mean area in terms of Δ_1 and f_1 :

$$A_{mean} = 2\pi (K_1 f_1 + K_2) \Delta_1$$

where

$$K_1 = \frac{3}{8} \left[1 - \frac{T_2^2}{(b-a)^2} \right]$$

$$K_2 = \frac{1}{8} \left[c + \frac{T_2}{2} + \frac{3cT_2}{(b-a)} + \frac{aT_2}{(b-a)} \right. \\ \left. + \frac{3T_2^2}{2(b-a)} + \frac{3T_2^2 a}{(b-a)^2} \right]$$

Taking the limit as $\Delta_1 \rightarrow dr$ and $A_{\text{mean}} \rightarrow dA$,

$$dA = 2\pi (K_1 r + K_2) dr$$

The length of the flux tube is given by

$$L = \pi R_m$$

or

$$L = \frac{\pi}{2} (K_4 - r K_3)$$

where

$$K_3 = \left[1 + \frac{T_2}{(b-a)} \right]$$

$$K_4 = \left[c + \frac{T_2}{2} + \frac{T_2 a}{(b-a)} \right]$$

The permeance of this space can then be written

$$P = \mu_0 \int_a^b \frac{dA}{L}$$

Upon completing the integration, the following expression for the permeance is obtained.

$$P = 2\mu_0 \left\{ \frac{- \left[c + \frac{T_2}{2} + \frac{T_2 a}{(b-a)} \right]}{1 + \frac{T_2}{(b-a)}} \cdot \quad (3.37) \right. \\ \left. \ln \left[\frac{c - T_2/2 - b}{c + T_2/2 - a} \right] - \frac{3}{4} (b - a - T_2) \right\}$$

The approximate reluctance of this space is then the reciprocal of the permeance. The total open circuit reluctance for Design A is the reluctance just derived in parallel with the reluctance between the shell and the magnet given in Equation (3.20).

Using a similar analysis, the open circuit permeance for the inside shell magnet design is

given by

$$P = 2\gamma_0 \left\{ \frac{-[cT_2 + (c-b)(a-T_2)]}{1 + \frac{T_2}{(b-a)}} \right\} \quad (3.38)$$

$$\ln \left[\frac{c - T_2/2 - b}{c + T_2/2 - a} \right] - \frac{3}{4} (b - a - T_2) \right\}$$

3.3.5 Flux Density Distribution in the Shell and Ceiling

The flux density distribution in the steel parts will be determined using a one-dimensional model for the case when the magnet is in contact with the ceiling. It is at this zero gap point that the steel has maximum flux density. In the magnet design, the thicknesses of the steel shell and ceiling will be set so that the maximum flux density in these parts is somewhere below the saturation value for the material.

The basis of the following derivation is the assumption that the ceramic disc magnet emits a constant flux density over the two annular surfaces in contact with the shell and ceiling when the magnet is at zero gap. This assumption is a good one provided that the steel is not saturated and still has a reasonably high permeability.

For the case in point, the permeability of the magnet, which is essentially the same as free space,

will be very much smaller than that of the steel. This means that, even though the lengths of the flux paths will vary from the inside to the outside radius of the magnet, the flux density emitted by the magnet will be relatively insensitive to these variations. In other words, due to the low magnet permeability and high steel permeability, the magnet looks like a source of constant flux.

Design A

Consider the outside shell design shown in Figure 3.6. The flux emitted by the magnet can be written

$$\phi = 2\pi B_m \int_a^b r dr \quad b \geq r \geq a$$

or

$$\phi = B_m \pi (b^2 - a^2) \quad b \geq r \geq a \quad (3.39)$$

where B_m is the flux density on the magnet recoil line at zero field strength.

The mean flux density in the iron is given by the following equations for a constant T_1 :

$$B_s = \frac{B_m}{2T_1} \left(r - \frac{a^2}{r} \right) \quad b \geq r \geq a \quad (3.40)$$

and

$$B_s = \frac{B_m(b^2 - a^2)}{2T_1 r} \quad (c - T_2/2) \geq r \geq b \quad (3.41)$$

This flux density distribution is shown graphically in Figure 3.7.

It can be seen from this Figure that the maximum flux density occurs at $r = b$ and has the value

$$B_{s \max} = \frac{B_m(b^2 - a^2)}{2T_1 b} \quad r = b \quad (3.42)$$

The flux density in this portion of the shell can be held at a theoretical constant value by tapering the thickness of the shell in accordance with Equations (3.40) and (3.41). However, this

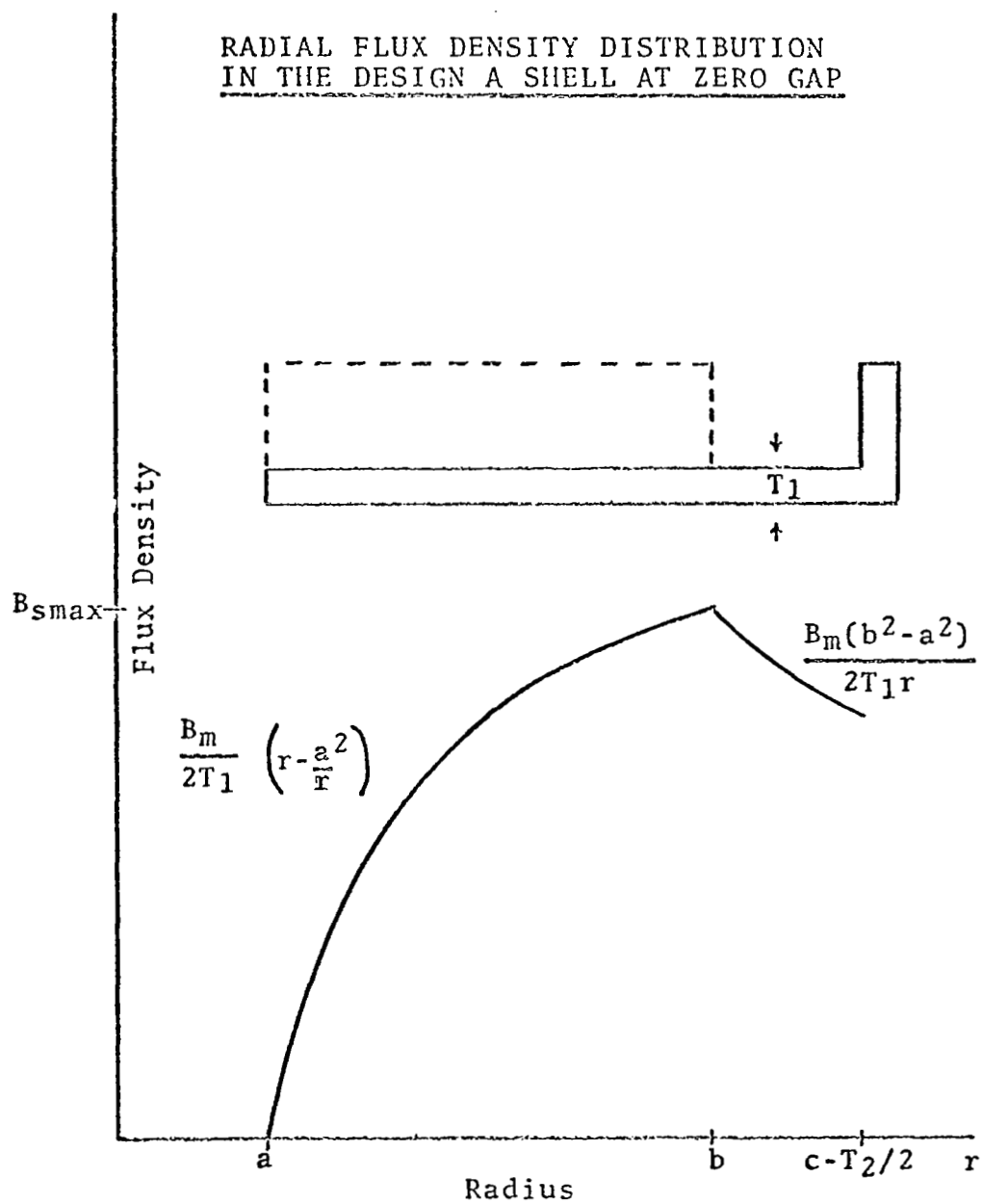


Figure 3.7

possibility is eliminated in Design A because the shell would have minimum thickness in the region in which the external load would be applied.

The flux density in the cylindrical portion of the shell is

$$B_s = \frac{B_m (b^2 - a^2)}{2cT_2} \quad (3.43)$$

The flux density in the ceiling is given by

$$B_c = \frac{B_m}{2T_c} \left(r - \frac{a^2}{r} \right) \quad b \geq r \geq a \quad (3.44)$$

$$B_c = \frac{B_m}{2T_c} \frac{(b^2 - a^2)}{r} \quad (c - T_2/2) \geq r \geq b \quad (3.45)$$

The maximum flux density in the ceiling is

$$B_{c \max} = \frac{B_m (b^2 - a^2)}{2T_c b} \quad r = b \quad (3.46)$$

Design B

The geometry of the inside shell is shown in Figure 3.6. Again assuming that the magnet is a source of constant flux across its surface, the flux at any section of the shell for $b \leq r \leq c$ is given by

$$\phi = B_m \pi (c^2 - r^2) \quad (3.47)$$

The mean flux density across the thickness of the shell between these radii can be written

$$B_s = \frac{B_m}{2T_1} \left(\frac{c^2}{r} - r \right) \quad b \leq r \leq c \quad (3.48)$$

Since no new flux is being introduced into the shell between radii b and a , the mean flux density across any section there is

$$B_s = \frac{B_m}{2rT_1} (c^2 - b^2) \quad a \leq r \leq b \quad (3.49)$$

The radial flux distribution given by Equations

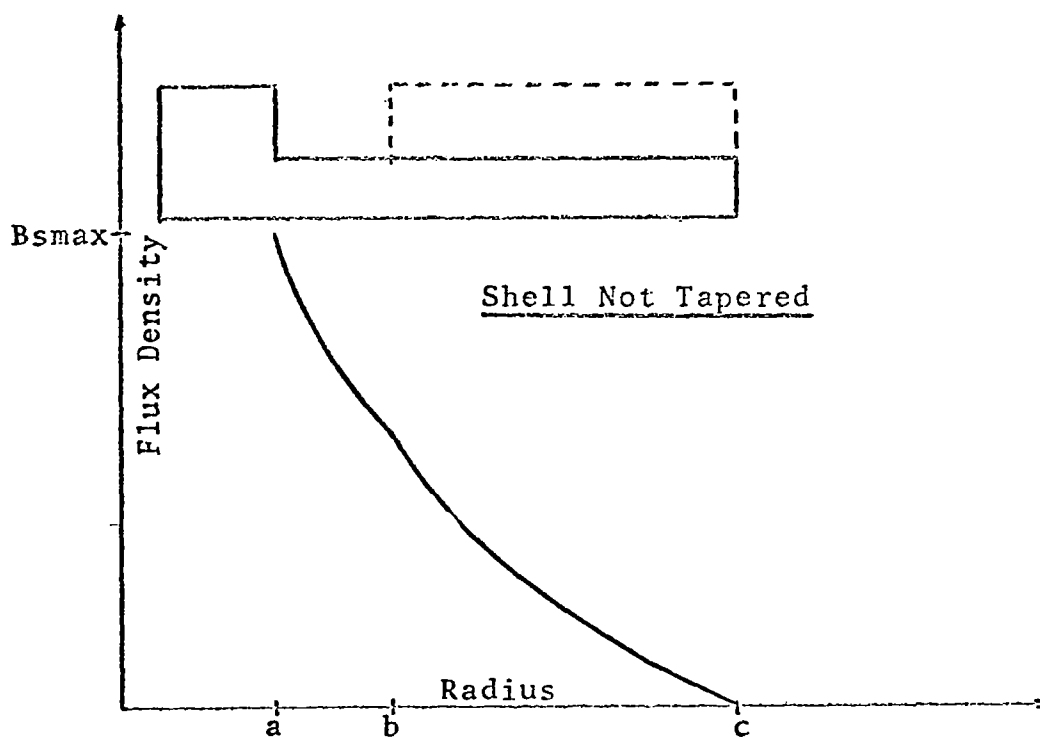
(3.48) and (3.49) is shown in Figure 3.8 for constant T_1 .

It can be seen from this Figure that the maximum radial flux density for constant T_1 occurs at the radius a and has the value

$$B_{s \max} = \frac{B_m}{2aT_1} (c^2 - b^2) \quad r=a \quad (3.50)$$

Since the maximum flux density for the inside shell design does occur at the radius a , it is desirable to taper the shell from a maximum thickness at that point to a minimum thickness at c . By doing this, one can conserve weight plus have the thickest part of the shell in the center where the air fitting must be installed and the external load applied. For the outside shell design, tapering was not recommended for structural reasons. However, for the inside shell, it may be tapered yielding a structurally sound and lighter design.

Prototype inside shells were designed to have a straight taper from a to c . One of these is shown



RADIAL FLUX DENSITY DISTRIBUTION
IN THE DESIGN B SHELL AT ZERO GAP

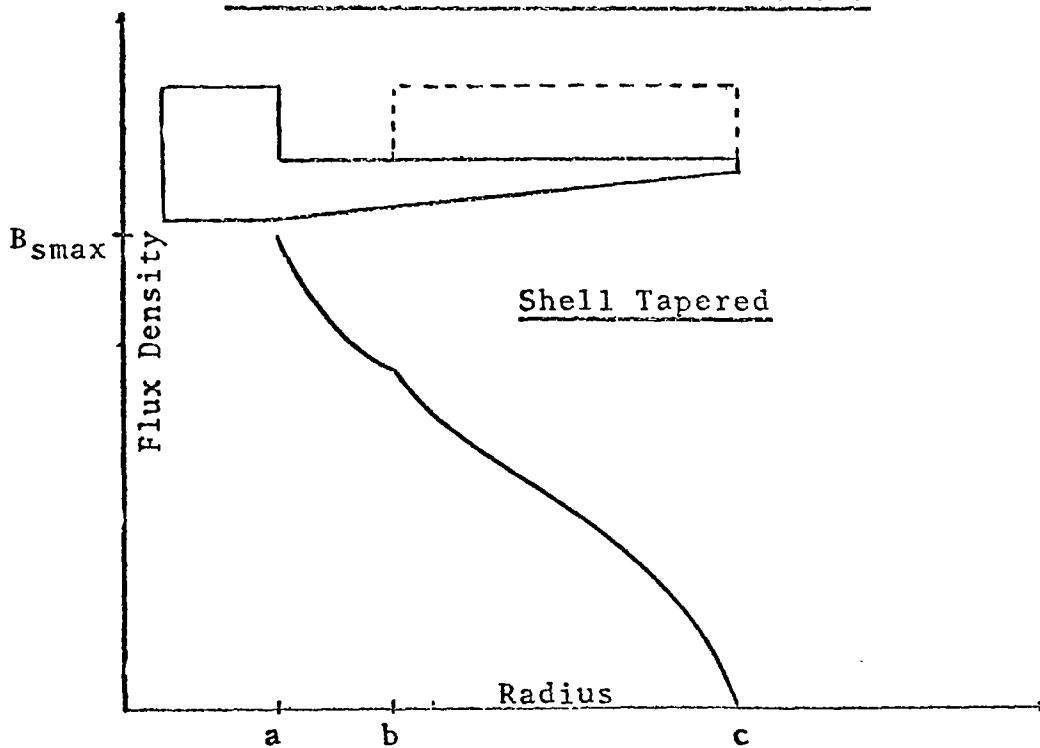
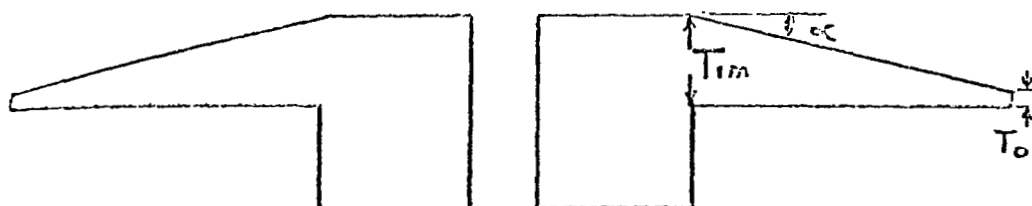


Figure 3.8

in the figure below:



The thickness of this shell is given by the following equation:

$$T_1 = -r \tan \alpha + (T_{im} + a \tan \alpha) \quad a \leq r \leq c$$

The flux density distribution in the shell is then modified as follows:

$$B_s = \frac{B_m (c^2 - r^2)}{2r (-r \tan \alpha + T_{im} + a \tan \alpha)} \quad b \leq r \leq c$$

and

$$B_s = \frac{B_m (c^2 - b^2)}{2r (-r \tan \alpha + T_{im} + a \tan \alpha)} \quad a \leq r \leq b$$

The modified radial flux density distribution due to this taper is also shown in Figure 3.8.

The maximum flux density is still at the radius a . However, the rest of the material in the shell is being worked at a higher flux density thereby economizing on weight.

In the cylindrical portion of the shell, the mean flux density parallel to the axis of the magnet is

$$B_s = \frac{B_m (c^2 - b^2)}{T_2 (2a - T_2)} \quad a - T_2 \leq r \leq a \quad (3.51)$$

The radial flux density distribution in the ceiling for the inside shell design is given by

$$B_c = \frac{B_m}{2T_c} \left(\frac{c^2}{r} - r \right) \quad b \leq r \leq c \quad (3.52)$$

$$B_c = \frac{B_m}{2rT_c} (c^2 - b^2) \quad a \leq r \leq b \quad (3.53)$$

The maximum flux density in the ceiling is again at a .

$$B_{c \max} = \frac{B_m}{2aT_c} (c^2 - b^2) \quad r=a \quad (3.54)$$

This method of approximating the Index V demagnetization curve by two straight lines is quite accurate with the exception of approximately 5% error in the region of the knee.

The values for the magnetic source potentials V_{01} and V_{02} can be found directly from the actual demagnetization curve, Figure 3.4, once the thickness of the magnet disc is known. That is,

$$V_{01} = H_{01} T_M$$

$$V_{02} = H_{02} T_M$$

where, from Figure 3.4, it can be seen that

$$H_{01} = 3660. \text{ oersteds}$$

$$H_{02} = 2200. \text{ oersteds}$$

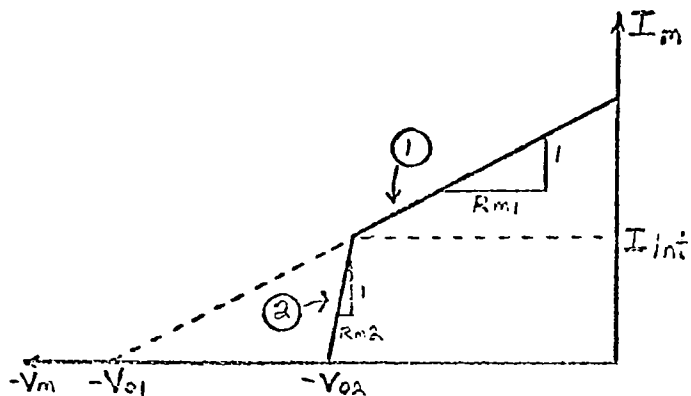
The approximate open circuit reluctance for a disc magnet magnetized with its shell in place can be found by considering the reluctance given by Equation (3.37) in parallel with that of Equation (3.20) for the outside shell design, or the reluctance given by Equation (3.38) in parallel with the value

3.3.6 Theoretical Magnet Force Characteristic

Due to obvious theoretical simplification and the basic similarity between the inside and outside shell designs, the following theoretical force characteristic is applicable to both designs. All that will be necessary to obtain the force characteristic for either design is to substitute into the developed equations the applicable reluctances derived in Section 3.3.5.

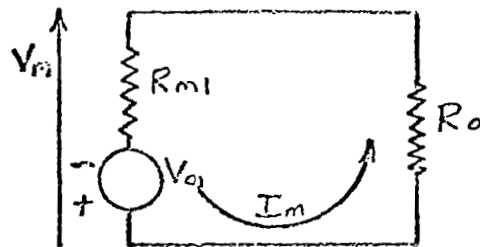
Open Circuit Analysis

For the ceramic material Index V, it is first necessary to determine the recoil line on which the magnet will be operating. Consider the approximation to the Index V demagnetization curve on the $I - V$ plane shown below



given by Equation (3.19) for the inside shell design.

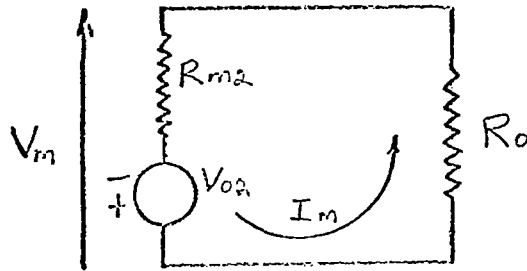
The open circuit state can be found by first hypothesizing that the magnet state is line 1. If this is true, then the following simple circuit is applicable:



Then, the magnet flux is given by

$$I_m = \frac{V_{o1}}{R_o + R_{m1}}$$

If $I_m > I_{int}$, then the hypothesis is true and the open circuit state has been determined. If $I_m < I_{int}$, then the state must lie on curve 2 and the following circuit may be used:



The open circuit magnet flux is then

$$I_m = \frac{V_o2}{R_o + R_{m2}}$$

For either case, the open circuit magnet potential is

$$V_m = -R_o I_m$$

The source potential of the magnet recoil line can now be written

$$V_{om} = -V_m + R_m I_m \quad (3.55)$$

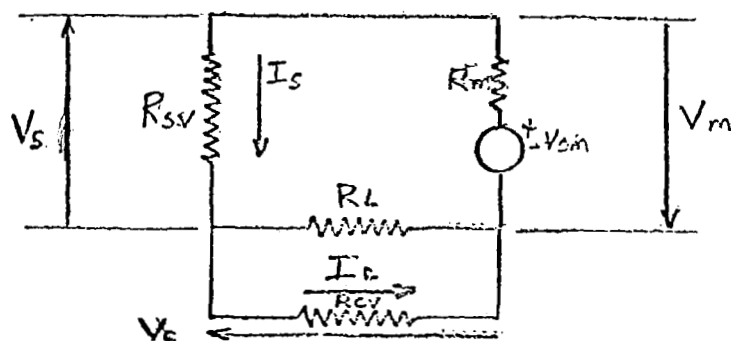
For the material Index VI-A, the preceding calculation is not necessary, since the source potential of the recoil line can be determined directly from the Index VI-A demagnetization curve.

$$V_{om} = H_{om} T_m \quad (3.56)$$

where $H_{om} = 3000$. oersteds.

Closed Circuit Analysis

We now must determine the recoil lines on which the steel parts will operate. In the I-V plane, the steel virgin magnetization curve is approximated by a straight line from the origin. The following circuit can be used to describe the state of the magnetic system upon contact with a virgin steel ceiling:



From the preceding circuit, it can be seen that

$$I_s = \frac{V_{om} (R_L + R_{cv})}{(R_m + R_{sv})(R_L + R_{cv}) + R_L R_{cv}}$$

$$V_s = \frac{V_{om} R_{sv} (R_L + R_{cv})}{(R_m + R_{sv})(R_L + R_{cv}) + R_L R_{cv}}$$

$$I_c = \frac{V_{om} R_L}{(R_m + R_{sv})(R_L + R_{cv}) + R_L R_{cv}}$$

$$V_c = \frac{V_{om} R_{cv} R_L}{(R_m + R_{sv})(R_L + R_{cv}) + R_L R_{cv}}$$

Upon retraction of the magnet from the ceiling, the magnetic source potentials of the shell and ceiling are then respectively

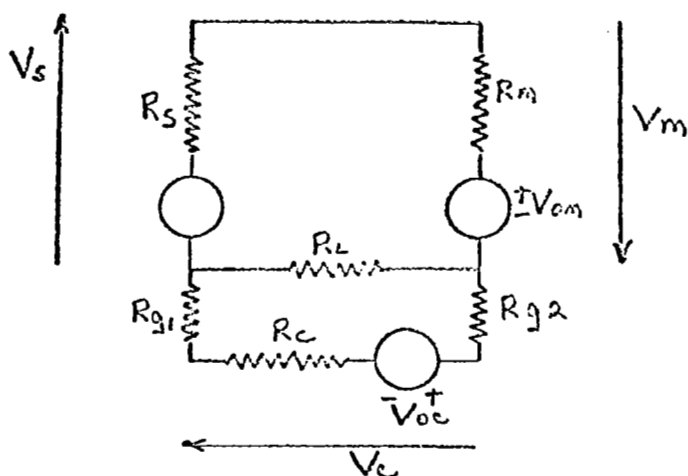
$$V_{os} = I_s R_s - V_s \quad (3.57)$$

$$V_{oc} = I_c R_c - V_c \quad (3.58)$$

It should be noted that the source potential and the recoil permeability completely determine the material's recoil line.

Operating Circuit Analysis

The following magnetic circuit will be used to represent the system upon the retraction of the magnet to some small gap from the ceiling:



For the above circuit, the flux through each circuit element is given by

$$I_m = \frac{(R_{g1} + R_{g2} + R_L + R_c)(V_m + V_s) + R_L V_{oc}}{(R_m + R_s + R_L)(R_{g1} + R_{g2} + R_L + R_c) - R_L^2}$$

$$I_c = \frac{V_{oc} \left\{ (R_m + R_s + R_L)(R_{g1} + R_{g2} + R_L + R_c) - R_L^2 \right\} + R_L \left\{ (R_{g1} + R_{g2} + R_L + R_c)(V_{om} + V_{os}) + R_L V_{oc} \right\}}{(R_{g1} + R_{g2} + R_L + R_c) \left\{ (R_m + R_s + R_L)(R_{g1} + R_{g2} + R_L + R_c) - R_L^2 \right\}}$$

$$I_s = I_m$$

$$I_{g1} = I_c$$

$$I_{g2} = I_c$$

$$I_L = I_m - I_c$$

System Energy and Force

The expressions for the change in energy stored in each circuit element have been derived in Section 3.3.3. On taking the partial derivative of the energy stored in each element with respect to air gap, we obtain the component of force due to the change in energy in that element.

$$F_m = R_m I_m I_m' - V_{om} I_m'$$

$$F_s = R_s I_s I_s' - V_{os} I_s'$$

$$F_c = R_c I_c I_c' - V_{oc} I_c'$$

$$F_{g1} = \frac{R_{g1}' I_{g1}^2}{2} + R_{g1} I_{g1} I_{g1}'$$

$$F_{g2} = \frac{R_{g2}' I_{g2}^2}{2} + R_{g2} I_{g2} I_{g2}'$$

$$\text{where } I_m' = \frac{-R_L (R_{g1}' + R_{g2}') [R_L (V_{om} + V_{os}) + (R_m + R_s + R_L) V_{oc}]}{[(R_m + R_s + R_L)(R_{g1} + R_{g2} + R_L + R_c) - R_L^2]^2}$$

$$I_s' = I_m'$$

$$I_c' = \frac{(R_{g1} + R_{g2} + R_L + R_c) R_L I_m' - (V_{oc} + R_L I_m)(R_{g1}' + R_{g2}')}{(R_{g1} + R_{g2} + R_L + R_c)^2}$$

$$I_L' = I_m' - I_c'$$

$$I_{g1}' = I_c'$$

$$I_{g2}' = I_c'$$

The total force acting on the system is the sum of the component forces

$$F_T = F_m + F_s + F_L + F_c + F_{g1} + F_{g2} \quad (3.59)$$

Unfortunately, due to the nature of the energy analysis, we cannot say what the force distribution on the magnet structure is. For instance, the force component F_S is not the force acting on the magnet shell; it is simply the force due to the change in energy stored in the shell. A good example of this point is the leakage force F_L , since it is absurd to think of a force acting on a volume of free space.

3.4 MAGNET OPTIMIZATION

Since the magnet is the prime contributor to the magnetic air bearing's total weight and supplies the load-carrying capacity, the first step in designing an optimum bearing is to design an optimum magnet.

By definition, an optimum magnet is one that has a maximum force-to-weight ratio at a chosen air gap. The performance function is thus given by

$$\Gamma \equiv \frac{F_r}{W_r}$$

Γ will be a function of the magnet's geometry, material, and air gap. For this optimization, the magnetic materials will be chosen and the air gap fixed at some value. Thus, the performance is considered a function of the design dimensions only.

$$\Gamma = \Gamma(x_i) \quad i = 1, 2, 3, \dots, n$$

where the x_i 's are the magnet's dimensions.

Because of the complexity of this theoretical performance function, the optimization was conducted using a numerical technique and run on a digital computer. The following discussion is a summary of

the numerical optimization technique.

To find the maximum value of Γ for all possible values of x_i , we start at some test point x_i^0 and take a small excursion (ϵ) in one variable and measure the corresponding secant gradient of Γ .

$$g_i^0 = \frac{\Delta \Gamma}{\Delta x_i} = \frac{\Gamma(x_j^0 + \epsilon \delta_{ij}) - \Gamma_0}{\epsilon}$$

If g_i^0 is positive, Γ is locally increasing; if g_i^0 is negative, Γ is locally decreasing in the direction of x_i . The vector g_i^0 therefore points in the direction of maximum increase of Γ to a first approximation.

The unit vector which points in this direction can be written

$$n_i^0 = \frac{g_i^0}{\sqrt{g_j^0 g_j^0}} \quad \text{for } g_j^0 \neq 0$$

We now step to a new point on the performance surface taking the anticipated steepest ascent

$$x_i' = x_i^0 + n_i D$$

where D is the step size.

At this new point of higher performance, the gradient is again measured and the cycle is repeated. This procedure leads to the following general relationships for climbing the performance hill:

$$g_i^K = \frac{\Gamma(x_j^K + \epsilon \delta_{ij}) - \Gamma_x}{\epsilon}$$

$$n_i^K = \frac{g_i^K}{\sqrt{g_j^K g_j^K \sum_{j=1}^n \delta_{jj}^2}}$$

$$x_i^{K+1} = x_i^K + n_i^K D$$

$$\Gamma_{K+1} = \Gamma(x_i^{K+1})$$

The computer programs used in predicting and optimizing magnet performance are presented in Appendix D.

Experimentally, it was found that bearings using the outside shell magnet designs were statically unstable in the tipping mode. For this reason, detailed optimization data will not be presented for this design. A more detailed discussion of this instability problem will be given in Section 4.0. Force characteristics for prototype outside shell

magnets will be presented in Section 3.5 for the purpose of evaluating the accuracy of the theory.

The inside shell magnet design was optimized theoretically at an air gap of 6 mils. This was done for the two magnetic materials, Indox V and Indox VI-A. In addition, maximum steel flux densities at 14 and 16 kilogauss were considered.

Mild steel was chosen as the shell material and the shells were tapered as shown in Figure 3.8 to minimize weight.

The optimization was conducted by constraining the outside radius and then varying the various geometric parameters to obtain a maximum force-to-weight ratio at 6 mils. The magnet thickness was constrained by a minimum of .2 inches. Tests were conducted from various starting points to assure that the optimum design found was the overall optimum rather than just a local maximum.

Figures 3.9 through 3.16 show the optimum design parameters, force and weight, as a function of magnet

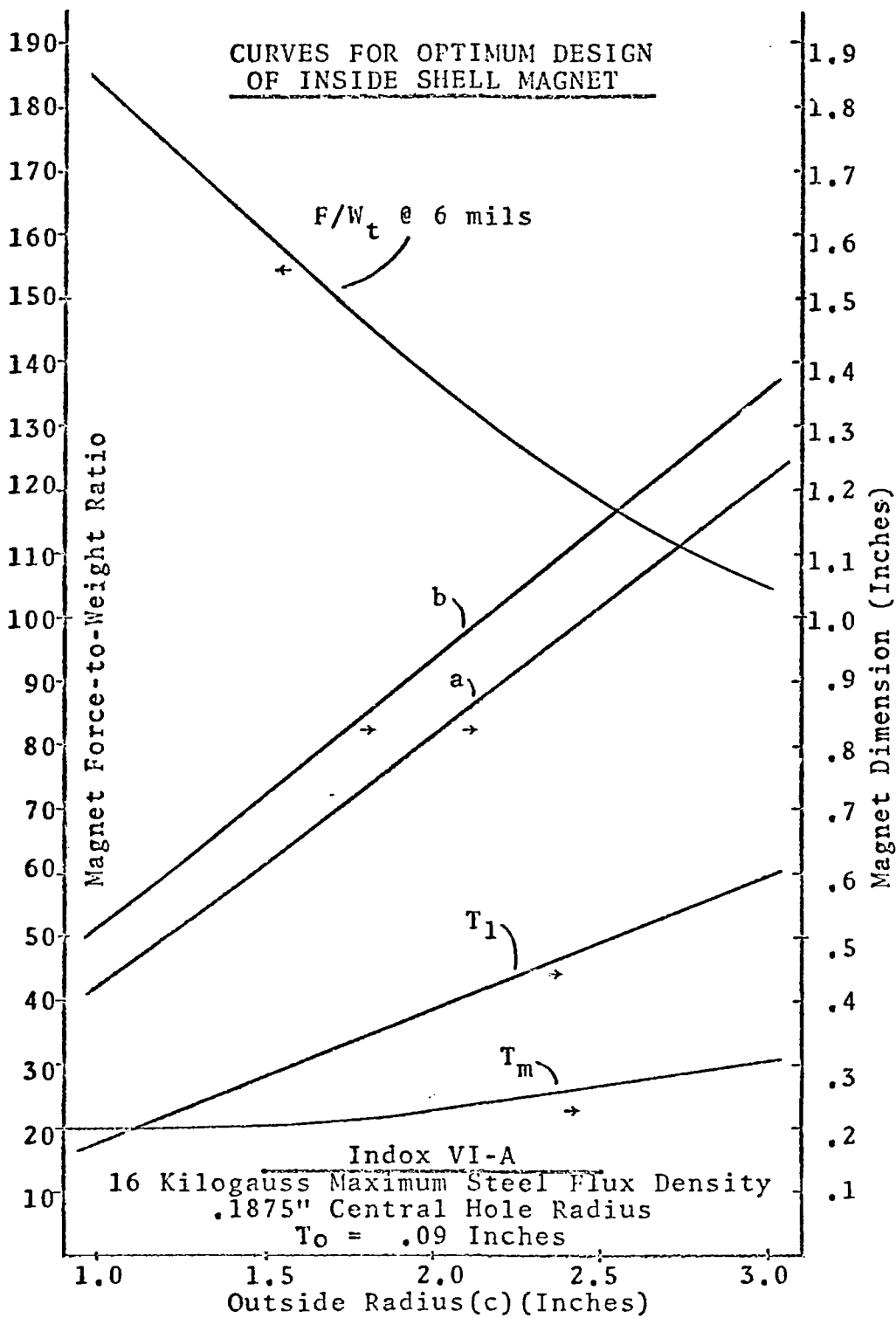


Figure 3.9

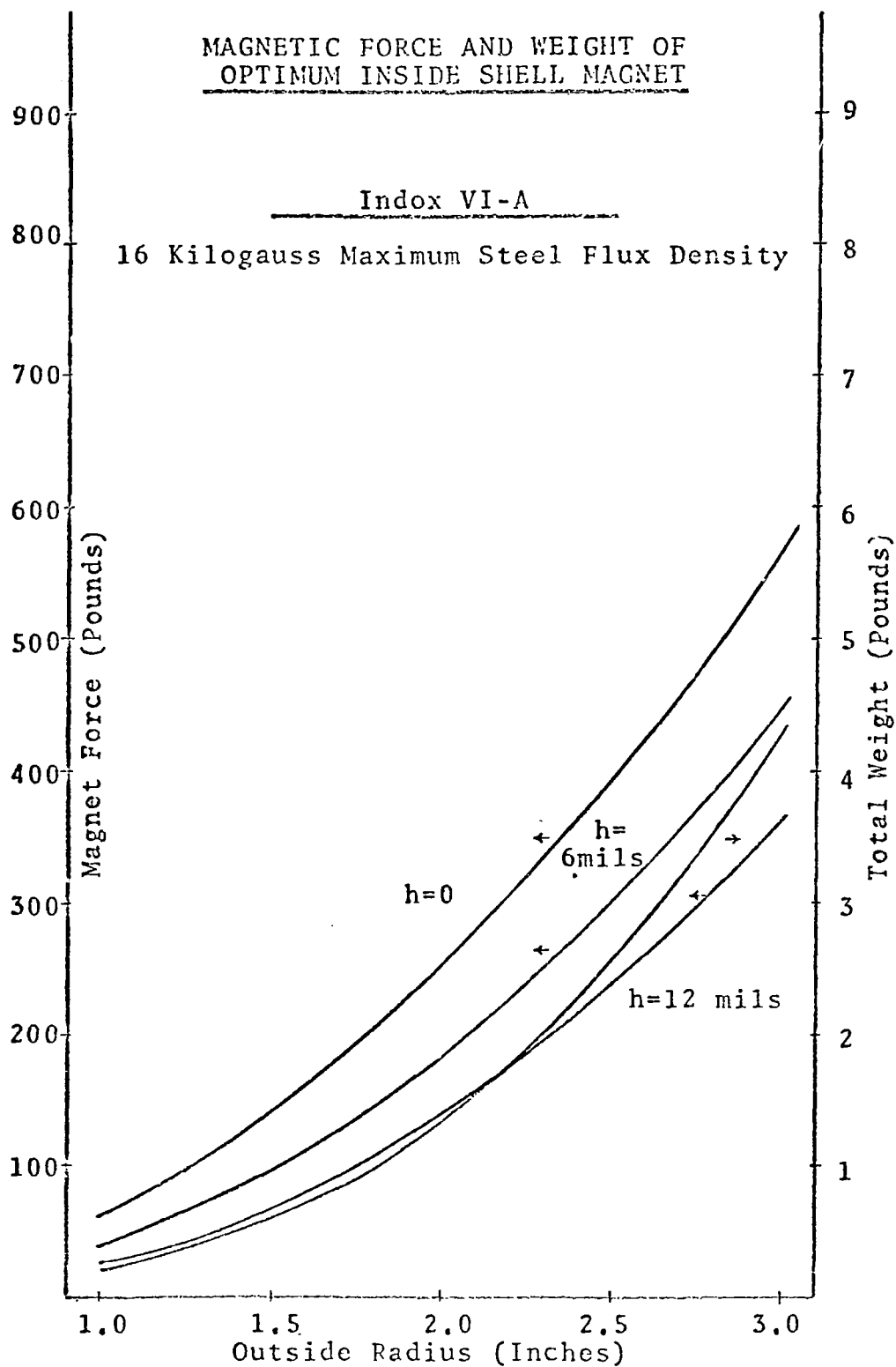


Figure 3.10

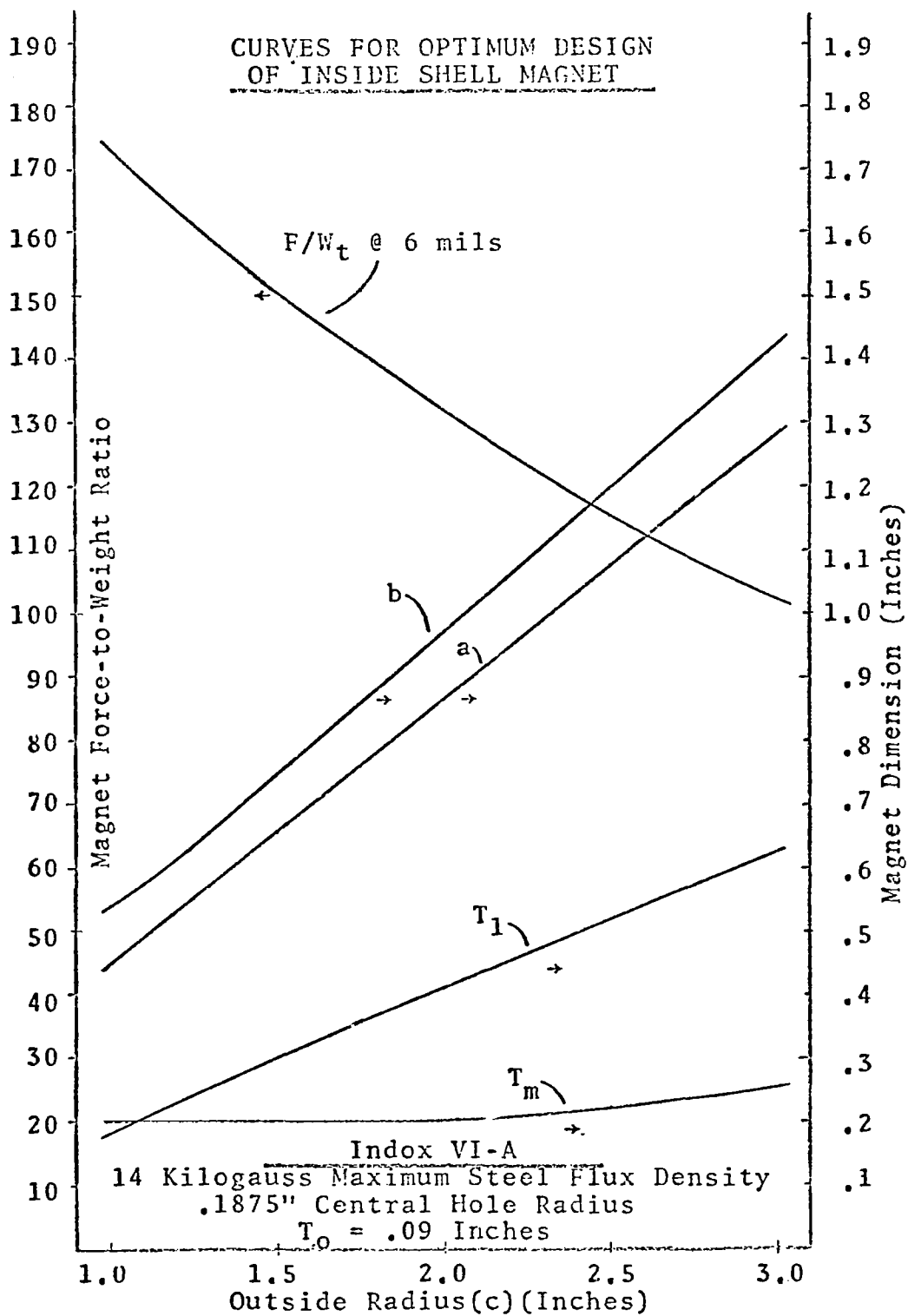


Figure 3.11

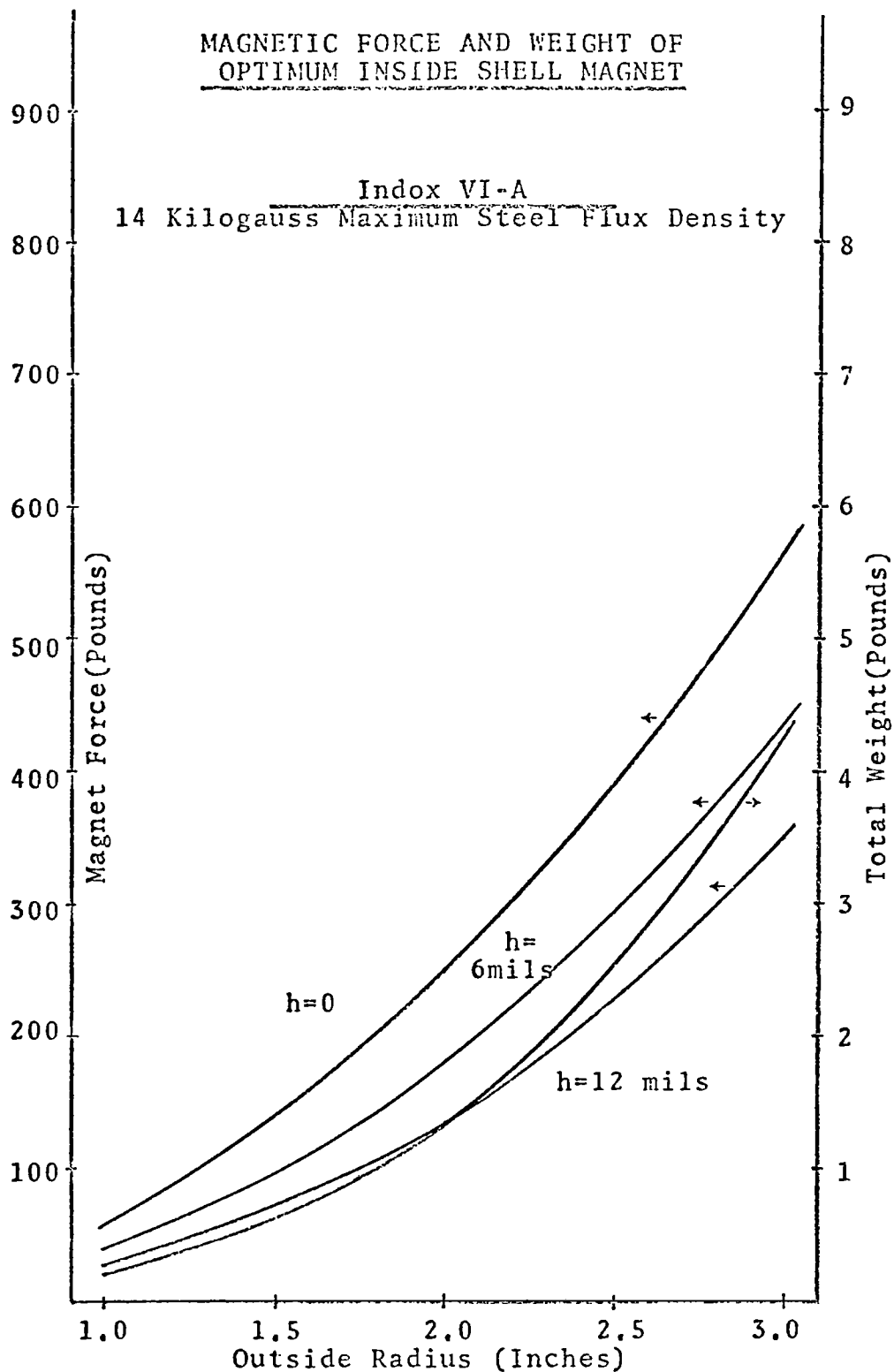
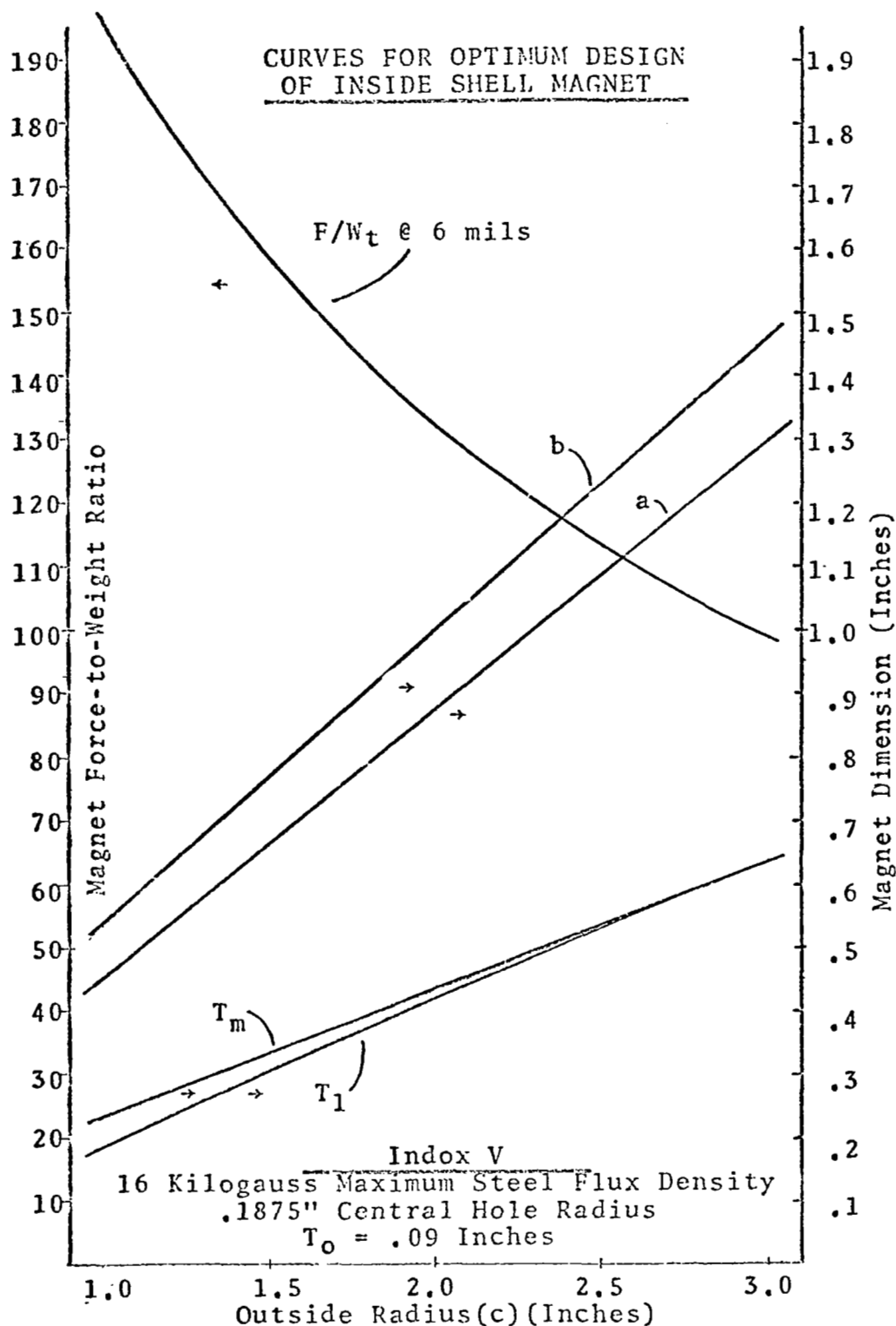


Figure 3.12



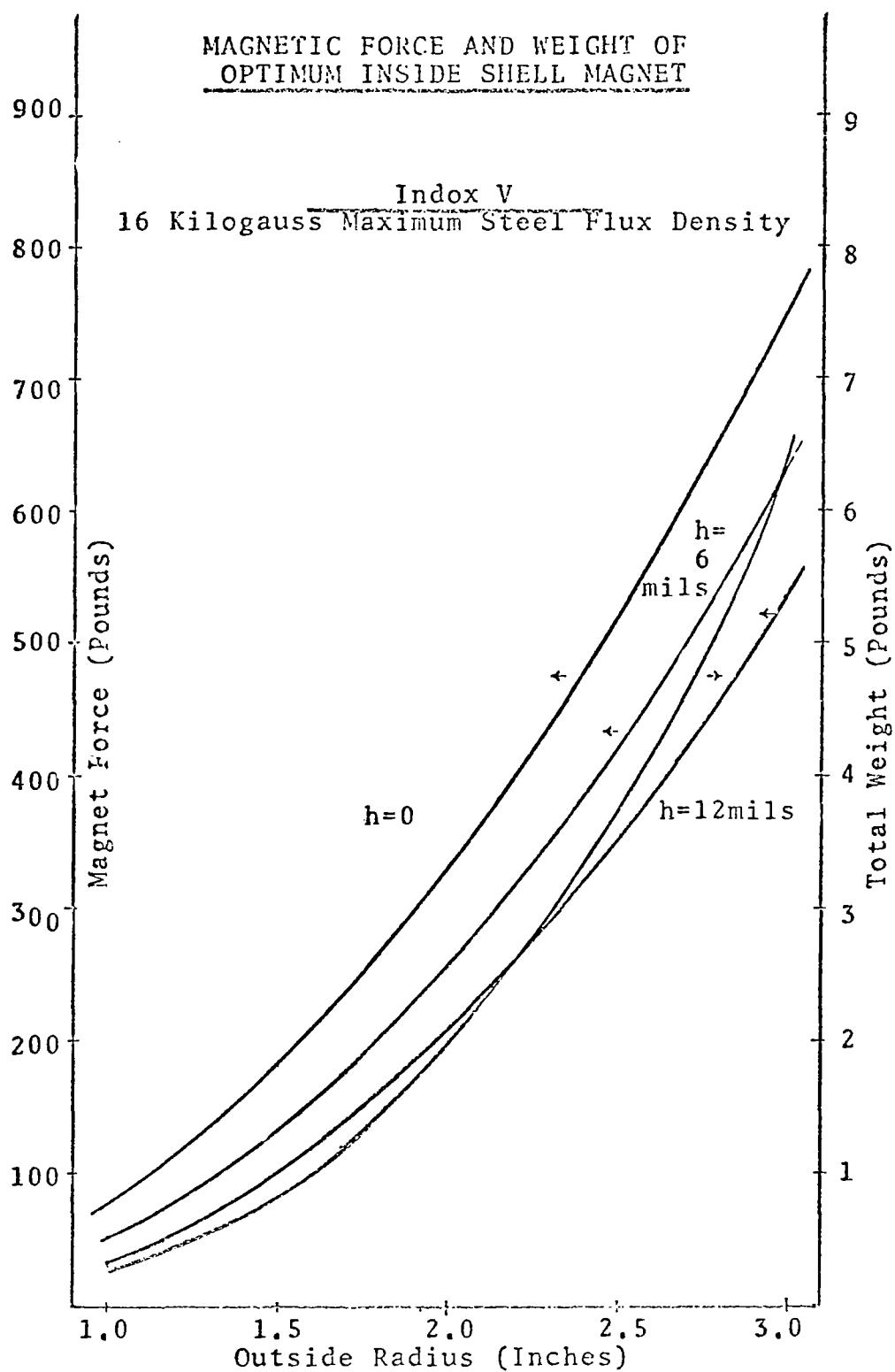


Figure 3.14

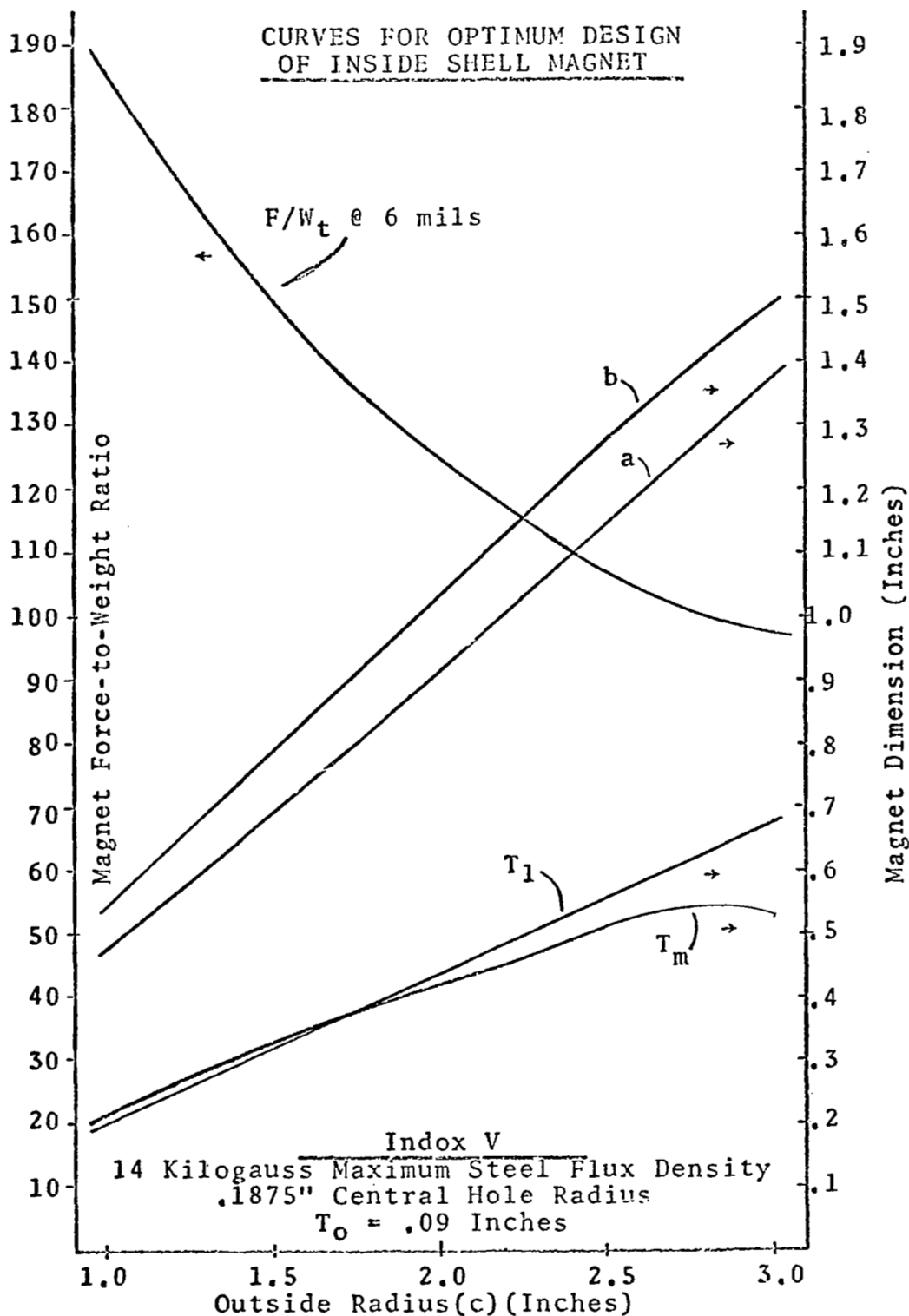


Figure 3.15

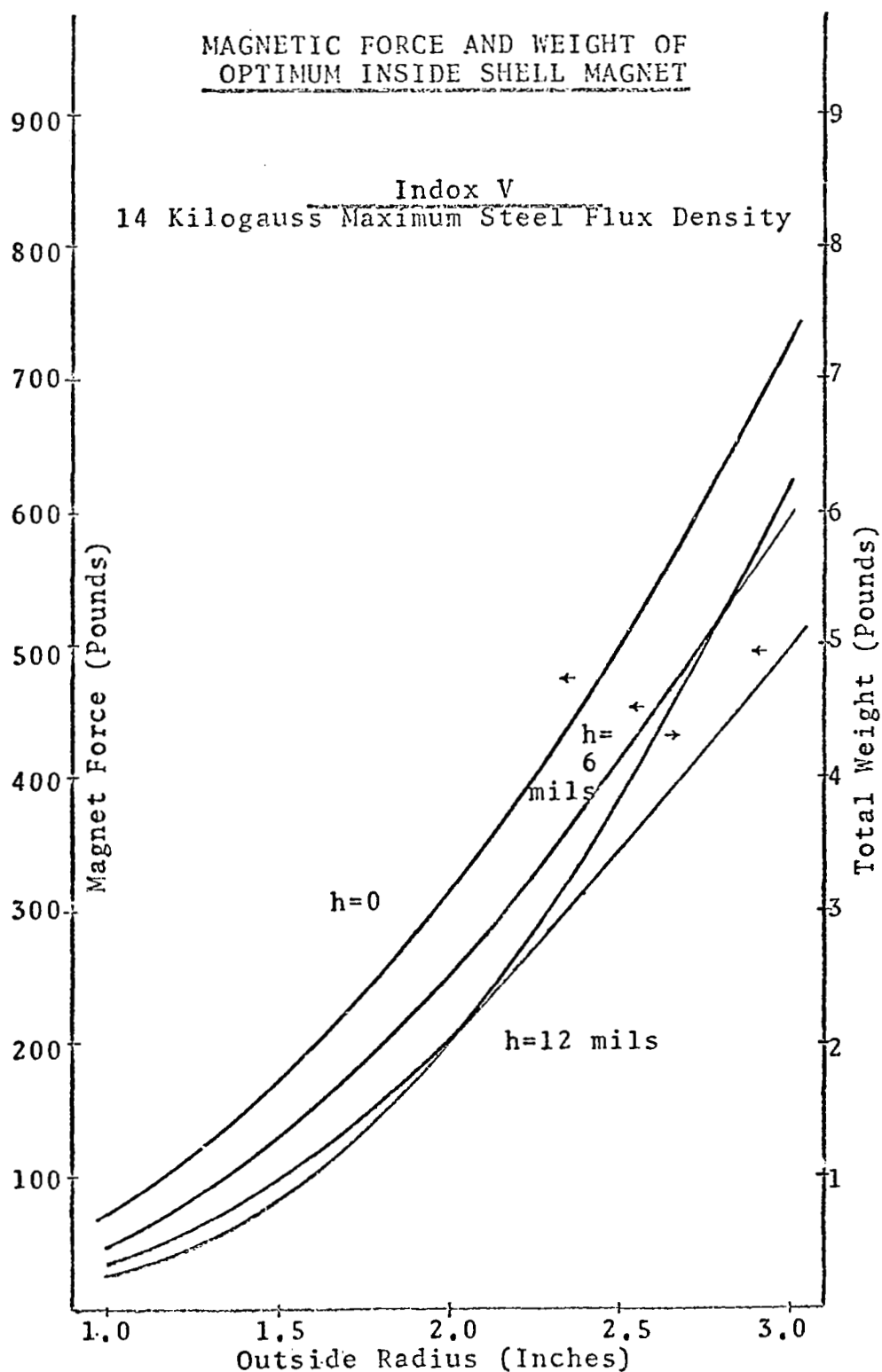


Figure 3.16

outside radius. It should be noted that the force-to-weight ratio increases with decreasing magnet size (e.g., Figure 3.9). This is generally the case in magnet design. The curves for optimum magnet geometry can be used as follows:

Suppose it is decided to use Indox VI-A, have a maximum steel flux density of 14 kilogauss, and have a developed force at 6 mils of 200 pounds. From Figure 3.12 it can be seen that the magnet's outside radius should be 2.1 inches and that the magnet will weigh 1.5 pounds. The geometry of the magnet can be obtained from Figure 3.11 as follows:

$$\begin{aligned}a &= 0.91'' \\b &= 1.2'' \\T_1 &= .435'' \\T_m &= .205'' \\T_o &= .09''\end{aligned}$$

Since the flux passing through the ceiling will be the same as that passing through the steel shell, the ceiling thickness should be equal to T_1 to prevent ceiling saturation and to develop maximum force.

It should be noted that, by increasing the maximum steel flux density from 14 to 16 kilogauss for a

particular magnetic material, there is a small increase in performance and a small decrease in ceiling thickness. For this reason, 16 kilogauss was used as the maximum steel flux density for prototype inside shell designs.

3.5 COMPARISON OF THEORETICAL AND EXPERIMENTAL RESULTS

Since prototype magnet design was limited to off-the-shelf ceramic discs, the geometry of these magnets is not theoretically optimum. The steel shells, however, were designed to yield the theoretical maximum force-to-weight ratio given the geometry of the magnet disc as a constraint.

Figures 3.17 through 3.21 show the theoretical and experimental force characteristics for three outside shell and two inside shell magnets. In all cases, the theoretical curve lies above the experimental curve. This discrepancy increases with gap. The error is presumably caused by flux leakage paths that were neglected in the theory. An example of such a leakage path is from the exposed portions of the steel shell to the ceiling.

Figures 3.19 and 3.20 can be used to compare the outside shell and tapered inside shell magnet designs since both tests were performed with the same Indox V ceramic disc. The inside shell design develops 400 pounds at zero gap as compared to 340 pounds for the

COMPARISON OF THEORETICAL AND EXPERIMENTAL MAGNET FORCE CHARACTERISTICS

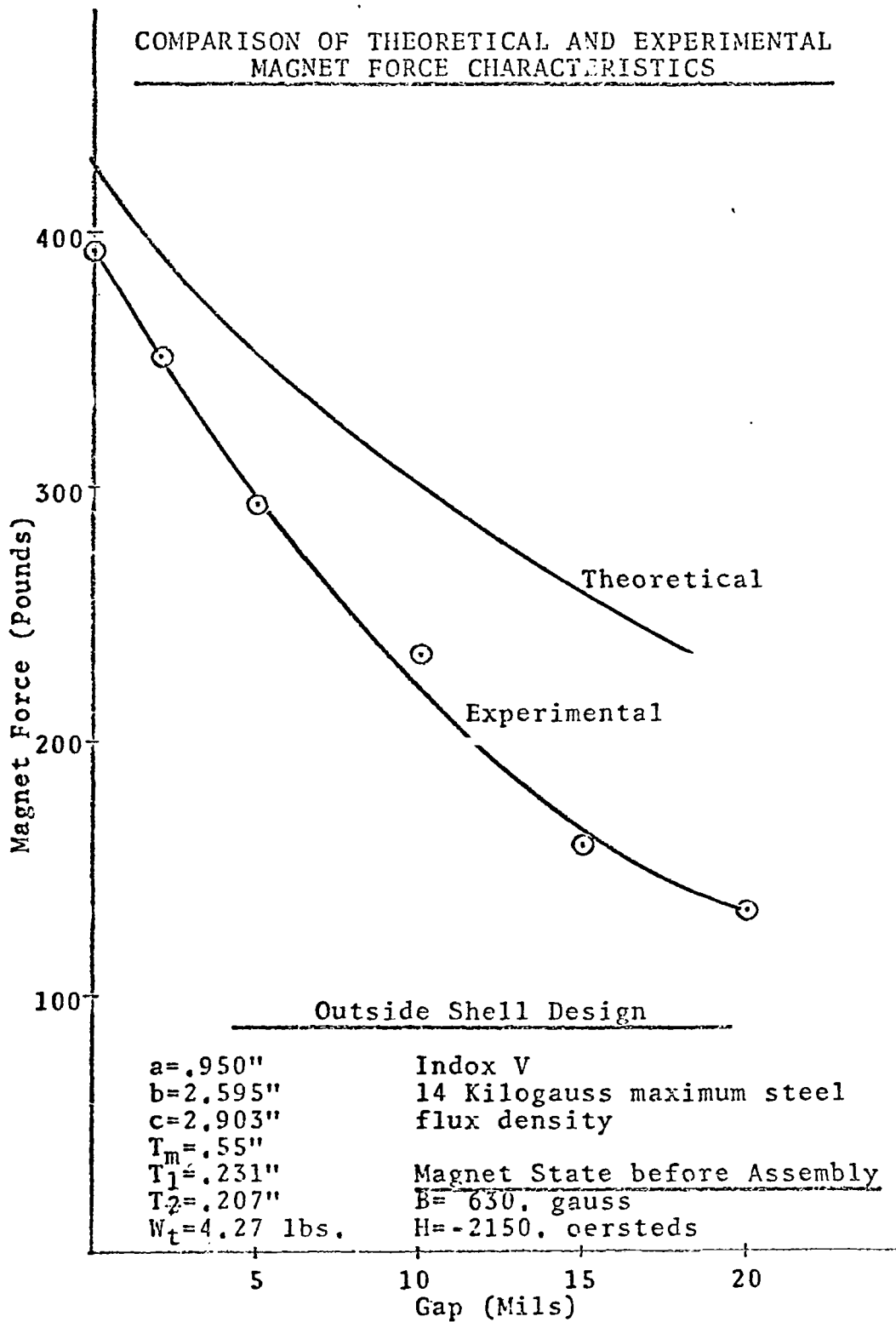


Figure 3.17

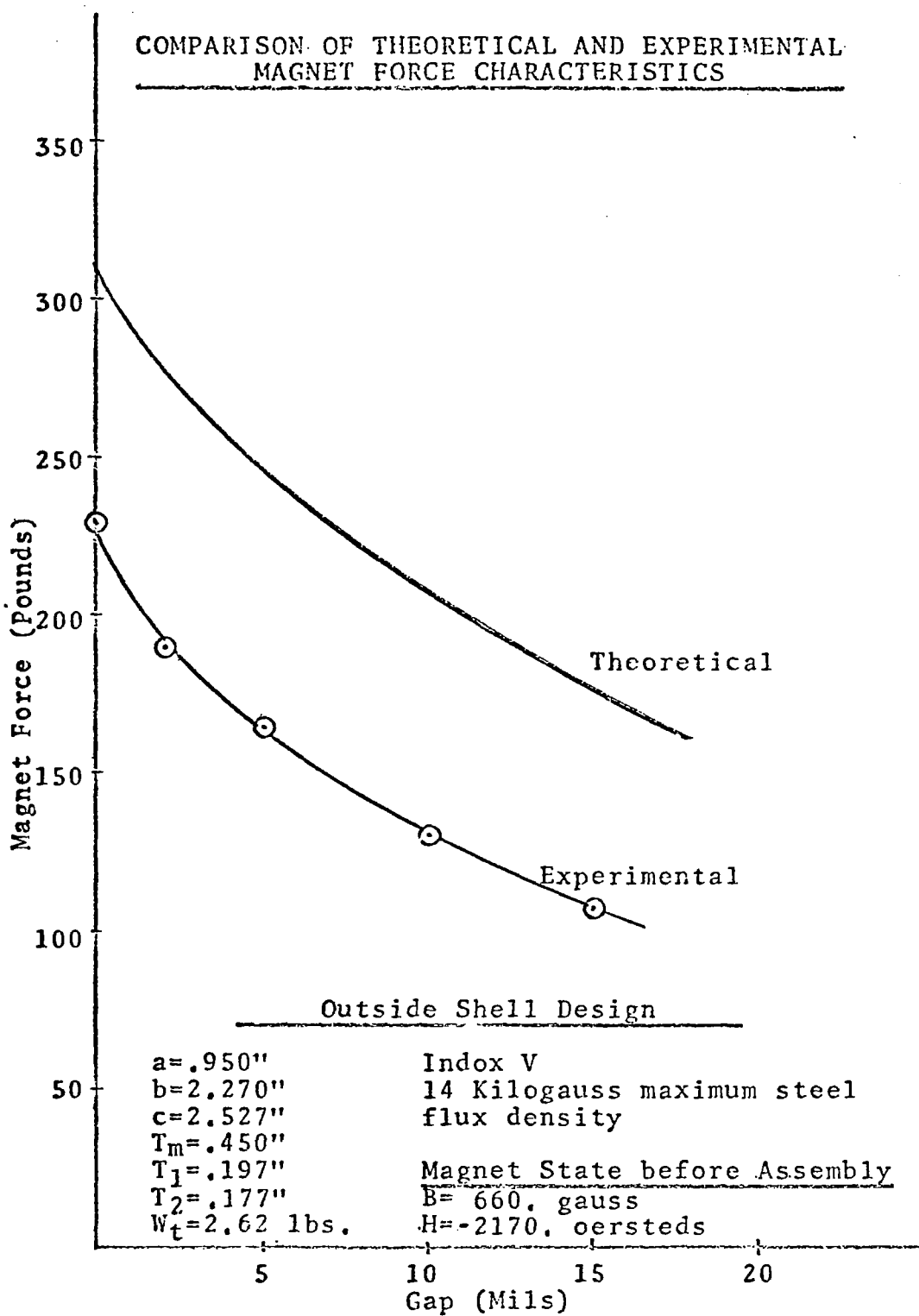


Figure 3.18

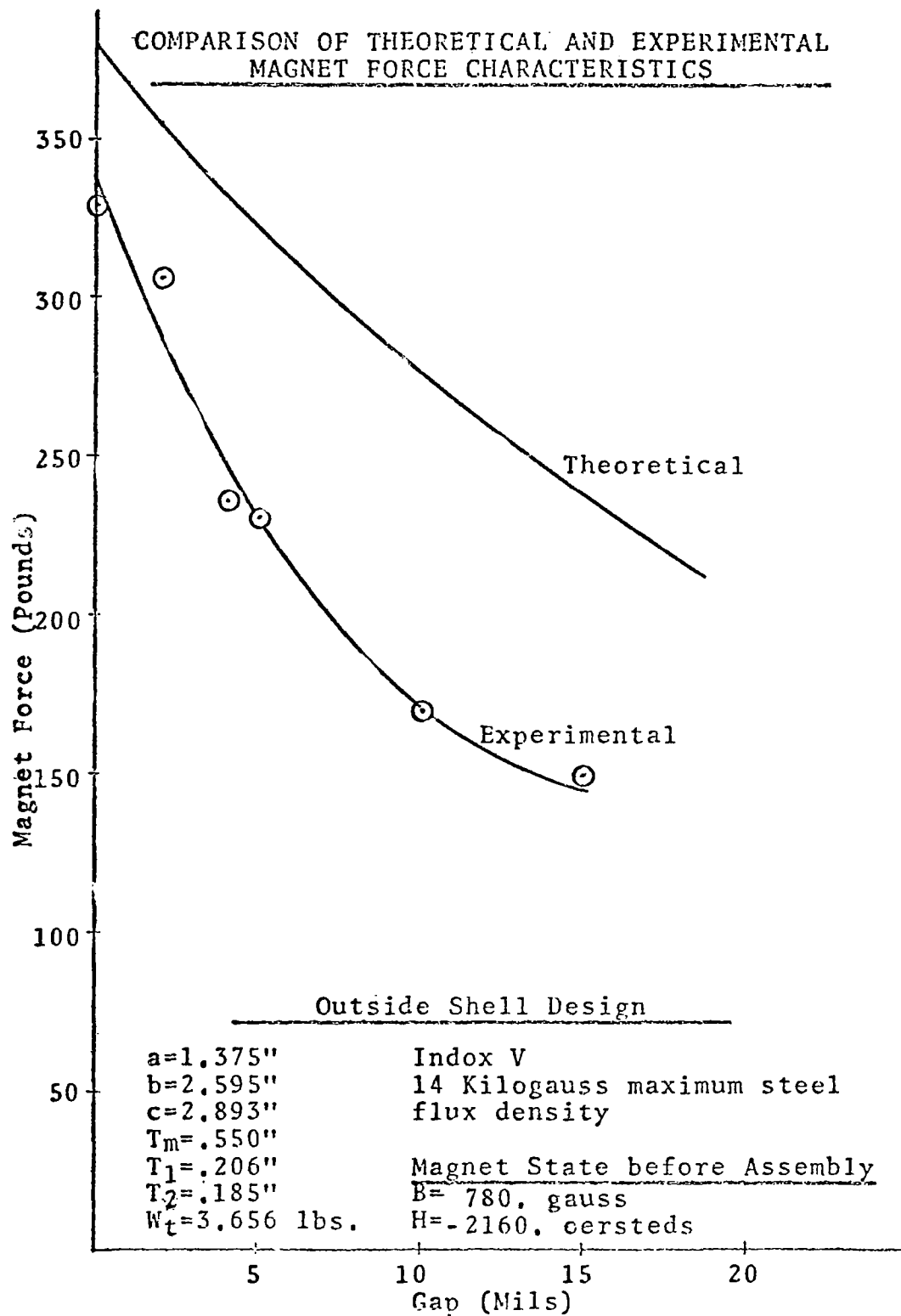


Figure 3.19

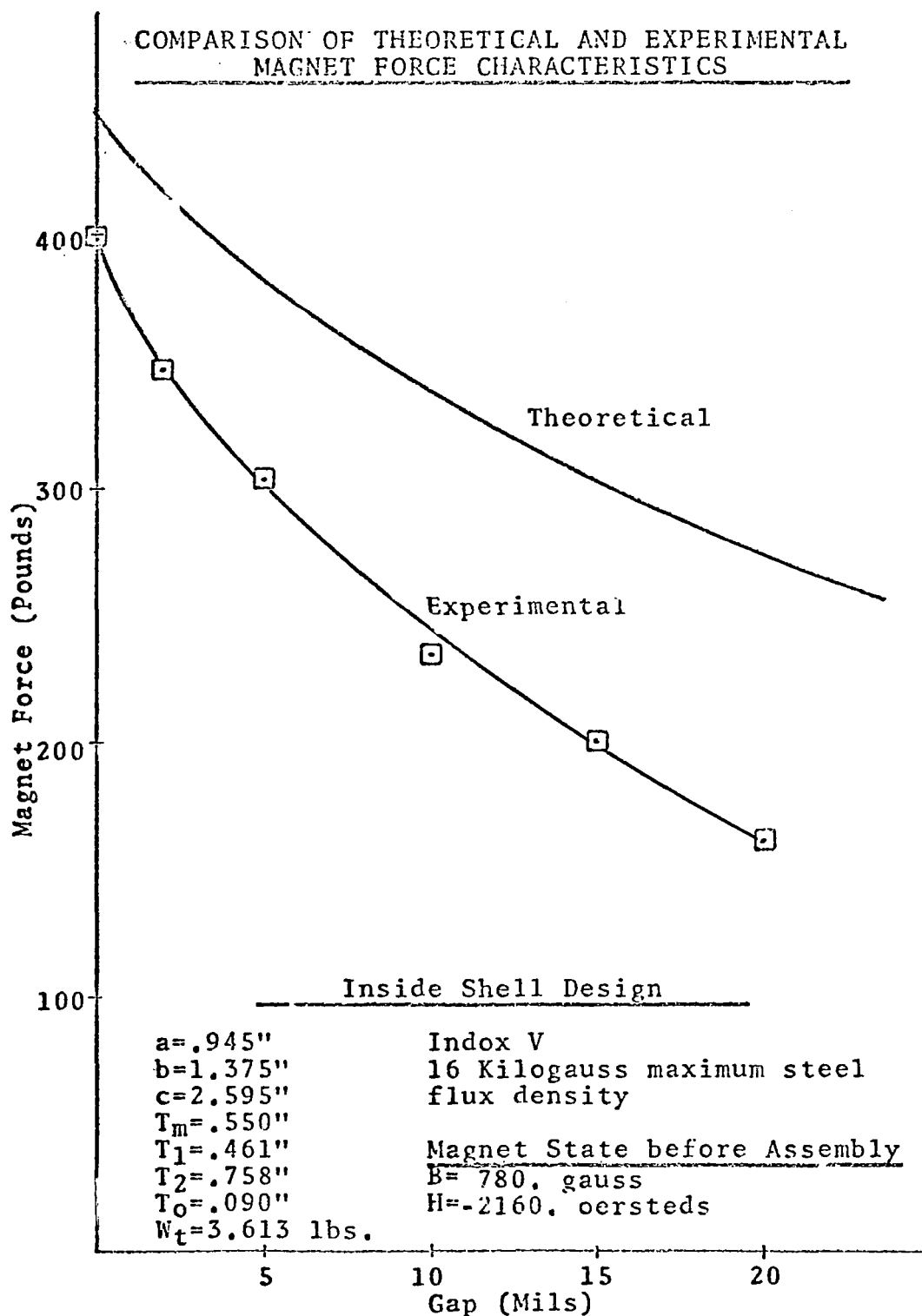


Figure 3.20

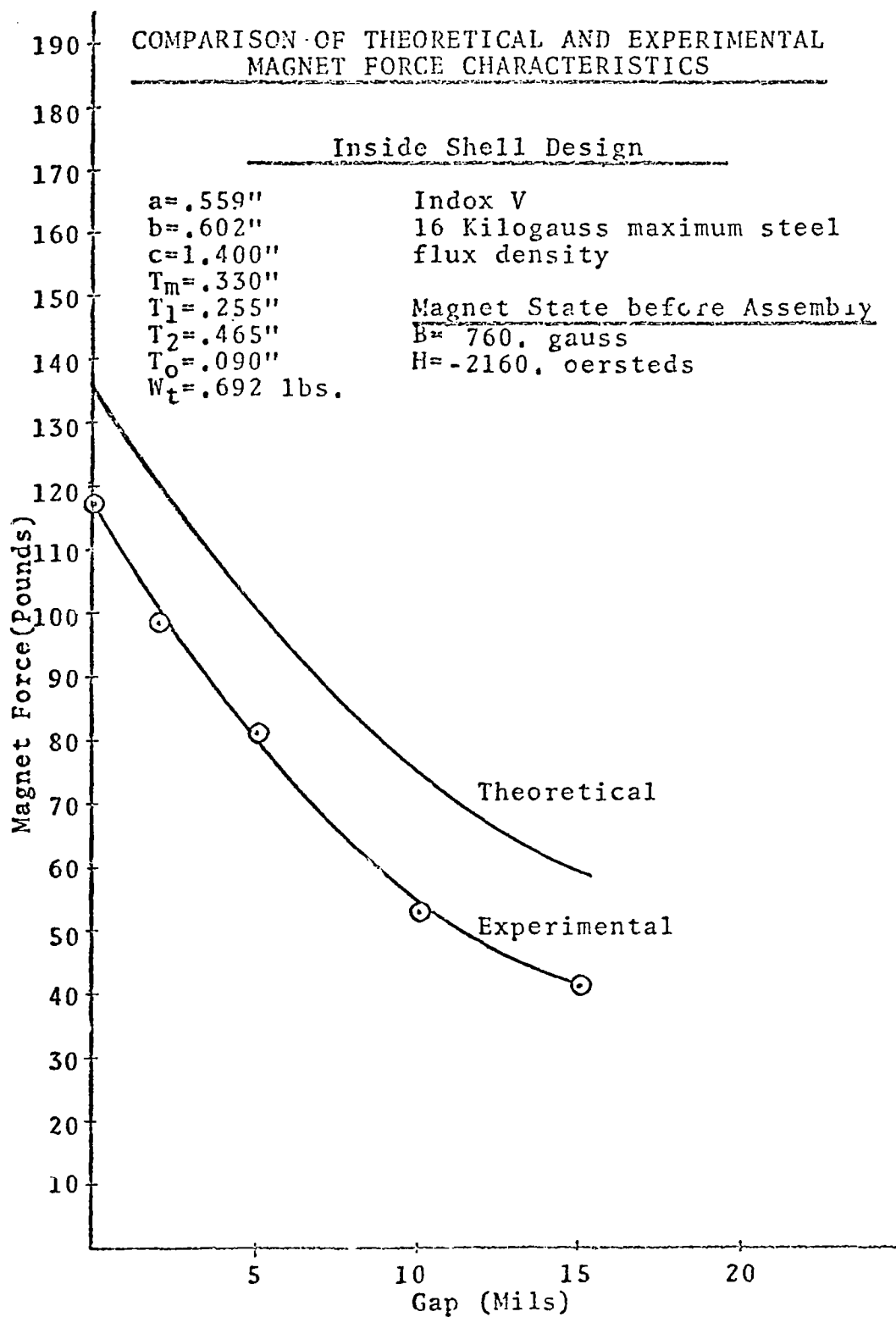


Figure 3.21

outside shell design. Both designs have approximately the same weight.

There are two possible reasons for the incongruency between these results and those obtained from the Indiana General Corporation (see Figure 3.3) which indicate that the outside shell should have a superior force-to-weight ratio.⁽¹⁰⁾ One reason is that the experimental inside shell was tapered, yielding a weight savings over the design first considered. The other reason is that the inside shell was designed with a maximum steel flux density of 16 kilogauss, whereas the outside shell was designed to 14 kilogauss.

The mean error between theoretical and experimental force characteristics as a function of air gap is shown in Figure 3.22. A K factor, defined as one minus the mean error, is also shown in this Figure. This factor may be used to bring the force characteristics of the theoretically optimum magnet designs presented in Section 3.4 into better agreement with experiment. For example, if one wishes to design a magnet that has a 200-pound pull at 6 mils, he need only divide the desired force by the K factor at the gap, obtaining

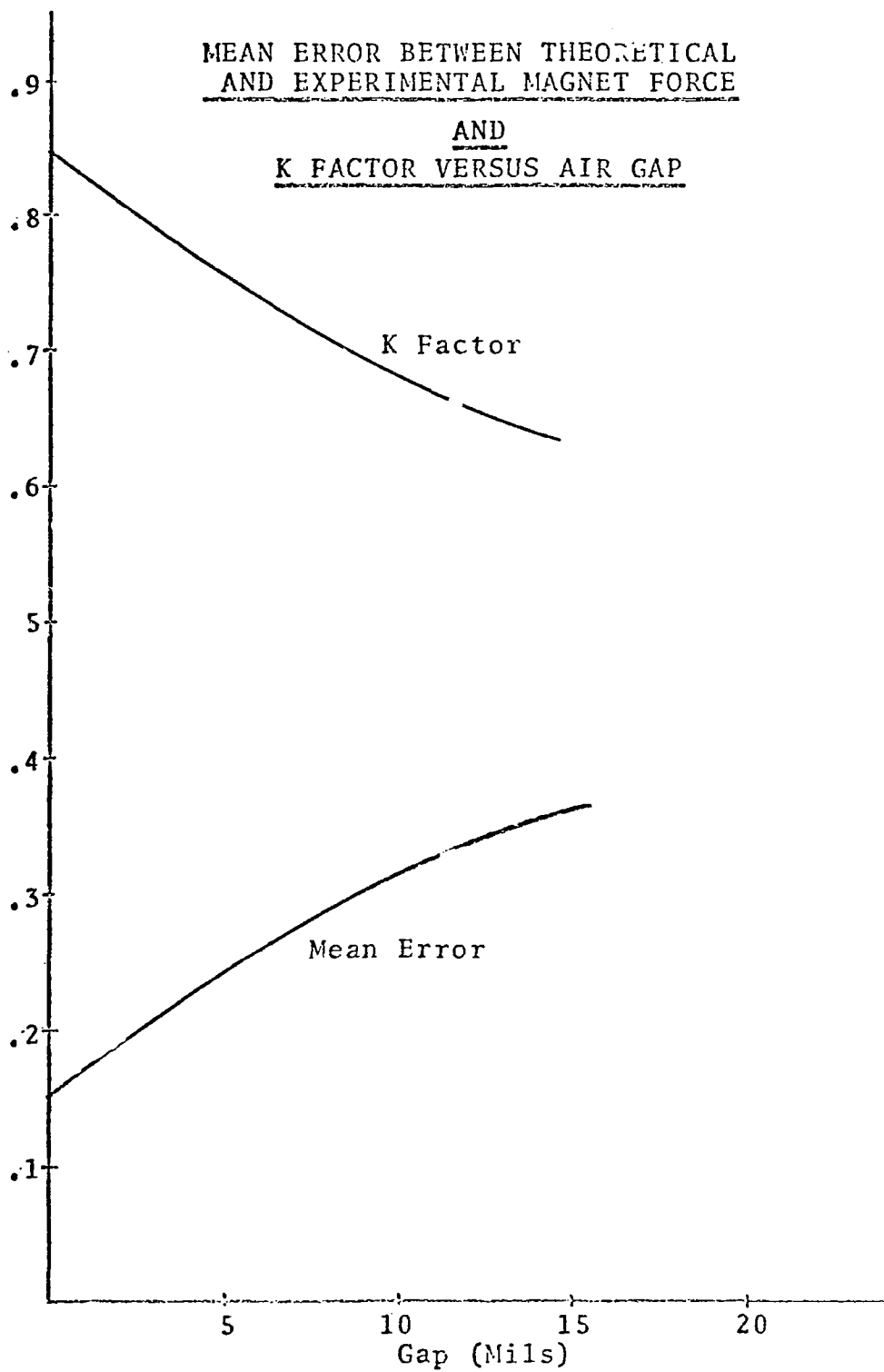


Figure 3.22

270 pounds, and then find the optimum geometry for this magnet force. The design obtained should yield approximately 200 pounds at 6 mils.

4.0 MAGNETIC AIR BEARING DESIGN

The outside shell magnet design, which seemed promising because of its high force-to-weight ratio and low required ceiling thickness, is not suitable as a magnet for use in a magnetic air bearing. This magnet, when used with an air bearing, is unstable in the tipping mode; whereas an air bearing using the inside shell design is not.

This can be explained by using a simpler theory for the magnet force than was used in the preceding analysis. The theory states that the force produced by a magnet is proportional to the square of the flux density in the air gap.⁽¹³⁾ Therefore, since the outside shell design has its highest air gap flux density at the outer diameter, the majority of the magnet force is generated in this area. This magnet will therefore produce a large unstable tipping moment. The inside shell magnet, on the other hand, has its highest flux density concentrated in the center; therefore, its unstable moment is minimized.

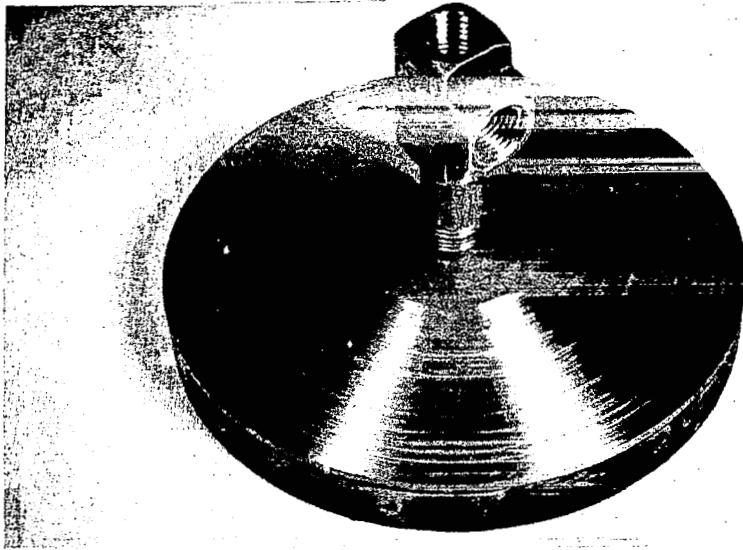
Two inside shell magnets were fabricated and their experimental force characteristics are presented in Figures 3.20 and 3.21. Both of these magnets were used successfully as magnetic air bearings without any observed tipping instability. The larger of these inside shell magnetic air bearings is shown in Figure 4.1.

Design Considerations

It is desirable from the standpoint of utilizing a magnet to its full potential to operate at as small a gap as possible. The minimum practical operating gap has been experimentally determined to be approximately 4 mils. In conjunction with this minimum gap, the maximum ceiling surface tolerance was investigated for the condition of no perceptible contact between the bearing and the ceiling. This flatness tolerance was found to be approximately ± 1.5 mils over the bearing diameter.

Since the steel ceiling is the major cost item in the magnetic air bearing system and its cost greatly increases with decreasing allowable surface

INSIDE SHELL MAGNETIC AIR BEARING



Max Rated Force = 250 lbs. @ 70 psig Supply Press.

Net Weight = 3.62 lbs.

Required Ceiling Thickness = .461 Inches

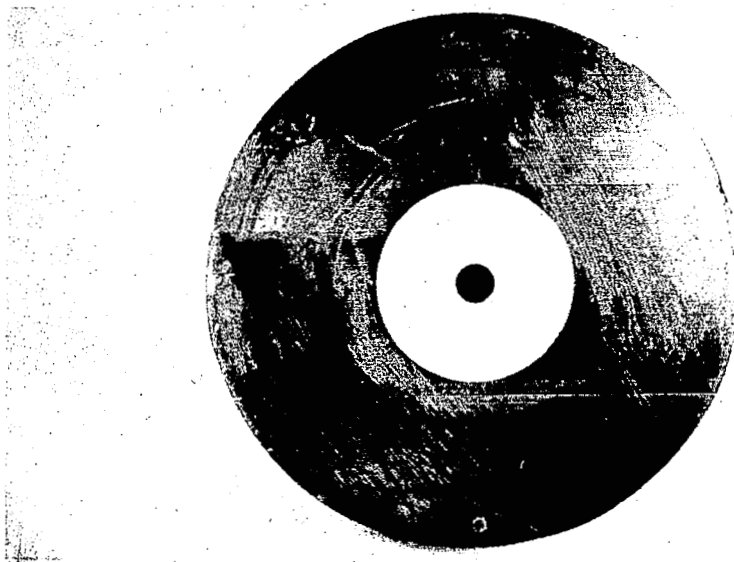


Figure 4.1

tolerance, it is considered essential to design a bearing with a small outside diameter. It has been shown that the required ceiling thickness is a linear function of an optimum magnet's outside diameter. Thus, when reducing the thickness of the ceiling, the size of the magnet should be proportionately reduced. Since magnet force-to-weight ratio increases with decreasing size, one can fabricate a lighter and more efficient design by clustering a number of small magnets than by using one large magnet.

In contrast to these size limitations, it is shown in Figures 2.9 through 2.11 that the stiffness of a bearing increases with outside diameter; but since stiffness also increases with orifice size and supply pressure, the efficient application of these two parameters can bring the stiffness to a satisfactory level.

Through the process of increasing orifice size and supply pressure, air flow will also increase. It is obvious that increased air flow will demand

a larger air compressor.

Thus, although one can design a theoretically optimum magnet, it is impractical to speak of an overall optimum magnetic air bearing since compromises must be made in a practical design.

Design Procedure

The no load gap of an air bearing is a measure of the maximum operating gap of a magnetic air bearing with the same geometry. This parameter should be compatible with the selected gap operating range, 4 to 6 mils. No load gap as a function of orifice radius is presented in Figures 2.12 and 2.13. From Figure 2.12, it can be seen that a bearing with an outside radius of 1 inch will have a no load gap below 6 mils; therefore, such a bearing will operate too close to the surface. On the other hand, a bearing with a 3-inch outside radius will have a no load gap ranging from approximately 9 to 12 mils; therefore an excessive amount of magnetic force will go into air bearing compression rather than in developing holding force

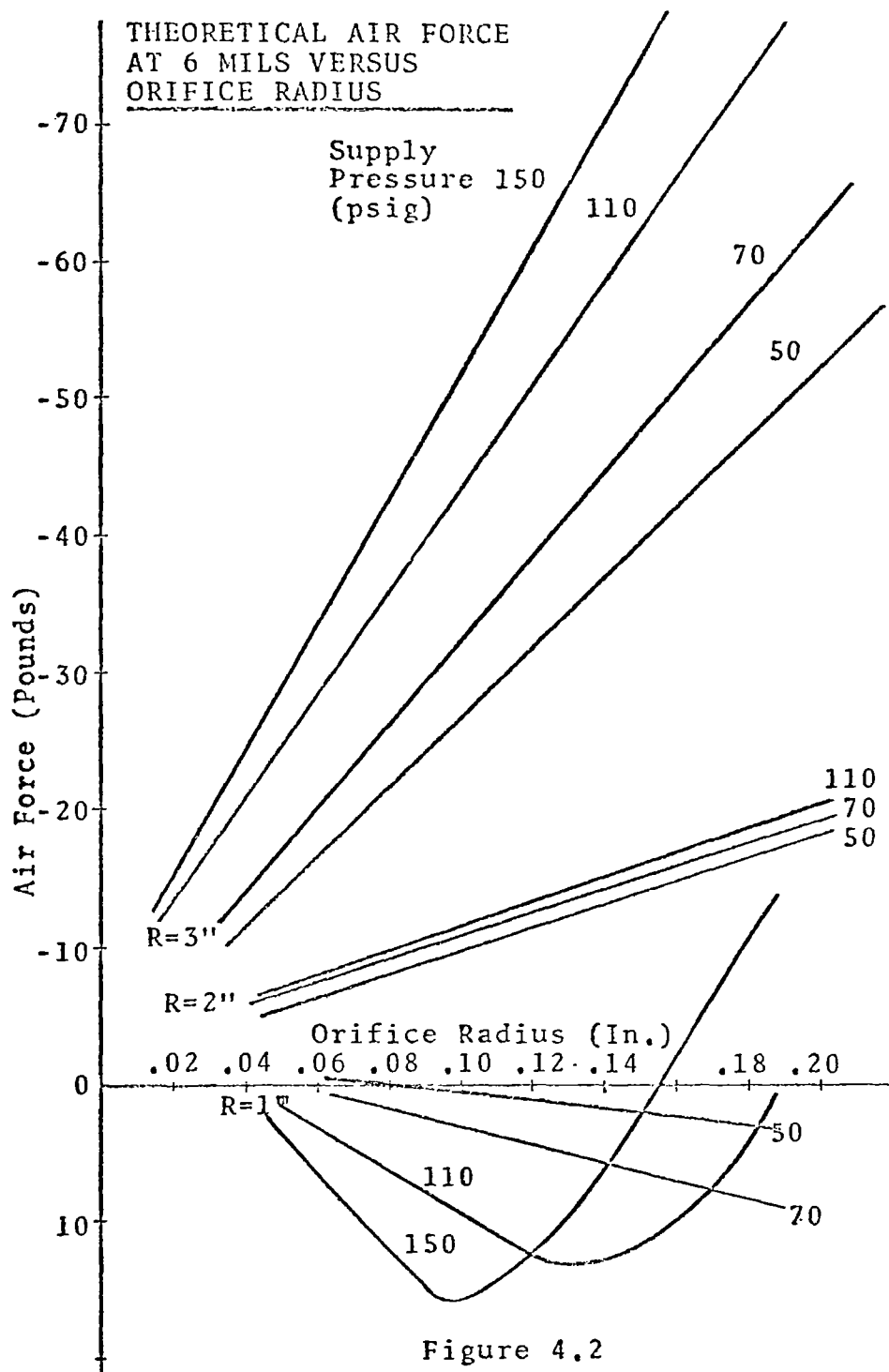
in the operating range.

For compatibility of no load gap and operating range, the outside radius of the air bearing should be limited to a maximum of 2 inches and a minimum which is somewhat greater than 1 inch. For maximum force in this size range, the outside radius of the magnetic air bearing should be the same as the outside radius of the magnet. The optimum inside shell magnets are capable of producing a maximum magnet force at 6 mils ranging from 37 pounds for a 1-inch outside radius to 190 pounds for a 2-inch outside radius using Indox V and from 30 to 134 pounds using Indox VI-A. These magnet forces were obtained from Figures 3.14 and 3.10 respectively and were decreased from their theoretical values by multiplying by the K factor at 6 mils given in Figure 3.22. It should be stated again that the only advantage in using Indox VI-A rather than Indox V is that the magnet need not be magnetized after assembly in the steel shell.

One can begin the design of a magnetic air bearing by first selecting a magnet material and a maximum

desired operating force within the above-mentioned ranges. The orifice radius should be sized for minimum no load gap. It can be seen from Figures 2.12 and 2.13 that .125 inches will approximately give this minimum in the outside radius range considered.

Once an orifice radius is selected, the flow characteristic can be determined from the flow gradient-versus-orifice radius curve given in Figure 2.18. From the magnitude of the selected force, the designer should have an approximate idea of the outside radius of the bearing. By using Figure 4.2, one can obtain the approximate air force at 6 mils. The strange behavior of these curves for a 1-inch outside radius is a result of the shock wave approaching the outside radius of the bearing. In this figure, negative air force represents external compression of the air bearing. Therefore, if negative, the force read from this graph represents the portion of the magnet's force at 6 mils that will be used in compression of the air bearing. By simply adding this compressive air force to the desired maximum operating force, one can obtain the required magnet force at



this air gap.

By dividing the obtained magnet force by the relevant K factor and referring to Figures 3.13 and 3.14 for Index V or Figures 3.10 and 3.12 for Index VI-A, the magnet's geometry, weight, and theoretical force characteristics are obtained. The magnet's theoretical force characteristic should be modified by using the K factor and plotted as a function of air gap.

An approximate straight line air force characteristic in the operating range can now also be plotted using the air force at 6 mils and by estimating stiffness given in Figures 2.6 through 2.8. The approximate magnetic air bearing force characteristic can now be obtained by graphically adding the air force to the magnet force. This procedure may have to be iterated several times before the desired air bearing force characteristic is obtained.

The force characteristic obtained by this procedure will be only a rough engineering estimate. For a more accurate design analysis, after the magnet

size has been determined, the computer program given in Appendix B should be used to obtain the air force characteristic. The air force can then be summed graphically with the modified magnet force to obtain the air bearing force-versus-gap characteristic.

This design procedure can then be summarized as follows:

1. Select a maximum magnetic air bearing force and an operating pressure.
2. Determine the orifice radius based on the minimum no load gap criterion.
3. Estimate the outside radius of the magnet and the air force at 6 mils from Figure 4.2
4. Add the desired force to the compressive air force.¹
5. Take the force resulting from Step 4 and divide by the K factor to

¹The force obtained in this step represents the actual magnet force required at 6 mils.

obtain the theoretical magnet force
at 6 mils.

6. Select a magnet material.
7. Using the theoretical magnet force from Step 5, obtain the magnet's geometry from Figures 3.10 through 3.16.
8. Estimate approximate air **force** characteristic or, if more accuracy is desired, use the computer program in Appendix B.
9. Graphically sum the modified magnet force and air force characteristics to obtain the magnetic air bearing force-versus-gap curve.

A prototype magnetic air bearing cluster is shown in Figure 4.3. These bearings are 4 inches in diameter, have an orifice radius of .0938 inches, and have a maximum rated force at 6 mils of 50 pounds. The magnet used in this design is an Alnico V side pole weighing

PROTOTYPE MAGNETIC AIR BEARING CLUSTER

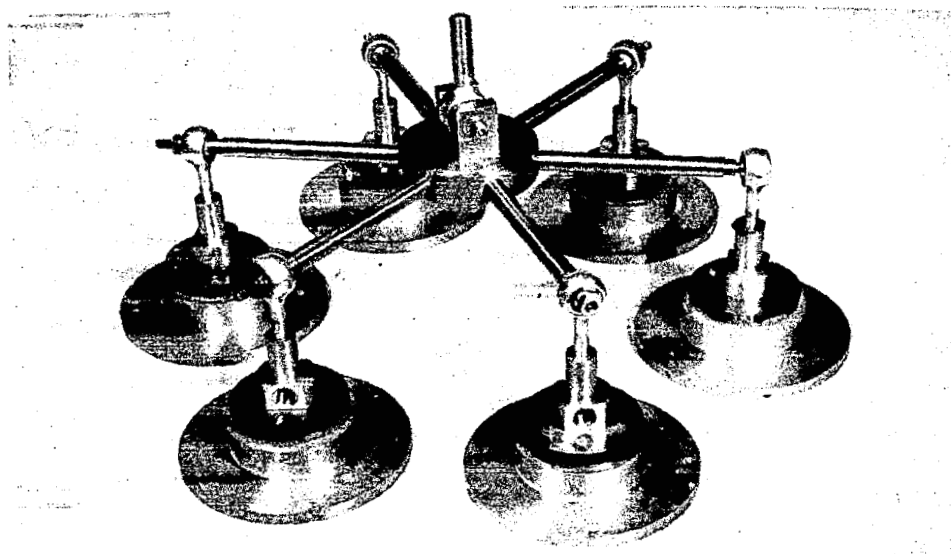
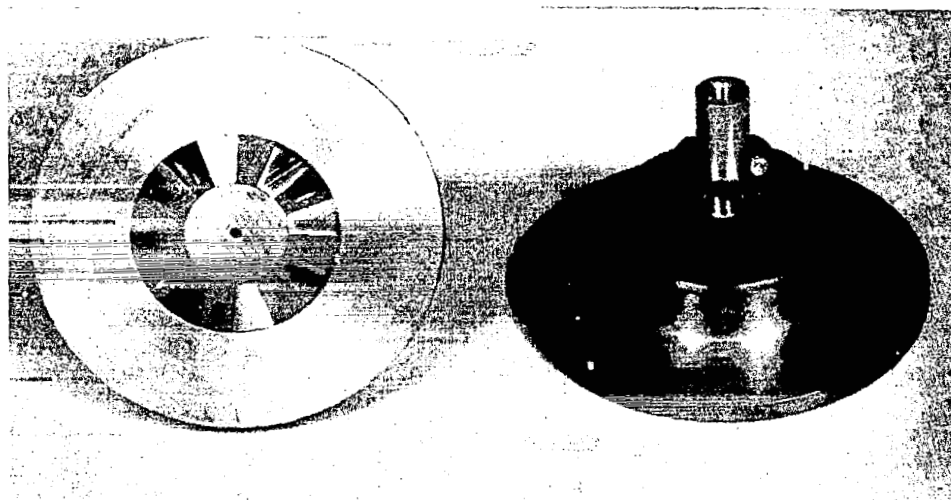


Figure 4.3

.702 pounds and having a breakaway force and resulting magnetic air bearing force characteristic as shown in Figure 4.4.

Since this cluster is composed of six such air bearings, it has a maximum rated force of 300 pounds. This device will be used to support 5/6 of a man's torso and head weight in the prototype vertical lunar gravity simulator described in The Design of a Vertical Lunar Gravity Simulator by R. J. Morgen.⁽¹⁾

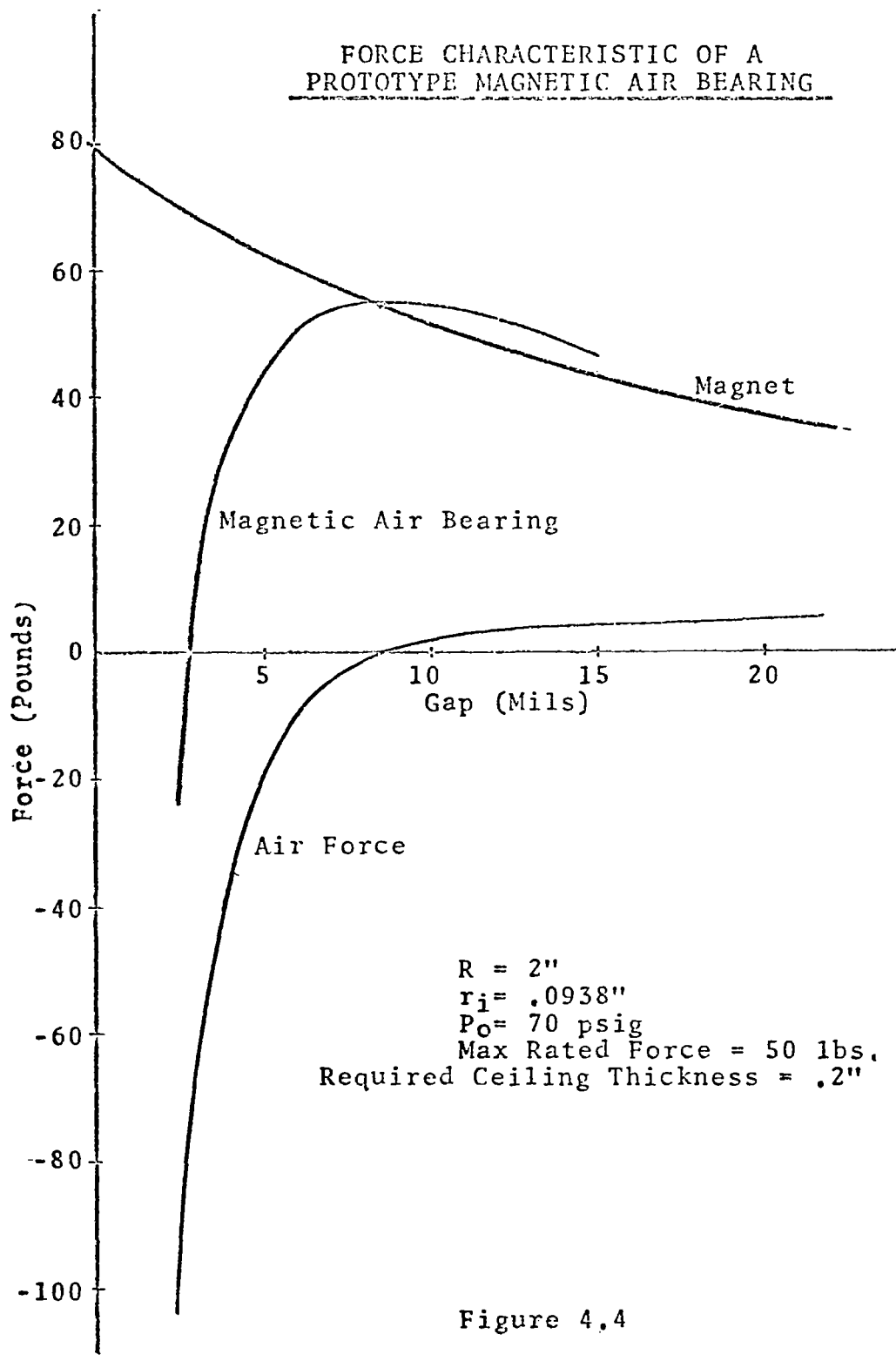


Figure 4.4

5.0 CONCLUSIONS

The theoretical air bearing force and flow characteristics are in good agreement with experimental data. Thus, this theory may be used with sufficient accuracy for air bearing design.

The outside shell ceramic disc magnet, which seemed promising based on shape compatibility and high force-to-weight ratio, is not suitable as a magnetic air bearing permanent magnet because it is prone to a tipping instability.

The tapered inside shell ceramic magnet, based on an experimental comparison using the same ceramic disc, was found to have a higher force-to-weight ratio than the outside shell design. Two prototype inside shell magnets were used as magnetic air bearings with no observed tipping instability. Since these experimental magnets cover the majority of the magnet size range considered in the theoretical optimization, it can be concluded that tipping instability is not a problem with this magnet design.

Comparison of theoretical and experimental magnet force characteristics indicate that in all cases the theory predicts a higher force than found by experiment. The mean error for this discrepancy ranged from 15% at zero gap to 36% at 15 mils.

Magnetic air bearings using the inside shell magnet design should range from something greater than two inches to four inches in diameter.

When designing a magnetic air bearing with a high load capacity, it is more efficient to cluster several small bearings than to use one large bearing.

LIST OF REFERENCES

1. Morgen, R. J. "The Design of a Lunar Gravity Simulator" (unpublished Master's dissertation, Case Institute of Technology, June 1967); also published as NASA CR-1234.
2. Gross, W. A. Gas Film Lubrication New York: Wiler, 1962
3. Mori, Huruo. "A Theoretical Investigation of Pressure Depression in Externally Pressurized Gas-Lubricated Circular Thrust Bearings" J. Basic Eng., Trans. ASME, 83, 1961. pp.201-208
4. Stahler, A. F. "Further Comment on the Pressure Depression Effect in Externally Pressurized Gas-Lubricated Bearings" ASLE Trans. 7, 1964 pp. 366-376
5. Bisson, E. E. and Anderson, W. J. Advanced Bearing Technology Scientific and Technical Information Division, National Aeronautics and Space Administration, 1965
6. Robinson, G. M. "A Special Analytical Study of Air Lubricated Bearings for Jet Aircraft Engines" Final technical report F-A1914, Contract No. NAW 6473. National Advisory Committee for Aeronautics, Feb. 15, 1957
7. Shapiro, A. H. The Dynamics and Thermodynamics of Compressible Fluid Flow Vol. 1 New York: The Ronald Press Company, 1953
8. Wylie, C. R. Advanced Engineering Mathematics New York: McGraw-Hill, 1960

9. Blackburn, J. F. et al Fluid Power Control
Cambridge, Mass: M.I.T. Press, 1960
10. "Short Cut for Holding Magnet Design" Form 371,
Indiana General Corp., Magnet Division,
Valparaiso, Ind., n.d.
11. "Design and Application of Permanent Magnets"
Manual 7, Indiana General Corp., Magnet
Division, Valparaiso, Ind., n.d.
12. "Indox Ceramic Permanent Magnets" Manual 8,
Indiana General Corp., Magnet Division,
Valparaiso, Ind., n.d.
13. Hammond, P. Electromagnetism for Engineers
New York: MacMillan Co., 1964
14. Plonsey, R. and Collin, R. E. Principles and
Applications of Electromagnetic Fields
New York: McGraw-Hill, 1961
15. Boast, W. B. Vector Fields New York: Harper
& Row, 1964
16. Spreadbury, F. G. Permanent Magnets London:
Sir Isaac Pitman & Sons, Ltd., 1949

APPENDIX A

Introduction

This appendix contains an abbreviated version of an analysis of the dynamic behavior of a vertical suspension type simulator. The system to be analysed is shown in Figure A1.

The system components consist of one magnetic air pad, a back-to-back negator spring assembly and the subject mass. The subject mass will be considered to be inanimate. The negator spring assembly housing is attached to the air pad by a ball joint. If the system is confined to move in a plane perpendicular to the ceiling, its position can be defined by three generalized coordinates; namely, the position of the air pad center of gravity, the angle between the extended negator springs and the vertical, and the distance from the ball joint to the subject mass. An important assumption must be made, however, before these three coordinates can correctly determine the position of the system. This is that the extended portion of the negator spring does not bend in the plane of motion. This is probably a valid assumption for the orientation of the negator springs shown in Figure A1.*

* Note that the width of the negator spring is parallel to the plane of motion.

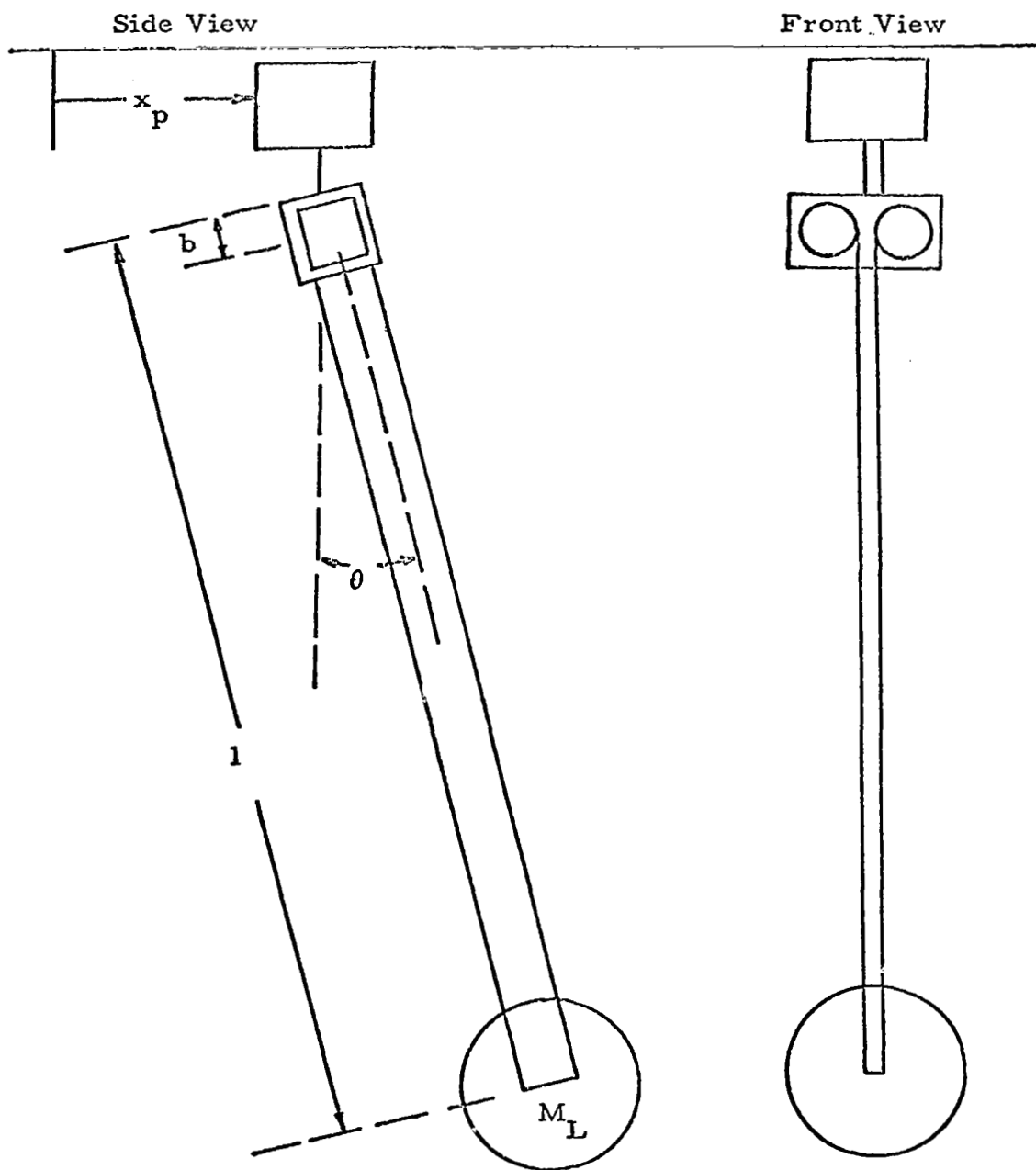


Figure A1
Lunar Gravity Simulator Model

If, however, the negator spring assembly were rotated through 90 degrees, the width of the negator springs would be perpendicular to the plane of motion. Due to the very low rigidity of the negator springs in this direction, the assumption would no longer apply and the three coordinates would not suffice in locating the system.

The following are the assumptions which will be made in the derivation of the dynamic equations:

1. The extended portion of the negator spring is rigid and inextensible.
2. The air pad moves with negligible friction.
3. The up-and-down dynamics of the air pad are so small that they can be neglected.
4. The ball joint has negligible friction.
5. The air drag on the system is negligible.
6. The motion of the system is planar.
7. The negator spring system has a constant force for any elongation.

The parameters used in the analysis are defined as follows:

- | | |
|----------|--|
| x_p | Location of the center of gravity of the air pad. |
| θ | Angle that the extended portion of the negator spring makes with the vertical. |
| l | The distance from the ball joint to the center of gravity of the subject mass. |
| a | The distance from the center of gravity of the air pad to the ball joint. |

b	The distance from the ball joint to the center of gravity of the negator spring spools and housing.
r_s	Radius of a negator spring spool.
R	Radius of the coiled portion of negator spring.
W	Width of the negator spring.
t	Thickness of the negator spring.
L	Total length of a negator spring.
D_{cg}	The center of gravity of the system of masses suspended from the ball joint measured from that point.
λ	A distance parallel to any point on the extended portion of the negator spring.
x	Horizontal distance from a reference point.
y	Vertical distance from a reference point.
M_L	Mass of the subject.
M_p	Mass of the air pad.
M_h	Mass of the negator spring housing.
M_s	Mass of a negator spring spool containing bearings.
M_e	Mass of the extended portion of one negator spring.
M_c	Mass of the coiled portion of one negator spring.
ρ	The density of the negator spring material.
I_{s0}	Moment of inertia of one spool about the ball joint.
I_{c0}	Moment of inertia of the coiled portion of one negator spring about the ball joint.
I_{h0}	Moment of inertia of the negator spring housing about the ball joint.
I_{sa}	Moment of inertia of one spool about its axis of rotation.

I_c	Moment of inertia of the coiled portion of one negator spring about the axis of rotation.
F	The force output of both negator springs.
T	The kinetic energy of the system.
Q	A generalized force.
D_m	Damping coefficient.
τ	A torque.
τ_f	Coulomb bearing friction torque.

Kinetic Energy of the Extended Portions of Negator Springs

With reference to Figure A1, the position of any element of mass along the extended portion of the negator spring can be written

$$\begin{aligned}x &= x_p + \lambda \sin(\theta) \\ y &= a - \lambda \cos(\theta) .\end{aligned}$$

The component velocities of any element of mass can be found by differentiating the above positions with respect to time.

$$\begin{aligned}\dot{x}_\lambda &= \dot{x}_p + \dot{\lambda} \sin(\theta) + \lambda \dot{\theta} \cos(\theta) \\ \dot{y}_\lambda &= \dot{\lambda} \cos(\theta) + \lambda \dot{\theta} \sin(\theta)\end{aligned}$$

The kinetic energy of the extended portions of both negator springs can be written as

$$T_e = \rho w t \int_b^1 (\dot{x}_\lambda^2 + \dot{y}_\lambda^2) d\lambda \quad .$$

Upon substitution of the squares of the component velocities into the above expression, the kinetic energy can be written

$$T_e = \rho w t \int_b^1 (\dot{x}_p^2 + \dot{\lambda}^2 + \lambda^2 \dot{\theta}^2 + 2\dot{x}_p \lambda \sin(\theta) + 2\dot{x}_p \lambda \dot{\theta} \cos(\theta)) d\lambda \quad .$$

It should be noted that $\dot{\lambda}$ is a constant over the integration which takes place at any instant of time. In addition, $\dot{\lambda}$ must be equal to \dot{l} due to physical constraint. Upon completing the integration and making the above-mentioned substitution, the kinetic energy of the extended portion of both negator springs can be expressed as follows:

$$T_e = \rho w t \{ [\dot{x}_p^2 + \dot{l}^2 + 2\dot{x}_p \dot{l} \sin(\theta)] [1 - b] + \frac{\dot{\theta}^2}{3} [1^3 - b^3] + \dot{x}_p \dot{\theta} \cos(\theta) [1^2 - b^2] \} \quad .$$

Kinetic Energy of the Subject Mass

For the sake of simplicity, the mass M_L will be assumed concentrated at a point. The coordinates of this point are

$$x_L = x_p + l \sin(\theta)$$

$$y_L = -a - l \cos(\theta)$$

$$\dot{x}_L = \dot{x}_p + l \dot{\theta} \sin(\theta) + l \ddot{\theta} \cos(\theta)$$

$$\dot{y}_L = -\dot{x}_p \cos(\theta) + l \ddot{\theta} \sin(\theta) \quad .$$

The kinetic energy of the mass can be written

$$T_L = \frac{1}{2} M_L (\dot{x}_L^2 + \dot{y}_L^2) \quad .$$

Upon making the appropriate substitutions, the kinetic energy of the subject mass is

$$\begin{aligned} T_L = \frac{1}{2} M_L (\dot{x}_p^2 + \dot{l}^2 + l^2 \dot{\theta}^2 + 2 \dot{x}_p \dot{l} \sin(\theta) \\ + 2 \dot{x}_p l \ddot{\theta} \cos(\theta)) \quad . \end{aligned}$$

Kinetic Energy of the Negator Spring Housing

The coordinates of the center of gravity of the negator spring housing are

$$x_h = x_p + b \sin(\theta)$$

$$y_h = -a - b \cos(\theta) \quad .$$

The velocities are

$$\dot{x}_h = \dot{x}_p + b \ddot{\theta} \cos(\theta)$$

$$\dot{y}_h = b \ddot{\theta} \sin(\theta) \quad .$$

The kinetic energy of the housing can then be written
as

$$T_h = \frac{1}{2} M_h (\dot{x}_p^2 + b^2 \dot{\theta}^2 + 2 \dot{x}_p b \dot{\theta} \cos(\theta)) + \frac{1}{2} I_{hcg} \dot{\theta}^2 .$$

Using the parallel axis theorem, the moment of inertia of the housing about the ball joint is

$$I_{h\theta} = I_{hcg} + M_h b^2 .$$

Substituting this equation into the expression for kinetic energy yields the following:

$$T_h = \frac{1}{2} M_h (\dot{x}_p^2 + 2 \dot{x}_p b \dot{\theta} \cos(\theta)) + \frac{1}{2} I_{h\theta} \dot{\theta}^2 .$$

Kinetic Energy of Both Negator Spring Spools

The coordinates of the center of gravity of the two-spool combination are

$$x_s = x_p + b \sin(\theta)$$

$$y_s = -a - b \cos(\theta) .$$

The corresponding velocities of this center of mass are

$$\dot{x}_s = \dot{x}_p + b \dot{\theta} \cos(\theta)$$

$$\dot{y}_s = b \dot{\theta} \sin(\theta) .$$

The spools rotate with an angular velocity $\dot{\alpha}$. This angular velocity is a function of both \dot{l} and l , and can be

expressed as

$$\dot{\alpha} = \frac{\dot{l}}{R} \quad R = \sqrt{\frac{t}{\pi}(L + b - l) + r_s^2}$$

where R is the variable radius of a coil. The expression for R is derived in the next section.

Solving for the kinetic energy due to translation of the center of mass plus that due to rotation about the center of mass gives

$$T_s = M_s \left[\dot{x}_p^2 + 2 \dot{x}_p b \dot{\theta} \cos(\theta) \right] + I_{s0} \dot{\theta}^2 + I_s \alpha \frac{\dot{l}^2}{\left[\frac{t}{\pi}(L + b - l) + r_s^2 \right]} .$$

Kinetic Energy of the Coiled Portions of Both Negator Springs

The coordinates of the center of mass of the coil are

$$x_c = x_p + b \sin(\theta)$$

$$y_c = -a - b \cos(\theta) .$$

It should be noted that these coordinates are not a function of the variable l .

The velocities of the center of mass are

$$\dot{x}_c = \dot{x}_p + b \dot{\theta} \cos(\theta)$$

$$\dot{y}_c = b \dot{\theta} \sin(\theta) .$$

The kinetic energy of the coil can be expressed as

$$T_c = M_c (\dot{x}_p + 2\dot{x}_p b \dot{\theta} \cos(\theta)) + I_{c\theta} \dot{\theta}^2 + I_{ac} \frac{\dot{l}^2}{R^2} .$$

The parameters M_c , $I_{c\theta}$, and I_{ac} are functions of the distance l . It can be easily seen that the mass of one coil is

$$M_c = \rho w t (L + b - l) .$$

The radius of the coil can be found from the evaluation of the following integral:

$$\int_{r_s}^R r dr = \int_0^C \frac{t}{2\pi} ds .$$

Where C is the length of the coiled negator spring and ds is an element of arc length:

$$C = L + b - l .$$

Upon evaluation of the above integral, R is found:

$$R = \sqrt{\frac{t}{\pi} (L + b - l) + r_s^2} .$$

The moment of inertia of one coil about its cylindrical axis is

$$I_{ac} = \frac{\pi}{2} \rho w [R^4 - r_s^4] .$$

The moment of inertia of a coil about an axis perpendicular to the axis of symmetry through the ball joint is

$$I_{\theta c} = m_c \left[\frac{(R^2 - r_s^2)}{4} + \frac{w^2}{12} + b^2 \right]$$

Making the appropriate substitutions, the kinetic energy of both coils is found.

$$\begin{aligned}
 T_c = & \rho w t (L + b - 1) (\dot{x}_p^2 + 2 \dot{x}_p b \dot{\theta} \cos(\theta) \\
 & + \rho w t (L + b - 1) \left[\frac{t}{4\pi} (L + b - 1) + \frac{W^2}{12} + b^2 \right] \dot{\theta}^2 \\
 & + \frac{1}{2} \rho w t (L + b - 1) \frac{\left[\frac{t}{\pi} (L + b - 1) + 2r_s^2 \right] \dot{l}^2}{\left[\frac{t}{\pi} (L + b - 1) + r_s^2 \right]} .
 \end{aligned}$$

Kinetic Energy of the Air Pad

The kinetic energy of the air pad can be simply expressed by

$$T_p = \frac{1}{2} m_p \dot{x}_p^2 .$$

Kinetic Energy of the System

The kinetic energy of the system is the summation of the kinetic energies of the component masses:

$$T = T_e + T_l + T_h + T_s + T_c + T_p .$$

Generalized Forces

Because of the negligible air drag assumption, the generalized force due to a variation in x_b is

$$Q_{x_b} = 0 \quad .$$

Using the assumptions of negligible air drag and friction in the ball joint, the generalized force due to the variation of θ is

$$Q_\theta = -g(M_L + M_h + 2M_g + 2M_c + 2M_e)D_{cg} \sin(\theta) \quad .$$

Where D_{cg} is the center of mass of the system suspended below the ball joint.

$$D_{cg} = \frac{b(2M_s + M_h) + 1M_L + 2\rho wtbL + \rho wt(1-b)^2}{M_L + M_h + 2M_s + 2M_c + 2M_e}$$

Q_θ can now be expressed as

$$Q_\theta = -g[b(2M_s + M_h) + 1M_L + 2\rho wtbL + \rho wt(1-b)^2] \sin(\theta) \quad .$$

In calculating the generalized force due to a variation in l , the frictional torque in the bearings of one negator spring spool is assumed to be of the form

$$\tau = -(D_m \dot{\alpha} + \frac{\dot{\alpha}}{|\dot{\alpha}|} \tau_f) \quad .$$

The frictional torque contains a viscous friction term and a coulomb friction term. It will be assumed that these are independent of the load applied to the bearing because the variation in the bearing load should be small.

The frictional force due to this torque can be written
 $f = \frac{2\pi}{R}$ making the substitution $\dot{\alpha} = \frac{\dot{l}}{R}$.

The frictional force due to the bearings in the spools is

$$f = -2(D_m \frac{\dot{l}}{R^2} + \frac{\dot{l}}{|\dot{l}|} \frac{\tau_f}{R}) .$$

The generalized force due to a variation in l is

$$Q_1 = (2M_e + M_1)g \cos(\theta) - 2(D_m \frac{\dot{l}}{R^2} + \frac{\dot{l}}{|\dot{l}|} \tau_f) - F .$$

Substituting the expressions for M_e and R into the above equation, Q_1 is found in terms of the generalized coordinates.

$$Q_1 = [2\rho w t(1-b) + M_L]g \cos(\theta) - \frac{2[D_m \dot{l} + \frac{\dot{l}}{|\dot{l}|} \tau_f \sqrt{\frac{t}{\pi} (L+b-1) + r_s^2}]}{\frac{t}{\pi} (L+b-1) + r_s^2} - F$$

Derivation of Dynamic Equations

Using the method of Lagrange, three dynamic equations will be derived. There will be one equation for each generalized coordinate or degree of freedom.

The first equation of motion for the system is

$$\frac{d}{dt} \left(\frac{\partial T}{\partial \dot{x}_p} \right) - \frac{\partial T}{\partial x_p} = Q_{xp}$$

$$\frac{\partial T}{\partial x} = 0 = Q_{xp} .$$

Then
$$\frac{d}{dt} \left(\frac{\partial T}{\partial \dot{x}_p} \right) = 0 \quad .$$

It is seen that the coordinate x_p can be ignored from the standpoint of the dynamics of the system. Furthermore, the above equation is immediately integrable and has the form

$$\frac{\partial T}{\partial \dot{x}_p} = \text{const.}$$

Since the quantity $\frac{\partial T}{\partial \dot{x}_p}$ is the momentum associated with the coordinate \dot{x}_p , the previous equation is a statement of conservation of momentum in the x_p direction.

Carrying out the required differentiation, this equation becomes

$$\begin{aligned} & (M_p + M_h + 2M_s + 2\rho w t L + M_L) \ddot{x}_p + (M_h + 2M_s + 2\rho w t L) b \ddot{\theta} \cos(\theta) \\ & + M_L [\dot{l} \sin(\theta) + l \ddot{\theta} \cos(\theta) + \rho w t [(1-b)^2 \ddot{\theta} \cos(\theta) \\ & + 2(1-b) \dot{l} \sin(\theta)]] = \text{const.} \end{aligned}$$

The second equation of motion for the system is

$$\frac{d}{dt} \left(\frac{\partial T}{\partial \dot{\theta}} \right) - \frac{\partial T}{\partial \theta} = Q_\theta \quad .$$

Performing the required differentiations yields:

$$\begin{aligned}
& \ddot{\theta} \left[\frac{2}{3} \rho w t (l^3 - b^3) + M_L l^2 + I_{h\theta} + 2I_{s\theta} + \rho w t (L+b-l) \left(\frac{t}{4\pi} (L+b-l) + \frac{r_s^2}{2} + \frac{w^2}{12} + b^2 \right) \right] \\
& + \dot{\theta} \left[2\rho w t l^2 + 2M_L l - 2\rho w t \left(\frac{t}{2\pi} (L+b-l) + \frac{r_s^2}{2} + \frac{w^2}{12} + b^2 \right) \right] \\
& + \ddot{x}_p [\rho w t \cos(\theta) (l^2 - b^2) + M_L l \cos(\theta) + 2b \cos(\theta) \\
& \left(\frac{1}{2} M_h + M_s + \rho w t (L+b-l) \right)] + g [b (2M_s + M_L) + l M_L + 2\rho w t b L + \rho w t (l-b)^2] \\
& \sin(\theta) = 0
\end{aligned}$$

The third equation of motion for the system is

$$\frac{d}{dt} \left(\frac{\partial T}{\partial \dot{l}} \right) - \frac{\partial T}{\partial l} = Q_l$$

The evaluation of this equation yields:

$$\begin{aligned}
& \ddot{l} \left\{ 2\rho w t (l-b) + M_L + \frac{2I_{sa} + \rho w t (L+b-l) \left[\frac{t}{\pi} (L+b-l) + 2r_s^2 \right]}{\frac{t}{\pi} (L+b-l) + r_s^2} \right\} \\
& + \ddot{x}_p [2\rho w t \sin(\theta) (l-b) + M_L \sin(\theta)] \\
& + \frac{t}{\pi} \dot{l}^2 \left\{ \frac{I_{sa} + \frac{1}{2} \rho w t (L+b-l) \left[\frac{t}{\pi} (L+b-l) + 2r_s^2 \right]}{\left[\frac{t}{\pi} (L+b-l) + r_s^2 \right]^2} \right\} \\
& + \dot{\theta}^2 \left\{ \rho w t \left[\frac{t}{2\pi} (L+b-l) + \frac{w^2}{12} + \frac{r_s^2}{2} + b^2 \right] - \rho w t l^2 - M_L l \right\} \\
& = [2\rho w t (l-b) + M_L] g \cos(\theta) - F - \frac{2[D_m \dot{l} + \tau_f \operatorname{sgn}(\dot{l})] \sqrt{\frac{t}{\pi} (L+b-l) + r_s^2}}{\frac{t}{\pi} (L+b-l) + r_s^2}
\end{aligned}$$

APPENDIX B

```

A LST
A FOR MAPS
C   MAG AIR PAD SUPER SONIC SUBSONIC FLOW
   DIMENSION R(10000),P(10000),F(6000),DER1(2000),DER1I(4000),
   IREN(10000),GAP(20)
   1 FORMAT( )
   9 FORMAT(3X 41H THE FIRST DO LOOP RANGE HAS BEEN EXCEEDED )
  10 FORMAT(3X 42H THE SECOND DO LOOP RANGE HAS BEEN EXCEEDED)
  11 FORMAT(14X 3HURF9X3HUR09X3HUP010X2HCD9X4HSCFM8X4H(LAM8X4HRRBAR)
  12 FORMAT(10X7E12.6)
  13 FORMAT(13X6HUPSTAR6X6HURHOST6X5HCSTAR7X4HUGAP8X5HFORCE)
  14 FORMAT(10X5E12.6)
  15 FORMAT(17X1HR10X1HP9X1HF6X4HDER18X3HREN)
  16 FORMAT(3X16.5E10.5)
  17 FORMAT(17X1HR10X1HP9X1HF6X5HDER119X3HREN)
  18 FORMAT(3X16.5E10.5)
  19 FORMAT(41H*****. SHOCK WAVE *****)
  20 FORMAT(17X1HR10X1HP9X3HREN)
  21 FORMAT(3X16.3E10.5)
  24 FORMAT(40H*****)
  25 FORMAT(2X 11HSTEP IN GAP)
  26 FORMAT(2X39H THE FLOW IS NO LONGER CHOKED AT ANNULUS)
  33 FORMAT(2X 32H THE FLOW AT THE ANNULUS IS SONIC)
  30 FORMAT(2X 35H THE FLOW AT THE ANNULUS IS SUBSONIC)
  31 FORMAT(15X 3HP11 9X 3HUMI 7X 4HRRHO1 9X 4HUGAP 7X 5HFORCE)
  32 FORMAT(10X 5E12.6)
C   SFI UP VALUES TO BE USED IN THIS PROGRAM
C   UP IN LB/IN2, URHO IN LB*SEC2/IN4, VI IN LB*SEC/IN2, GFLOW IN
C   LB*SEC/IN, CSTAR IN IN/SEC
   READ(5,1)(URF,URO,UPO,CD)
   GAP(1)=0.002
   GAP(2)=0.003
   CC=7.65E-9
   VI=2.58E-9
   URHO0=UPO*CC
   UPA=14.7
   URHOA=1.145E-7
   PI=3.14159
   RRAR=URF/URO
   FFE=.0025
   G = 1.4
   R(1)=1.
   RR=1.0
   H=0.005
   H=.01
   SMALL = 0.00001
   A=(FF*G)/(G-1.)
   H=G-1.0
   D=G+1.0
   DO 240 K=1,2
   N=1
   UPSTAR=0.5283*UPO
   URHOST=0.6339*URHO0

```



```

CSTAR=SQRT((G*UPSTAR)/URHOST)
UMI=1.
DFL=.1
UGAP=GAP(K)
ICUND=1
CK=(24.*VI*URO*ALOG(URF/URO)*SQRT(G*UPA/URHOA))/(UGAP**2)
45 PT1=(UMI*CK+SQRT((UMI*CK)**2+4.*UPA**2))/2.
IF(UPSTAR.GT.PI1) GO TO 80
PI2=UP0/((1.+(R*UMI**2)/2.)*(G/H))
IF(AHS(PI1-PI2)-0.001) 178,178,48
48 IF(PI1-PI2) 60,178,50
50 UMI=UMI-DEL
GO TO 45
60 UMI=UMI+DEL
DFL=DEL/2.
GO TO 45
80 ULAM=URO*FF/UGAP
IF((URO/(2.0*UGAP)).LT.1.0) GO TO 250
GFLOW=2.0*3.1416*URO*UGAP*URHOST*CSTAR*CD
SCFM=(GFLOW*32.174*12.0*60.0)/(0.0753)
C=URO/UGAP
Q = (1.0 - A*B*C)
DER2 = 1.0/(R**2*D*Q)
DER3 = (-1.0)*(4.0*G)/(B**3*D**2*Q) + (2.0*A*C)/(B**2*D*Q**2)
DER4 = (24.0*G**2)/(B**4*D**3*Q) - (6.0)/(B**3*D**2*Q) -
1(12.0*G*A*C)/(B**3*D**2*Q**2) + (6.0*A**2*C**2)/(B**2*D*Q**3) +
2(3.0)/(B**4*D**2*Q**3)
C CALC R(1), R(2), R(3)
DO 100 N = 1,3
F(N) = G + N*H
R(N)=1.0+(DER2*(N*H)**2)/2.0+(DER3*(N*H)**3)/6.0
1+(DER4*(N*H)**4)/24.0
REN(N)=GFLOW/(2.0*PI*R(N)*VI*URO)
P(N) = (1.0/R(N))*SQRT((R*D)/(F(N)**2-1.0))
SL1=UPSTAR*(P(1)-1.0)/(URO*(R(1)-1.0))
E1=UPSTAR-SL1*URO
IF(N.EQ. 1)
1TF=2*3.1416*(SL1*URO**3*(R(1)**3-1.0)/3+E1*URO**2*(R(1)**2-1.0)/2)
IF(N.NE. 1)
1SI=UPSTAR*(P(N)-P(N-1))/(URO*(R(N)-R(N-1)))
IF(N.NE. 1)
1E=UPSTAR*P(N-1)-SL*URO*R(N-1)
IF(N.NE. 1)
1TF=2.0*3.1416*( SL*URO**3*(R(N)**3-R(N-1)**3)/3+
2E*URO**2*(R(N)**2-R(N-1)**2)/2.0)+TF
100 DER1(N) = (F(N)-G)/(R*(F(N)**2 - 1.0)*(1.0/R(N) -
1A*C*(F(N)- 1.0)))
C START ITERATIVE LOOPS
DO 130 N = 4,2000
F(N) = G + N*H
IF (N.EQ. 4)
1R1=RR+4*H*(2*DER1(1)-DER1(2)+2*DER1(3))/3
IF(N.NE. 4)
1R1=R(N-4)+4*H*(2*DER1(N-3)-DER1(N-2)+2*DER1(N-1))/3

```

```

110 DER1(N) = (F(N) - G)/(H*(F(N)**2 - 1.0)*(1.0/R1 - A*C*(F(N) - 1.0)))
1)
R2=R(N-2)+H*(DER1(N-2)+4*DER1(N-1)+DER1(N))/3
C TEST FOR CONVERGENCE
IF(ABS(R1-R2) .LT. SMALL) GO TO 120
R1=R2
GO TO 110
120 R(N)=R2
RFN(N)=GFLOW/(2.0*PI*R(N)*VI*URO)
P(N) = (1.0/R(N))*SQRT((B*D)/(F(N)**2-1.0))
SL=UPSTAR*(P(N)-P(N-1))/(URO*(R(N)-R(N-1)))
E=UPSTAR*P(N-1)-SL*URO*R(N-1)
TF=2.0*3.1416*( SL*URO**3*(R(N)**3-R(N-1)**3)/3+
1E*URO**2*(R(N)**2-R(N-1)**2)/2.0)+TF
SX =SQRT((F(N)-1.0)/B)
PY =P(N)*((2.0*G*SX **2)/(D-B/D)
SHOCK =((URHOA*UGAP**2*UPSTAR**2)/(24.0*VI*URO*UPA*
1SQRT(G*UPSTAR*URHOST)))*((PY **2-(UPA**2)/(UPSTAR**2))/ALOG(URF/
2(URO*R(N))))/CD
IF(SHOCK .LT. 1.0) GO TO 180
IF (DER1(N).GT.1.0) GO TO 140
130 CONTINUE
135 GO TO 210
140 M = N + 1
L = M - 1
DER1I(M-3)=1.0/DER1(M-3)
DER1I(M-2) = 1.0/DER1(M-2)
DER1I(M-1) = 1.0/DER1(M-1)
DO 170 N=M,10000
R(N) = R(M-1) + (N+1-M)*H
RFN(N)=GFLOW/(2.0*PI*R(N)*VI*URO)
F1 = F(N-4) + 4*H*(2*DER1I(N-3) - DER1I(N-2) + 2*DER1I(N-1))/3
150 DER1I(N) = (H*(F1**2-1.0)*(1.0/R(N) - A*C*(F1 - 1.0)))/(F1 - G)
F2 = F(N-2) + H*(DER1I(N-2)+ 4*DER1I(N-1) + DER1I(N))/3.0
C TEST FOR CONVERGENCE
IF(ABS(F1 - F2).LT.SMALL) GO TO 160
F1 = F2
GO TO 150
160 F(N) = F2
P(N) = (1.0/R(N))*(SQRT((B*D)/(F(N)**2-1.0)))
SL=UPSTAR*(P(N)-P(N-1))/(URO*(R(N)-R(N-1)))
E=UPSTAR*P(N-1)-SL*URO*R(N-1)
TF=2.0*3.1416*( SL*URO**3*(R(N)**3-R(N-1)**3)/3+
1E*URO**2*(R(N)**2-R(N-1)**2)/2.0)+TF
SX =SQRT((F(N)-1.0)/H)
PY =P(N)*((2.0*G*SX **2)/(D-B/D)
SHOCK =((URHOA*UGAP**2*UPSTAR**2)/(24.0*VI*URO*UPA*
1SQRT(G*UPSTAR*URHOST)))*((PY **2-(UPA**2)/(UPSTAR**2))/ALOG(URF/
2(URO*R(N))))/CD
IF(SHOCK .LT. 1.0) GO TO 180
170 CONTINUE
175 GO TO 220
178 PY=1.0
UPSTAR=P11

```

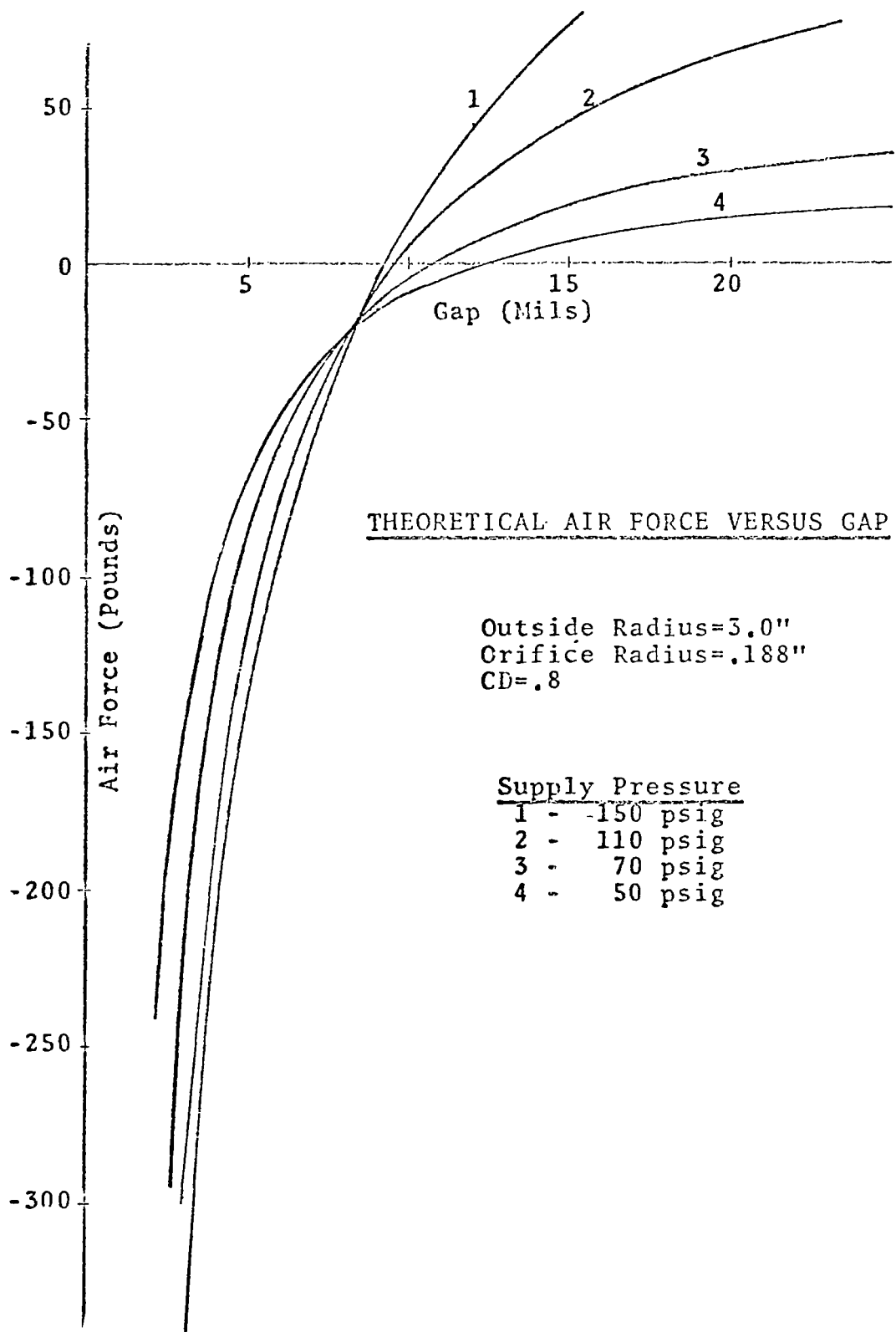
```

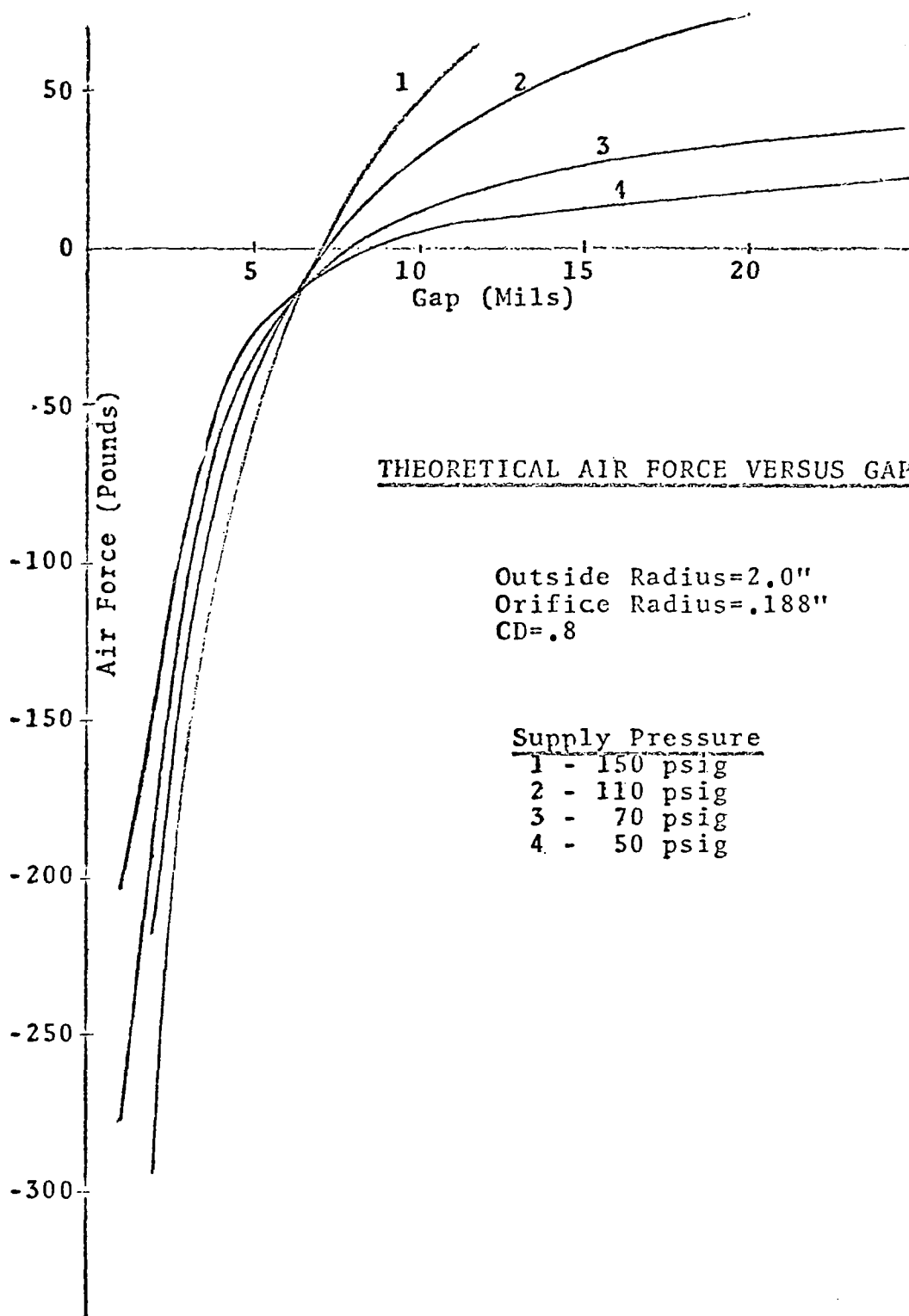
URHOST=URH00/((1.+(B*UMI**2)/2.))**(1./B))
GFLOW=2.*3.1416*(URO*UGAP*URHOST*UMI*SQR(T(G*PI1/URHOST))*CU
SCFM=(GFLOW*32.174*12.0*60.0)/(0.0753)
ICOND=2
180 NN = N
MM = NN+1
LL=MM-1
I=(URF/URO-R(LL))/H
J=LL+I
DO 190 N=MM,J
R(N)=R(LL)+(N+1-MM)*H
RFN(N)=GFLOW/(2.0*PI*R(N)*VI*URO)
P(N)=PY *SQR(1.0-(1.0-(UPA/(PY *UPSTAR))**2)*(ALOG(R(N)/R(L
1L))/ALOG(URF/(R(LL)*URO))))
SI=UPSTAR*(P(N)-P(N-1))/(URO*(R(N)-R(N-1)))
E=UPSTAR*P(N-1)-SI*URO*R(N-1)
190 TF=2.0*3.1416*( SL*URO**3*(R(N)**3-R(N-1)**3)/3+
1E*URO**2*(R(N)**2-R(N-1)**2)/2.0)+TF
200 GO TO 230
210 WRITE(6,9)
220 WRITE(6,10)
230 FORCE = TF + 3.1416*(URO**2*UPO - URF**2*UPA)
KK=L/10
JJ=(NN-L)/5
IT=(J-MM)/10
WRITE(6,11)
WRITE(6,12) (URF,URO,UPO,CD,SCFM,ULAM, RBAR)
IF(ICOND.EQ.2) GO TO 235
WRITE(6,33)
WRITE(6,13)
WRITE(6,14) (UPSTAR,URHOST,CSTAR,UGAP,FORCE)
WRITE(6,15)
WRITE(6,16) (N,R(N),P(N),F(N),DER1(N),REN(N),N=1,L,KK)
WRITE(6,18) (L,R(L),P(L),F(L),DER1(L),REN(L))
WRITE(6,17)
WRITE(6,18) (N,R(N),P(N),F(N),DER1(N),REN(N),N=M,NN,JJ)
WRITE(6,18) (NN,R(NN),P(NN),F(NN),DER1(NN),REN(NN))
WRITE(6,19)
GO TO 237
235 WRITE(6,30)
WRITE(6,31)
WRITE(6,32) (PI1,UMI,URHOST,UGAP,FORCE)
237 WRITE(6,20)
WRITE(6,21) (N,R(N),P(N),REN(N),N=MM,J,II)
WRITE(6,24)
240 WRITE(6,25)
GO TO 260
250 WRITE(6,26)
260 CONTINUE
END
FIN

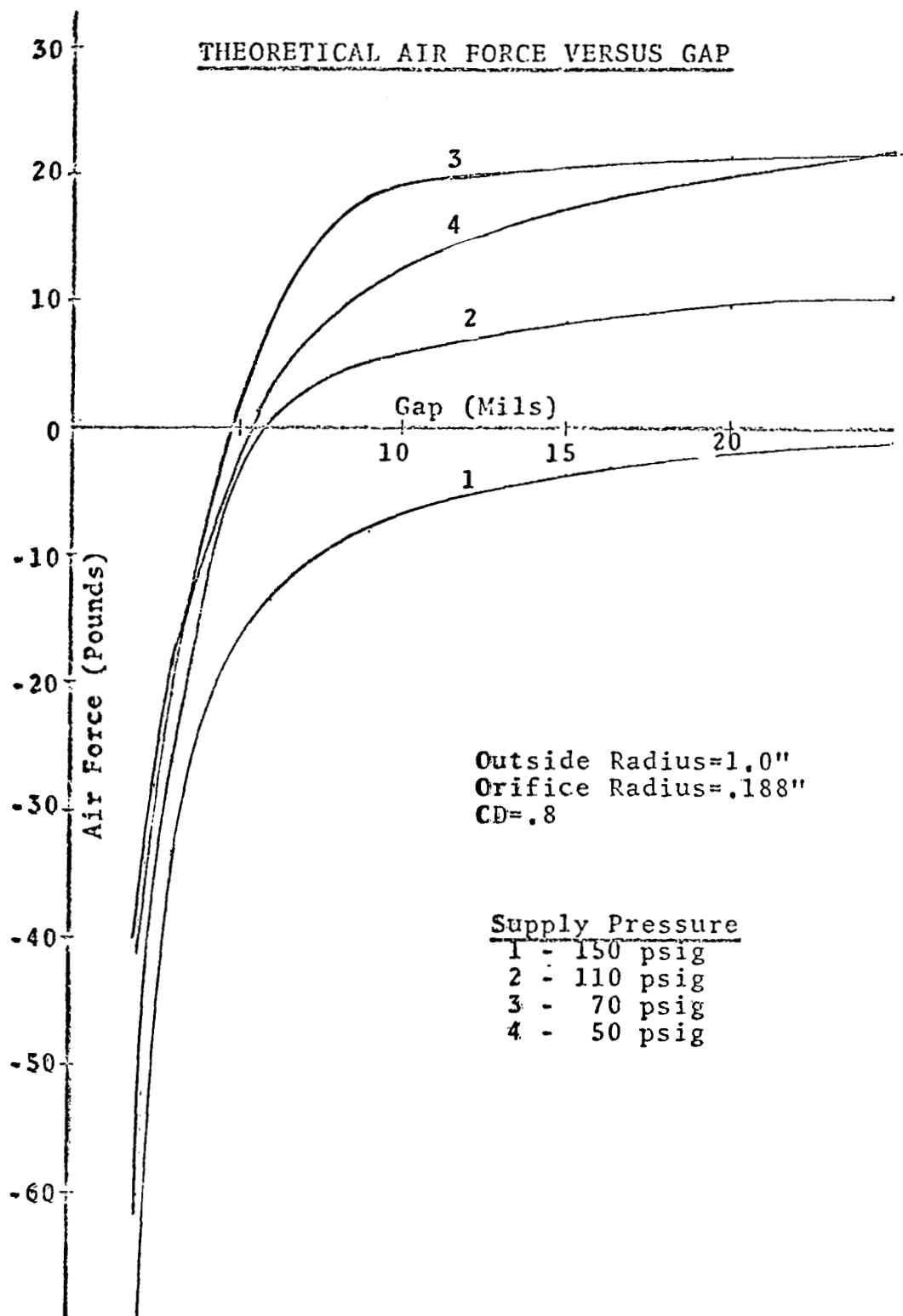
```

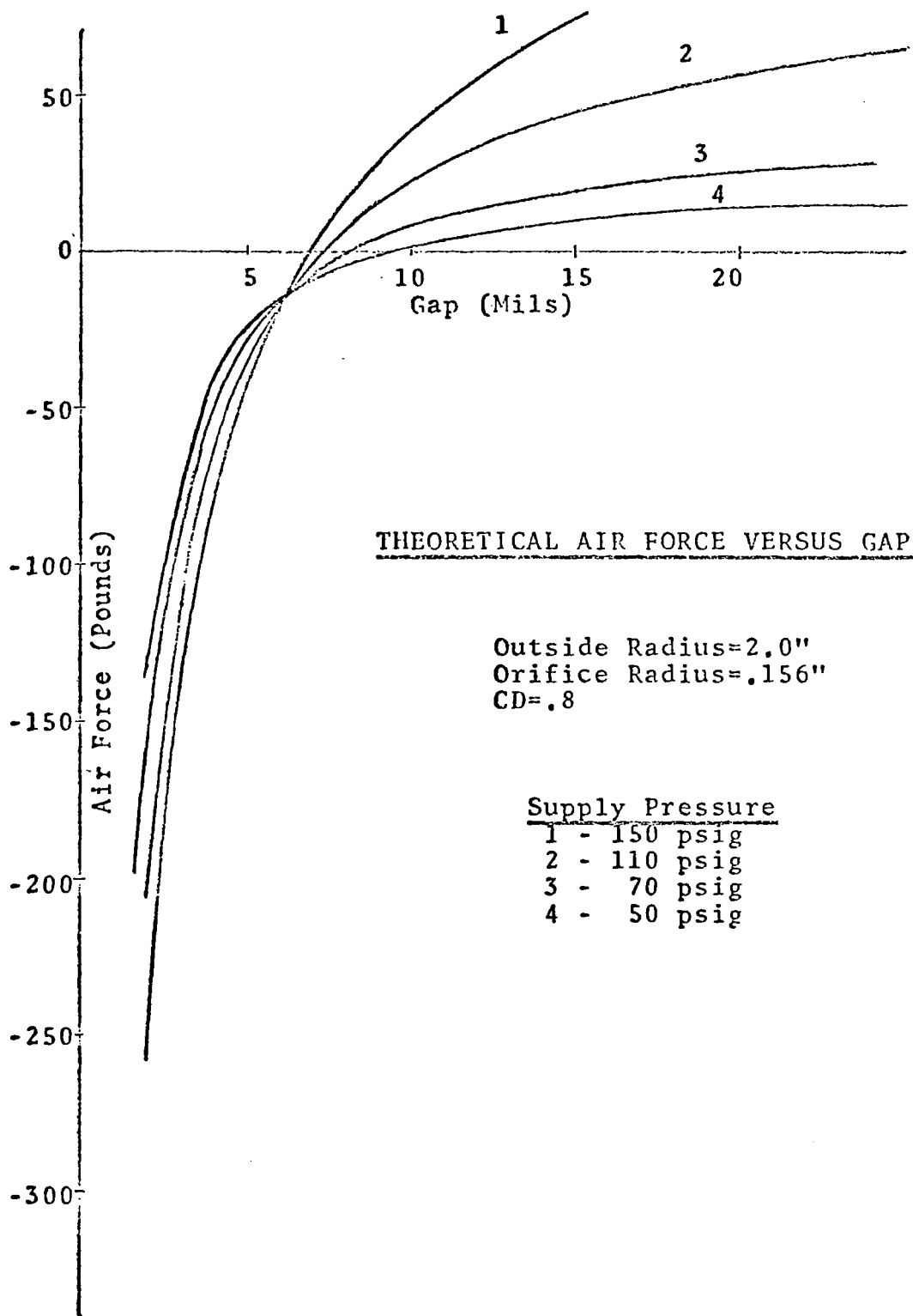
APPENDIX C

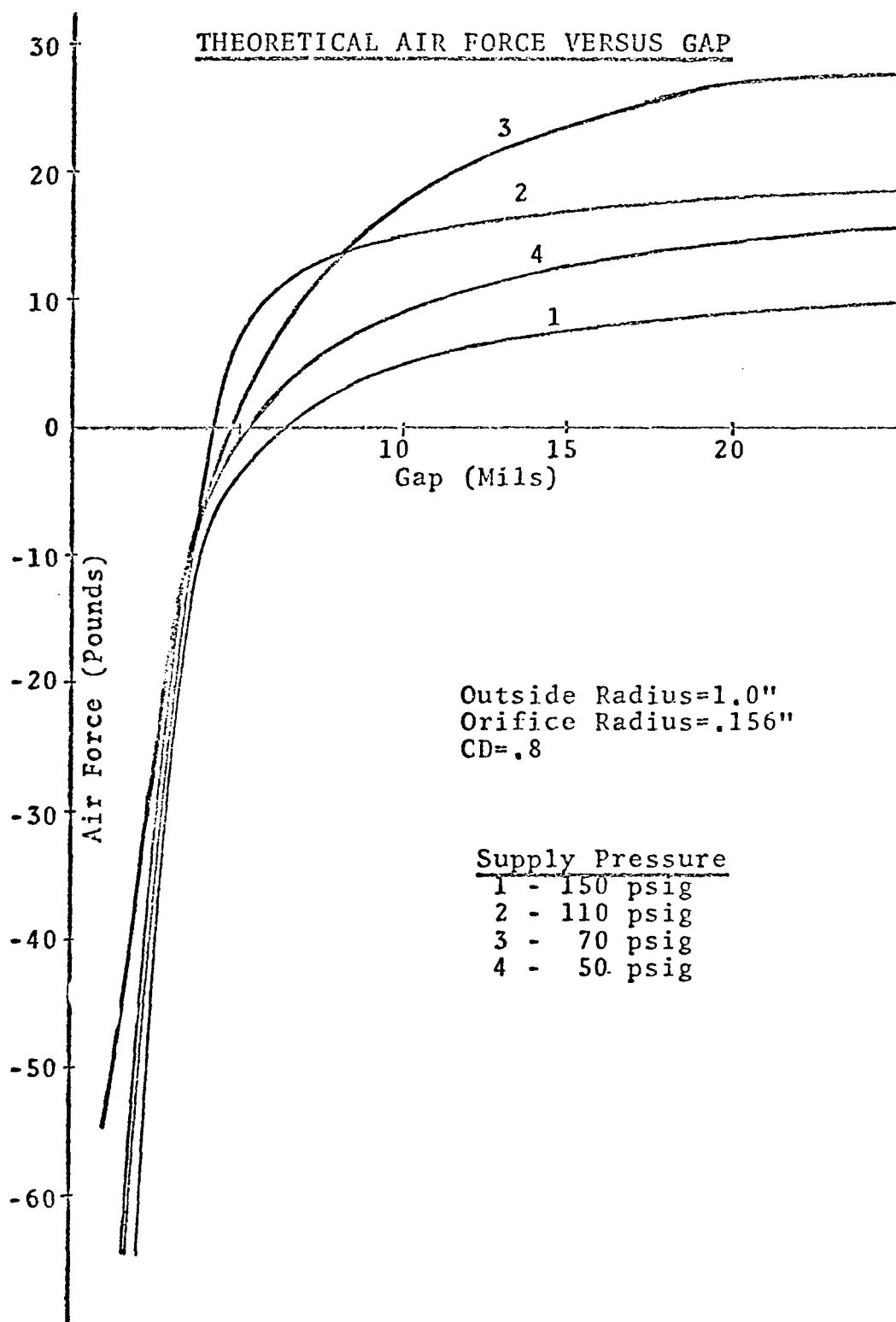
THEORETICAL AIR FORCE VERSUS GAP CHARACTERISTICS

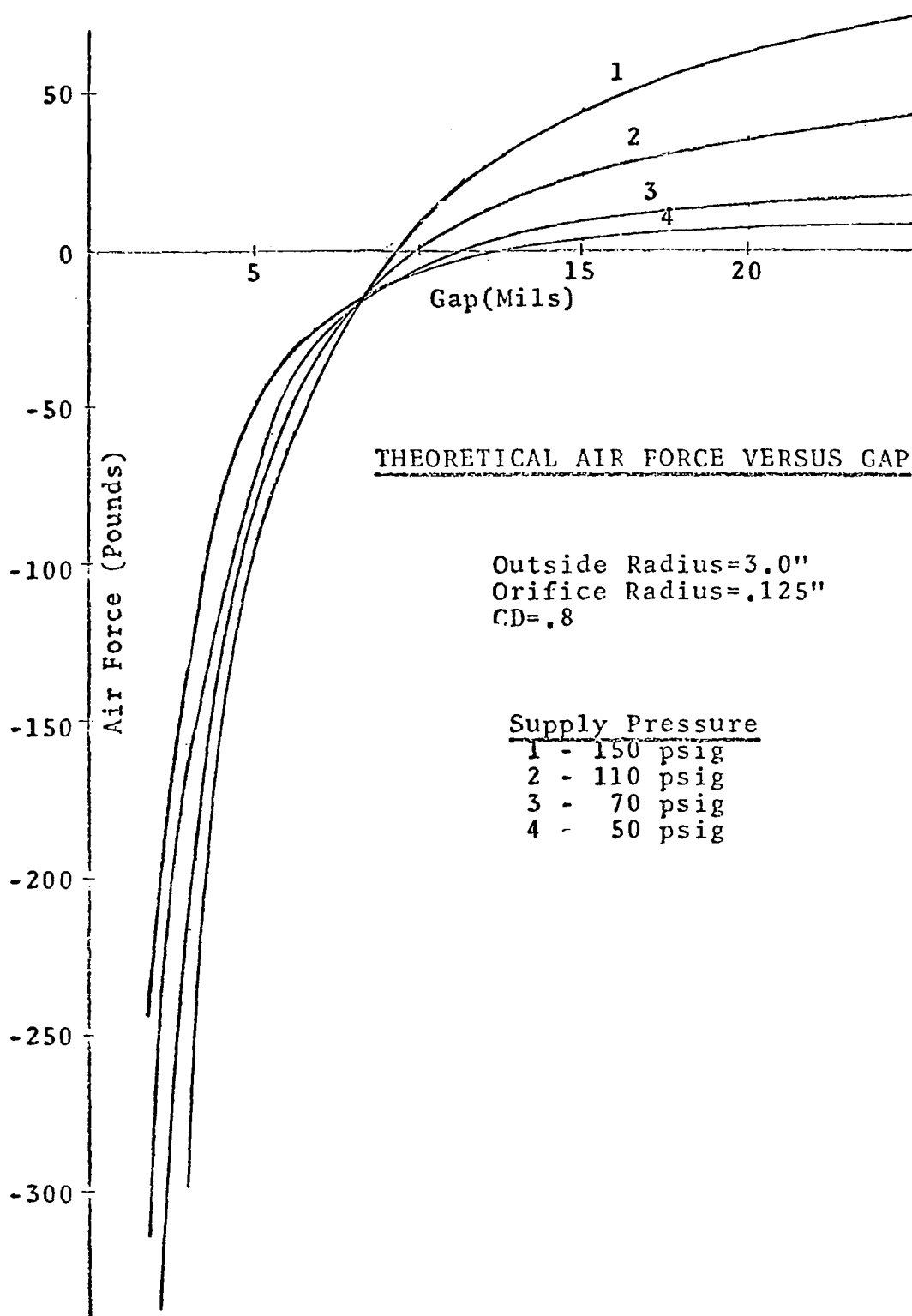


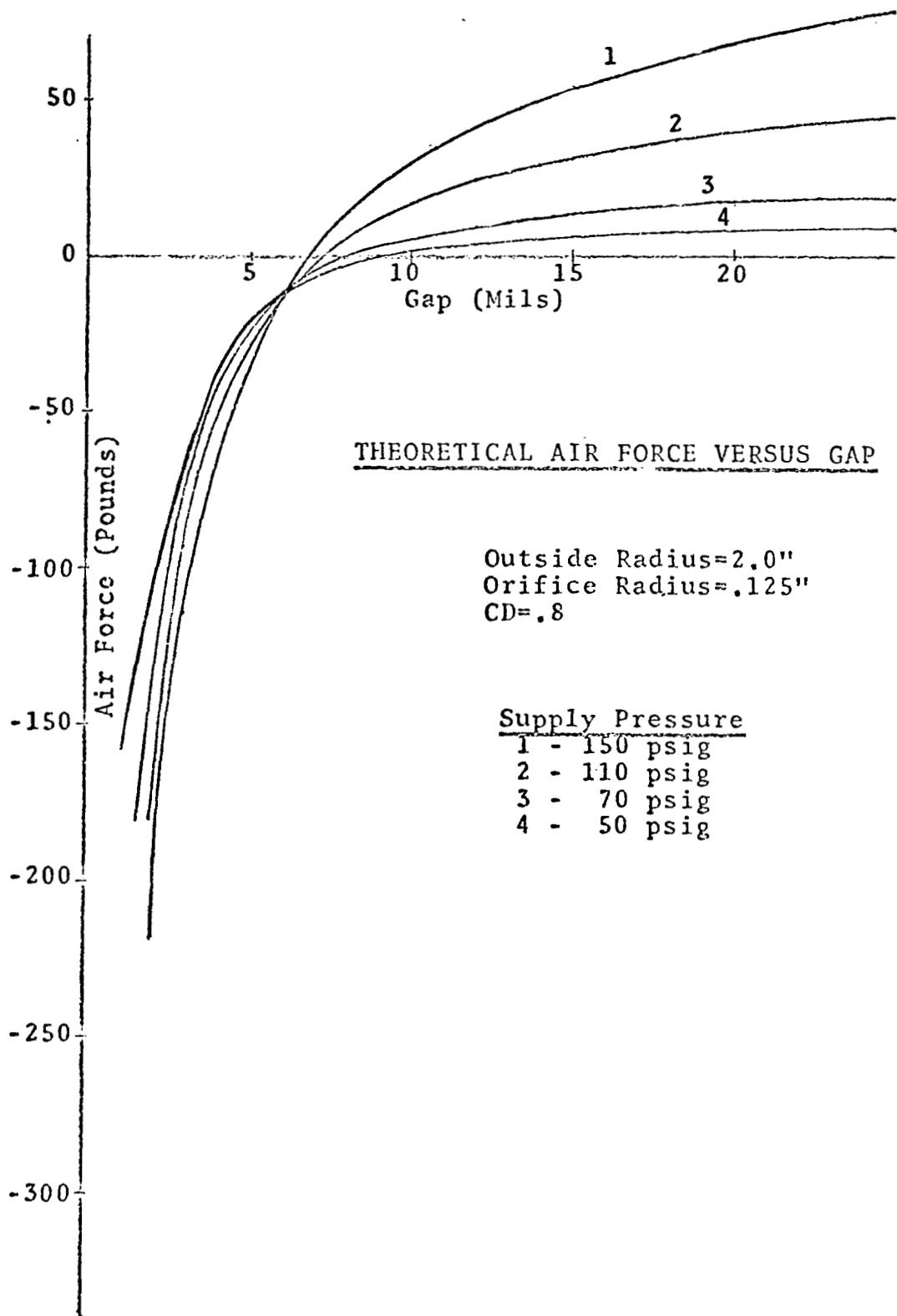


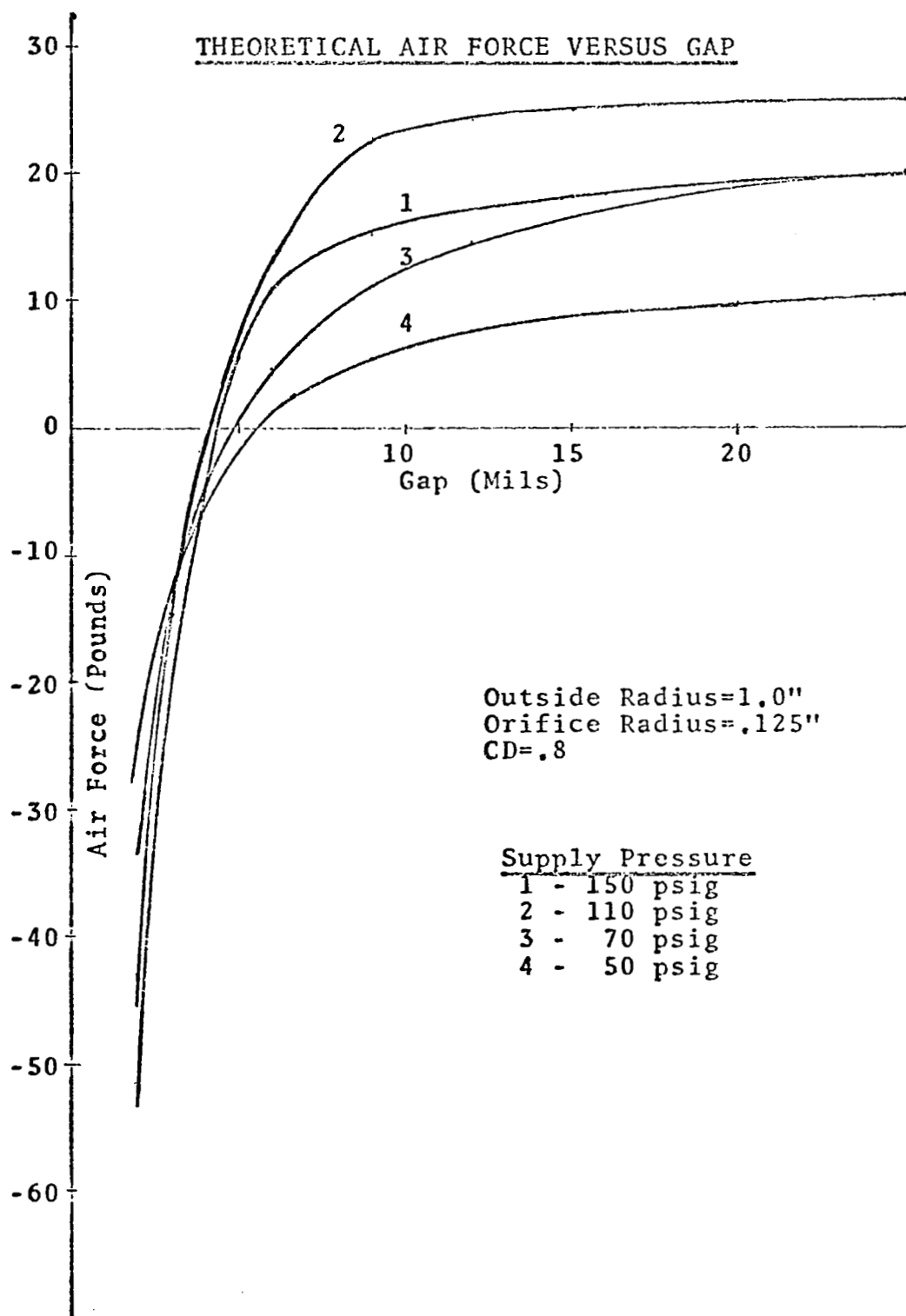


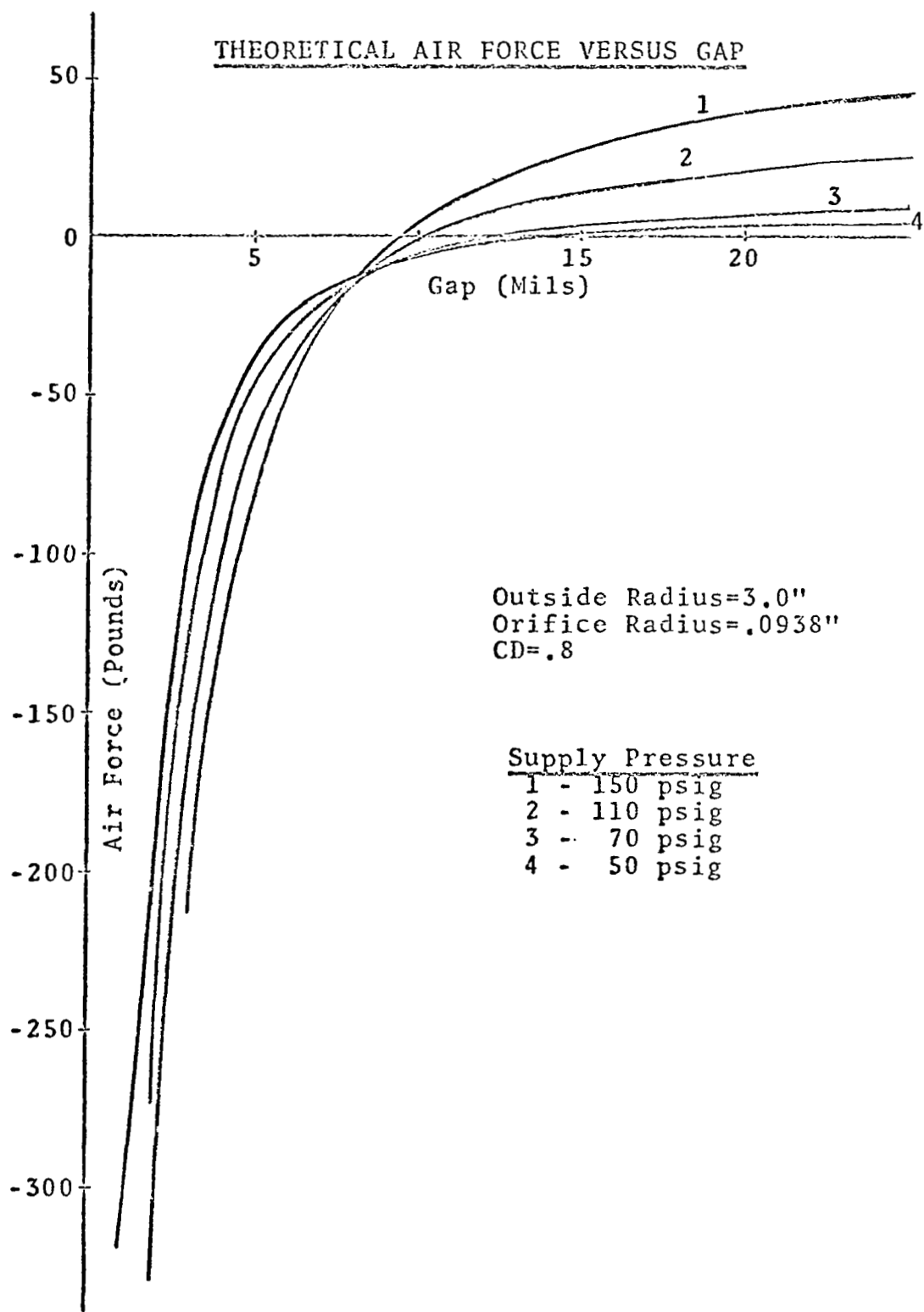


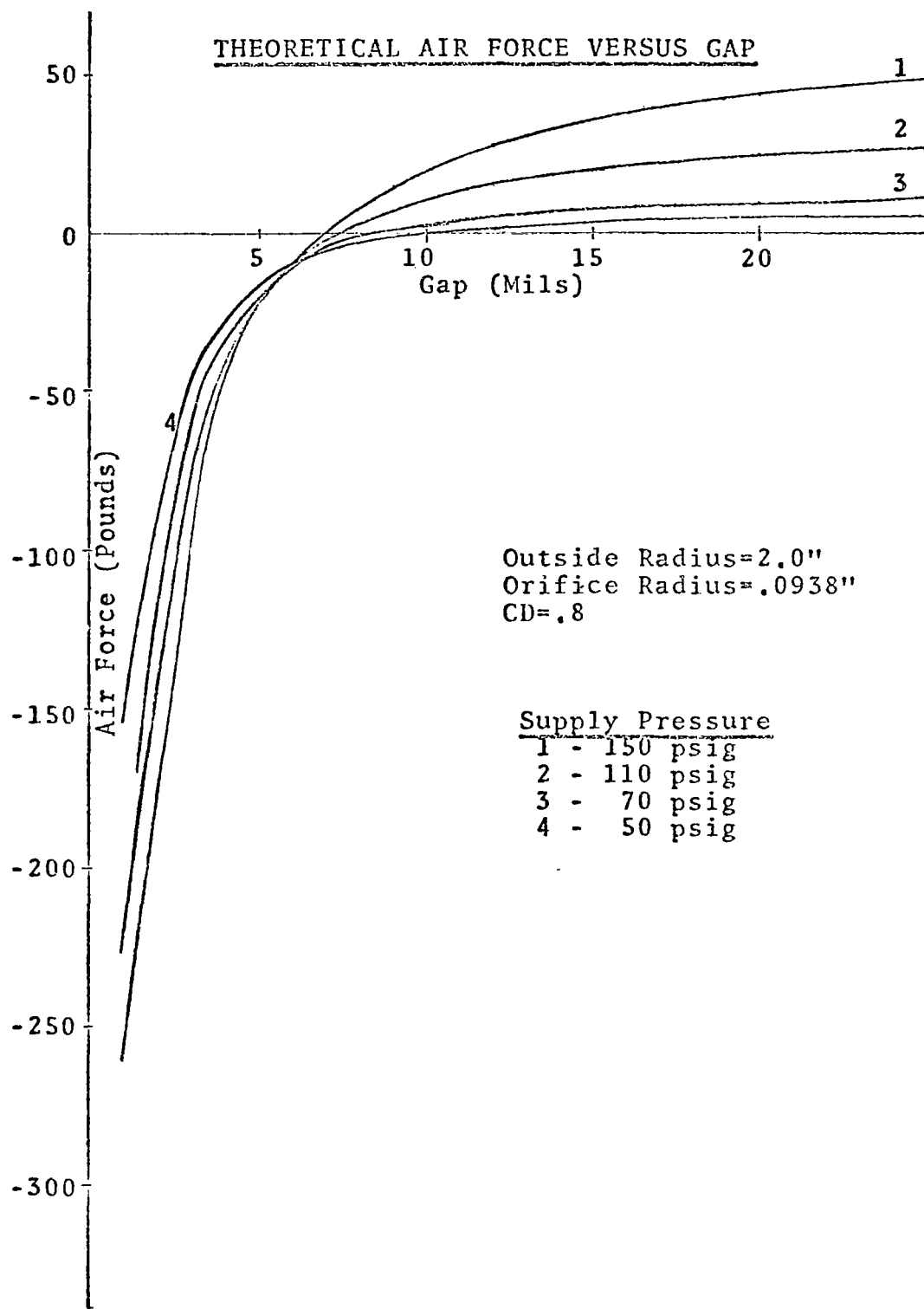


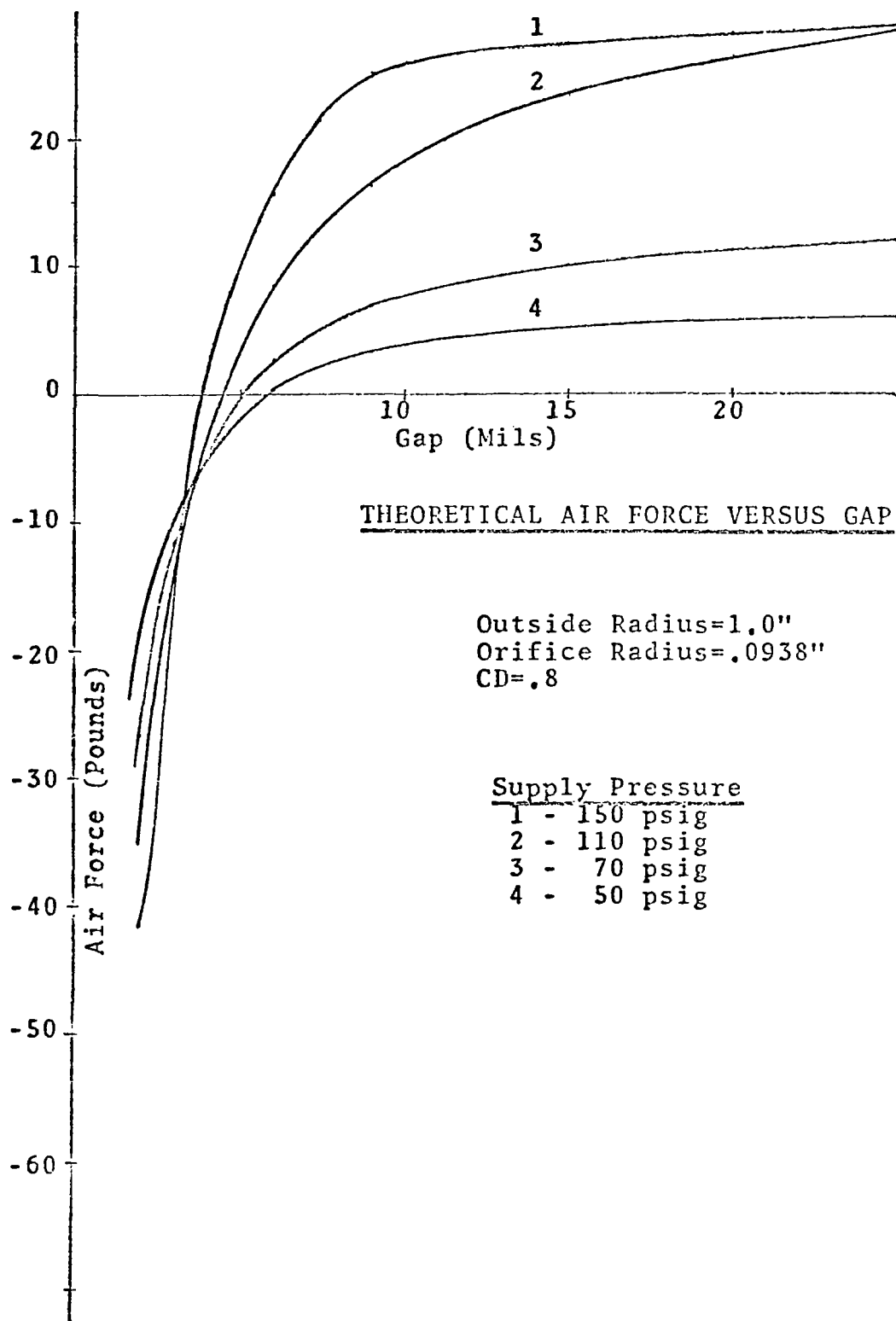




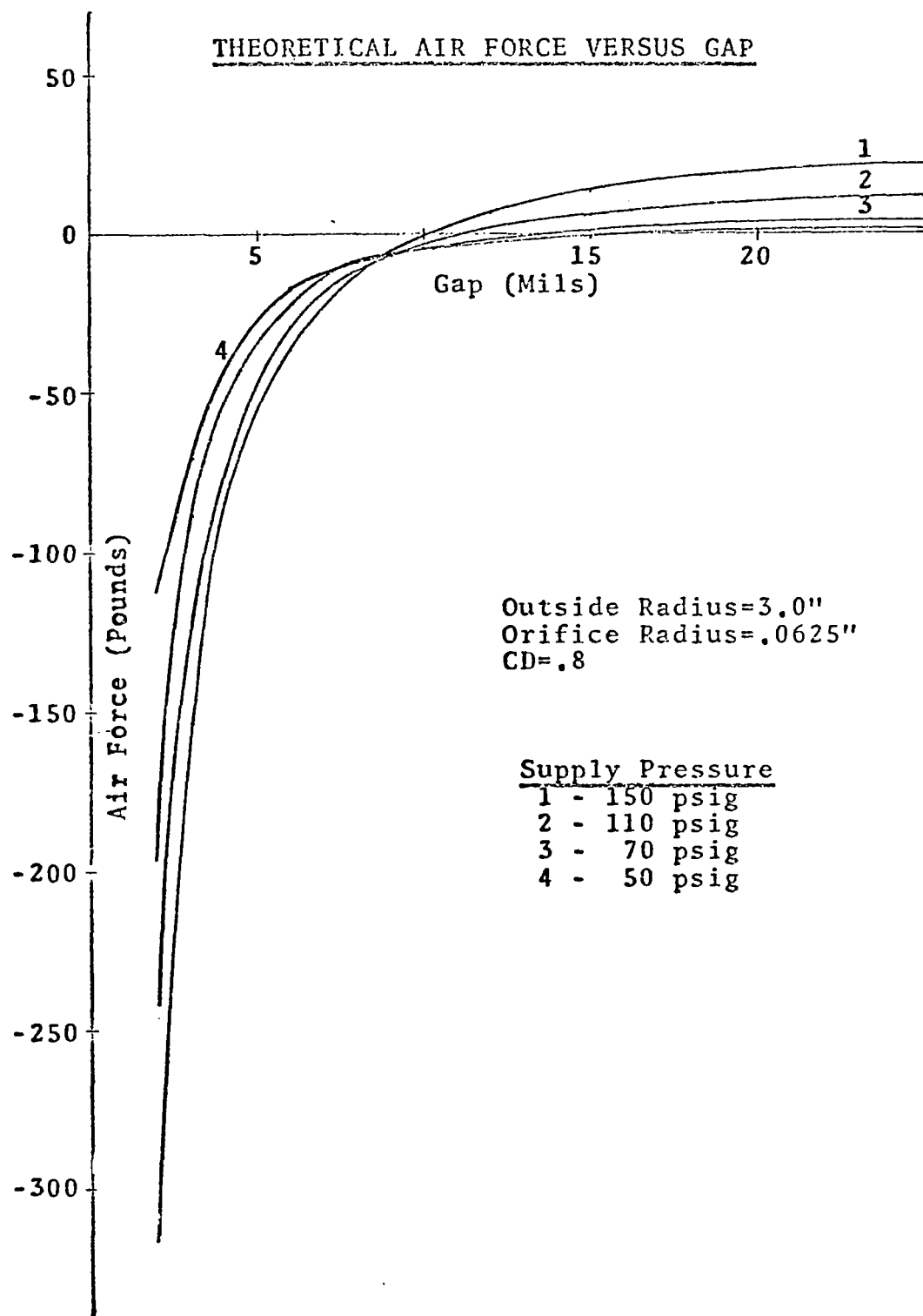


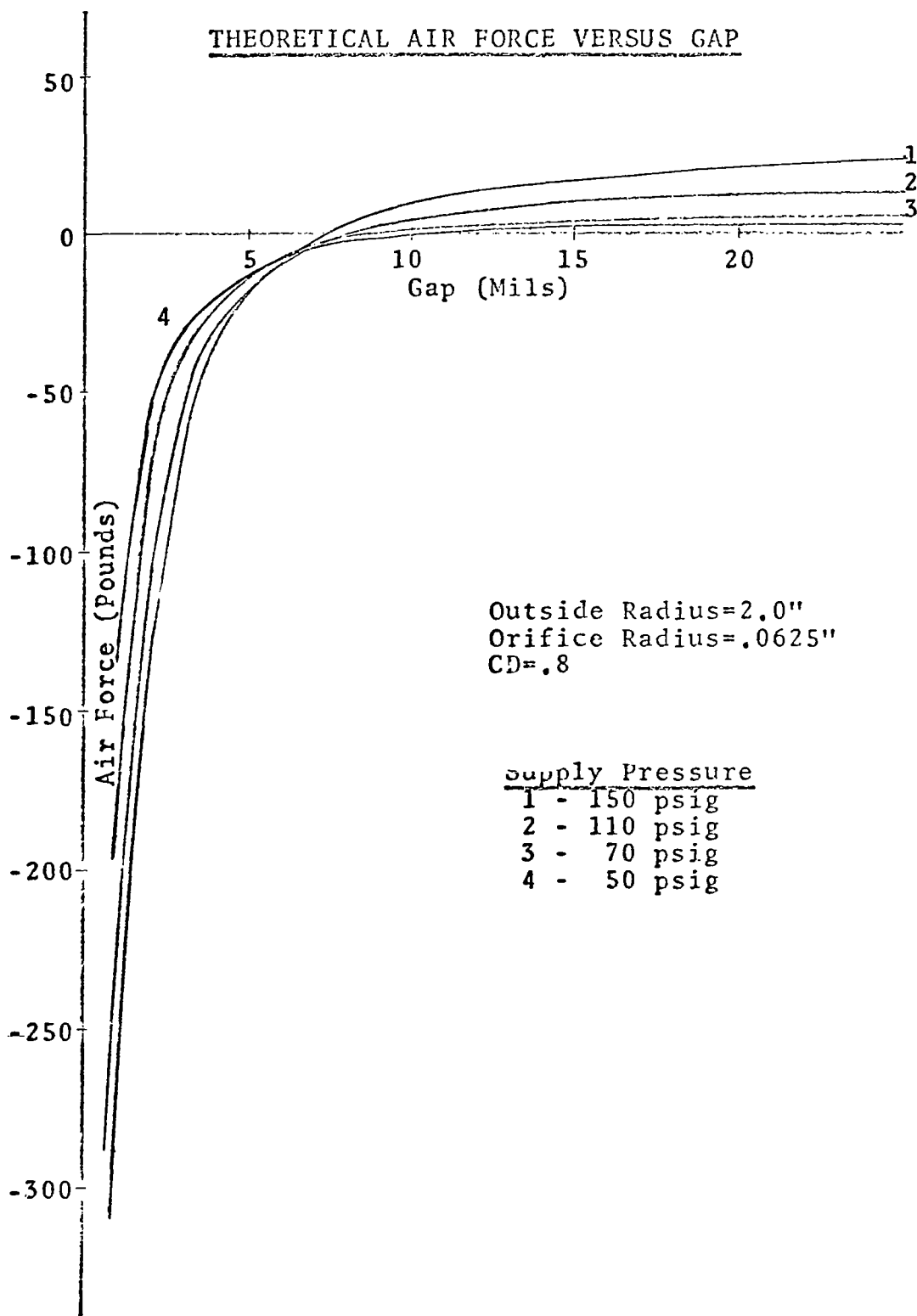


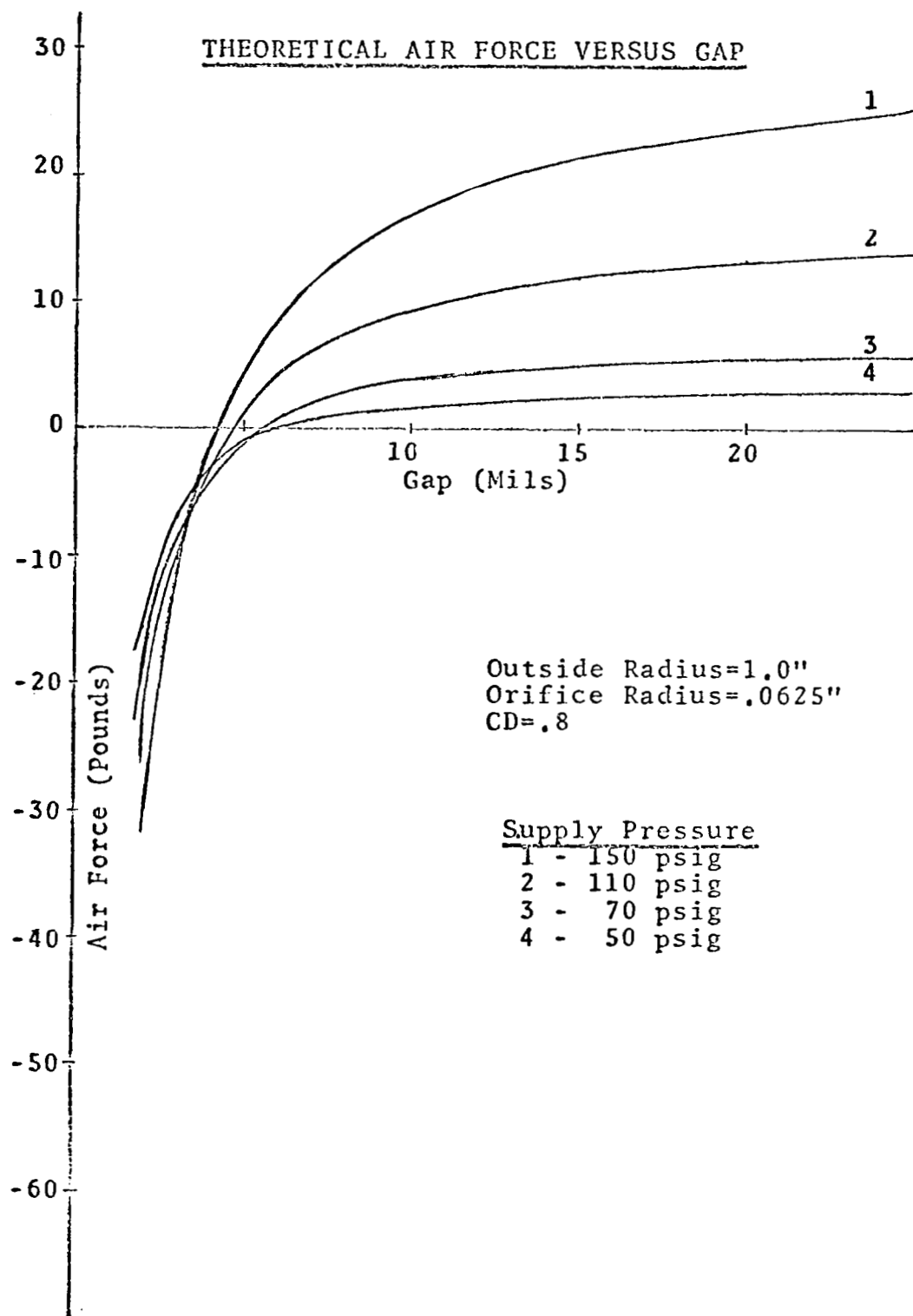


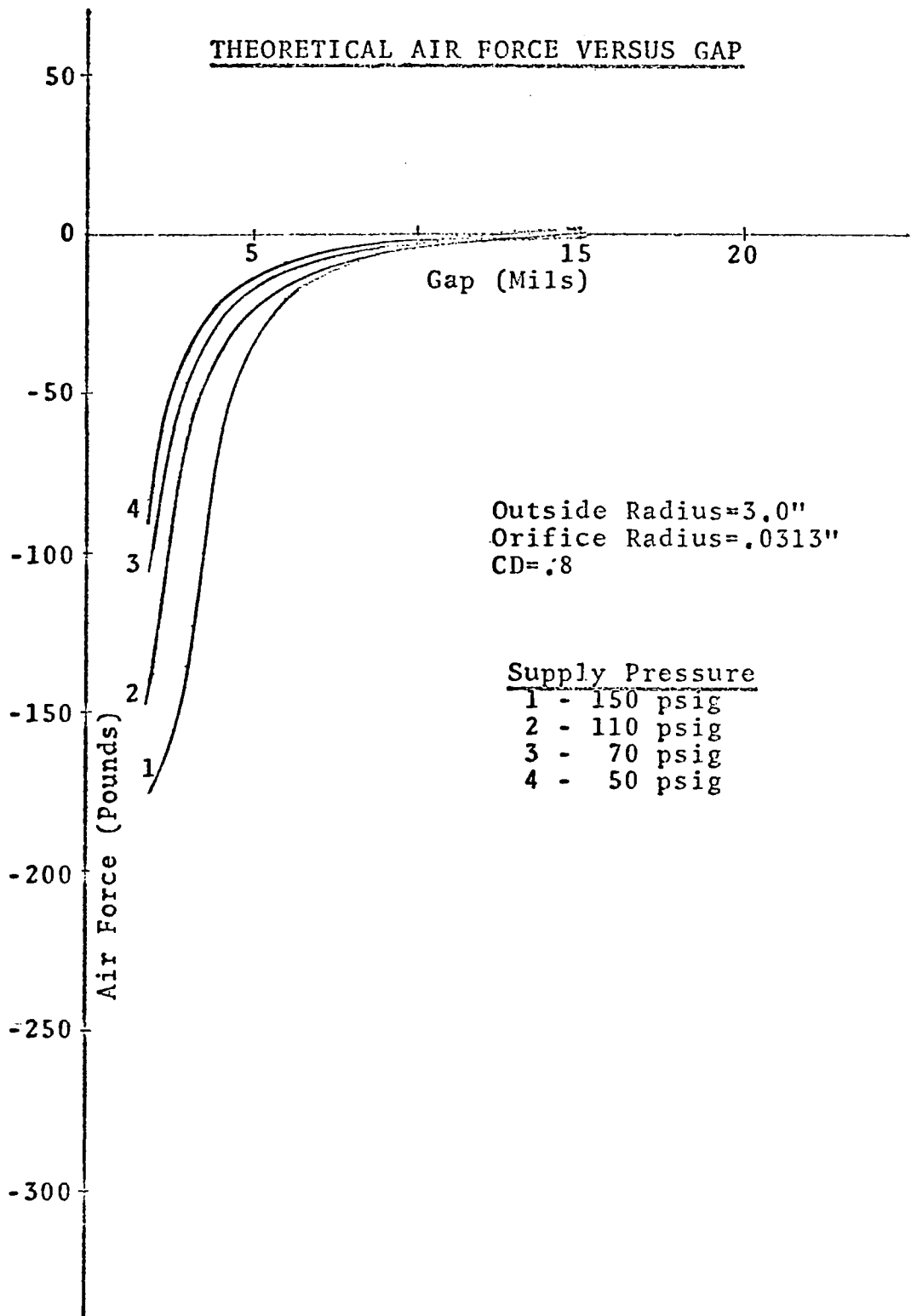


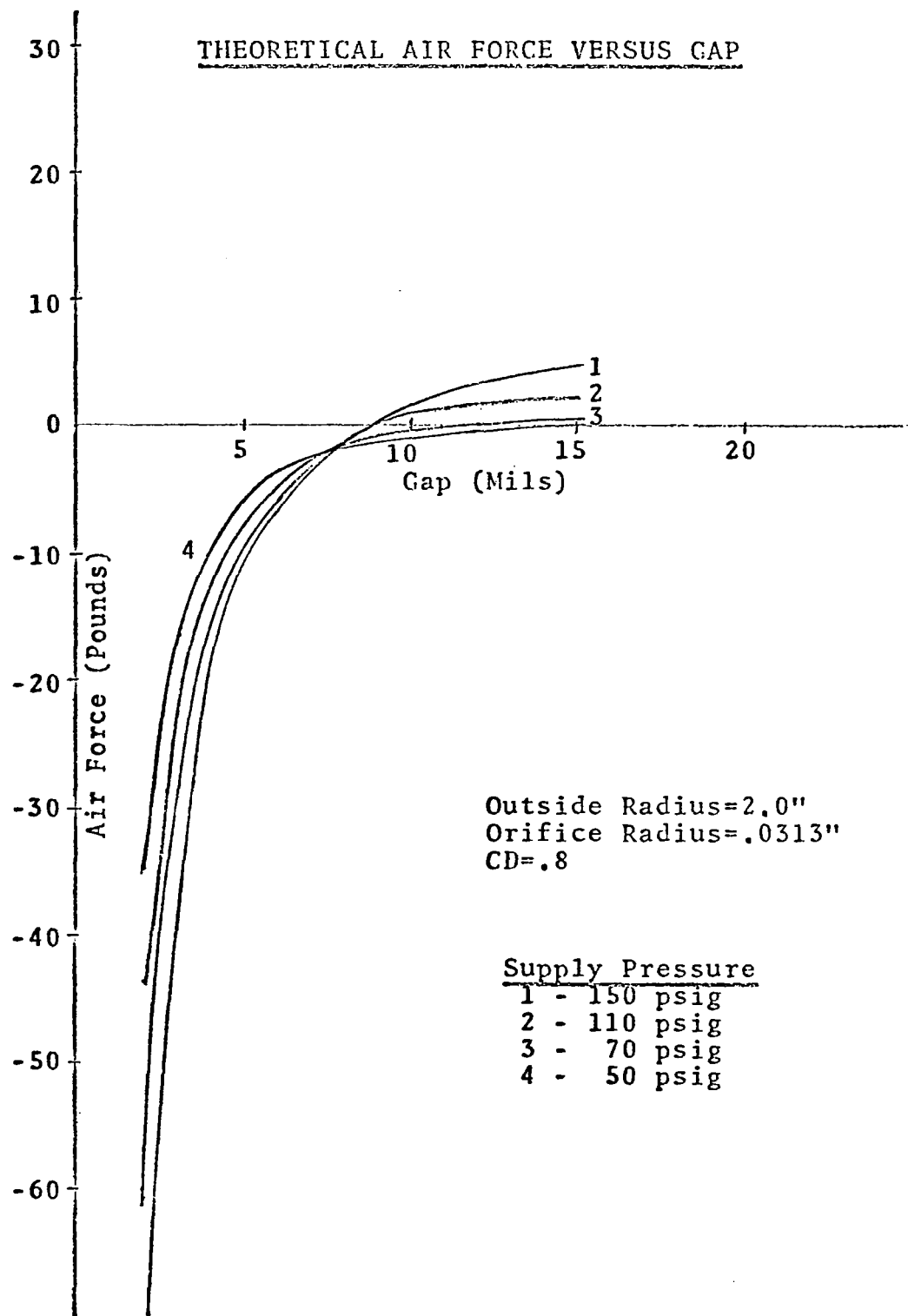
THEORETICAL AIR FORCE VERSUS GAP

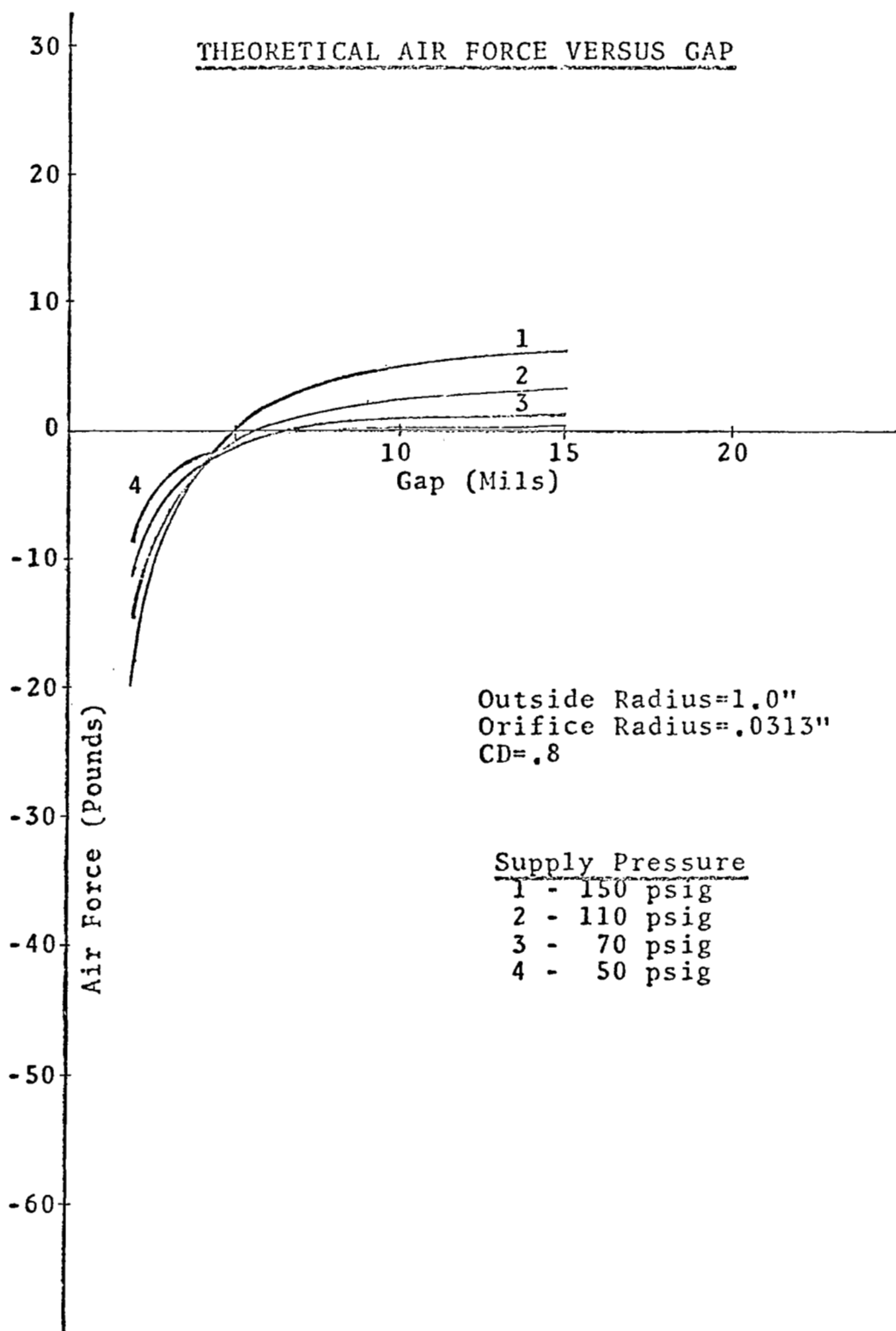












APPENDIX D

```

C  INSIDE SHELL  OPTIMIZATION
C  SOLID CORE
C  INDOX VI A
1  FORMAT(1)
2  FORMAT(5X 3E10.6)
10 FORMAT(5X3HRD26X3HRD16X3HRD36X3HRD06X2HTM7X2HT17X2HT27X2HWM
17X2HWS7X2HWE7X2HWT)
11 FORMAT(2X 1E9.4)
12 FORMAT(10X2HFM10X2HFS10X2HFC10X2HFL10X3HFG19X3HFG29X2HFT10X3HPI9X3HGPS1
13HGAP)
13 FORMAT(5X 9E12.5)
C  ALL INPUTS MUST BE IN THE FOLLOWING UNITS LENGTH(INCH): FLUX
C  DENSITY(GAUSS), MAGNETIC INTENSITY( OERSTED), DENSITY(POUNDS PER
C  INCH CUBE), PERMEABILITY(GAUSS PER OERSTED)
C  ALL CALC ARE IN MKS SYSTEM
DEL=.1
DEL=.015
DEL=DEL*.0254
E=.01
E=E*.025
SMALL=.0001
SMALL=0.001
SMALL=.00001
PI=3.14159
U11=1.
U21=1.
PO=4.0*PI*10.0**(-7)
CLEAR=0.0
CLEAR=CLEAR*.0254
TO=0.09
TO=TO*.0254
STEP=0.001
STEP=STEP*.0254
X=0.006
X=X*.0254
KK=26
C  IRON PROPERTIES
RHOS=0.28
RHOS=RHOS*4.448/(0.0254**3)
PIV=560.0
PIV=PIV*PO
PIR=347.0

```

```

PIR=PIR*PO
BIMAX=14000.0
BIMAX=BIMAX*10.0**(-4)
C INDOX VI A PROPERTIES
RHOM=.162
RHOM=RHOM*4.448/(0.0254**3)
PMR=1.08
PMR=PMR*PO
WOM=3000.
WOM=WOM*79.58
BMMAX=3250.0
BMMAX=BMMAX*10.0**(-4)
C FILLER
RHOF=0.0361
RHOF=RHOF*4.448/(0.0254**3)
C GEOMETRY
READ(5,1)(RD2,TM,RD0)
WRITE(6,2)(RD2,TM,RD0)
RD2=RD2*0.0254
TM=TM*0.0254
RD0=RD0*0.0254
RR1=SQRT((BMMAX*RD2**2+BIMAX*RD0**2)/(BIMAX+BMMAX))
RRD1=RR1+0.000254
RD1=RRD1
PHI=0.0
100 AM=PI*(RD2**2-RD1**2)
RM=TM/(PMR*AM)
VOM=WOM*TM
PD3=SQRT((BMMAX*AM+BIMAX*PI*RD0**2)/(BIMAX*PI))
T2=RD3-RD0
T1=BMMAX*AM/(PI*BIMAX*RD3*2.)
TC=T1
C CALC TOTAL WEIGHT
IF(T1.LT.T0) T0=T1
SL=(T0-T1)/(RD2-RD3)
V1=2.0*PI*(SL*(RD2**3-RD3**3)/3.0+(T1-SL*RD3)*(RD2**2-RD3**2)/2.)
WS=RHOS*(PI*(TM+CLEAR+T1)*(RD3**2-RD0**2)+V1)
WM=RHOM*AM*TM
WF=RHOF*PI*(TM+CLEAR)*(RD1**2-RD3**2)
WT=WS+WM+WF
C CLOSED CIRCUIT CALC
RS1=(RD2-RD1)/(AM+2.*PI*RD1*T1)
RS2=ALOG(RD1/RD3)/(2.*PI*T1)
RS3=(T1+T2)/(8.*(RD3*T1+(RD3-T2/2.)*T2))
RS4=TM/(2.*PI*(RD3-T2/2.)*T2)
RSV=(RS1+RS2+RS3+RS4)/PIV
RC1=(RD2-RD1)/(AM+2.*PI*RD1*TC)
RC2=RS2*T1/TC
RC3=(TC+T2)/(8.*(RD3*TC+(RD3-T2/2.)*T2))
RCV=(RC1+RC2+RC3)/PIV
RL=RS2*T1*2.0/(PO*TM)
RLPRCV=RL+RCV
CS1=WOM*RLPRCV/((RM+RSV)*PLPRCV +RL*RCV)
VS1=RSV*CS1

```

```

VC1=CS1*RCV*RL/RLPCV
CC1=VC1/RCV
RS=RSV*PIV/PIR
RC=RCV*PIV/PIR
VOS=CS1*RS-VS1
VOC=CC1*RC-VC1
PG1P=1./12.*P1*P0*(RD3-T2/2.)*T2)
RG2P=1.0/(P0*AM)
RGP=PG1P+RG2P
R1=RM+RS+RL
RLSQ=RL**2
RG1=X*RG1P
RG2=X*RG2P
R2=RG1+RG2+RL+RC
CM=(R2*(VOM+VOS)+RL*VOC)/(R1*R2-RLSQ)
CC=(VOC+RL*CM)/R2
CL=CM-CC
CMP=-RL*RG2P*(RL*(VOM+VOS)+R1*VOC)/((R1*R2-RLSQ)**2)
CCP=(R2*RL*CM-(VOC+RL*CM)*RGP)/(R2**2)
CLP=CMP-CCP
FM=RM*CM*CMP-VOM*CMP
FS=RS*CM*CMP-VOS*CMP
FC=RC*CC*CCP-VOC*CCP
FL=RL*CL*CLP
FG1=(RG1P*CC**2)/2+RG1*CC*CCP
FG2=(RG2P*CC**2)/2+RG2*CC*CCP
FT=FM+FS+FC+FL+FG1+FG2
IF(ICOND.EQ.3) GO TO 130
IF(ICOND.EQ.2) GO TO 120
PHICOM=ABS(FT/WT-PHI)
PHI=FT/WT
IF(PHICOM.LT.SMALL) GO TO 150
110 RD1=RD1+E
ICOND=2
GO TO 100
120 PHIRD1=FT/WT
G1=PHIRD1-PHI
RD1=RD1-E
TM=TM+E
ICOND=3
GO TO 100
130 PHITM=FT/WT
TM=TM-E
G2=PHITM-PHI
D=50PT(G1**2+G2**2)
AN1=G1/D
AN2=G2/D
U12=G1/ABS(G1)
U22=G2/ABS(G2)
Q1=U11*U12
Q2=U21*U22
IF((Q1.LT.0).AND.(Q2.LT.0)) GO TO 140
GO TO 145
END DEL=DEL/2.

```



```

E=E/2.
145 RD1=RD1+AN1*DEL
TM=TM+AN2*DFL
ICOND=1
U11=U12
U21=U22
GO TO 100
150 CONTINUE
RD2E=RD2/0.0254
RD1E=RD1/0.0254
RD3E=RD3/0.0254
RD0E=RD0/0.0254
TME=TM/0.0254
T1E=T1/0.0254
T2E=T2/0.0254
WME=WM/4.44A
WSE=WS/4.44A
WFE=WF/4.44A
WTE=WT/4.44A
WRITE(6,10)
WRITE(6,11)(RD2E,RD1E,RD3E,RD0E,TME,T1E,T2E,WME,WSE,WFE,WTE)
WRITE(6,12)
DO 180 K=1,KK
PB=K-1
Y=BB*STEP
RG1=Y*RG1P
RG2=(X+CLEAR)*RG2P
R2=RG1+RG2+RL+RC
CM=(R2*(VOM+VOS)+RL*VOC)/(R1*R2-RLSQ)
CC=(VOC+RL*CM)/R2
CL=CM-CC
CMP=-RL*RG1*(RL*(VOM+VOS)+R1*VOC)/((R1*R2-RLSQ)**2)
CCP=(R2*RL*CM-(VOC+RL*CM)*RG1)/(R2**2)
CLP=CM-CMP
FM=RM*CM*CMP-VOM*CMP
FS=RS*CM*CMP-VOS*CMP
FC=RC*CC*CCP-VOC*CCP
FL=RL*CL*CLP
FG1=(RG1P*CC**2)/2+RG1*CC*CCP
FG2=(RG2P*CC**2)/2+RG2*CC*CCP
FT=FM+FS+FC+FG1+FG2
FME=FM/4.44A
FSE=FS/4.44A
FCE=FC/4.44A
FLE=FL/4.44A
FG1E=FG1/4.448
FG2E=FG2/4.448
FTE=FT/4.44A
PHI=FTE/WTE
X=X/0.0254
WRITE(6,13)(FME,FSE,FCE,FLE,FG1E,FG2E,FTE,PHI,X)
180 CONTINUE
END

```

```

Δ LIST
Δ FOR MAG
C MAGNET SHELL OPTIMAZATION AND FORCE PROG INDOX V
1 FORMAT( )
12 FORMAT(5X 2HEM 7X 2HES 7X 2HEC 7X 2HFL 7X 3HEG1 6X 3HEG2 6X 3HEFF
15X 5HREACH 5X 3HPHI 7X 2HFT 7X 3HGAP)
13 FORMAT(2X 11E9.4)
14 FORMAT(14X 3HGAP)
15 FORMAT(10X F10.5)
16 FORMAT(5X 3HRD1 6X 3HRD2 6X 3HRD3 6X 2HTM 7X 2HT1 7X 2HT2 7X 2HWM
17X 2HWS 7X 2HWP 7X 2HWF 7X 2HWT 7X 2HFI 7X 3HPHI)
17 FORMAT(2X 12E9.4,E12.6)
19 FORMAT(5X 3E10.5)
C ALL INPUTS MUST BE IN THE FOLLOWING UNITS LENGTH(INCH), FLUX
C DENSITY(GAUSS), MAGNETIC INTENSITY( OERSTED), DENSITY(POUNDS PER
C INCH CUBE), PERMEABILITY(GAUSS PER OERSTED)
C ALL CALC ARE IN MKS SYSTEM
PI=3.1416
PO=4*PI*10.0**-7
L=U
TINY=1.000
TINY=TINY*10.0**-4
CLEAR=0.000
CLEAR=CLEAR*0.0254
STEP=0.001
STEP=STEP*0.0254
SMALL=1.0 E-7
SMALL=0.0001
NN=3
KK=26
C IRON PROPERTIES
RHOS=0.280
RHOS=RHOS*4.448/(0.0254**3)
PIV=1170.0
PIR=500.0
RIMAX=14000.0
PIV=PIV*PO
PIR=PIR*PO
RIMAX=RIMAX*10**-4
C INDOX V PROPERTIES
RHOM=.181
PMV1=1.05
PMV2=26.3
PMR=1.05
H01=3660.0
H02=2200.0
HINT=PMV1*PMV2*(H01-H02)/(PMV2-PMV1)
RMMAX2=3840.0
RHOM=RHOM*4.448/(0.0254**3)
PMV1=PMV1*PO
PMV2=PMV2*PO
PMR=PMR*PO
H01=H01*79.5A

```

```

H02=H02*79.5R
HINT=RINT*10.0**-4
BMMAX2=BMMAX*10.0**-4
C PIUG MG AND FILLER EPOXY
RHOP=0.065
RHOF=0.0361
RHOP=RHOP*4.448/(0.0254**3)
RHOF=RHOF*4.448/(0.0254**3)
RD0=0.25
RD0=RD0*0.0254
C INITIAL GEOMETRY
READ(5,1)(RD2,RD1,TM,AK)
RD3=RD2+0.500
RD1=RD1*0.0254*AK
RD2=RD2*0.0254*AK
RD3=RD3*0.0254*AK
TM=TM*0.0254*AK
JCOND=1
DO 180 N=1,NN
DEL=.05
DFL=0.01
DFL=0.1
DEL=DEL*0.0254
E=0.00001
E=0.01
E=0.1
E=E*0.0254
D=1.0/E
PHI=0.00
X=(N+4)*STEP
U31=-1.000
WRITE(6,14)
XF=X/0.0254
WRITE(6,15)(XE)
WRITE(6,16)
50 AM=PI*(RD2**2-RD1**2)
55 BMMAX=BMMAX2
T2=BMMAX*AM/(2*PI*RD3*BIMAX)
IF((RD3-T2/2.-RD2).LT.0.0) RD3=RD2+T2/2.+0.0001
PER01=2.0*P0*(-((RD3+T2/2+T2*RD1/(RD2-RD1))*ALOG((RD3-T2/2.-
1RD2)/(RD3+T2/2.-RD1)))/(1.0+T2/(RD2-RD1))-3.0*(RD2-RD1-T2)/4.0)
PER02=PI*P0*TM/ALOG((RD3-T2/2)/RD2)
R0=1.0/(PER01+PER02)
V01=H01*TM
V02=H02*TM
RM=TM/(PMR*AM)
ROM1=TM/(PMV1*AM)
ROM2=TM/(PMV2*AM)
CINT=RINT*AM
CF=V01/(ROM1+R0)
IF(CF.GT.CINT) GO TO 60
CF=V02/(ROM2+R0)
60 VF=-R0*CF
RF=CF/AM

```

```

HF=VF/TM
VOM=-VF+RM*CF
HMMAX2=PMR*VOM/TM
COMPHM=ABS(BMMAX-BMMAX2)
IF(COMPHM.LT.TINY) GO TO 70
GO TO 55
70 T1=T2*RD3/RD2
TC=T1
C CALC TOTAL WEIGHT
WM=RHOM*AM*TM
WS=RHOS*PI*((RD3+T2/2)**2-RD1**2)*T1+2*RD3*T2*TM
WP=RHOP*PI*(RD1**2-RD0**2)*(TM+T1)
WF=RHOF*PI*((RD3-T2/2)**2-RD2**2)*TM
WT=WM+WS+WP+WF
C CLOSED CIRCUIT CALC
RS1=(RD2-RD1)/(AM+2*PI*RD2*T1)
RS2=ALOG((RD3-T2/2)/RD2)/(2*PI*T1)
RS3=(T1+T2)/(4*((RD3-T2/2)*T1+RD3*T2))
RS4=TM/(2*PI*RD3*T2)
RSV=(RS1+RS2+RS3+RS4)/PIV
RC1=(RD2-RD1)/(AM+2*PI*RD2*TC)
RC2=RS2*T1/TC
RC3=(TC+T2)/(4*((RD3-T2/2)*TC+RD3*T2))
RCV=(RC1+RC2+RC3)/PIV
RL=RS2*T1*2.0/(PO*TM)
RLPRCV=RL+RCV
CS1=VOM*RLPRCV/((RM+RSV)*RLPRCV+RL*RCV)
VS1=RSV*CS1
VC1=CS1*RCV*RL/RLPRCV
CC1=VC1/RCV
RS=RSV*PIV/PIR
RC=RCV*PIV/PIR
VOS=CS1*RS-VS1
VOC=CC1*RC-VC1
RG1P=1.0/(2*PI*PO*RD3*T2)
RG2P=1.0/(PO*AM)
RGP=RG1P+RG2P
R1=RM+RS+RL
RLSQ=RL**2
RG1=X*RG1P
RG2=X*RG2P
R2=RG1+RG2+RL+RC
CM=(R2*(VOM+VOS)+RL*VOC)/(R1*R2-RLSQ)
CC=(VOC+RL*CM)/R2
CL=CM-CC
CMP=-RL*RGP*(RL*(VOM+VOS)+R1*VOC)/((R1*R2-RLSQ)**2)
CCP=(R2*RL*CMP-(VOC+RL*CM)*RGP)/(R2**2)
CLP=CM-CMP
FM=RM*CM*CMP-VOM*CMP
FS=RS*CM*CMP-VOS*CMP
FC=RC*CC*CCP-VOC*CCP
FL=RL*CL*CLP
FG1=(RG1P*CC**2)/2+RG1*CC*CCP
FG2=(RG2P*CC**2)/2+RG2*CC*CCP

```

```

FT=FM+FS+FC+FL+FG1+FG2
GO TO 104
102 WRITE(6,12)
DO 103 K=1,KK
X=(K-1)*STEP
RG1=X*RG1P
RG2=(X+CLEAR)*RG2P
R2=RG1+RG2+RL+RC
CM=(R2*(VOM+VOS)+RL*VOC)/(R1*R2-RLSQ)
CC=(VOC+RL*CM)/R2
CL=CM-CC
CMP=-RL*RG1*(RL*(VOM+VOS)+R1*VOC)/((R1*R2-RLSQ)**2)
CCP=(R2*RL*CM-(VOC+RL*CM)*RG1)/(R2**2)
CLP=CMP-CCP
FM=RM*CM*CMP-VOM*CMP
FS=RS*CM*CMP-VOS*CMP
FC=RC*CC*CCP-VOC*CCP
FI=RL*CL*CLP
FG1=(RG1P*CC**2)/2+RG1*CC*CCP
FG2=(RG2P*CC**2)/2+RG2*CC*CCP
FM=FM/4.448
FS=FS/4.448
FC=FC/4.448
FI=FI/4.448
FG1=FG1/4.448
FG2=FG2/4.448
FT=FM+FS+FC+FL+FG1+FG2
PHI=FT/WTE
X=X/0.0254
EFF=FT*X/WME
REACH=X/SQRT(FT)
WRITE(6,13)(FM,FS,FC,FL,FG1,FG2,EFF,REACH,PHI,FT,X)
103 CONTINUE
GO TO 180
104 IF(ICOND.EQ. 4) GO TO 130
PHICOM=ABS(FT/WT-PHI)
PHI=FT/WT
L=L+1
IF(L.EQ. 10) GO TO 105
GO TO 108
105 T1E=T1/0.0254
T2E=T2/0.0254
RD1E=RD1/0.0254
RD2E=RD2/0.0254
RD3E=RD3/0.0254
TME=TM/0.0254
WME=WM/4.448
WSE=WS/4.448
WPE=WP/4.448
WFE=WF/4.448
WTE=WME+WSE+WPE+WFE
FTE=FT/4.448
WRITE(6,17)(RD1E,RD2E,RD3E,TME,T1E,T2E,WME,WSE,WPE,WFE,WTE,FTE,PH
11)

```

```

WRITE(6,19)(HF,HE,COMPHM)
L=0
IF((PHICOM.LT.SMALL).AND.(N.EQ.2)) GO TO 102
IF(PHICOM.LT.SMALL) GO TO 180
108 ICOND=4
RD3=RD3+E
GO TO 50
130 PHIRU3=FT/WT
G3=(PHIRU3-PHI)/(E*D)
RD3=RD3-E
D=ABS(G3)
U32=G3/ABS(G3)
Q3=U31*U32
IF(Q3.LT.0.0) GO TO 142
GO TO 145
142 DEL=DEL/2
E=L/2
145 RD3=RD3+U32*DEL
RD3MIN=RD2+T2/2.0
IF(RD3.GT.RD3MIN) GO TO 148
RD3=RD3MIN+0.0001
148 CONTINUE
ICOND=1
U31=U32
GO TO 50
180 CONTINUE
END
FIN

```